SPbGASU
1832

ARCHITECTURE & ENGINEERING

Volume 10
Issue 4
December, 2025

By Architects. For Architects.
By Engineers. For Engineers.

Architecture
Civil and Structural Engineering
Mechanics of Materials
Building and Construction
Urban Planning and Development
Transportation Issues in Construction
Geotechnical Engineering and Engineering Geology
Designing, Operation and Service
of Construction Site Engines

eISSN: 2500-0055
http://aej.spbgasu.ru/

Architecture and Engineering

Volume 10 Issue 4 (2025)

ISSN: 2500–0055

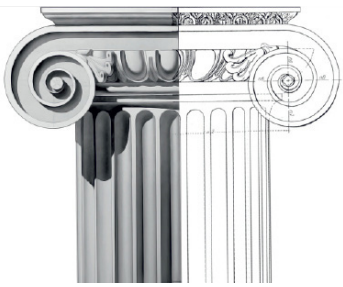

CONTENTS

Architecture and Engineering
peer-reviewed scientific journal
Start date: 2016/03
4 issues per year

Founder, Publisher:
Saint Petersburg State University of Architecture and Civil Engineering

Indexing:
Scopus, Russian Science Citation Index, Directory of Open Access Journals (DOAJ), Google Scholar, Index Copernicus, Ulrich's Periodicals Directory, WorldCat, Bielefeld Academic Search Engine (BASE), Library of University of Cambridge and CyberLeninka

Corresponding address:
4 Vtoraya Krasnoarmejskaja Str.,
St. Petersburg, 190005, Russia

Website: http://aej.spbgasu.ru/
Phone: +7(812) 316 48 49
Email: aejeditorialoffice@gmail.com

Date of issue: December 30, 2025

The Journal was re-registered by the Federal Service for Supervision of Communications, Information Technologies and Mass Communications (Roskomnadzor) on May 31, 2017;
registration certificate of media organization El No. FS77–70026

DOI: 10.23968/2500-0055-2025-10-4-3-16

IMPACT OF ADAPTIVE BIOMIMETIC BUILDING SKINS ON INDOOR THERMAL COMFORT: A COMPUTATIONAL EVALUATION

Selma Saci Hadef[1]*, Sara Khelil[2], Djamel Alkama[3]

[1] Civil Engineering and Hydraulics Laboratory (LGCH), Department of Architecture, Faculty of Sciences and Technology, 8 Mai 1945 University, Guelma, Algeria

[2] Built Environment Resilience Laboratory (BERLab), Department of Architecture, Faculty of Sciences and Technology, Mohamed Khider University, Biskra, Algeria

[3] Architecture, Sustainability and Resilient Cities Laboratory, Department of Architecture, Faculty of Sciences and Technology, 8 Mai 1945 University, Guelma, Algeria

*Corresponding author's email: sacihadef.selma@univ-guelma.dz

Abstract

Introduction. Recent advances in computational design have transformed architectural facades from static envelopes into dynamic systems capable of adapting to environmental conditions in order to enhance thermal comfort and energy efficiency. **Purpose of the study**. This study aims to evaluate the thermal performance of an adaptive biomimetic building skin (ABBS), inspired by plant thermoregulation mechanisms, applied to a typical residential building located in Guelma, Algeria, which is characterized by a hot Mediterranean climate. **Methods**. Following the thermal validation of a base model, the research integrated two complementary approaches: a problem-driven biomimetic strategy to define the morphology and kinetic behavior of facade modules, and a parametric simulation workflow developed in Rhino Grasshopper, coupled with the Ladybug and Honeybee plugins for environmental and energy analysis. The ABBS was tested under five aperture configurations (−30° to +30°) across east, south, and west orientations during representative summer and winter periods, based on the ASHRAE Standard 55 adaptive comfort model**. Results.** The results demonstrate that the best-performing scenarios achieved up to a 17.7 % reduction in overheating hours during summer and up to a 22 % improvement in thermal comfort during winter through enhanced passive solar gains**.** This study confirms the potential of bio-inspired responsive facades to optimize indoor thermal conditions and highlights the effectiveness of computational biomimicry as a pathway toward climate-adaptive and energy-efficient architectural envelopes contributing to sustainable building design.

Keywords: biomimicry; adaptive building skins; computational design; parametric simulation; thermal comfort.

Introduction

In the context of climate change and the urgency of energy transition, the building sector plays a pivotal role, accounting for approximately 30 % of global energy consumption and 26 % of greenhouse gas emissions (International Energy Agency, 2023). Nearly 60 % of this energy is allocated to heating and cooling systems (Al-Obaidi et al., 2017) to ensure adequate thermal comfort (Betman et al., 2024). Consequently, reducing this demand has become a strategic priority for achieving carbon neutrality by 2050 (Sommese et al., 2022). The building envelope, particularly glazed surfaces, offers significant potential for optimization (Öztürk et al., 2024), as it can account for up to 60 % of a building's total thermal gains and losses (Kheybari et al., 2025). In continuous interaction with dynamic environmental factors such as solar radiation and outdoor air temperature (Tabadkani et al., 2021), the envelope strongly influences heat transfer processes, thereby affecting occupants' thermal comfort (Abbaas et al., 2023). In response to these challenges, the capacity of the building envelope to adapt to fluctuating climatic conditions has become a key strategy for enhancing overall building performance. In this context, dynamic facades have emerged as innovative technological solutions capable of adjusting their thermal, optical, and morphological properties in real time in response to climatic conditions, solar exposure, or seasonal variations (Hosseini et al., 2021). These responsive systems offer an effective solution to the growing demands for sustainability and occupant comfort (Elhennawi and Sameh, 2025). Goharian et al. (2025) classify adaptive facades into several categories, ranging from passive systems based on orientation strategies or intrinsic material properties, to active, intelligent, and kinetic solutions that integrate movable elements and real-time control technologies. These approaches are further expanded by interactive

or switchable facades capable of modifying their physical or optical behavior directly in response to environmental stimuli. Among these strategies, biomimetic facades are particularly noteworthy for their ability to emulate adaptive mechanisms found in nature. By translating biological responses into architectural systems, biomimetic design enables the development of responsive, autonomous, and energy-efficient building envelopes aligned with contemporary requirements for sustainability and thermal comfort. Nature, particularly plants, offers a wide range of adaptive strategies for responding to environmental fluctuations (Bijari et al., 2025). Despite their immobility, similar to buildings, plants have evolved mechanisms to react to external stimuli such as light, temperature, and humidity (Sheikh and Asghar, 2019). These responses often manifest as movements in specific organs, including leaves, stems, or petals. Plant movements are generally classified into two main types: tropisms, which are directional responses, and nastic movements, which are non-directional (Shahin et al., 2023). In particular, temperature variations can induce thermotropic and thermonastic behaviors, which serve as valuable natural models for dynamic adaptation in architectural applications.

These natural mechanisms have become a fundamental source of inspiration for the development of dynamic biomimetic envelopes capable of reconfiguring themselves in response to ambient thermal conditions, thereby improving both energy efficiency and occupant comfort (Saci Hadef et al., 2025). The advancement of computational design understood as the use of algorithmic and parametric tools to generate, simulate, and optimize architectural forms and behaviors has been instrumental in translating these biological strategies into architectural applications. In particular, parametric modeling environments such as Grasshopper enable the simulation and iterative refinement of complex adaptive behaviors with a high degree of precision (Maksoud et al., 2023). When coupled with the integration of smart materials responsive to environmental inputs, computational tools facilitate the design of low-energy systems that dynamically react to changing conditions (Brzezicki 2024a; Sommese et al., 2024). This synergy between biology, algorithmic design, and materials science has given rise to a new generation of responsive architectural skins that align energy performance with enhanced indoor comfort (Altameemi and Jabbar, 2025; Soliman and Bo, 2023).

Numerous studies, including those by Hadbaoui (2018), Khelil et al. (2020), Kuru et al. (2018), Mohamed Abd El-Rahman et al. (2020), and Soliman and Bo (2023), demonstrated the effectiveness of adaptive biomimetic envelopes in improving building thermal comfort. Drawing on plant-based thermoregulatory mechanisms and developed through computational design workflows particularly parametric platforms that enable the rapid generation, simulation, and optimization of multiple facade configurations these studies have produced responsive systems capable of modulating indoor conditions by reducing indoor temperatures and shortening periods of thermal discomfort across a wide range of climatic contexts.

These findings highlight the relevance of computational design in emulating the complex adaptive behaviors observed in the plant kingdom, thereby providing a robust foundation for the development of durable, high-performance, and responsive building envelopes. Nevertheless, two major gaps remain. First, most existing research focuses on office or commercial buildings, largely overlooking the residential sector, despite its significant share in global energy consumption. In Algeria, the residential sector is considered the most energy-intensive, accounting for 43 % of total national energy use (APRUE, 2019). Second, the majority of studies primarily address hot-arid climates, leaving warm Mediterranean climates (Csa) largely unexplored in biomimetic approaches to indoor thermal comfort.

The present study seeks to address these gaps by applying a computational biomimetic approach to residential buildings located within this climatic context. To this end, an adaptive biomimetic facade inspired by the morphological and behavioral adaptation mechanisms of the Heavenly Blue flower (*Ipomoea tricolor*) is proposed. The prototype is applied to a residential building situated in Guelma, Algeria, representative of a hot Mediterranean climate (Csa) (Fig. 1), a context that remains underexplored in current biomimetic research. Leveraging a parametric design workflow developed in Rhino Grasshopper, the proposed kinetic facade is designed and simulated to modulate its aperture in response to solar orientation and seasonal variations. Performance is evaluated through thermal simulations based on the adaptive comfort model defined by the ASHRAE Standard 55, with a particular focus on reducing thermal discomfort hours in order to lower heating and cooling energy demands. By extending biomimetic strategies to the residential sector, this work aims to deliver an architectural solution that integrates energy efficiency, indoor thermal comfort, and ecological innovation, thereby contributing to the broader objectives of energy transition and sustainable development.

Methods

To achieve the objectives of this research, a structured, multi-phase methodology was developed to assess the thermal performance of the proposed adaptive biomimetic facade system. The process begins with a climatic characterization of the

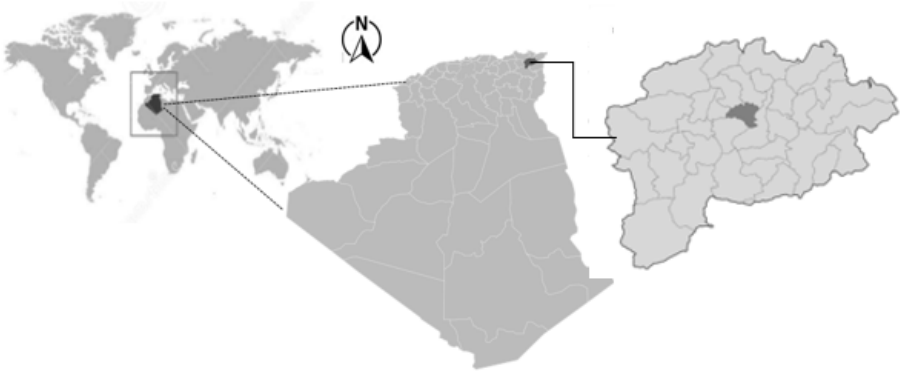

Fig. 1. Geographic location of the study area in Guelma, northeastern Algeria

study site, followed by a detailed description of the case study building. On-site measurements are then conducted to calibrate and validate a baseline thermal model. Subsequently, a biomimetic design approach is applied to develop the adaptive facade prototype. Finally, dynamic thermal simulations are performed to evaluate and compare the performance of the proposed solution with that of the existing envelope under both summer and winter conditions.

Climate Analysis

According to the Köppen Geiger climate classification, Guelma (northeastern Algeria) is characterized by a hot Mediterranean climate (Csa), defined by dry summers and cold, humid winters. Solar path diagrams (Figs. 2 and 3), generated for this location using the Climate Consultant software and based on the adaptive comfort model from the California Energy Code 2013, indicate that during the summer period, 1,385 hours per year require external shading, whereas 260 hours benefit from direct solar gains to maintain indoor comfort. In winter, this pattern is reversed: 1,096 hours require solar gains, while 566 hours demand shading when outdoor temperatures exceed 27°C. These results highlight the necessity of balancing effective solar protection during summer with optimal solar access in winter.

Case Study Description

The space under investigation is a room located on the third floor of a typical residential building in the “19 Juin” residential area, southeast of Guelma (36°45′18.67″ N, 7°42′74.09″ E). Positioned at an intermediate level, as shown in Fig. 4, in order to limit thermal gains from both the roof and the ground, the space measures 5.20 × 5.75 m with a ceiling height of 3.06 m. Oriented due east, it is fitted with a 3.00 × 1.60 m window, resulting in a window-to-wall ratio (WWR) of 30 %. Such a ratio is considered relatively high, increasing the risk of summer overheating as well as winter heat losses.

Validation Model

To validate the simulation model, a real residential living room was selected as the case study. On-site measurements were conducted on January 23 and July 25, representing extreme winter and summer conditions, respectively (Figs. 4 and 5).

Temperature data were collected at two-hour intervals from 8:00 a.m. to 6:00 p.m. using a Hanna HI991003 digital thermometer positioned 1 m above

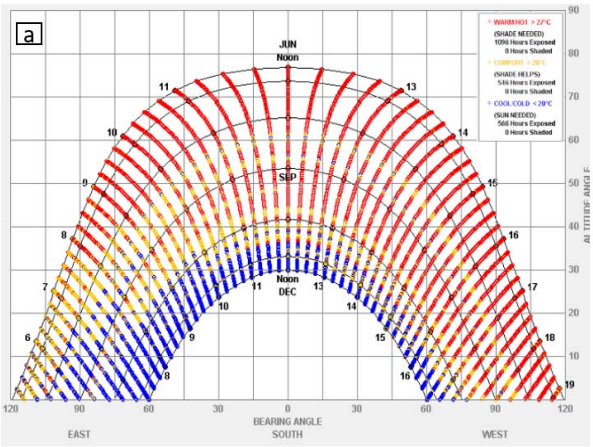

Fig. 2. Solar path diagrams for the city of Guelma, summer solstice

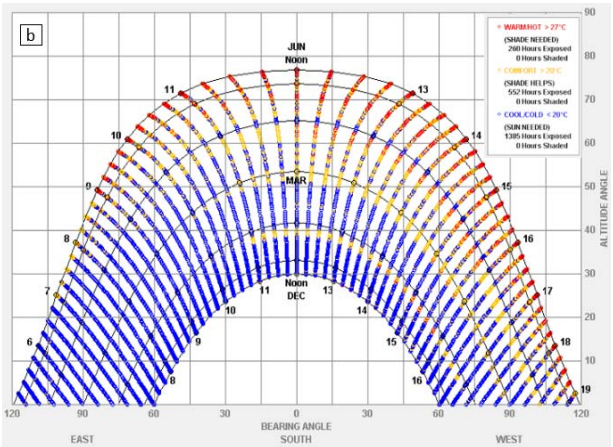

Fig. 3. Solar path diagrams for the city of Guelma, winter solstice

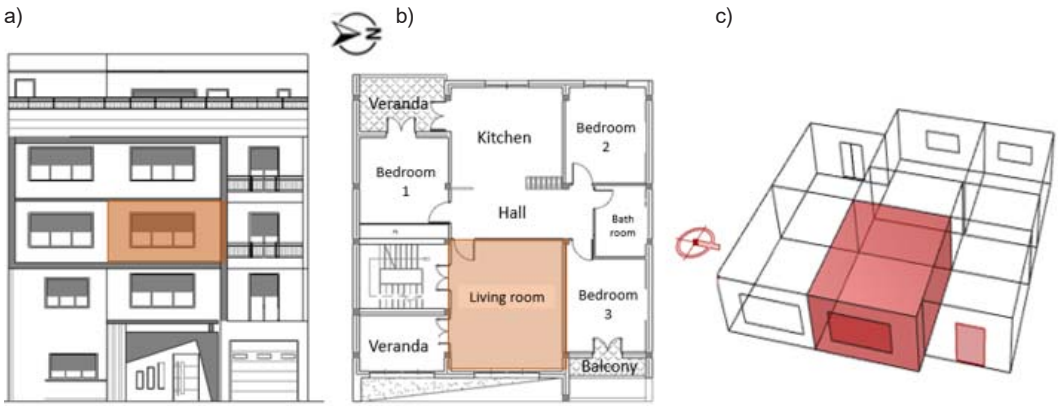

Fig. 4. Case study room: (a) facade view, (b) floor plan (scale 1:50), and (c) 3D perspective

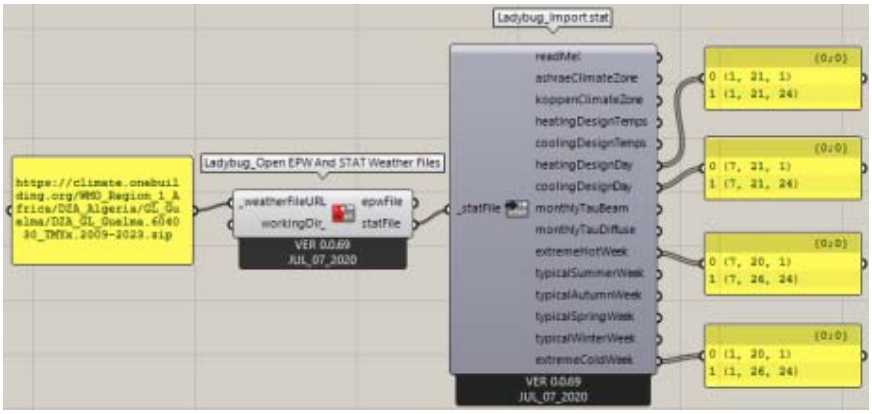

Fig. 5. Grasshopper parametric script used to identify representative days and extreme seasonal weeks for the climatic analysis of Guelma

the floor, in accordance with ASHRAE Guideline 14 (Chaturvedi et al., 2024). To ensure data reliability, indoor conditions were kept stable throughout the monitoring period: the HVAC system, lighting, and electrical appliances were turned off; the space remained unoccupied; and all doors, windows, and shading devices were controlled to eliminate internal and external heat gains. The resulting distribution of simulated operative temperatures is presented in Fig. 6.

To assess the accuracy of the simulation model, two statistical performance indicators were calculated: the mean bias error (MBE) and the coefficient of variation of the root mean square error (CV (RMSE)), using the following ASHRAE formulas:

$$MBE = \frac{\sum_{i=1}^{n}(Mi - Si)}{\sum_{i=1}^{n} Mi}; \quad (1)$$

$$CV\left(RMSE\right) = \frac{1}{\bar{y}}\sqrt{\frac{\sum_{i=1}^{n}(Mi - Si)^2}{n}}, \quad (2)$$

where *Mi* is the measured value, *Si* is the simulated value, *n* is the total number of values considered in the calculation ,and $\bar{y}$ is the mean of the measured values.

The results indicate excellent agreement between measured and simulated data, with an MBE of 0.1 % and a CV (RMSE) of 1.1 % during the summer period, and an MBE of −1.32 % and a CV (RMSE) of 2.92 % during the winter period. These values are well within the acceptable limits defined by ASHRAE Guideline 14-2014, which recommends an MBE within ±10 % and a CV (RMSE) below 30 %.

Adaptive Biomimetic Building Skin (ABBS) Design

The development of the adaptive facade system is based on a structured biomimetic design approach, articulated around the observation, abstraction, and transposition of principles derived from natural systems.

The biological inspiration is drawn from the Heavenly Blue Morning Glory (*Ipomoea tricolor*), a climbing plant characterized by phototropic and thermonastic movements of its petals. These petals unfold during daytime under the combined influence of light and temperature and close at night or under cooler conditions, following a helical kinetic motion driven by differential cell growth between the adaxial and abaxial surfaces. Fig.7 illustrates the open and closed states of the flower.

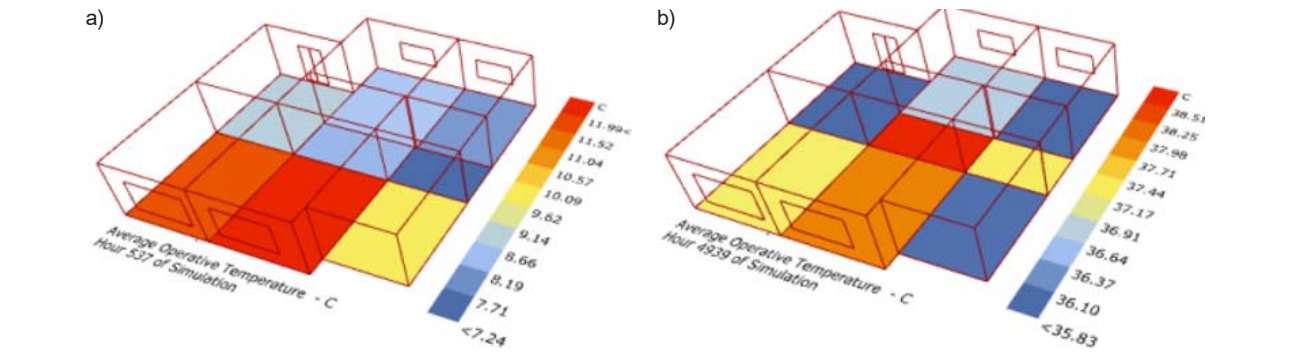

Fig. 6. Simulated distribution of operative temperature on the third floor, including the case study room: (a) hot summer day at 8:00 a.m.; (b) cold winter day at 4:00 p.m

Each facade module rotates around its longitudinal axis, reproducing this natural opening and closing mechanism within an angular range from −30° (closed state) to +30° (fully open state), with 15° increments, as illustrated in Fig. 8. Six modules are radially arranged around a fixed central axis, forming a kinetic cell capable of modulating the facade's solar permeability (Saci Hadef et al. 2025).

The functional transposition of this adaptive behavior led to the integration of shape memory polymers (SMPs), which are smart materials capable of altering their geometric configuration in response to thermal stimulation (Brzezicki 2024b). This material choice enables the system to adjust its morphology in real time according to climatic conditions: during summer, the elements expand to reduce solar gains, whereas in winter, they close to enhance passive solar heat gains (Chayaamor-Heil and Laracuente, 2020; Naeem et al., 2024). Consequently, the biomimetic process, rooted in an understanding of the thermal and photic interactions of *Ipomoea tricolor*, results in an autonomous kinetic facade system that integrates energy efficiency, seasonal adaptability, and a living-inspired architectural expression.

Fig. 7. Dynamic responses of Ipomoea tricolor (Heavenly Blue Morning Glory) to light and temperature variations

Building Thermal Performance Simulations

In this study, the thermal performance of the building was simulated using Rhinoceros 3D and Grasshopper, with the integration of the Ladybug and Honeybee plugins for energy analysis. Climate data in EPW format were imported via the One Climate Building platform, and simulations were carried out using the EnergyPlus engine. The 3D model was assigned the necessary physical properties to evaluate adaptive thermal comfort conditions.

The adaptive comfort chart, developed in accordance with ASHRAE Standard 55 and the EN 15251 Class I model (Amoruso et al., 2019), visualizes the comfort zone corresponding to an 80 % acceptability threshold, based on the relationship between indoor operative temperature and prevailing outdoor temperature (Lakhdari et al., 2021).

This diagram enables the identification of temperature combinations leading to thermal discomfort and provides a calculation of the total annual comfort hours within the analyzed zones (Lucarelli and Carlo, 2020).

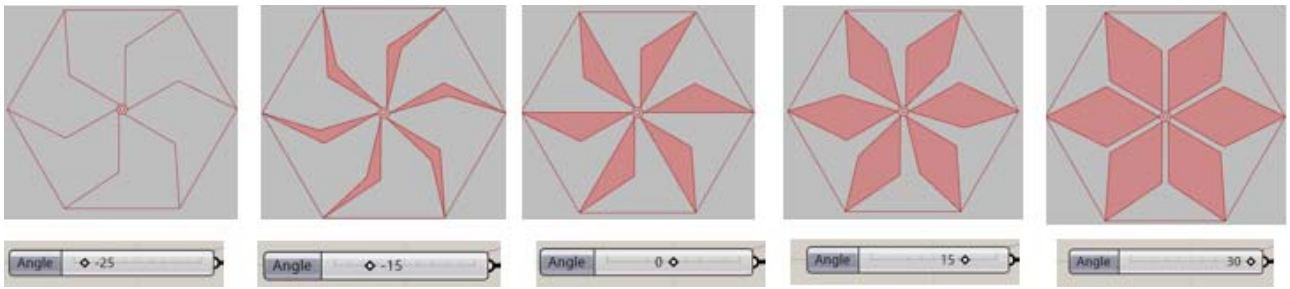

Fig. 8. Script of a single shading system unit under various configurations according to the orientation angle

Thermal Simulation Inputs

Within the Rhinoceros 3D environment and its Grasshopper plugin, the simulation parameters were classified as constant (fixed) and variable, according to their role in model construction and their influence on the simulation scenarios.

Constant parameters include the invariant characteristics of the simulation model, which were maintained identically across all investigated variants. These parameters relate to the following aspects.

Geometry (Modeling)

The test space (living room) (Fig. 9) was modeled in Rhinoceros 3D and integrated into Grasshopper for parametric simulation. This approach allows for the precise adjustment of shading system configurations in accordance with the defined scenarios.

Construction Materials

The building's structural system consists of reinforced concrete columns and beams. The materials composing each building element including the external and internal walls, intermediate floor, ground slab, roof, and windows were defined in Grasshopper, incorporating their thermo physical characteristics (Fig. 10). For opaque elements, the parameters considered include thermal conductivity, density, and specific heat capacity. For transparent elements, the selected indicators are thermal transmittance (U-value), solar heat gain coefficient (SHGC), and visible transmittance (VT). All thermophysical properties were defined in accordance with the Algerian Thermal Regulation (DTR, 1997).

Occupancy Profile

The living room, as the main space of the apartment, is primarily occupied during the afternoon and evening, from 12:00 p.m. to 12:00 a.m. (Lahmar et al., 2022), with a constant occupancy rate of 100 % (five occupants) after work or school hours. This occupancy profile accounts for recurrent domestic activities such as family gatherings and recreational activities (e.g., watching television, reading, and studying).

Temperature Setpoints and HVAC System

The indoor temperature setpoints were defined as 20°C during the winter heating period and 26°C during the summer cooling period.

The simulated HVAC system corresponds to an Ideal Loads Air System with a coefficient of performance (COP) of 2.7. This system does not represent a specific HVAC technology but instead calculates the ideal heating and cooling loads required to maintain the defined thermal comfort conditions.

Artificial Lighting

Artificial lighting levels were defined based on the installed fixtures and occupancy schedules, ensuring a lighting power density appropriate for the functional requirements of the living room. In accordance with ASHRAE recommendations, the minimum illuminance level was set to 300 lux to ensure adequate visual comfort during occupied periods (Fig. 11).

Equipment Loads

Internal electrical loads were estimated based on appliances commonly used in a residential living

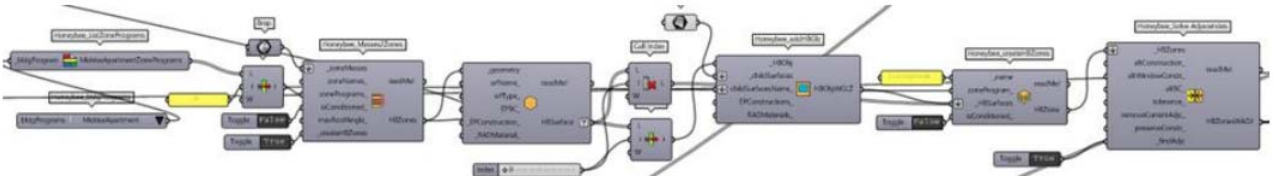

Fig. 9. Parametric definition of the test model generated in Grasshopper

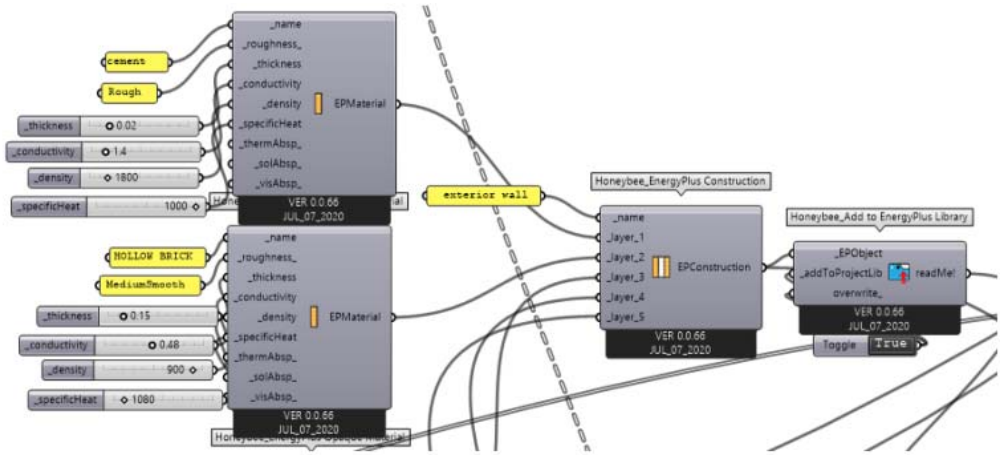

Fig. 10. Parametric definition of the external wall materials of the case study generated in Grasshopper

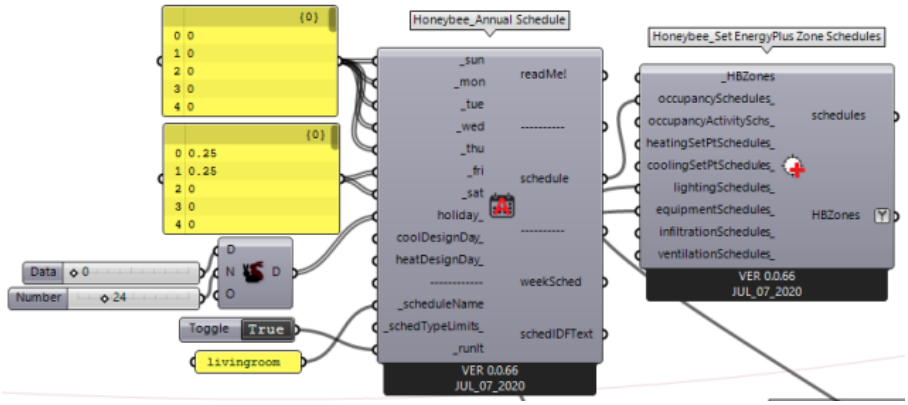

Fig. 11. Script defining the occupancy profile generated in Grasshopper

room, including a television, a set-top box or internet box, table or floor lamps, and chargers for electronic devices (e.g., phones and tablets). Based on these appliances, the total internal electrical load was set to 5 W/m², in accordance with reference values for residential living spaces (Fig. 12).

Shifting to the variable parameters, which represent the adjustable factors aimed at assessing their impact on the building's thermal and energy performance. This study focused on two main variables.

Orientation

Building orientation significantly influences solar exposure and heat gains, thereby affecting thermal and energy performance. Orientation was analyzed along three principal directions: 0° (south), 90° (west), and 270° (east), with 90° increments. The north orientation (180°) was excluded due to its limited exposure to direct solar radiation, which reduces its relevance for evaluating passive solar gains.

Rotation Angle of the Solar Control System

The behavior of the biomimetic shading device was analyzed through five louver opening configurations corresponding to the following rotation angles: −30° (fully open, 100 % opening), −15° (75 % opening), 0° (50 % opening), +15° (25 % opening), and +30° (fully closed, 0 % opening).

Results and Discussion

This section examines the impact of the adaptive biomimetic building skin (ABBS) on reducing thermal discomfort hours during both summer and winter periods. The analysis compares thermal performance before and after ABBS integration across three facade orientations (east, south, and west), each evaluated under five rotational configurations ranging from fully open (−30°) to fully closed (+30°), with a 15° interval between successive positions.

Thermal Performance before ABBS Integration

During the summer period, the analysis of the adaptive comfort chart indicates that, across all orientations. The results presented in Fig. 13 reveal that the majority of simulated hours fall outside the comfort zone defined by ASHRAE Standard 55 (outdoor temperatures between 18 °C and 28 °C, and indoor operative temperatures between 18 °C and 24 °C).

This reflects a high incidence of thermal discomfort caused by overheating, particularly when

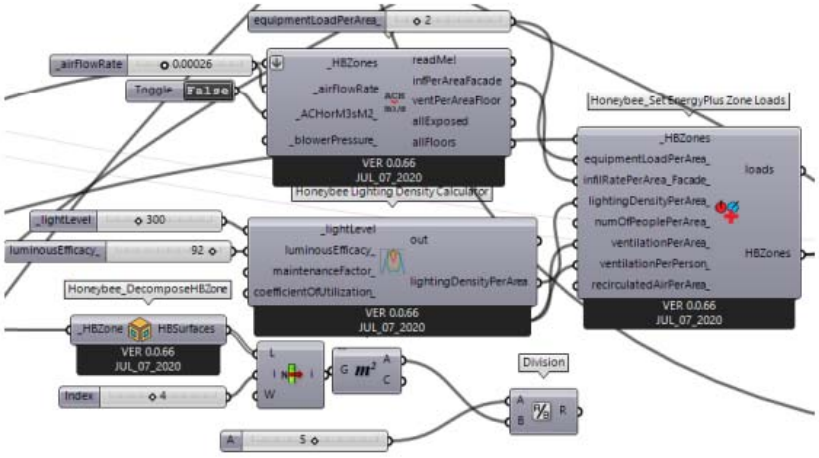

Fig. 12. Script defining the internal equipment loads generated in Grasshopper

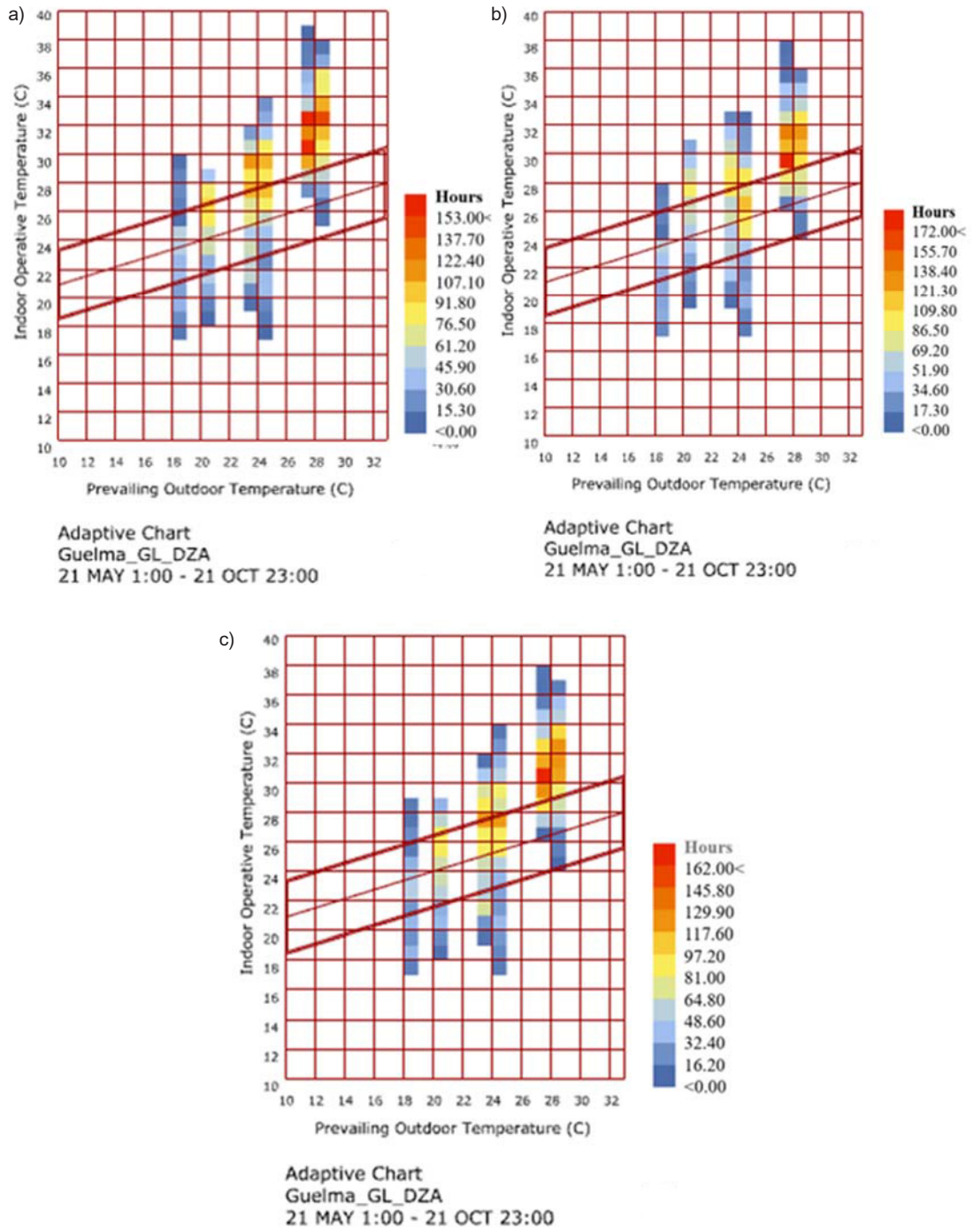

Fig. 13. Adaptive comfort model diagrams for the summer period before ABBS integration: (a) east facade, (b) south facade, and (c) west facade

outdoor temperatures exceed 28°C, resulting in indoor operative temperatures reaching up to 38°C, far above the recommended comfort thresholds. The progression of solar exposure throughout the day significantly affects indoor thermal conditions. For the east-facing facade, more than 153 hours of thermal discomfort were recorded, primarily due to direct solar radiation during the morning hours. This early exposure leads to a rapid increase in indoor operative temperatures. For the south-facing facade, discomfort levels are even higher, exceeding 172 hours, as a result of prolonged solar gains throughout the day, which cause continuous heat accumulation within the indoor space. The west-facing facade registers more than 162 hours of discomfort, predominantly during the late afternoon, when solar intensity peaks and exacerbates overheating during the final hours of the diurnal cycle.

In winter, the adaptive comfort charts reveal a pattern opposite to that observed during the summer period: thermal discomfort is primarily driven by low indoor temperatures, which frequently fall below the

comfort range defined by ASHRAE Standard 55, particularly when outdoor temperatures drop below 18°C. In the case study, the east-facing room with single glazing records up to 203 hours of thermal discomfort, reflecting significant heat losses and insufficient morning solar gains to compensate for nighttime heat loss. By comparison, the south-facing facade registers 185 hours of discomfort (Fig. 14), likely benefiting from more favorable solar exposure during daytime hours. The west-facing facade records 196 hours of discomfort (Fig.15), as late-afternoon solar gains generally prove insufficient to offset morning cool conditions, resulting in extended periods of thermal discomfort.

Thermal Performance after ABBS Integration

During the summer period, the integration of the adaptive biomimetic building skin (ABBS) leads to a notable reduction in thermal discomfort hours, as shown in Fig. 16, with performance varying according to facade orientation and system rotation angle. On the east facade, a partial closure at −15° results in only a marginal improvement of 1 % (3 hours). The neutral position (0°) yields a more substantial reduction of 11.56 % (20 hours), while the +15° configuration ensures the optimal performance, with a 12.71 % decrease (22 hours). This improvement is likely attributable to effective morning solar shading combined with sufficient natural daylight penetration.

However, a greater closure at +30° slightly reduces this benefit, resulting in a 10.98 % reduction (19 hours), possibly due to diminished ventilation and increased heat accumulation within the space. For the south-facing facade, a −15° rotation provides a limited improvement of 2.85 % (5 hours), which appears insufficient to counteract intense midday solar gains. The most effective configuration is the neutral position (0°), achieving a 17.71 % reduction (31 hours), likely offering a balanced compromise between solar protection and daylight access. Further closure at +15° and +30° yields diminishing returns, with reductions of 10.85 % (19 hours) and 6.78 % (12 hours), respectively. These results suggest that excessive shading may hinder natural ventilation and contribute to thermal stagnation during peak heat periods. On the west facade, a −15° opening results in a modest improvement of 2.47 % (4 hours), primarily effective during the early afternoon.

Notably, the neutral position (0°) leads to an increase in discomfort by 6.79 % (+11 hours), indicating an inadequate response to late-afternoon solar exposure. In contrast, the +15° configuration demonstrates the best performance for this orientation, reducing discomfort by 6.79 % (11 hours), while the +30° setting yields a limited improvement of 3.09 % (5 hours).

During the winter period, the impact of the adaptive biomimetic building skin (ABBS) on indoor thermal comfort exhibits a clear trend of improvement with increasing device aperture, particularly for orientations with significant solar exposure (Fig. 17).

Under the fully closed condition (+30°), the case study initially records 196 hours of thermal discomfort. Progressive opening of the system leads to incremental reductions: at +15°, discomfort

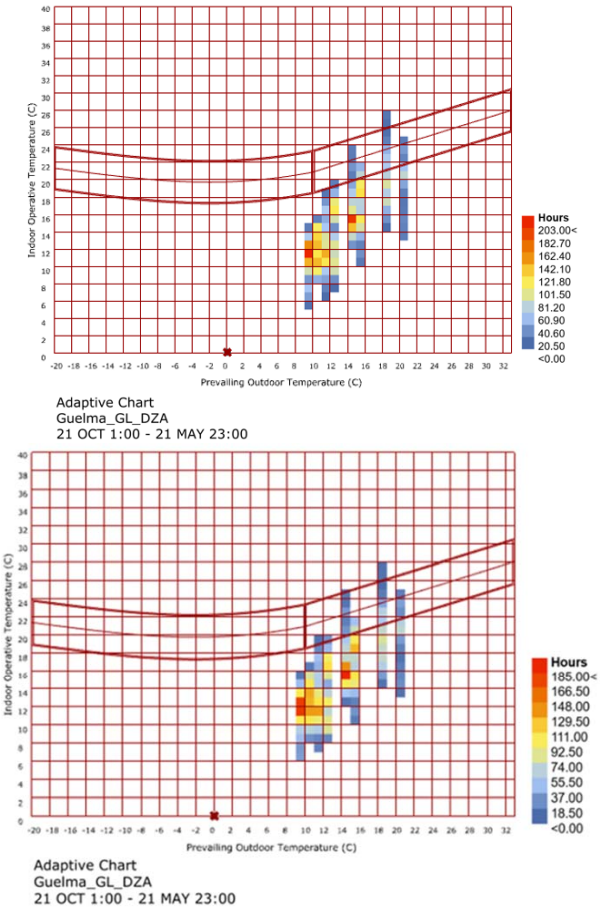

Fig. 14. Adaptive comfort model diagrams for the winter period without ABBS integration: east facade (top) and south facade (bottom)

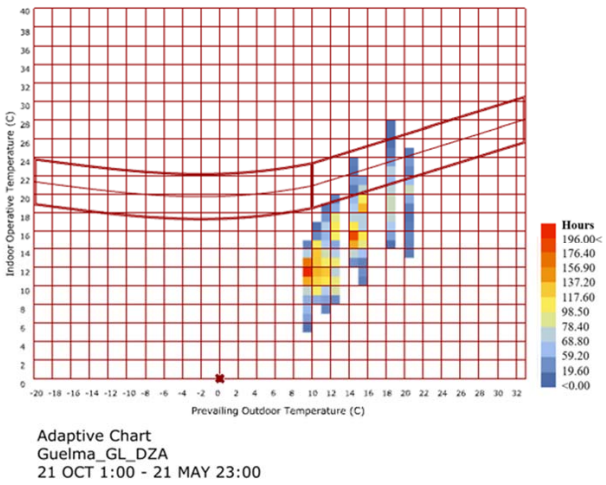

Fig. 15. Adaptive comfort model diagrams for the winter period without ABBS integration: west facade

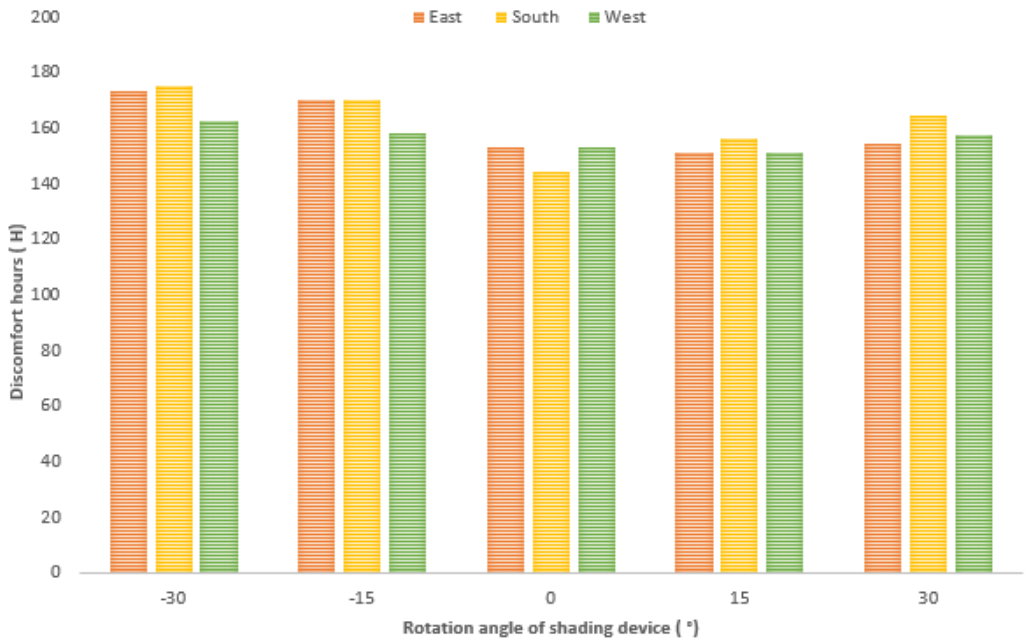

Fig. 16. Impact of ABBS integration on thermal discomfort hours during the summer period

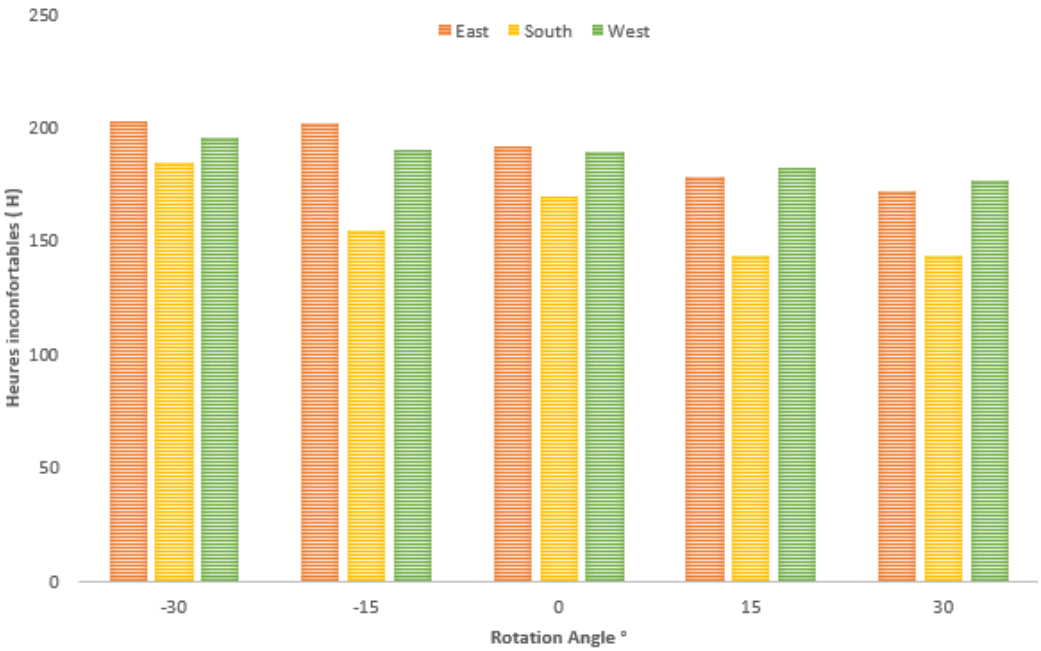

Fig. 17. Impact of ABBS integration on thermal discomfort hours during the winter period

decreases to 190 hours (2.95 %), and to 189 hours (3.44 %) at the neutral position. Larger openings at −15° and −30° further enhance comfort, reducing discomfort hours to 182 (6.89 %) and reaching a minimum of 177 hours (9.69 %), respectively.

On the east facade, where morning solar gains are critical during winter, a gradual opening of the ABBS leads to a significant reduction in thermal discomfort. A partial opening at +15° yields only a minor improvement of 0.49 % (1 hour), whereas the neutral configuration (0°) achieves a 5.41 % reduction (11 hours). Wider openings at −15° and −30° provide greater benefits, reducing discomfort hours to 178 (12.31 %) and 172 (15.27 %), respectively. These results indicate that increased exposure to early-day solar radiation enhances heat gains and helps compensate for nighttime heat losses for this orientation.

For the west-facing room, which these findings highlight the benefit of maximizing afternoon solar input in mitigating cold-related discomfort in winter. The south façade, which receives the highest solar

exposure throughout the day, presents the greatest potential for thermal improvement. Under the fully closed configuration (+30°), thermal discomfort is estimated at 185 hours. Opening the system to +15° significantly reduces discomfort to 155 hours (16.21 %), while the neutral position (0°) results in 160 hours (13.51 %). Wider apertures at −15° and −30° deliver the most substantial improvements, reducing discomfort to 144 hours (22.16 %), underscoring the effectiveness of maximizing passive solar gains through increased facade openness during the winter months.

Overall, the simulation results confirm the thermal regulatory potential of the ABBS system across different orientations and seasonal conditions. During summer, the east and west facades benefit most from partial closure (+15°), which effectively moderates solar heat gains while preserving ventilation. In winter, wider openings (−15°) enhance passive solar heating and reduce thermal discomfort. For the south facade, the neutral configuration (0°) emerges as a consistent compromise, performing effectively in both seasons by balancing solar shading with adequate daylight access. These findings validate the contribution of orientation-adaptive facade mechanisms and demonstrate the applicability of biomimetic strategies in improving thermal performance while reducing heating and cooling energy demands.

Conclusion

The simulation results confirm the potential of computational approaches for the design of biomimetic adaptive envelopes capable of enhancing thermal comfort in residential buildings. Based on parametric modeling in Rhino Grasshopper and dynamic thermal simulations using the Ladybug and Honeybee plugins, the ABBS system evaluated across multiple orientations, facade configurations, and seasonal conditions demonstrates a significant capacity to reduce periods of thermal discomfort by dynamically modulating solar gains and indoor operative temperatures. This performance is achieved through rotational adjustments inspired by the thermonastic behavior of *Ipomoea tricolor*, which prove particularly effective for facades exposed to intense solar radiation in summer and low-angle sunlight during winter. The proposed computational biomimetic approach represents a notable advancement in architectural innovation, enabling the translation of complex biological mechanisms into adaptive, high-performance building envelope solutions. This study is distinguished by its methodological integration of biomimicry and algorithmic design, providing a robust framework for the development of responsive and resilient envelope systems that simultaneously optimize thermal comfort, energy performance, and daylight availability.

Although the findings are derived from numerical simulations, they establish a solid foundation for future experimental validation under real or controlled conditions. Furthermore, the proposed computational framework may be extended through multi-objective optimization incorporating thermal comfort, daylighting, and energy performance criteria, in order to assess the transferability of the system to other climatic contexts and building typologies. The application of this approach has the potential to support the design of scalable and adaptive building envelopes that enhance thermal comfort, improve energy efficiency, and promote environmental sustainability, in line with the principles of sustainable architecture.

References

Abbaas, E. Sh., Ismail, M., Saif, A. A., and Ghazali, M. A. (2023). Impact of window shading on the thermal performance of residential buildings of different forms in Jordan. *Architecture and Engineering*, Vol. 8, Issue 1, pp. 25–36. DOI: 10.23968/2500-0055-2023-8-1-25-36.

Al-Obaidi, K.M., Azzam Ismail, M., Hussein, H., and Abdul Rahman, A. M. (2017). Biomimetic building skins: an adaptive approach. *Renewable and Sustainable Energy Reviews*, Vol. 79, pp. 1472–1491. DOI: 10.1016/j.rser.2017.05.028.

Altameemi, A. Sh. and Jabbar, A. M. (2025). Using digital software to design interactive smart canopies for the outdoor environment. *Architecture and Engineering*, Vol. 10, Issue 2, pp. 19–32. DOI: 10.23968/2500-0055-2025-10-2-19-32.

Amoruso, F. M., Dietrich, U., and Schuetze, T. (2019). Indoor thermal comfort improvement through the integrated BIM-parametric workflow-based sustainable renovation of an exemplary apartment in Seoul, Korea. *Sustainability*, Vol. 11, Issue 14, 3950. DOI: 10.3390/su11143950.

APRUE (Agence Nationale pour la Promotion et la Rationalisation de l'Utilisation de l'Énergie) (2019). *Rapport annuel sur la maîtrise de l'énergie en Algérie*. Algiers: APRUE. , pp. 1–18 (p. 2).

Betman, A., Balter, J., Donato, S. M., and Ganem, C. (2024). Influencia de los parámetros de diseño de protecciones solares en la eficiencia energética en climas áridos templados fríos, Mendoza, Argentina. *Hábitat Sustentable*, Vol. 14, No. 2, pp. 122–133. DOI: 10.22320/07190700.2024.14.02.10.

Bijari, M., Aflaki, A., and Esfandiari, M. (2025). Plants inspired biomimetics architecture in modern buildings: a review of form, function and energy. *Biomimetics*, Vol. 10, Issue 2, 124. DOI: 10.3390/biomimetics10020124.

Brzezicki, M. (2024). A systematic review of the most recent concepts in kinetic shading systems with a focus on biomimetics: a motion/deformation analysis. *Sustainability*, Vol. 16, Issue 13, 5697. DOI: 10.3390/su16135697.

Chaturvedi, P. K., Kumar, N., and Lamba, R. (2024). Multi-objective optimization for visual, thermal, and cooling energy performance of building envelope design in the composite climate of Jaipur (India). *Energy & Environment*, Vol. 36, Issue 7, pp. 3545–3569. DOI: 10.1177/0958305X241228513.

Chayaamor-Heil, N. and Laracuente, N. M. (2018). *Bio-inspired passive kinetic solar shading device for a responsive architectural envelope. In: 13th Conference on Advanced Building Skins, Session: Biomimetics for Energy Efficient Building Envelopes, October 1–2, 2018, Bern, Switzerland.*

D.T.R C3-2 (1997). Réglementation thermique des bâtiments d'habitation : Règles de calcul des déperditions calorifiques (Fascicule 1). Document technique réglementaire. Alger : Ministère de l'Habitat et de l'Urbanisme

Elhennawi, E. M. and Sameh, H. S. H. (2025). Impact of breathing facades and biomimicry on ventilation and indoor air quality. *Architecture and Engineering*, Vol. 10, Issue 3, pp. 28–39. DOI: 10.23968/2500-0055-2025-10-3-28-39.

Goharian, A., Mahdavinejad, M., Ghazazani, S., Hosseini, S. M., Zamani, Z., Yavari, H., Ghafarpoor, F., and Shoghi, F. (2025). Designing adaptability strategy to a novel kinetic adaptive façade (NKAF); toward a pioneering method in dynamic-objects daylight simulation (post-processing). *Journal of Daylighting*, Vol. 12, Issue 1, pp. 69–90. DOI: 10.15627/jd.2025.5.

Hadbaoui, H. (2018). *Pratique du biomimétisme dans l'architecture bioclimatique : Essai sur la performance énergétique des enveloppes architecturales autonomes responsives dans un climat aride*. Biomimicry in bioclimatic architecture: An investigation into the energy performance of autonomous responsive building envelopes in an arid climate]. Magister's thesis (Climatic Architecture and Environment), Salah Boubnider Constantine 3 University. Algeria. DOI: 10.13140/RG.2.2.17409.97126

Hosseini, S. M., Mohammadi, M., Schröder, T., and Guerra-Santin, O. (2021). Bio-inspired interactive kinetic façade: using dynamic transitory-sensitive area to improve multiple occupants' visual comfort. *Frontiers of Architectural Research*, Vol. 10, Issue 4, pp. 821–837. DOI: 10.1016/j.foar.2021.07.004.

International Energy Agency (2023). *Energy Efficiency 2023*. [online] Available at: https://www.iea.org/reports/energy-efficiency-2023 [Date accessed: May 07, 2024].

Khelil, S., Khelil, A. E., Korkmaz, K., and Zemmouri, N. (2020). Raising the efficiency of deployable building facades with Biomimetics for hot and arid regions. In: *Architecture, Technology and Innovation 2020, "Smart Buildings, Smart Cities", April 27–30, 2020, Izmir, Turkey*.

Kheybari, A. G., Gutai, M., Mok, B., and Cavana, G. (2025). Thermal comfort of standard and advanced glazed building envelopes. *Energy and Buildings*, Vol. 329, 115211. DOI: 10.1016/j.enbuild.2024.115211.

Kuru, A., Fiorito, F., Oldfield, P., and Bonser, S. P. (2018). Multi-functional biomimetic adaptive façades: a case study. In: *FACADE 2018 – Final Conference of COST Action TU1403 "Adaptive facades network", November 26–27, 2018, Lucerne, Switzerland*.

Lahmar, I., Cannavale, A., Martellotta, F., and Zemmouri, N. (2022). The impact of building orientation and window-to-wall ratio on the performance of electrochromic glazing in hot arid climates: a parametric assessment. *Buildings*, Vol. 12, Issue 6, 724. DOI: 10.3390/buildings12060724.

Lakhdari, K., Sriti, L., and Painter, B. (2021). Parametric optimization of daylight, thermal and energy performance of middle school classrooms, case of hot and dry regions. *Building and Environment*, Vol. 204, 108173. DOI: 10.1016/j.buildenv.2021.108173.

Lucarelli, C. D. C. and Carlo, J. C. (2020). Parametric modeling simulation for an origami shaped canopy. *Frontiers of Architectural Research*, Vol. 9, Issue 1, pp. 67–81. DOI: 10.1016/j.foar.2019.08.001.

Maksoud, A., Al-Beer, H. B., Hussien, A. A., Dirar, S., Mushtaha, E., and Yahia, M. W. (2023). Computational design for futuristic environmentally adaptive building forms and structures. *Architecture and Engineering*, Vol. 8, Issue 1, pp. 13–24. DOI: 10.23968/2500-0055-2023-8-1-13-24.

Mohamed Abd El-Rahman, S., Ibrahim Esmail, S., Bakr Khalil, H., and El-Razaz, Z. (2020). Biomimicry inspired adaptive building envelope in hot climate. *Engineering Research Journal*, Vol. 166, pp. 30–47. DOI: 10.21608/erj.2020.135274.

Naeem, N., Abdin, A., and Saleh, A. (2024). An approach to using shape memory alloys in kinetic facades to improve the thermal performance of office building spaces. *Civil Engineering and Architecture*, Vol. 12, No. 1, pp. 326–349. DOI: 10.13189/cea.2024.120125.

Öztürk, B., Mutlu-Avinç, G., and Arslan-Selçuk, S. (2024). Enhancing energy efficiency in glass facades through biomimetic design strategies. *Hábitat Sustentable*, Vol. 14, No. 1, pp. 34–43. DOI: 10.22320/07190700.2024.14.01.03.

Saci Hadef, S., Khelil, S., and Alkama, D. (2025). Building energy performance assessment based on a bio-inspired kinetic shading devices. *Scientific Journal of King Faisal University: Basic and Applied Sciences*, Vol. 26, Issue 2, pp. 36–42. DOI: 10.37575/b/eng/250018.

Shahin, A., Nessim, A., and Steit, M. (2023). Bio-based adaptive skins: investigating the impact of using shape-morphing skins on the energy consumption of administrative buildings. *Engineering Research Journal (Shoubra)*, Vol. 52, Issue 3, pp. 135–147. DOI: 10.21608/erjsh.2023.201094.1159.

Sheikh, W. T. and Asghar, Q. (2019). Adaptive biomimetic facades: enhancing energy efficiency of highly glazed buildings. *Frontiers of Architectural Research*, Vol. 8, Issue 3, pp. 319–331. DOI: 10.1016/j.foar.2019.06.001.

Soliman, M. E. and Bo, S. (2023). An innovative multifunctional biomimetic adaptive building envelope based on a novel integrated methodology of merging biological mechanisms. *Journal of Building Engineering*, Vol. 76, 106995. DOI: 10.1016/j.jobe.2023.106995.

Sommese, F., Badarnah, L., and Ausiello, G. (2022). A critical review of biomimetic building envelopes: towards a bio-adaptive model from nature to architecture. *Renewable and Sustainable Energy Reviews*, Vol. 169, 112850. DOI: 10.1016/j.rser.2022.112850.

Sommese, F., Hosseini, S. M., Badarnah, L., Capozzi, F., Giordano, S., Ambrogi, V., and Ausiello, G. (2024). Light-responsive kinetic façade system inspired by the *Gazania* flower: a biomimetic approach in parametric design for daylighting. *Building and Environment*, Vol. 247, 111052. DOI: 10.1016/j.buildenv.2023.111052.

Tabadkani, A., Roetzel, A., Li, H. X., and Tsangrassoulis, A. (2021). Design approaches and typologies of adaptive facades: a review. *Automation in Construction*, Vol. 121, 103450. DOI: 10.1016/j.autcon.2020.103450.

ВЛИЯНИЕ АДАПТИВНЫХ БИОМИМЕТИЧЕСКИХ ОБОЛОЧЕК ЗДАНИЙ НА ВНУТРЕННИЙ ТЕПЛОВОЙ КОМФОРТ: ВЫЧИСЛИТЕЛЬНЫЙ ОЦЕНКА

Сельма Саки Хадеф[1]*, Сара Хелиль[2], Джамель Алкама[3]

[1] Лаборатория гражданского строительства и гидравлики (LGCH), кафедра архитектуры, факультет наук и технологий, Университет 8 мая 1945 года, Гельма, Алжир

[2] Лаборатория устойчивости застройки (BERLab), кафедра архитектуры, факультет наук и технологий, Университет Мохамеда Хидера, Бискра, Алжир

[3] Лаборатория устойчивых городов и устойчивой архитектуры, кафедра архитектуры, факультет наук и технологий, Университет 8 мая 1945 года, Гельма, Алжир

*E-mail: sacihadef.selma@univ-guelma.dz

Аннотация

Введение. Современные достижения в области вычислительного проектирования способствовали переходу архитектурных фасадов от статичных оболочек к динамическим системам, способным адаптироваться к условиям окружающей среды с целью повышения теплового комфорта и энергоэффективности. **Целью данной работы** является оценка тепловой эффективности адаптивной биомиметической оболочки здания, вдохновленной механизмами терморегуляции растений, на примере типового жилого здания в городе Гельма (Алжир), расположенного в условиях жаркого средиземноморского климата. **Методы**. После валидации базовой тепловой модели здания в исследовании были применены два взаимодополняющих подхода: проблемно-ориентированная биомиметическая стратегия, направленная на формирование морфологии и кинетического поведения фасадных модулей, а также параметрическое моделирование в среде Rhino Grasshopper с использованием плагинов Ladybug и Honeybee для климатического и энергетического анализа. Система адаптивной биомиметической оболочки здания была протестирована при пяти конфигурациях раскрытия (от −30° до +30°) для восточной, южной и западной ориентаций в репрезентативные летний и зимний периоды с использованием адаптивной модели теплового комфорта ASHRAE Standard 55**.** Полученные **результаты** показывают, что наиболее эффективные сценарии обеспечивают снижение часов перегрева до 17,7 % в летний период и повышение уровня теплового комфорта до 22 % в зимний период за счет усиления пассивных солнечных теплопоступлений**.** Исследование подтверждает потенциал биомиметических адаптивных фасадов в оптимизации внутренних тепловых условий и подчеркивает эффективность вычислительной биомиметики как перспективного направления в разработке климатически адаптивных и энергоэффективных архитектурных оболочек, способствующих устойчивому развитию зданий.

Ключевые слова: биомиметика; адаптивные оболочки зданий; вычислительное проектирование; параметрическое моделирование; тепловой комфорт.

DOI: 10.23968/2500-0055-2025-10-4-17-28

DETERIORATION OF THE BUILDING STONE OF THE THERMAL BATHS IN THE WEST OF CAESAREA OF MAURETANIA (CHERCHELL, ALGERIA)

Abla Brahmi*, Messaoud Hamiane, Kamel Bouzetine

Materials, Processes and Environment Research Unit (URMPE), Faculty of Technology, M'Hamed Bougara University, Boumerdes, Frantz Fanon, 35000, Algeria

*Corresponding author's email: a.brahmi@univ-boumerdes.dz

Abstract

Inroduction. The thermal baths located in the western part of ancient Caesarea Mauretaniae, dating from the late second century AD, were constructed using a combination of flat bricks and blocks made from stones of various lithologies, nearly 90 % of which are calcarenite. **This study aims** to assess the state of conseration of this stone used in one of the most significant thermal structures within the built heritage of Cherchell. **Methods.** The investigation involved determining the physico-mechanical properties of selected samples, collecting rainwater, and recording in situ thermo-hygrometric parameters. Sound and weathered surfaces were characterised using polarizing microscopy, scanning electron microscopy coupled with energy-dispersive X-ray spectroscopy (SEM-EDX), and X-ray diffraction (XRD). **Results.** Field observations reveal advanced deterioration of the calcarenite, manifested by the formation of black crusts, alveolization, granular disintegration, and superficial salt efflorescences. Physico-chemical analyses confirm the presence of marine-derived salts, as well as deposits associated with atmospheric pollution. The combined dataset indicates that the deterioration dynamics of the calcarenite are driven by marine salt inputs and atmospheric pollutants, whose effects are amplified by local climatic conditions. These interacting factors account for the accelerated degradation processes observed within the studied thermal structures.

Keywords: West Cherchell thermal baths; calcarenite; alteration; sea salts; atmospheric pollution.

Introduction

The former Caesarea of Mauretania, now known as Cherchell, is a coastal town located approximately 100 kilometers west of Algiers and 28 kilometers west of Tipaza, the capital of the wilaya to which it is administratively attached (Gsell, 1952). The settlement lies on a Tyrrhenian sandstone terrace forming a narrow strip a few hundred meters wide between the sea and the first mountain slopes (Chennaoui, 2016; Leveau, 1984). It is situated at the foot of the Atlas Mountains in Cherchell (Benseddik and Potter, 1993). The climate of Cherchell lies within a transitional zone between the humid eastern region of Algeria and the arid western region. The precise boundary between these two climatic areas remains uncertain, with some sources placing it in the Chenoua region and others in Algiers (Yacono, 1955). Annual average rainfall reaches 635 mm, with temperatures ranging from 28°C in summer to 10.7°C in winter. Humidity levels vary considerably, from a minimum of 50 % in summer to a maximum of 90–95 % during winter (Leveau, 1984).

The city contains numerous public buildings dating to the Roman period, including theaters, amphitheaters, and thermal baths. Among these, the great thermal baths of the western sector are particularly noteworthy (Gsell, 1901). Their historical importance earned them the later designation "Sultan's Palace". They are among the few surviving ruins of Caesarea that remain visible today (Fig. 1).

The significance of any archaeological site is reflected in its cultural heritage value, which in turn justifies its preservation, conservation, and ongoing maintenance (Darvill, 1995; Feilden and Jokilehto, 1998).

The decision to focus this study on the thermal baths of western Cherchell was based on several factors: their cultural and historical importance, the exceptional quality of their architectural design, and their prominent position within the urban fabric. Their construction employed a combination of flat bricks and stone blocks from different lithologies, with calcarenite accounting for nearly 90 % of the material. The architectural layout was meticulously planned and executed according to a perfectly symmetrical scheme (Leveau, 1984).

Calcarenite is easily workable and transportable, particularly by sea, owing to its composition and

For citations: Brahmi, A., Hamiane, M., Bouzetine, K. (2025). Deterioration of the building stone of the thermal baths in the west of caesarea of Mauretania (Cherchell, Algeria). Architecture and Engineering, No 4 (10), pp. 17–28.
DOI: 10.23968/2500-0055-2025-10-4-17-28.

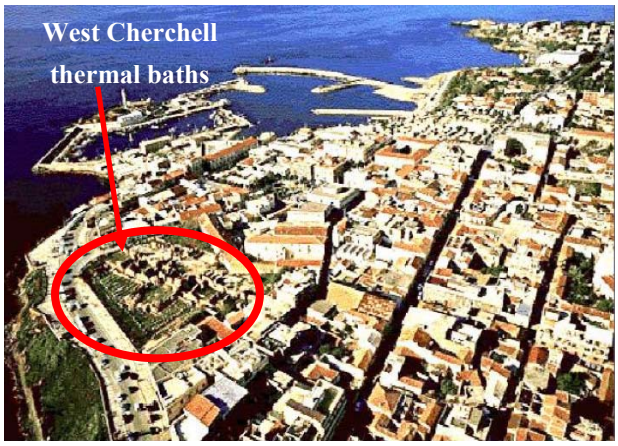

Fig. 1. Oblique photo of the thermal baths in the West of Cherchell (© Yann Arthus Bertrand)

grain size distribution. Its predominantly coastal occurrence further facilitated its use. Consequently, this stone has been widely employed in both domestic and monumental architecture (Jockey, 2006).

However, stone deterioration remains a persistent issue. The objective of this research is to contribute to the conservation of these archaeological remains by raising awareness of the need for multidisciplinary interventions and for analytical and testing methods adapted to heritage stone materials. Until recently, studies of stone decay focused exclusively on the intrinsic properties of the material itself; only in the last decades an environmental approach has been introduced to address this limitation. In this study, both approaches were used to analyze the phenomena occurring at the rock–atmosphere interface.

Indeed, the deterioration of building stones is often compared to the effects of disease — most commonly cancer — affecting the “health” of a building and ultimately leading to its decay (Malaga-Starzec et al., 2000). This phenomenon results from a combination of meteorological, architectural, and material-related factors (Camuffo and Bernardi, 1990; Dessandier, 1995; Thomas, 1938). Although rocks in their natural state and stones used in construction are subject to similar alteration factors and show comparable deterioration patterns, the kinetics of alteration are accelerated when stones are used in buildings (Jeannette, 2004). This is due to specific exposure conditions, including the use of stones laid against bedding (i.e., placed perpendicular to the strata), the juxtaposition of stones of varying quality or lithology, and the insertion of mortars between blocks — which may themselves act as a source of salts. One of the primary causes of stone decay in built structures is salt weathering (Arnold and Zehnder, 1989; Camuffo, 1998). It is widely accepted that stresses generated by salt crystallization in porous materials can exceed their mechanical strength.

Furthermore, air pollution — particularly from vehicle emissions and high concentrations of sulfur dioxide — significantly contributes to the deterioration of monuments. The dark deposits and black crusts frequently observed on monuments are largely composed of calcium sulfate formed through the reaction between sulfur dioxide and calcium carbonate in limestone (Zaouia et al., 2014).

Pollution in the Study Area

A synthesis of the findings from numerous studies and research projects examining the impact of industrial activities on the environment indicates that two principal categories of pollution sources affect the study area.

The first category comprises **stationary sources**. A total of 16 landfills have been identified across the 28 municipalities of the wilaya, in addition to other waste disposal sites. Most of these facilities fail to comply with technical standards and are located in close proximity to urban areas. The contamination of water sources is primarily attributable to the discharge of urban and industrial wastewater, directly affecting surface water, groundwater, and marine environments. Along the coastline of the Tipaza wilaya, 102 sea outfalls have been identified, discharging a total of 74,266 m³/day of wastewater.

The 14 coastal municipalities account for 60 of these outfalls (42,672 m³/day), representing 59 % of the discharges and 57.4 % of the total volume released (Grimes, 2011).

The city of Cherchell is characterized by a high concentration of pollution sources distributed along its coastline. Rapid population growth has led to a significant increase in wastewater production, resulting in the direct discharge of substantial volumes into the marine environment (Tazi and Touahir, 2011).

A study by Benderradji and Ferhat (2011) identified several discharge points near the study site, including:

- the outfalls from the city center and the El Kettar conurbation, located a few meters from the site, below the level of the bus stops;
- the outfall serving the city center and the fishery;
- the outfall from the Cherchell Military Academy, located below the level of the Bab El Ghareb monument;
- three outfalls east of the port, at a location known as Sidi Braham;
- additional discharges related to ongoing development and extension works at the port.

The second category consists of **mobile sources**. These derive primarily from transportation — private vehicles and public transit — whose emissions are released within the study area. The bus stop located at the exit of the thermal baths constitutes a major source of pollution, noise, and continuous vibrations. The high volume of daily traffic passing

directly in front of the site further exacerbates the environmental impact. The concentration of these pollutants has increased in recent years, largely due to the intensive use of diesel fuel, which is composed of a complex mixture of branched and cyclic alkanes. These emissions contribute significantly to the degradation of heritage materials, particularly stone, by promoting the formation of black crusts and other chemical alterations (Lefèvre and Ausset, 2001).

All these sources release harmful pollutants, including CO, CO_2, SO_2, and NO_2. Consequently, they play a major role in the accelerated deterioration of cultural heritage, particularly through oxidation processes affecting materials such as stone masonry, as highlighted in Ozga et al. (2009).

Main Forms of Deterioration Prevalent in the Study Area

The principal forms of destructive alteration observed at the thermal baths in the west of Cherchell, particularly affecting calcarenite stone, can be classified into three categories: alveolization and sandy disintegration, black crusts, and efflorescences and subflorescences (Fig. 2).

In the western thermal baths, efflorescences are evident in the central sections of the walls, on the northeastern sides of both promenades, and in the frigidarium. These appear as clusters of white, powdery crystals on the stone surface, which shows a high degree of disintegration.

It is also important to note that the walls of these thermal baths were constructed using a combination of flat bricks and stones of varying lithologies, with calcarenite accounting for 90 % of the total. The juxtaposition of visually similar stones with differing petrophysical properties can accelerate the degradation of one of them (Dessandier, 1995). For example, a stone that permits only limited fluid migration, when placed adjacent to a stone with higher permeability, will hinder the homogeneous circulation of fluids between them.

Methods

The study presented in this paper concerns the aging of the calcarenite stones that form the walls of the so-called Cherchell thermal baths. Since stone alteration results from its interaction with the environment, it is necessary to examine the aging processes by characterizing both the material and the local climatic conditions to which it is exposed.

The investigation began with the characterization of the physico-mechanical properties of stone

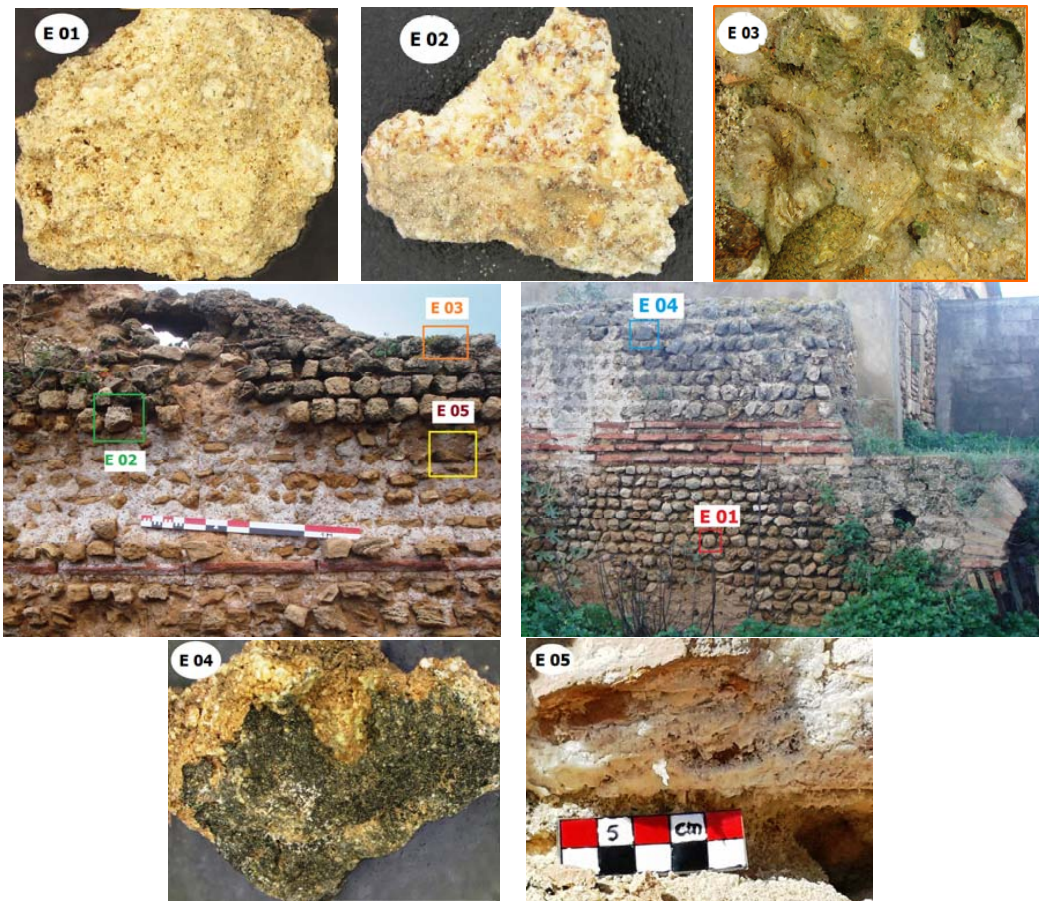

Fig. 2. Location of the stones selected for sampling (E01: stone considered sound; E02: stone exhibiting sandy disintegration; E03: stone with alveolization and incrustation; E04: stone with black crust; E05: stone with efflorescence), West Cherchell thermal baths

samples extracted from the West Cherchell thermal baths and from an ancient quarry located approximately five kilometers west of the site, at Cape Haouch Taberkoût Mohamed, in an area known as “la Cave Hardy” (Leveau, 1984), between Cherchell and Hadjret-en-Nous. The analyses revealed a perfect petrographic match between the stone from this quarry and that used in the thermal baths, confirming the probable exploitation of this deposit for the construction of the thermal complex.

The physico-mechanical properties of the samples were determined in accordance with the relevant standards: bulk density and total porosity were evaluated according to NF EN 1936, water absorption was measured following NF EN 13755, and uniaxial compressive strength was determined in accordance with NF EN 1926.

A temperature and humidity logger was installed at the site to record meteorological data (temperature and humidity) for assessing the risk of damage to stones exposed to local environmental conditions. In-situ measurements were collected by placing sensors between calcarenite blocks at the most representative area of deterioration, located at the right walkway level on the northeast side. Data were recorded over an eight-month period (1 August 2017 to 1 April 2018).

Sampling and instrumental analysis: To provide a qualitative description of stone deterioration in relation to environmental parameters, it was essential to select samples representative of the material and to perform a detailed analysis in order to understand fully the harmful impact of pollution.

Laboratory investigations included a range of observational and analytical techniques applied to both the stone samples and the preliminary rainwater samples collected in situ in March 2018. This made it possible to compare altered and sound stones and to identify alteration products using qualitative methods.

Microscopic and mineralogical analyses were carried out using an Olympus polarizing microscope for the petrographic description of the stone and a Philips XL 30 ESEM scanning electron microscope (SEM-EDX) for direct analysis of unprepared samples.

In addition, powdered samples were analyzed using a BRUKER D8-FOCUS X-ray powder diffractometer. The results are presented in Table 1.

The total elemental concentration in the insoluble fraction of the three collected rainwater samples was determined by X-ray fluorescence spectroscopy (XRF). These concentrations were converted into micromoles per liter and are presented in Table 2. The soluble fraction was analyzed separately. The pH, conductivity and volume of each rainwater sample were measured immediately upon arrival at the laboratory. Major cations analyzed included sodium (Na^+), potassium (K^+), calcium (Ca^{2+}), magnesium (Mg^{2+}), and hydrogen (H^+), while major anions included chloride (Cl^-), nitrate (NO_3^-) and sulfate (SO_4^{2-}). The pH was determined by pH-metry; Na^+, K^+, Ca^{2+}, and Mg^{2+} concentrations were quantified by flame atomic absorption spectrometry (FAAS); and Cl^-, NO_3^- and SO_4^{2-} by ion chromatography (IC).

The concentrations of major elements, expressed in micromoles per liter (µmol/L), are presented in Table 3. The ionic balances, expressed in milliequivalents per liter (µeq/L) and calculated from the sum of cations (Σ^+) and anions (Σ^-), are provided at the end of Table 3. Two ions — NH_4^+ and HCO_3^- — could not be measured.

Results and Discussion

The successive interactions between the environment and the material lead to progressive surface modifications. As alteration advances, it penetrates deeper into the stone, resulting in increasingly significant material loss. The rate and extent of deterioration depend on the intrinsic properties of the material and the aggressiveness of the surrounding environment.

Visual observations and analytical investigations have made it possible to identify the probable factors and mechanisms responsible for the alteration of the calcarenite used in the construction of the Western Cherchell thermal baths, particularly those linked to the influence of a coastal climate within an urban setting.

Petrographic Examination

The initial findings of our petrographic investigation of the calcarenite, particularly the stone sampled from the study site, show that it is a porous material with a reddish patina and gray fracture surface, exhibiting a lumpy appearance and belonging to the category of carbonate-cemented sandstones (microsparites). It is formed from consolidated or lithified dunes composed of carbonate and silicate grains (mainly quartz). These fossils attest to the high sea levels of the recent Pleistocene (Tyrrhenian) period.

In the thin section shown in Fig. 3, quartz grains of varying sizes with angular outlines are visible, embedded in a carbonate matrix containing abundant red algae (rhodophytes) and numerous fossils and fossil fragments. The fossil assemblage includes foraminifera such as *Globigerinoides sp.*, *Globorotalia sp.*, and *Miliolida*, as well as fragments of lamellibranch shells. The abundance of bioclastic components and their strong carbonate cementation result in a compact rock well suited for construction.

However, the rock displays high porosity, which facilitates water circulation and consequently increases its susceptibility to alteration processes.

Physical and Mechanical Properties

For sample E05, which exhibited efflorescence, the determination of physico-mechanical properties was not possible due to its extreme fragility.

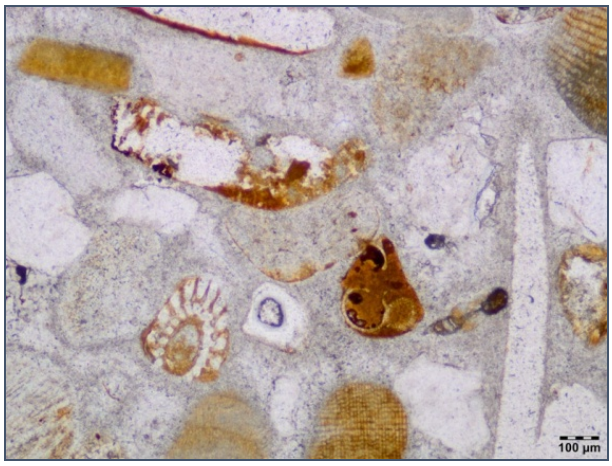

Fig. 3. Micromorphology of the calcarenite stone from the study site under an optical microscope

The analysis of the physical and mechanical properties of the calcarenite samples reveals a clear distinction between sound stones (C-H and E01) and altered stones (E02, E03, E04).

Samples C-H and E01 exhibit higher density values, indicating a more compact structure with fewer voids, compared with samples E02, E03, and E04. This contrast is especially marked in sample E03 (density = 1.4 g/cm³), reflecting significant material loss attributable to weathering processes such as dissolution or microcracking. With regard to porosity, samples C-H and E01 display values of 24 % and 31 %, respectively, corresponding to moderate porosity typical of calcarenites. In contrast, the altered samples show a substantial increase in porosity, reaching 46 % in sample E03, which indicates deterioration of the internal structure associated with a rise in interconnected voids. Similarly, the sound samples (C-H and E01) exhibit low water absorption, likely due to their limited porosity and discontinuous pore network. The altered samples (E02, E03, E04), however, display markedly higher absorption values, with sample E03 reaching up to 29 %. This confirms the presence of open porosity and a heightened sensitivity to water — conditions that accelerate weathering.

Finally, a pronounced decrease in mechanical strength is observed, most notably in sample E03, directly resulting from the loss of internal cohesion induced by degradation processes.

SEM-EDX Observation

The use of a scanning electron microscope (SEM) enabled the identification of salts present both on the surface and within the internal structure of the stone samples.

SEM imaging of sample 470, taken from stone E04 and characterized by a black surface crust, revealed the presence of gypsum, appearing as prismatic crystals arranged without preferential orientation (Fig. 4A). In contrast, a combination of sodium, calcium, and sulfur was detected within the fissures of sample 544 from stone E03 (Fig. 4B). Furthermore, halite in its typical cubic habit (Fig. 4C) was identified within the pore spaces in the deeper zone of sample 464 from stone E02, which exhibited alveolization.

The examination indicates that the rate of corrosion and deterioration of the calcarenite is influenced by multiple factors, with atmospheric pollution functioning as a complex, multiparametric driver. As demonstrated by Haber et al. (1988) in comparable cases, the stone surfaces display varying degrees of damage resulting from severe air-pollution effects, which are modulated by several parameters, particularly the presence of water.

The formation of aggressive, hard saline crusts on the stone surfaces — such as gypsum ($CaSO_4 \cdot 2H_2O$) and salts produced through calcite dissolution ($CaCO_3$) — observed on sample E05 is primarily attributed to corrosive chemical mechanisms triggered by atmospheric pollution (Van Grieken et al., 1998). These effects are further intensified by synergistic interactions with acid rain or other moisture inputs. For example, the sulfates observed on certain stone surfaces are generated through reactions between SO_2 and $CaCO_3$, as documented in numerous studies (Fassina, 1988; Russ et al., 1999). Once salts infiltrate the pore network and crystallize, cyclic recrystallization produces stresses that eventually cause the rupture of stone surfaces, as reported by Lewin (1982). This process is strongly influenced by salt concentration, chemical composition, and the number of wet–dry cycles (Binda et al., 1985).

Salt efflorescence and subflorescence affect both the pore network and the surfaces of samples

Table 1. **Physical and mechanical properties of the stone samples analyzed**

	Sample					
	C-H	**E01**	**E02**	**E03**	**E04**	**E05**
Density ρ_a (g/cm³)	2.2	1.9	1.7	1.4	1.8	–
Total porosity N_{tot} (%)	24	31	42	46	38	–
Water absorption (%)	11	16	22	29	21	–
Uniaxial compressive strength R_c (MPa)	16.57	13.21	7.2	5.45	9.67	–
C-H: Calcarenite sample from the ancient **Cave Hardy** quarry						

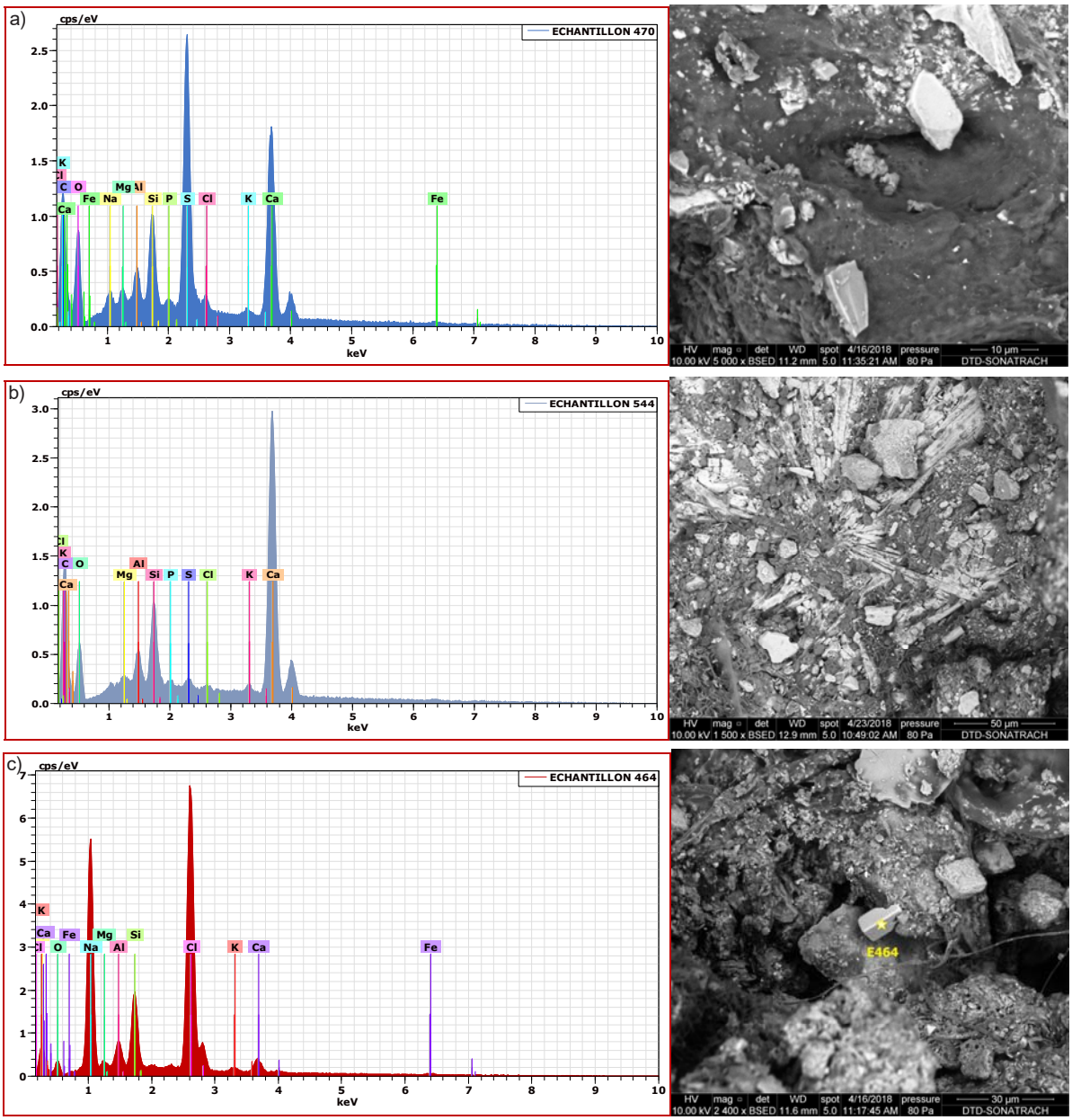

Fig. 4 (A, B, C). SEM micrographs and corresponding EDX spectra showing deterioration agents identified in the stone samples

E02 and E05. This is due to cycles of crystallization and recrystallization of salts originating from marine aerosols or acid rain, particularly following drying phases induced by air temperature or airflow. These phenomena are associated with the presence of halite crystals, which are considered the most potentially damaging salts to the rocks in which they precipitate, particularly limestone. This is because halite exerts one of the highest crystallization pressures, as discussed by Hammecker (1993) and Mirwald et al. (1988).

The concept of crystallization pressure has long been debated. However, Desarnaud et al. (2016) reported measurements obtained using highly specialized instrumentation indicating that disjoining pressures can reach — and even exceed — hundreds of megapascals. Such extremely high pressures surpass the mechanical strength of most rocks. In addition, salts crystallizing within porous media generate tensile stresses to which rigid stones offer little resistance. Therefore, these salts and their crystallization processes are highly effective in fracturing the stone due to its porosity (Bromblet, 2020). Moreover, in the absence of rainfall during the dry season, dissolution–crystallization cycles of salts may continue through simple halite solvation. The repetition of these cycles generates low-intensity bursts that promote deeper penetration of salts. The year-round continuation of these mechanisms amplifies these bursts and contributes

to the progressive degradation of the stone through alveolization and disintegration.

X-ray Powder Diffraction Analysis

According to the results presented in Table 2, the samples fall into two main categories based on their degree of preservation.

The first group comprises samples considered to be in satisfactory condition. The first sample (C-H) was collected from the ancient Cave Hardy quarry, while the second sample (E01) was taken from a sheltered wall within the Cherchell thermal complex, protected from direct weathering. Mineralogical analysis shows that both stones consist predominantly of calcite ($CaCO_3$), with a minor amount of quartz (SiO_2). In addition, traces of clinochlore associated with micas were detected in sample E01.

The second group includes samples taken from visibly deteriorated areas (E02, E03, E04, and E05). These samples contain significant proportions of major phases such as calcite ($CaCO_3$), as well as minor phases including quartz (SiO_2), micas, and gypsum ($CaSO_4 \cdot 2H_2O$). Trace minerals such as mirabilite ($Na_2SO_4 \cdot 10H_2O$), kaolinite ($Al_2Si_2O_5(OH)_4$), and nitratine ($NaNO_3$) were also identified as surface accumulations.

The X-ray analysis shows that the sound sample is mainly composed of the crystalline phases listed above, confirming that this calcarenite may be classified as a sandy limestone.

In contrast, the surfaces of the altered samples (E03, E04, and E05) exhibit highly deteriorated mineralogical characteristics. These surfaces contain saline alteration minerals, predominantly gypsum and halite. Gypsum forms through chemical alteration caused by reactions between polluting gases (SO_2 and NO_x) and the dominant ions present on the stone surface. This behavior is typical of carbonate stones exposed to polluted environments, especially following the evaporation of moisture, as demonstrated by El-Gohary (2008, 2011).

Many salts are inherently unstable and may transform into different states depending on the amount of water incorporated in their structure. For example, calcium sulfate can absorb moisture and convert into gypsum, accompanied by a 42 % volume increase. Similarly, thenardite (Na_2SO_4) can transform into mirabilite ($Na_2SO_4 \cdot 10H_2O$), which can exhibit a volume increase of approximately 300 % (Price, 1997).

Sample E03, taken from a calcarenite stone showing alveolization, contains the crystalline mirabilite phase. It is well established that crystallization of sodium sulfate solutions can produce three different phases depending on the water content: thenardite (Na_2SO_4, anhydrous phase), mirabilite ($Na_2SO_4 \cdot 10H_2O$, decahydrate), and a heptahydrate phase. Both the heptahydrate and the decahydrate (mirabilite) are unstable. The critical temperature — representing the threshold between slight and severe damage caused by salt crystallization — is approximately 32.4°C, which is also the stability limit for mirabilite. Tsui et al. (2003) showed that the most severe deterioration occurs when sodium sulfate crystallizes below the temperature at which mirabilite forms. These findings were corroborated by Angeli et al. (2010) through experimental aging tests on limestone conducted under controlled temperature and sodium sulfate concentration.

Temperature and Humidity Measurement

The temperature and humidity data reveal pronounced seasonal fluctuations. For instance, the lowest temperature recorded during the measurement period occurred on December 20, 2017 at 6:53 a.m., reaching 6.5°C with a relative humidity of 95 %. On March 23, 2018 at 7:09 a.m., another minimum of 5°C was recorded, accompanied by a relative humidity of 88 %. Conversely, the highest temperature, 37.5°C with a relative humidity of 32 %, was measured on August 1, 2017 at 5:33 p.m.

Table 2. **Mineralogical composition of the analyzed stone samples determined by X-ray diffraction (XRD)**

Detected minerals	Sample					
	C-H	E01	E02	E03	E04	E05
Calcite ($CaCO_3$)	***	***	***	***	***	--
Quartz (SiO_2)	**	**	**	**	**	--
Micas	--	*	--	*	--	--
Clinochlore($(Mg, Al)_6 (Si, Al)_4O_{10}(0H)_8$)	*	*	--	--	--	--
Kaolinite ($Al_2 (Si_2O_5) (OH)_4$)	--	--	--	*	--	--
Halite (NaCl)	--	--	*	--	**	***
Gypsum ($CaSO_4 \cdot 2H_2O$)	--	--	*	--	**	**
Mirabilite ($Na_2SO_4 \cdot 10H_2O$)	--	--	--	*	--	--
Nitratine ($NaNO_3$)	--	--	--	--	*	--

*** = *major minerals* ** = *minor minerals* * = *traces* -- = *undetectable*

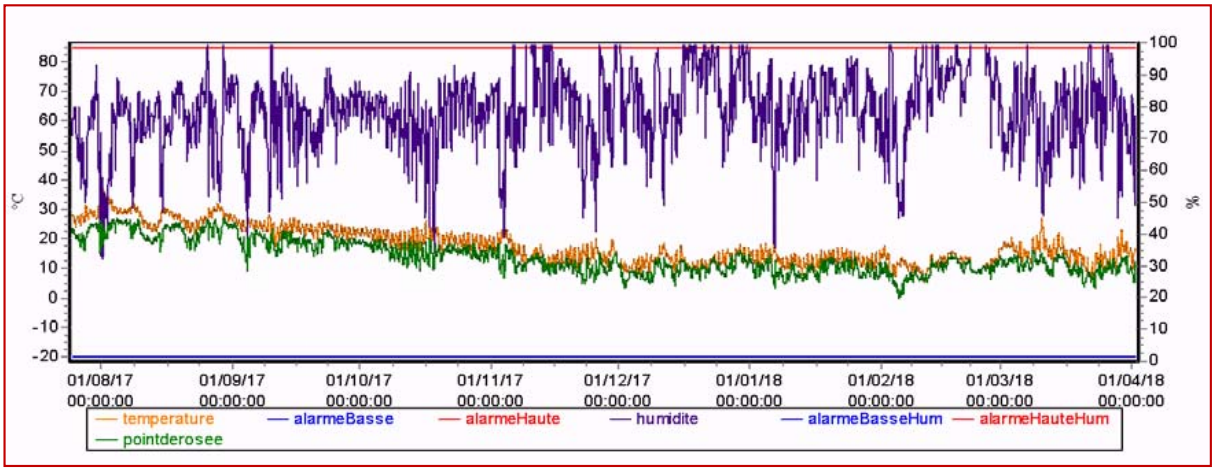

Fig. 5. Environmental measurements recorded at the site

Such climatic variations — particularly changes in air temperature — induce atmospheric weathering through alternating heating and cooling of stone surfaces. In climates combining high temperatures with elevated humidity, fluctuations in stone temperature regulate the presence of water within the material through evaporation–condensation processes. These fluctuations may cause direct deterioration of the stone through mineral dissolution, or may indirectly intensify weathering induced by other environmental factors.

It is evident that the severe deterioration of rocks containing salts is not solely due to the high crystallization pressures, but also to the frequency of dissolution–crystallization cycles. The recorded data clearly show variations in relative humidity between day and night. The studied stone was found to be contaminated with sodium chloride. During the daytime, when temperatures rise and relative humidity decreases, this salt crystallizes and remains stable. At night, as humidity increases and temperature drops, the salt dissolves, migrates within the pore network, and recrystallizes the following day once temperatures rise again and relative humidity falls below the threshold of 75 %. The hygroscopic behavior of halite enables the salt to remain mobile and active within the stone (Bromblet, 2020).

Rainwater Analysis Results

- *Insoluble fraction*
- *Soluble fraction*

Table 5 summarizes the marine contributions and excess levels of SO_4^{2-}, Cl^-, and NO_3^-, together with their respective percentages relative to total ion concentrations. It also reports both measured and calculated hydrogen-ion concentrations (H^+), as well as the neutralizing capacity (C_n).

Acid rain is defined as the deposition of gaseous pollutants and particulates that results in precipitation with a low pH. Atmospheric SO_2 and NO_2 are progressively oxidized to form two strong acids — H_2SO_4 and HNO_3 — which are subsequently incorporated into raindrops and transported to stone surfaces by acid precipitation (De Nevers, 2010).

Rainfall therefore acts as an efficient vector for transferring atmospheric pollutants to stone surfaces (Alomari, 2014).

Analytical results clearly show that the collected rainwater is slightly acidic (pH: 4.91; 5.12; 5.75), contrary to Algerian standards, which specify a pH range of 6.5 to 8.5 for natural waters.

Taking into account instrumental uncertainties and the inherent variability of atmospheric conditions, the pH of the first rainwater sample is distinctly more acidic (4.91) than that of samples 2 and 3 (5.12 and 5.74). These differences may be linked to the timing of rainfall events, during which partial neutralization of acids occurs within raindrops.

The analyses further show that marine-derived soluble elements — dominant in the soluble fraction (Table 4) — occur only in minor amounts in the insoluble fraction retained on filters (Table 3). In contrast, terrigenous elements (Al, Si, Ca, Fe) are markedly higher, particularly in rainwater sample 3.

Table 3. **Total elemental concentrations (µmol·l⁻¹) in the insoluble fraction retained on filters from the three rainwater samples collected at the West Cherchell thermal baths**

	Si	Al	Mg	Na	Cl	K	Ca	Ti	S	Fe	Mn	Zn
Rainwater sample 1	17.98	32.47	02.44	00.98	00.57	01.74	02.38	05.69	00.04	02.85	01.15	00.02
Rainwater sample 2	38.54	14.71	04.63	01.21	01.02	05.38	06.84	01.88	01.93	31.26	04.08	00.17
Rainwater sample 3	399.25	265.62	30.81	03.40	00.98	47.56	105.33	09.72	02.36	64.49	00.87	00.35

Table 4. **Concentrations of major elements (µmol·l^{-1}), pH, electrical conductivity (µS·cm^{-1}), and ionic balance (µeq·l^{-1}) of the three rainwater samples**

	Cond. (µS·cm^{-1})	pH	H^+	Mg^{2+}	Ca^{2+}	K^+	Na^+	SO_4^{2-}	Cl^-	NO_3^-	Σ^+	Σ^-
Rainwater sample 1	21.01	4.91	12.30	39.87	63.15	7.88	451.10	69.13	422.47	70.34	677	631
Rainwater sample 2	22.35	5.12	7.58	21.93	57.63	4.67	95.44	54.29	90.23	41.51	267	240
Rainwater sample 3	25.87	5.74	1.82	18.01	15.92	9.48	205.31	20.05	225.67	20.12	304	286

Table 5. **Marine contributions and excess levels of SO_4^{2-}, Cl^-, and NO_3^-, together with the neutralizing capacity (C_n) expressed in µmol·l^{-1}**

	Concentrations	SO_4^{2} (sea)	SO_4^{2} (excess)	Cl^- (sea)	Cl (excess)	NO_3^- (sea)	NO_3^- (excess)	H^+ (measured)	H^+ (calculated)	C_n
Rain-water sample 1	(µmol·l^{-1})	27.07	42.06	527.79	0	0	70.34	12.30	154.46	142.16
	%	40	60	–	–	–	–	–	–	92
Rain-water sample 2	(µmol·l^{-1})	5.73	48.56	111.66	0	0	41.51	7.58	138.63	131.05
	%	12	88	–	–	–	–	–	–	94
Rain-water sample 3	(µmol·l^{-1})	12.32	7.73	240.21	0	0	20.12	1.82	35.58	33.76
	%	62	38	–	–	–	–	–	–	95

The main ions identified are Na^+, Cl^-, Mg^{2+}, K^+, Ca^{2+} and SO^{2-}. These inorganic ionic species (Na^+, Cl^-, SO_4^{2-}) and the crust-derived inorganic cations (Mg^{2+}, Ca^{2+}) influence the chemistry of precipitation. While the presence of H^+ ions increases the acidity of rainwater, variations in the concentrations of alkaline ions play a key role in neutralizing precipitation and reducing its acidity. In polluted environments such as the study area, emissions of SO_2 and NO_x promote the formation of acid rain. This acidic precipitation, in conjunction with other ions, accelerates stone decay in the thermal baths. Acid rain reacts with calcium carbonate and other minerals, causing surface erosion, discoloration, and a progressive loss of material integrity.

Furthermore, the widespread presence of black crusts on the limestone blocks of the West Cherchell thermal baths supports the interpretation proposed by Cachier et al. (2004), who demonstrated that black crusts are among the most common alteration forms affecting limestone in urban environments. This phenomenon is attributed to the interaction between SO_2, PM_{10} particles, and acidic precipitation, whereby calcium carbonate ($CaCO_3$), the principal constituent of limestone, is converted into gypsum ($CaSO_4 \cdot 2H_2O$), leading to both mechanical and chemical deterioration of the exposed stonework. Moreover, during crust formation, particles containing amorphous carbon and heavy metals become trapped within the gypsum matrix, imparting the characteristic blackened appearance to the surface (Rovella et al., 2021), as observed on the stones of the West Cherchell thermal baths.

The analysis of ionic balances and pH confirms that acidic inputs from polluted areas, together with crustal compounds (particularly calcite), contribute simultaneously to the neutralization of acidity within raindrops. All three rainwater samples reveal a strong marine influence, as indicated by elevated levels of Na^+ and Cl^-. This explains the presence of marine salts — particularly halite, with a solubility of 365 g·L^{-1} at 20°C. Since these salts are readily soluble, they are easily transported by dilute aqueous solutions such as rainwater. Upon infiltration into stone and subsequent evaporation at the surface, these salts may re-concentrate and crystallize. The high solubility of these salts enables significant mobility and facilitates its accumulation in evaporation zones, especially at the stone surface. Salt crystallization is controlled by the porosity of the stone: it may occur at the surface as efflorescence, or several millimeters to centimeters beneath the surface as subflorescence, within the pore network (Bromblet, 2020).

Conclusion

The aim of this study was to identify the principal factors affecting the durability of the calcarenite used in the construction of the West Cherchell thermal baths. This involved assessing the conservation state of the material and evaluating several environmental parameters.

The observed alterations exhibit diverse morphologies, including disintegration, darkening, black crust formation, alveolization, and salt efflorescence. These forms of deterioration are intrinsic to the high porosity and specific textural characteristics of the calcarenite employed. Among the most common manifestations of sulfation in carbonate-rich stone are darkening and the development of superficial crusts. Surface soiling

is a complex process influenced by multiple factors, including ambient pollutant concentrations, deposition rates, the intrinsic properties of the stone (such as porosity and texture), and local microclimatic conditions. Surface orientation also significantly affects pollutant deposition, with vertical and shaded surfaces being particularly susceptible. As noted by Cioban et al. (2022), the interplay of these factors makes it difficult to quantify pollutant deposition rates precisely.

It is clear that stone degradation has accelerated significantly over recent decades, coinciding with the substantial expansion of the bus and automobile fleet in Cherchell. The extent of alteration varies with the degree of exposure to atmospheric agents and is exacerbated by the lack of protective structures at the site, leaving the ruins particularly vulnerable to weathering, including acid rain.

To better understand the interaction mechanisms between the atmosphere and the material, rainfall characteristics, temperature and humidity values, and microscopic and mineralogical features of the selected stone surfaces were examined. The results confirm that the marine climate contributes to the deterioration of the stone in question. The amount of salts — primarily sodium chloride (halite) — together with their dissolution–crystallization cycles and the frequency of these cycles at the site, plays a major role in the deterioration process. These cycles promote the formation of surface efflorescences, reflecting a substantial marine contribution to the stone, which is continuously exposed to both natural and polluted marine aerosols. However, it is important to emphasize that the deterioration observed in the study area most likely results from a complex interaction between acidic precipitation, natural and polluted marine aerosols, and architectural and material-related factors. This interaction is manifested in the disintegration and alveolization of the stone, as well as in the discernible recession of the surface in several areas.

References

Alomari, A. (2014). *Evaluation des risques d'altération d'origine thermo-hydro-mécanique des pierres du patrimoine bâti*. [online] Available at: https://theses.hal.science/tel-01069417/file/asaad.alomari_3619_vm.pdf [Date accessed 31/12/2016].

Angeli, M, Hébert, R, Menéndez, B, David, C., and Bigas, J.-P. (2010). Influence of temperature and salt concentration on the salt weathering of a sedimentary stone with sodium sulphate. *Engineering Geology*, Vol. 115, Issues 3–4, pp. 193–199. DOI: 10.1016/j.enggeo.2009.06.001.

Arnold, A and Zehnder, K. (1989). Salt weathering on monuments. In: *1st International Symposium on the Conservation of Monuments in the Mediterranean Basin,* Bari, Italy, June 7–10, 1989. [online] Available at: https://www.researchgate.net/publication/260552681_Salt_Weathering_on_Monuments [accessed on 13/12/2025].

Benderradji, A. and Ferhat, A. S. (2011). *Erosion du littoral de Cherchell: causes, conséquences et solution d'aménagement*. [online] Available at: https://virtuallibrary.enssmal.edu.dz/collection/item/5762-erosion-du-littoral-de-cherchell-causes-consequences-et-solution-d-amenagement?offset=1[Date accessed12/02/2018].

Benseddik, N. and Potter, T. W. (1993). *Fouilles du forum de Cherchel*. 1977-1981, ANAPMSH, Alger, P14.

Binda, L, Barronio, G, and Charola, A. E. (1985). Deterioration of porous materials due to salt crystallization under different thermo hygrometric conditions. I. Brick. In: Felix, G. (ed.). *5th International Congress of Deterioration and Conservation of Stone*. Lausanne: Presses Polytechniques, pp. 279–288.

Bromblet, P. (2020). *La conservation de la pierre en milieu salin.*, in Chimie et Alexandrie dans l'Antiquité, Maison de la Chimie, EDP Sciences, p. 71–84.

Cachier, H., Sarda-Estève, R., Oikonomou, K., Sciare, J., Bonazza, A., Sabbioni, C., Greco, M., Reyes, J., Hermosin, B., and Saiz-Jimenez, C. (2004). Aerosol characterization and sources in different European urban atmospheres: Paris, Seville, Florence and Milan. In: Saiz-Jimenez, C. (ed.). *Air Pollution and Cultural Heritage.* London: CRC Press, pp. 3–14.

Camuffo, D. (1998). *Microclimate for cultural heritage*. Amsterdam: Elsevier, 432 p.

Camuffo, D. and Bernardi, A. (1990). Atmospheric pollution and deterioration of monuments. In: *Advanced Workshop: Analytical Methodologies for the Investigation of Damaged Stones,* Pavia, Italy, September 14–21, 1990.

Chennaoui, Y. (2016). Notes sur le modèle urbanistique des villes portuaires de fondation andalouse au maghreb, après 1492: la medina de Cherchell (Algérie). *Le rôle des villes littorales du Maghreb dans l'histoire, RM2E - Revue de la Méditerranée*, Vol. 3, pp. 153–168.

Cioban, L. A, Dochia, M., Mureşan, C., and Chambre, D. R. (2022). Weathering and deterioration of carbonate stones from historical monuments: a review. *Scientific and Technical Bulletin, Series: Chemistry, Food Science and Engineering,* Vol. 19 (XX), pp. 15–33.

Darvill, T. (1995). Value system in archaeology. In Carman, J., Cooper, M., Firth, A., and Wheatley, D. (eds.). *Managing Archaeology.* New York: Routledge, pp. 59–69.

De Nevers, N. (2010). *Air pollution control engineering*. 2nd edition. Long Grove, IL: Waveland Press, 586 p.

Desarnaud, J., Bonn, D., and Shahidzadeh, N. (2016). The pressure induced by salt crystallization in confinement. *Scientific Reports,* Vol. 6, 30856. DOI: 10.1038/srep30856.

Dessandier, D. (1995). *Étude du milieu poreux et des propriétés de transfert des fluides du tuffeau blanc de Touraine: application à la durabilité des pierres en oeuvre*, Sciences de la terre. Géomatériaux.Tours, 280 p.

El-Gohary, M. A. (2008). Air pollution and aspects of stone degradation “Umayyed Liwân - Amman Citadel as a case study”. *Journal of Applied Sciences Research,* Vol. 4, Issue 6, pp. 669–682.

El-Gohary, M. A. (2011). Analytical investigations of disintegrated granite surface from the un-finished obelisk in Aswan. *ArcheoSciences,* No. 35, pp. 29–39. DOI: 10.4000/archeosciences.2909.

Fassina, V. (1988). Environmental pollution in relation to stone decay. In J. Rosvall & S. Aleby (Eds.), *Air Pollution and Conservation: Safeguarding our Architectural Heritage*. Elsevier Science Publishers B.V., Amsterdam, pp. 317–358.

Grimes, S. (2011). *Profil de durabilité dans quelques destinations touristiques méditerranéennes. La destination touristique pilote en Algérie : la zone côtière de Tipasa*. [online] Available at: https://planbleu.org/sites/default/files/publications/profil_durabilite_tourisme_algerie.pdf [date accessed 14/07/2019].

Gsell, S. (1901). *Les monuments antiques de l'Algérie. Vol. 1.* Paris: Paris: Ancienne Librairie Thorin et fils Alberts Fontemoing, 534 p.

Gsell, S. (1952). *Cherchel: antique Iol-Caesarea*. rééd. par le Service des antiquités de l'Algérie avec mise à jour par M. Leglay et E. S. Colozier, Alger, 125 p.

Haber, J., Haber, H., Kozlowski, R., Magiera, J., and Pluska, I. (1988). Air pollution and decay of architectural monuments in the city of Cracow. *Durability of Building Materials,* Vol. 5, Issues 3/4, pp. 499–547.

Hammecker, C. (1993). *Importance des transferts d'eau dans la dégradation des pierres en oeuvre*. PhD Thesis in Applied Sciences.

Jeannette, D. (2004). Les grès de la cathédrale : origines, évolutions et altérations. *Bulletin de la Société des Amis de la cathédrale de Strasbourg,* Vol. 26, pp. 157–172.

Jockey, P. (ed.) (2006). Marbres et autres roches de la Méditerranée antique : études interdisciplinaires. In: *Proceedings of the 8th International Conference of the Association for the Study of Marble and Other Stones Used in Antiquity (ASMOSIA),* Aix-en-Provence, France, June 12–18, 2006, 998 p.

Lefèvre, R.-A. and Ausset, P. (2001). Les effets de la pollution atmosphérique sur les matériaux du patrimoine bâti: la pierre et le verre. *Pollution Atmosphérique,* No. 172, pp. 571–588. DOI: 10.4267/pollution-atmospherique.2953.

Leveau, P. (1984). *Caesarea de Maurétanie. Une ville romaine et ses campagnes.* Rome: École Française de Rome, 576 p.

Lewin, S. Z. (1982). The mechanism of masonry decay through crystallisation. In *Conservation of Historic Stone Buildings and Monuments.* National Academy Press, Washington, D.C, pp. 120–144.

Malaga-Starzec, K, Sahlin, T., and Lindqvist, O. (2000). Laboratory investigations of weathering behaviour of fresh and impregnated limestone and sandstone from Central Sweden. In: Fassina, V. (ed.). *Proceedings of 9th International Congress on Deterioration and Conservation of Stone.* Amsterdam: Elsevier, pp. 349–356. DOI: 10.1016/B978-044450517-0/50117-3.

Mirwald, P., Kraus, K., and Wolff, A. (1988). *Stone deterioration on the Cathedral of Cologne, Rome*. Amsterdam, Oxford, New York: Elsevier, 22 p.

Ozga, I., Ghedini, N., Bonazza, A., Morselli, L., and Sabbioni, C. (2009). The importance of atmospheric particle monitoring in the protection of cultural heritage. *WIT Transactions on Ecology and the Environment,* Vol. 123, pp. 259–269. DOI: 10.2495/AIR090241.

Price, C. (1997). Salt damage in porous materials: a threat to the cultural heritage. *Archaeology International,* Vol. 1, No. 1, pp. 47–48. DOI: 10.5334/ai.0114.

Rovella, N., Aly, N., Comite, V., Randazzo, L., Fermo, P., Barca, D., Alvarez de Buergo, M., and La Russa, M. F. (2021). The environmental impact of air pollution on the built heritage of historic Cairo (Egypt). *Science of the Total Environment,* Vol. 764, 142905. DOI: 10.1016/j.scitotenv.2020.142905.

Russ, J., Kaluarachchi, W. D., Drummond, L., and Edwards, H. G. M. (1999). The nature of a whewellite-rich rock crust associated with pictographs in southwestern Texas. *Studies in Conservation,* Vol. 44, Issue 2, pp. 91–103. DOI: 10.2307/1506721.

Tazi, C. and Touahir, N. (2011). *Détermination de l'influence des rejets des eaux usées brutes sur la qualité bactériologique et physicochimique des eaux de mer. Cas d'EL KATTER (a proximité de port de Cherchell, wilaya de TIPAZA*. P22. [online] Available at: https://dspace.enssmal.edu.dz/items/4dff3aa5-110b-4367-8728-c8bef165b8aa [accessed on 14/12/2025].

Thomas, W. N. (1938). Experiments on the freezing of certain building materials. Building Research Technical Paper No. 17, Department of Scientific and Industrial Research, London

Tsui, N., Flatt, R. J., and Scherer, G. W. (2003). Crystallization damage by sodium sulfate. *Journal of Cultural Heritage,* Vol. 4, Issue 2, pp. 109–115. DOI: 10.1016/S1296-2074(03)00022-0.

Van Grieken, R., Delalieux, F., and Gysels, K. (1998). Cultural heritage and the environment. *Pure and Applied Chemistry,* Vol. 70, No. 12, pp. 2327–2331. DOI: 10.1351/pac199870122327.

Yacono, X. (1955). *La colonisation Des Plaines du Chélif*. Algiers: Impr. E. Imbert, Vol. 1, 136 p.

Zaouia, N., El Wartiti, M., Nahraoui, F. Z., and Dabi, S. (2014). Etude de l'altération de la calcarénite des monuments de Rabat: influence de la pollution atmosphérique et des aérosols marins. *MATEC Web of Conferences,* Vol. 11, 03015. DOI: 10.1051/matecconf/20141103015.

ДЕГРАДАЦИЯ СТРОИТЕЛЬНОГО КАМНЯ ТЕРМ ЗАПАДНОЙ ЧАСТИ КЕСАРИИ МАВРИТАНСКОЙ (ШЕРШЕЛЬ, АЛЖИР)

Абла Брахми*, Мессауд Хамиан, Кэмел Бузетин

Научно-исследовательский отдел «Материалы, процессы и окружающая среда», технологический факультет, Университет M'hamed Bougara, Бумердес, Франц Фанон, 35000, Алжир

*Email: a.brahmi@univ-boumerdes.dz

Аннотация

Введение. Термальные бани, расположенные в западной части древней Цезареи Мавретанской, датируемые концом II века н.э., были построены с использованием плоских кирпичей и блоков из камней различной литологии, почти 90 % которых составляют калькарениты. **Цель данного исследования —** оценить состояние сохранности этого камня, использованного в одном из наиболее значимых термальных сооружений в архитектурном наследии Шершеля. **Методы.** Исследование включало определение физико-механических свойств выбранных образцов, сбор дождевой воды и регистрацию термогигрометрических параметров на месте. Здоровые и выветренные поверхности были охарактеризованы с помощью поляризационной микроскопии, сканирующей электронной микроскопии в сочетании с энергодисперсионной рентгеновской спектроскопией (SEM-EDX) и рентгеновской дифракцией (XRD). **Результаты.** Полевые наблюдения показывают значительное разрушение калькаренита, проявляющееся в образовании черных корок, альвеолизации, гранулярном распаде и поверхностных солевых выцветаниях. Физико-химические анализы подтверждают наличие солей морского происхождения, а также отложений, связанных с загрязнением атмосферы. Совокупность данных указывает на то, что динамика разрушения калькаренита обусловлена поступлением морских солей и атмосферных загрязнителей, воздействие которых усиливается местными климатическими условиями. Эти взаимодействующие факторы объясняют ускоренные процессы деградации, наблюдаемые в исследуемых термальных структурах.

Ключевые слова: термы западной части Шершеля; калькаренит; выветривание; морские соли; атмосферное загрязнение.

DOI: 10.23968/2500-0055-2025-10-4-29-44

ARCHITECTURE AND HERITAGE DESIGN OF A HOTEL: BUILDING AND CONSTRUCTION IN DOWNTOWN AMMAN

Omar Jawabreh[1], Emad Al Dein Al Fahmawee[2], Rami Mahmoud[1], Oraib Alsbaihi[2], Mohamed Adel Atia[3]

[1] Department of Hotel Management, Faculty of Tourism and Hospitality, The University of Jordan, Aqaba Branch, Jordan

[2] Department of Interior Design, Faculty of Art, and Design, Applied Science Private University, Amman, Jordan

[3] Department of Hotel Management, Faculty of Tourism and Hotels, Minia University, Minya, Egypt

*Corresponding author's email: e_fahmawee@asu.edu.jo

Abstract

Introduction. This study examines the transformation of a historic building in downtown Amman, Jordan, into a heritage hotel, aiming to preserve architectural and cultural identity while meeting modern hospitality standards. As urban areas experience increasing development pressure, the challenge lies in maintaining structural integrity and historical character while integrating essential contemporary amenities. This research addresses these challenges and highlights the role of sustainable design in heritage hotels. Downtown Amman, rich in cultural heritage, provides an ideal setting for exploring adaptive reuse in hotel design. The study seeks to balance preservation and modernization, emphasizing the importance of heritage in tourism and cultural continuity. Given the complexity of the urban environment, architectural preservation supports both local identity and economic growth. **Methods.** The study employs a mixed-method approach, including case studies, literature review, and field analysis, to examine sustainable design interventions in heritage hotels. Particular attention was given to adaptive reuse, green building techniques, and regulatory frameworks. Interviews with stakeholders and site assessments provided practical insights into the restoration and adaptation process. **Results.** The results indicate that heritage hotels can successfully integrate cultural preservation with functionality, creating a sustainable model for historic sites. The adaptive use of energy-efficient systems and locally sourced materials enabled the hotel to retain its historic character while meeting the needs of contemporary guests. This approach proved both culturally significant and economically viable. **Discussion.** This research highlights the dual importance of heritage preservation and economic viability in urban centers such as Amman. Key challenges include strict regulatory compliance and modern building standards. The study recommends adopting more flexible regulations to support innovative design solutions and involving local communities to foster cultural engagement. The Amman project serves as a model for other cities, demonstrating that adaptive reuse can enhance urban heritage while supporting sustainable tourism.

Keywords: architecture; heritage design; heritage hotels; downtown.

Introduction

Amman, similar to many rapidly growing cities around the world, contains a significant number of open spaces interspersed with various types of buildings. These centrally located and highly marketable areas are believed to play an essential role in contributing to an architectural revival or in restoring the country's rich traditions. Such efforts aim to further support the rehabilitation of the urban landscape, attract tourists from different regions, and foster social interaction among the local population. This multifaceted approach requires a clear and comprehensive understanding of how prospective architectural changes may influence the identity of specific locations, as well as their broader significance to the local community or the nation as a whole (Jawabreh et al., 2024a). The study of architectural completion is fundamental to this discourse before proposing the necessary strategies for transforming the existing context into something new and vibrant. A well-conceived building design, therefore, is not merely an aesthetic pursuit; it is a thoughtful endeavor aimed at creating a structure that connects deeply with its inhabitants, resonates with their values, and meets the specific needs of the community. Within the field of architectural planning and design, the terminology used may not be new; however, the applications of these concepts have not always been articulated with the clarity and decisiveness required, particularly regarding their social implications. Conversely, heritage architecture can be appreciated for its ability to preserve not only physical structures and their names but also the significance of the places in which they are maintained. This preservation process often acts as a bridge between past and present, enabling a dialog that enriches the community's cultural fabric and ensures that the stories represented by these

For citations: Jawabreh, O., Al Fahmawee, E. A. D., Mahmoud, R., Alsbaihi, O., Atia, M. A. (2025). Architecture and heritage design of a hotel: building and construction in downtown Amman. Architecture and Engineering, No 4 (10), pp. 29–44. DOI: 10.23968/2500-0055-2025-10-4-29-44.

buildings are shared and celebrated for generations to come (Abuarkub et al., 2024; Jawabreh et al., 2023; Merakchi et al., 2024).

Understanding and recognizing the central concept that underscores the key argument of this essay is also essential for maintaining and supporting the proposals presented in the text. The significance of heritage resources, building integrity, and national preservation strategies is evaluated in a manner that allows broader discussions to connect more coherently. Attempts to capitalize on negative cultural aspects of the city may hinder complex transformations within the construction and real estate markets and impede processes of urban change (Jawabreh et al., 2024b; Alhmoud et al., 2025b). Stakeholders involved in these developments require a carefully balanced approach that considers both the use of cultural advantages and the implications of various project-site alternatives. Consequently, the findings of this study may provide valuable guidance to stakeholders in building and manufacturing, serving as a framework through which they can refine their private strategies or managerial policies within a broader strategic context. Furthermore, integrating traditional architectural elements with modern requirements demonstrates the need to establish goals that serve as a central argument for ensuring sustainability in contemporary society. The process of adaptation should involve a connection that transcends purely psychological and material needs, linking the significance of a property to the descriptive and communicative values rooted in cultural identity. The reclamation of historic buildings must comply with today's comprehensive standards to effectively achieve the intended public service objectives. Thus, this study is particularly relevant to sustainable historic rehabilitation, especially in areas characterized by intense commercial and residential activities in downtown districts (Qureshi et al., 2022; Waheeb, 2023; Alhmoud et al., 2025a).

Background of the Study

Amman, the capital city of the Hashemite Kingdom of Jordan, holds substantial cultural significance, preserved over the years by a society guided by a deep-rooted belief in cultural continuity and respect for history. Established in 7250 BC, the city was ruled by numerous ancient civilizations, including the Greeks, Romans, and Umayyads. Downtown Amman abounds with archaeological landmarks such as the Citadel, the Nymphaeum, and the Roman Theater (Al Fahmawee and Jawabreh, 2023; Esmail, 2023).

Architecture in Jordan has its own distinctive character, reflecting the influence of many civilizations and architectural styles. The result is a built environment that frequently combines locally developed forms with diverse architectural methods. Urban heritage, essentially the built environment, represents what remains long after today's newspapers are forgotten and tomorrow's fashion trends have passed. Unlike the city's high-rise apartment buildings, superhighways, and shopping centers, urban heritage has proven its value beyond contemporary needs, products, and trends (Al Fahmawee, 2021). Historic buildings, monuments, and districts interact closely with the community's lifestyle. This interaction ensures the continuity of both cultural principles and the physical materials that embody them. In doing so, urban heritage sustains the ongoing renewal of the very concept of "culture" and reinforces the meaning of "community" and "identity" in notable ways. Preserving heritage is essential because it stands as a living testament to the city's history and cultural identity. The heterogeneities, alienation, and disorientation found in new urban tourism areas must be carefully managed; their uniqueness forms the lens through which economic and cultural growth emerges and attracts investment. Visitors' discovery and engagement with these heritage elements will distinguish historic urban areas from other tourism products and provide the foundation for social, cultural, and economic development.

Amman's topography and architectural landscape narrate the city's rich historical background, as illustrated in Fig. 1. The caves containing twenty-five-thousand-year-old evidence and artifacts do not represent the complete historical tapestry that Amman has inherited over centuries. From ancient Rabbath-Ammon and Roman-era Philadelphia to the early Islamic and Ottoman city of Amman, the city at each stage of its historical narrative embodied the dominant cultural heritage of the time (Al Fahmawee, 2021). Cultural and architectural influences that shaped Amman's historical context include the Hellenistic, Byzantine, Roman, and Islamic periods, as presented in Fig. 2. These cultural layers have contributed to forming the city's overall character and have left a lasting imprint on its landscape and its people. Archaeological sites and monuments near the study area, such as the Roman Theater, the Nymphaeum, and the Citadel, which is located on one of Amman's seven hills, further reflect the depth of this heritage (Abder-Rahman Gil, 2023; Al Fahmawee, 2021; Al Tal et al., 2024; Daher, 2024).

Architectural Evolution

The evolution of architecture in Amman is highly distinctive and can be observed through the various layers of architectural growth that have taken shape over time. Before urban expansion, Amman was primarily known for its Citadel, where the city's rich history originated, marked by a relatively small Islamic monument that stands in stark contrast to the larger Roman architecture that once dominated the region. The second significant phase of architectural development occurred between the First and Second

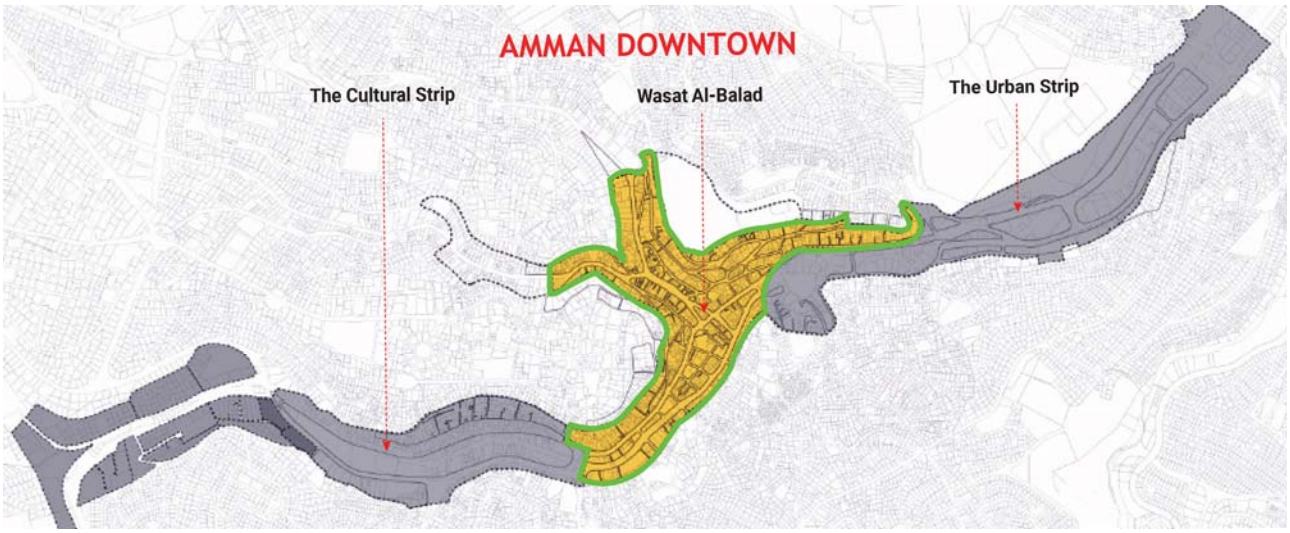

Fig. 1. Map of Amman downtown (source: the authors)

World Wars, when many settlers from Palestine and Syria began relocating to Amman in search of better opportunities. These settlers were primarily lower-class laborers and merchants seeking stability and livelihood in a growing city. As the old Citadel area, built mainly with local limestone, gradually expanded, the new inhabitants tended to live close to their workplaces, which contributed to a noticeable transformation in the architectural landscape. They built their homes using clay and stones sourced directly from the surrounding hills, which reflected a strong connection to the land. Locally available materials — such as unhewn stones and local limestone from As-Salt — helped shape the

Fig. 2. A view of the heritage hotel buildings near the historic Roman amphitheater (source: the authors)

unique character of these early structures. Over time, Residents began using modern construction materials, introduced through globalization, in their building methods, illustrating an innovative blend of traditional techniques and contemporary influences within Amman's continuously evolving urban fabric (Alqub and Mellin, 2020; Abdeljawad and Nagy, 2023; Al Tal et al., 2024).

This duality gave Amman a distinctive identity when compared with other Jordanian cities that developed during the same period. Amman became a kind of cultural memory, reflecting the diverse stories embedded within the city. The architectural guidelines that shaped the urban fabric of Amman mirror the social, political, and economic shifts experienced by its inhabitants. Different architectural landmarks symbolize different categories of narratives. The architecture of downtown Amman is characterized by high-density streets, narrow sidewalks, and crowded shops. The steep slope extending from the North City Gate downtown to Qaza Circle in the Embassies Quarter was originally developed from the top of the hill downwards, with terraced formations and retaining walls built of local fieldstone. The resulting impression of Amman's architectural use reveals a distinctly modern, manually crafted urban route.

Design Principles in Heritage Hotels

Keeping these detailed descriptions of cultural heritage in mind, one of the fundamental design principles for any captive-market heritage hotel seeking to revitalize historical buildings is to identify effective ways to encapsulate and convey the appealing elements of these significant features within the overall experience and presentation of the facility itself. The essential principles center on several key goals: reviving or reconstructing a richly historical atmosphere, harmonizing a variety of elements that capture attention and spark imagination, and integrating these with the comfort and welcoming environments expected by modern travelers. Furthermore, it is critical to strike a balance between preserving the appeal — or the "essence" — of history and providing the necessary comforts associated with the "essence" of the contemporary hotel industry. To successfully offer guests an "authentic experience", designers must skillfully utilize and present the physical environment in a way that reflects how local culture has historically expressed itself. In this context, it becomes vital to recreate the architectural and commercial culture of not just one but two distinct historical periods. In other words, the nuances of heritage design achieve the dual objectives of preserving and commodifying an appealing, persuasive, and potentially transformative past, enabling guests to connect deeply with history while still enjoying modern comforts (Rahaman et al., 2023; Tritto, 2020).

In such interventions, particularly where the physical environment of the past is still present, developing hybrid products that combine historical authenticity in interior spaces with spa and technological touchpoints in service areas represents a significant component of heritage design and construction. In other cases, creating this type of ambiance occurs through design and hotel management practices, such as lobby décor or cuisine that incorporates traditional cultural elements. Spas sometimes rely heavily on water features to create a desired atmosphere, even in settings where such elements may not be inherently meaningful or effective. Depending on the target clientele, spas often become central elements in constructing a genuinely authentic and/or luxurious design hotel, especially considering the number of Jordanian visitors. At the same time, the luxury market in Amman is expanding, with newly marketed luxury boutique hotels emerging from properties that were previously oriented toward a more local customer base.

Preservation vs. Modernization

It is always a recurring and thought-provoking question of how to approach the critical task of designing around an old building that holds historical significance. Several appealing options exist; one of the most common is to keep the building as it is, cherishing its original charm and maintaining it in as close to its original form as possible, while making only the necessary functional updates to enhance usability and the overall user experience. However, many historic structures are in urgent need of extensive facility and service upgrades that cannot be practically accommodated within the existing building envelope due to modern technological demands and standards. Some individuals strongly oppose the idea of integrating modern technology and contemporary facilities into an old building, arguing that such additions inevitably diminish the original atmosphere it once possessed in its days of glory. Thus, there is a strong expectation that designers must propose inventive and creative solutions that give heritage a renewed presence while ensuring that technological advancements and comfort can be harmoniously incorporated, preserving the character and essence of the original structure (Ribera et al., 2020; Zhong and Christopoulos, 2022; Ismail and Abd Elkader 2023; Jawabreh et al. 2025).

Some contemporary historians, when addressing similar cases of integrating new facilities without straying too far from the original fabric, consider this phase of a building's evolution to be worth preserving in its own right. At times, modern interventions even become catalysts for cultural or functional renewal. For example, an architect commissioned to design additions for a historic mosque initially proposed constructing a new, separate bathroom block to

avoid disrupting the integrity of the existing structure. During design workshops, however, the community asked whether incorporating the bathrooms inside the mosque could be an option, as such a facility had never previously existed there. The architect subsequently restructured the building and added an interior bathroom block, which became an important part of the project because it helped preserve the mosque's primary function and associated rituals. This example demonstrates that values related to historic and cultural significance are shaped not only by regulations and evolving standards but also by the ethics and needs of the community itself.

Challenges and Opportunities in Construction

The construction of heritage hotels — often undertaken strategically to maximize the inherent potential of neglected areas of the city — aims to revitalize these districts by making them eligible for ongoing development incentives such as tax breaks and expanded career opportunities for the local community. However, embarking on the construction of heritage hotels presents a wide range of challenges that must be navigated with care. One of the primary difficulties arises from the need for a high level of integration among multiple specialized professions. This integration is crucial because it involves experts who understand the intricacies and specific requirements associated with the construction and rehabilitation of historical structures (Al Fahmawee and Jawabreh, 2022b). In addition, the scale and nature of these projects demand a deep appreciation of archaeology, conservation design practices, and extensive specialized studies related to historic buildings and research methodologies used to document and analyze them. Moreover, the preservation regulations governing such projects are often perceived as exceptionally strict, creating significant obstacles that are closely tied to architecturally defined principles. Unfortunately, these rules do not always incorporate broader perspectives on value creation, which can further complicate the decision-making process. In practice, such constraints contribute to slow and often protracted decision-making, causing delays that can hinder investor engagement. These challenges are compounded by the substantial risks inherent in construction and the potential for high interest rates, which together limit investors' capacity to pursue projects focusing on historical preservation. Additionally, regulations related to conservation and preservation within urban planning frameworks can create an excessive number of procedural hurdles, making it extremely difficult — or at times nearly impossible — to secure the necessary approvals for development. This combination of challenges underscores the complexity of establishing heritage hotels that honor and preserve the integrity of a city's historical fabric (Al-Arab and Abbawi, 2023; Al Fahmawee and Jawabreh, 2022a; Eyyamoğlu and Akçay, 2022; Fabi et al., 2021).

Conversely, integrating a historic building or group of buildings into the broader management of the city also presents significant opportunities. It allows once-neglected areas to be revitalized and reimagined within an entirely new economic context. Although this process requires time and specialized expertise, it can generate opportunities for broader community participation and engagement in local governance. Furthermore, sustainable development encourages collaboration across sectors, helping to break down narrow operational silos and fostering shared interests among stakeholders. The planning and implementation of such heritage hotel projects are inherently complex and may require government landowners to grant permits that allow developers to complete essential preparatory work — at least at the level of restoration concepts and feasibility studies (Al Fahmawee, 2018). Heritage hotel projects demand significant effort and financial investment to restore buildings to professional historic-quality standards. In many cases, collaboration between local government entities and investors has supported and enabled independent design concepts that align with project goals while meeting the specific requirements of heritage facilities.

Urban Planning Regulations

Jordan's recent urban planning strategies and regulations concerning the preservation of historical sites represent two pivotal legal frameworks that have played a crucial role in protecting and maintaining numerous significant heritage locations throughout the region. These historical preservation sites are categorized into three main types: archaeological, religious, and military land. Each category is carefully supervised by specialists who serve on dedicated committees established within the relevant governmental departments. In addition, there is a specific commission responsible for overseeing ancient and traditional structures located in the heart of the downtown area. The reconsideration of these regulations, especially regarding buildings constructed after 1927, has attracted substantial interest and debate. In cases where violations occur, penalties such as fines, demolition of structures, or both may be imposed by the court to ensure compliance with the prescribed regulations. At times, however, the strict application of rules aimed at safeguarding the old city can hinder essential drivers of urban development. Although these measures are rooted in the intention to preserve historical integrity, they may make it difficult — particularly for health and safety reasons — to convert a deteriorated structure into a functional space that meets modern needs when regulations are enforced without flexibility. While the purpose behind such laws and regulations is commendable, they can inadvertently impede

economic efficiency and business operations. This can lead to significant consequences, including reduced interest from investors and business owners who may feel constrained by the regulatory environment. Therefore, achieving a careful balance between preserving cultural heritage and fostering conditions that support urban growth and economic vitality is essential (Alnsour et al., 2023; Salameh et al., 2022; Al Maani and Mubaideen, 2024).

There is a local government office responsible for providing urban services in every province of the country. The Ministry of Interior oversees these offices to ensure the proper delivery of services. Within the urban development departments of these offices, urban planners are directly appointed by senior officials. Consequently, before any construction begins, planning staff must review the architectural plans for landscapes, urban development zones, and real estate projects. Service offices verify the plans using accurate map coordinates and evaluate whether the proposed work is authorized. Only offices equipped with specific authority may engage in these duties. Four case studies in the downtown area demonstrate where the construction of a heritage-design hotel is viable and where it is not. Collaborative efforts that involve the community, along with other professional practices, can help develop new regulations that strike a balance between preservation and development.

Case Studies of Heritage Hotels: Heritage Conservation Challenges in Downtown Amman

Preserving original structures: One of the main challenges is maintaining the structural integrity of older buildings while meeting modern safety and hospitality standards. Balancing modernity and tradition: Hotels must provide contemporary amenities such as air conditioning, plumbing, and technological systems while preserving the building's historical character. Urban development pressure: With the rapid urbanization of Amman, heritage areas face continual pressure from new construction and increasingly tall contemporary buildings.

Le Royal Hotel, Amman. Architect: Richard Martinet — Modern Interpretation of Cultural Heritage

Introduction & project overview: Le Royal Hotel is one of Amman's most iconic architectural landmarks, strategically positioned atop Jabal Amman and overlooking the city's heritage district. Its elliptical form, inspired by the spiral minaret of Samarra, reflects a fusion of traditional Arab influences with modern engineering. Constructed using local stone and reinforced concrete, the hotel functions as a luxury hospitality destination, commercial center, and entertainment hub. Covering a land area of 12 dunums, the tower rises 110 meters above ground and comprises 31 floors, 6 of which are underground. With a total construction cost of approximately $190 million, the project commenced in 1998 and was completed in 2002. Design concept: The architectural approach emphasizes simplicity and elegance, ensuring that the elliptical structure maximizes panoramic views of the city. This form is enhanced by two grand spiral staircases extending from the second to the tenth floor, leading to a rooftop terrace that offers a breathtaking 360-degree view of Amman. The interior design blends Art Deco elements with contemporary aesthetics, incorporating stained glass panels, intricate mosaics, bronze and wood finishes, and geometric patterns that contribute to the hotel's distinctive grandeur. Functional layout: Le Royal Hotel integrates hospitality, retail, and entertainment functions within its multi-level structure.

The basement levels house essential services, including parking facilities, storage areas, and Jordan's largest banquet hall, which spans 1,400 square meters and accommodates up to 1,500 guests. The ground and lower floors feature a grand commercial atrium with luxury retail stores and reception areas designed for hotel guests and visitors. Entertainment and dining facilities are distributed across several floors, including a state-of-the-art cinema complex, fine-dining restaurants, and an expansive fitness and wellness center measuring 7,000 square meters. Guest accommodations, located between the 13th and 21st floors, include a mix of suites and standard rooms that offer both city and atrium views. The uppermost levels are dedicated to exclusive dining venues, a rooftop terrace, and essential technical service spaces. Architectural & technological features: Le Royal Hotel incorporates advanced technology and sustainable design features to enhance guest comfort and operational efficiency. The building is equipped with 31 high-speed elevators, a smart climate-control system, and energy-efficient lighting. Its façade is clad in locally quarried limestone in a warm yellow-beige tone, harmonizing with Amman's traditional architectural character while maintaining a distinctive and recognizable presence. The limited use of glass enhances privacy and reinforces the hotel's integration with its cultural surroundings. Conclusion: Le Royal Hotel stands as a remarkable example of modern Jordanian architecture, successfully blending heritage-inspired design with contemporary luxury. By integrating hospitality, business, and leisure functions within a single structure, it has become a symbol of urban development in Amman, offering residents and visitors a distinctive experience that reflects the city's rich cultural and architectural legacy, as shown in Figs. 3–4.

W Amman Hotel, Abdali, near Amman downtown Modern Interpretation of Cultural Heritage

Heritage & architecture: W Amman is a modern interpretation of Jordanian architecture. Although it is not a historic hotel, its futuristic design draws

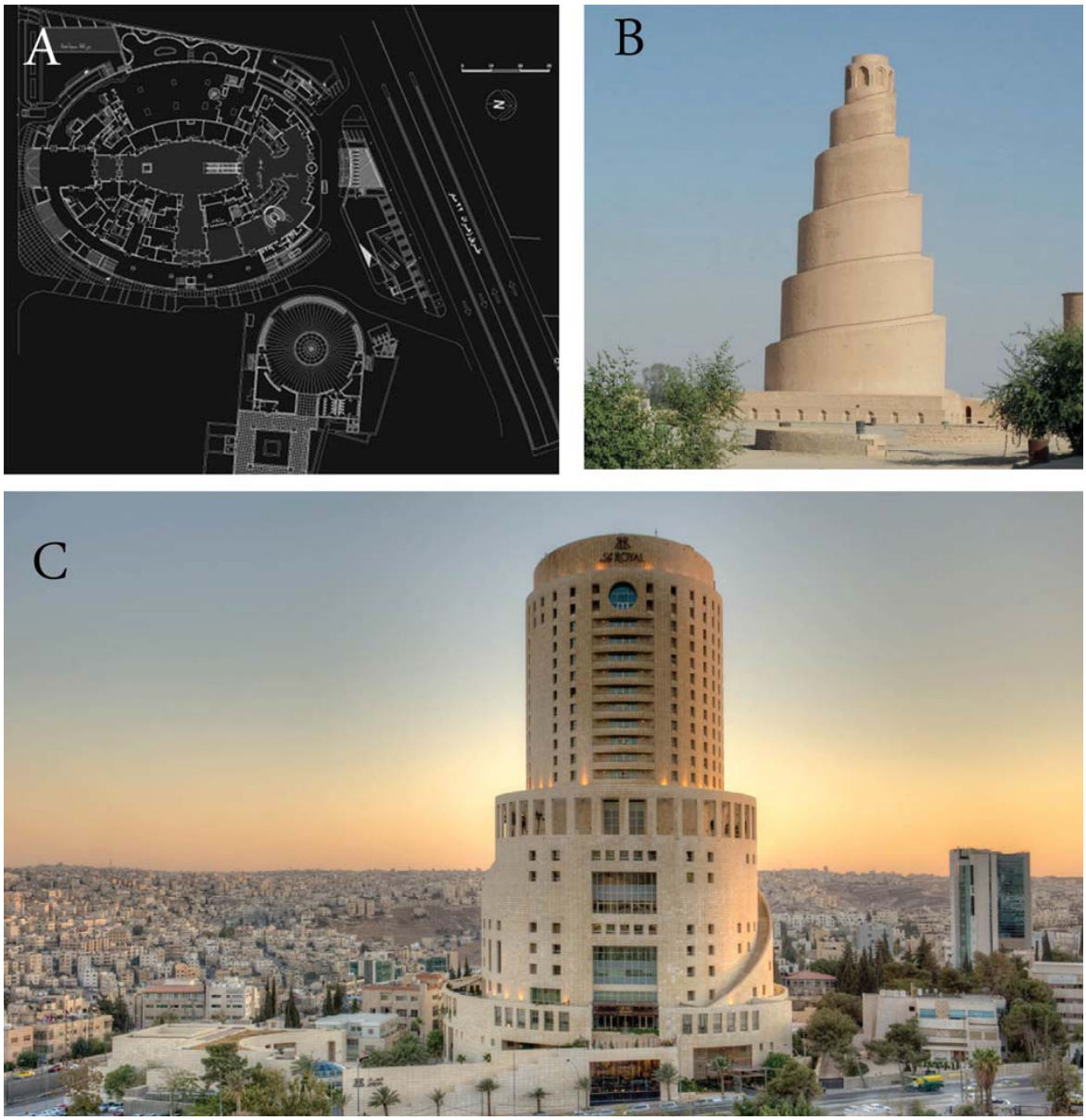

Fig. 3. A — The site plan of Le Royal Hotel (source: https://onkoshdor.blogspot.com/2017/08/blog-post_31.html). B — The spiral minaret of Samarra, which inspired the design of Le Royal Hotel (source: https://onkoshdor.blogspot.com/2017/08/blog-post_31.html). C — Le Royal Hotel's elliptical spiral structure as a significant architectural landmark in Amman (source: https://amman.leroyal.com)

inspiration from Jordan's cultural heritage and natural landscapes, including the rock formations of Petra, as shown in Fig. 4. The juxtaposition of historical and contemporary architecture in downtown Amman creates a striking contrast due to their close proximity (Al Fahmawee, 2022).

Design focus: The hotel incorporates subtle references to Jordan's past, such as interior elements inspired by the rose-red stone of Petra and furnishings that reflect Bedouin cultural influences.

Construction: The hotel is a contemporary tower designed to respect Amman's historical context while contributing to the city's modern skyline.

These case studies illustrate how heritage hotels in Amman successfully blend traditional architectural influences with modern hospitality, preserving the city's cultural identity while meeting the expectations of contemporary travelers.

Accommodation in the form of a heritage hotel — built within old buildings, historic neighborhoods, historical sites, or architecturally unique structures — reflects the identity of a place and creates opportunities for both community and heritage development through innovative management aligned with modern hotel standards. Conclusion: The case studies demonstrate that the integration of heritage-focused design within local contexts — particularly in specific districts, cities, historic restorations, and the adaptive reuse of commercial buildings — is essential. Restaurants and

Fig. 4. View of Le Royal Hotel and W Amman Hotel in a panoramic view of Amman's skyline as prominent architectural landmarks (source: www.outthere.travel/w-amman-amman-jordan)

recreational spaces help preserve cultural values, shape meaningful urban landscapes, and create tourist attractions that foster cultural appreciation, environmental stewardship, and sustainable economic benefits. The management approach also involves collaborating with local residents and communities across a variety of activities.

- *Locanda Boutique Hotel* — Transformation of a Heritage Building into a Modern Hotel in Downtown Amman

Locanda Boutique Hotel, located in the heart of Amman's cultural district, serves as a prime example of adaptive reuse in heritage conservation. Originally one of the oldest buildings in the area, the structure has long been a landmark of culture, entertainment, and hospitality in Amman. Converted into a hotel in the early 1970s, it underwent comprehensive rehabilitation and renovation in 2015, with a focus on preserving its architectural and historical identity while enhancing its functionality as a contemporary boutique hotel. As Jordan's first boutique hotel, Locanda has evolved into a vibrant cultural hub, combining heritage hospitality with the arts, as shown in Fig. 5. Its concept extends beyond accommodation, embracing a cultural mission that promotes the legacy of Arab music and musicians. The hotel features 14 uniquely themed rooms, each named after a renowned Arab musician who contributed to the development of Arabic music. Every room is meticulously designed to reflect the musician's personality, history, and artistic legacy, as illustrated in Fig. 6. Through carefully selected colors, furnishings, and decorative elements, the interior spaces create an immersive experience that allows guests to connect with Arab musical heritage. The individualized design approach at Locanda aligns with the narrative hotel concept, where each room tells a distinct story, offering guests a unique cultural experience (Al Fahmawee and Jawabreh, 2022b). This innovative design philosophy seeks to redefine the heritage hotel experience by transforming the property into a cultural haven where travelers, art enthusiasts, and local residents can engage with historical narratives and contemporary expressions.

The preservation of traditional architectural elements combined with modern hospitality standards ensures that Locanda Boutique Hotel remains both historically significant and functionally relevant. The design maintains a balance between authenticity and innovation, presenting a contemporary yet distinctly Arab aesthetic that offers foreign visitors a compelling insight into the region's culture. To further expand its cultural role, the hotel has incorporated a dedicated cinema that showcases classic Arab concerts and films, reinforcing its position as a cultural

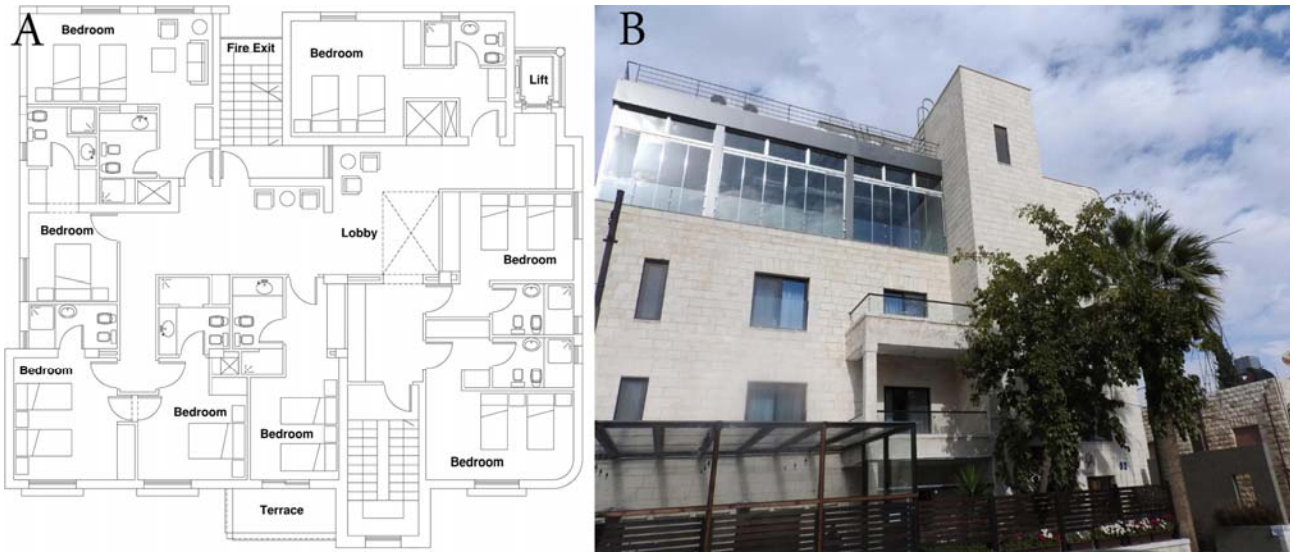

Fig. 5. A — Second-floor plan of the guest rooms. B — Locanda Hotel building after facade modification and the addition of glass surfaces (source: https://locandahotel.com/en/)

and artistic landmark. This addition enhances the multifunctionality of the space, positioning the hotel not only as a heritage conservation project but also as an active contributor to Amman's artistic and intellectual landscape. Locanda Boutique Hotel exemplifies how heritage buildings can be revitalized to serve modern needs without compromising their historical essence. By blending hospitality with cultural heritage, it has created a destination that celebrates Arab identity, making it a model for future heritage hotel projects in Amman and beyond.

- *Eco-Camps in the Wadi Rum Protected Area*

Wadi Rum Protected Area is a UNESCO World Heritage Site, and the headquarters for conservation and eco-tourism in the region is located in Rum Village. Captain's Desert Camp has received consistently high traveler ratings, reflecting its popularity among visitors. The tents at the camp are decorated in traditional Bedouin style, featuring warm interiors and access to shared bathroom facilities. Many units offer scenic mountain views. Captain's Desert Camp (Fig. 7) also provides a 24-hour front desk and barbecue facilities for guests. Another example is the Wadi Rum Night Luxury Camp within the Wadi Rum Protected Area. It integrates the natural scenery of rock and sand into its design and minimizes environmental impact by confining all interventions to a limited footprint, while ensuring unobstructed scenic viewpoints for visitors through the use of eco-friendly stargazing dome tents. All tent lodges also incorporate passive solar heating, natural insulation, windward ventilation, and nighttime radiative cooling.

Results and Discussion

Sustainability is crucial in the construction of new hotels, restaurants, and cafés. Most effective strategies for project sustainability are equally valuable in restoration and adaptive reuse projects as they are in newly constructed hotels. Energy-efficient windows, for example, can serve both sustainability goals and the need to maintain visual compatibility with heritage designs. White roof coatings, high-quality insulation, renewable and recycled materials, low-flow fixtures, and high-efficiency boilers and heating systems are applicable in structures regardless of whether heritage

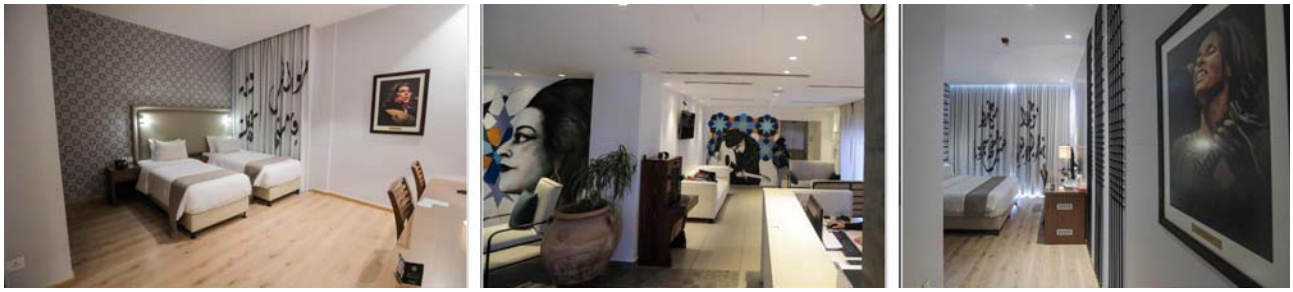

Fig. 6. Locanda Boutique Hotel room designs inspired by Arab musicians (source: https://locandahotel.com/en/)

Fig. 7. Captain's Desert Camp featuring tents adorned with authentic Bedouin designs, reflecting the region's rich cultural heritage (source: https://www.captains.jo/page.aspx?s=3&l=1&pg=9&ai=6&md=photos)

considerations are involved. In fact, wood windows and other cost-effective, environmentally friendly choices are particularly appropriate for such hotels.

However, attempting to construct a building entirely in the traditional way while expecting it to achieve high levels of sustainability is inherently flawed. Such a building is unlikely to be sustainable from a construction standpoint. A structure that requires significant amounts of energy merely to maintain its physical integrity cannot be considered sustainably built; when combined with expensive technical solutions, the initial cost often outweighs any potential long-term economic return. This is partly due to ongoing maintenance expenses and partly because of compromises required to preserve the historic building fabric, resulting in a consistently high energy-use index. Nevertheless, economic sustainability remains achievable, and it is good practice to implement thoughtful design strategies with such benchmarks in mind. Today, several hotels are being developed according to sustainable design principles, attracting tourists for whom environmental performance is appealing, though not always the primary concern.

Many construction decisions and methods relate directly to how well the chosen approach aligns with local culture, utilizes regionally available materials and craftspeople, and integrates the architecture into the broader geographical landscape. Energy consumption in such structures can be reduced by orienting the building appropriately within its environment, shading and screening openings, and using traditional features such as pointed arches. Insulation — through double-height spaces, appropriate roofing, and suitable wall materials — also has significant impact. Techniques that reduce the use of scarce resources and minimize waste in both materials and craftsmanship are essential for supporting the local community. Although modern construction benefits from extensive technological, engineering, and architectural research and development, many concepts related to contemporary green technologies — particularly in energy-efficient building envelope design and materials — play an important role in advancing environmentally responsible design.

Several measures and considerations demonstrate how high-tech solutions can be combined with traditional approaches. Modern technology plays an important role in preserving historical and heritage buildings; however, certain acceptable modifications that improve overall performance may also be viable. Green building techniques that are both technically sound and culturally appropriate can empower local craftspeople and create unique selling points through distinctive stylistic elements and low environmental impact. Contemporary architectural culture can sometimes appear superficial, treating the built environment merely as a consumable product — much like a designer sofa — rather than as an integral part of cultural identity. Certification programs, such as those awarding four-star environmental labels, can help integrate building technologies with local and regional preferences, cultural traditions, and regulatory requirements. Similarly, programs awarding energy-efficiency labels demonstrate to heritage hotel developers what can be achieved in terms of environmentally responsible design, performance, and production that align with current European standards.

- Many heritage buildings retain inherent green qualities, including the use of durable, renewable, biodegradable, recyclable, and locally sourced materials.

- Several hotels adopt measures prompted by tourism-sector development to protect the environment. A large percentage of heritage hotels and their managing authorities prioritize water-saving efforts and limit the environmental impact of their operations. The use of environmentally friendly materials reflects a clear intent to operate as sustainably as possible.

- Many sites provide bicycle storage facilities as an alternative to private car travel.

A number of constructions are uniquely designed and well known for their reliance on traditional, ecologically and culturally appropriate, and energy-efficient materials and technologies. Development costs and financial feasibility assessments for heritage sites increasingly incorporate recognized green

label standards. Green technologies therefore play a crucial role in validating the sustainability of heritage preservation and tourism-related projects. Today, green philosophy is gradually merging with green construction and maintenance practices. Ultimately, these methods require significant investment in cultural integrity, recognition, enhanced knowledge, and meaningful content.

This paper has begun to explore the role that design and heritage elements play in shaping the visitor experience within hotels. The value of hotels embedding local culture, history, urban fabric, and architectural identity has been clearly identified. Visiting a heritage site is often described as “a journey into the past — a sensory and tactile experience”. Creating a “period setting” aligns with the expectations of the growing number of heritage tourists. As such, heritage hotels actively construct this experiential environment in situ, within a context that extends beyond the immediate boundaries of the hotel itself.

Architecture and design effects may be understood along two dimensions. The first relates to their function as physical artifacts that heritage tourists directly engage with. The second underscores the role of hotels as both artifacts and cultural exploration spaces, rooted in local knowledge and expertise. In heritage hotels, the concept of destination design — defined as the integration of functional and aesthetic requirements tailored to a combination of tangible heritage resources and intangible traditional values — must also be addressed.

Two essential themes consistently emerge throughout the secondary literature on heritage hotel design. The first is the concept of cultural immersion and the overarching aim of crafting guest experiences that convey a sense of authenticity. The second concerns service quality, particularly the effect of credible, knowledgeable staff engagement on guest satisfaction. In contemporary hotel design, authenticity has overtaken location as the primary determinant of value. The degree to which a hotel can transport and immerse guests in the character of its setting has become a central benchmark. A sense of meaningful authenticity is achieved when the design roots the hotel firmly within its environment and reflects an understanding of its cultural origins. Good design assimilates local tradition rather than superimposing it. With respect to service delivery, hotel operators who commit to multidimensional staff training significantly increase their ability to command premium pricing from satisfied guests.

In terms of architecture and design, the expression of culture and local conventions often shifts depending on the scale of intervention. Some international hotel professionals may view ground-floor areas — such as restaurants, lobbies, and gardens — as the primary guest interface points and therefore place particular emphasis on their visual appeal and design ethos. In contrast, major room and floor refurbishments may require a more explicit integration and articulation of cultural vernaculars. For hotel developers, designers, and managers, the central challenge in creating an authentic guest experience lies in incorporating visual and cultural references that appear intuitive and unforced. Displays of local art, history, and tradition allow hotel lobbies to embody a sense of place, serving as both cultural touchpoints for residents and emotional drawcards for returning domestic travelers. When well-informed concierges and tour-desk staff share local knowledge with pride, they use cultural artifacts and stories as interpretive tools, enhancing the guest experience and fostering deeper engagement.

However, the careful integration of cultural elements into architectural design must not compromise guest comfort and convenience. Much of modern architecture resists local specificity through its uniformity and superficial differences. Generic architectural solutions can create a disconnect between guests and the spaces they inhabit, as such designs appear imposed rather than organically rooted in their surroundings. Interviews with several hoteliers revealed extensive discussion about their design philosophies and the manner in which they integrate and reference local culture. It is entirely possible that evolving guest demographics and shifting tourism preferences will influence the success of locally designed hotels in the future. For example, a cherished mid-century modern aesthetic in a Tuscan village may become less desirable when travelers — driven by new economic realities — shift en masse to emerging low-budget destinations near yet-undiscovered coastal areas. For the purposes of this discussion, the challenge lies in examining how local design can subtly enhance the guest experience without overshadowing comfort, while continuing to offer a meaningful and memorable temporary residence.

Economic Benefits of Heritage Hotels In addition to the inherent cultural value of historic buildings, heritage hotels can — when successfully managed — generate significant monetary value. A heritage accommodation business can bring several key financial benefits to a community. One of the primary advantages of converting historic buildings into heritage hotels is their ability to attract visitors to a district, thereby promoting and conserving its character. These establishments also stimulate local economies by generating additional expenditure for surrounding businesses. In a downtown context, converting a historic public building into a heritage-design hotel could positively impact nearby commercial activities. Tour companies, for instance, could include the hotel in their itineraries of historic attractions. In addition, the

presence of such accommodation could increase property values for other businesses along the surrounding streets.

A major economic benefit of heritage hotels is their ability to generate employment opportunities, particularly in larger establishments. While job creation is one motivation for converting the Telephone Exchange building into a heritage hotel, stakeholders also aim to maintain the building as an active component of Newcastle's urban fabric, rather than simply preserving it as a static relic. Another important economic advantage is that heritage hotels promote sustainability at both local and regional levels. By attracting visitors from within the region, across the country, and overseas, these hotels help strengthen the visibility and economic resilience of their respective areas. In many cities, numerous historic buildings have been adapted for commercial use, including conversion into hotels.

This growing trend in adaptive reuse helps counteract urban decline by encouraging investment and revitalization. Heritage hotels generate revenue through a combination of lodging, dining, guided tours, and social or corporate events. The most successful heritage venues provide all of these services. Attendance at historic sites, tours, restaurants, and related activities has steadily increased. "Heritage tourists" — travelers with a particular interest in cultural and historical destinations — tend to be experienced, well-educated, and higher-than-average earners. They frequently seek out small family-owned restaurants, local cuisine, and cultural exhibitions, contributing to the rise in services connected to heritage lodges.

The average length of stay in smaller lodges and historic inns has increased, even when overall visitor numbers are lower, as nature-based and heritage tourists often plan multi-stop trips that include various cultural sites. Reports indicate that 20–25 % of leisure travel spending is directed toward heritage-related services and accommodation. Observations of local businesses support these findings. Several studies highlight the importance of effective marketing and management in heritage hotels, emphasizing their potential to offer unique and distinctive services. Combining strong heritage management practices with evocative marketing campaigns helps communicate the cultural value and differentiation of a heritage venue or product. Research in heritage events management has revealed similar patterns. For example, one tourism study and a cultural heritage seminar identified commercial opportunities that arise from linking heritage venues with targeted marketing and media campaigns. Moreover, multiple reports indicate that heritage properties can see revenue increases of around 10 % when hosting events. In many contexts, conferences organized by local businesses can attract commercial partners and strengthen connections between stakeholders. The owners of the land and facilities that host such events benefit directly from new partnerships and from the influx of visitors.

Conclusion

Several insights have emerged from this paper, which has sought to analyze the most significant issues related to architecture and heritage hotel design. Architecture and heritage hotel design converge into a form of architectural refinement shaped by established conceptions of architectural practice. Constructing a hotel building in downtown Amman can be associated with both architectural and construction innovations; however, this process also presents a series of creative contradictions. The formal design and construction challenges specific to such architectural experimentation include preserving the urban context, integrating regional and site-specific aesthetics, and harmonizing modern technologies with long-standing traditions. Additional challenges arise from the need to translate ancestral architectural aesthetics into contemporary hospitality functions — functions that evolve constantly — and from creating intimate, residential-feeling spaces suitable for accommodating the temporary needs of guests. Although these issues are recognized, long-term solutions depend on strategic planning and creative leadership within heritage conservation projects. The primary contribution of this paper is to advance the ongoing discourse on context in contemporary architecture, offering an example that enriches counter-arguments in the field. Challenges undoubtedly remain in preserving and incorporating architectural heritage as a dynamic system within retail design and hotel development. Further work on heritage hotels in different cities will continue to reveal, address, and resolve such challenges. Heritage enhancement is becoming increasingly essential for urban environments under threat. Developments in heritage hotel construction constitute a viable strategy for investment and conservation, and patterns emerging from this study offer meaningful insight. Future recommendations may help stakeholders better understand the multifaceted requirements of a successful heritage hotel, particularly with regard to integrating sustainable development principles. Continued debate is necessary to determine the types of applications through which design principles may be effectively tested. Buildings that utilize such approaches are likely to employ significant amounts of eco-friendly materials. For heritage hotels, successful architecture and design must involve not only commercial urban regeneration but also a reinterpretation of heritage in the urban environment. Heritage contributes to the visitor experience for both local residents and international guests. Hotel

designs that preserve local heritage not only attract a diverse audience but also contribute directly to the methodologies that underpin their success.

A persistent focus in heritage hotel construction is the incorporation of sustainability. Environmentally responsible design practices will become increasingly expected as the field continues to evolve and integrate new technological advancements. One of the most significant operational changes in the future will be the broader application of technologies that assist with reducing energy loss, improving building performance, and enhancing visitor engagement. Additional technological features — such as mobile check-ins and interactive storytelling — can substantially improve operational efficiency. Cultural storytelling through design will become even more prevalent, immersing guests and helping them feel grounded and connected to the building and its context. Adaptive reuse is not a new trend, but it remains a powerful concept influencing emerging markets globally. It fulfills commercial, residential, and hospitality needs while preserving significant buildings.

The local community will also play an essential role in shaping the future of heritage hospitality in the city. Recent initiatives by the local municipalities to gather community input aim to craft design and development solutions for urban revitalization. Community involvement ensures that local stories are visible and shared with tourists and that local interests are represented. Greater emphasis will be placed on historic artifacts, traditional building methods, and genuine appreciation for handcrafted elements. Existing trends — such as the shift toward authenticity and genuinely local experiences — will continue. As consumers increasingly prioritize health-conscious lifestyles and meaningful spaces, these tendencies will shape future design directions. Ongoing community participation in construction, renovation, and revitalization efforts helps create a “my home is your home” atmosphere that benefits both residents and visitors.

References

Abdeljawad, N. and Nagy, I. (2023). Evaluation urban land use related policies to reduce urban sprawl environmental consequences in Amman City-Jordan compared with other two cities. *WSEAS Transactions on Environment and Development*, Vol. 19, pp. 119–137. DOI: 10.37394/232015.2023.19.11.

Abder-Rahman Gil, I. (2023). *The representation of Amman in the Arabic novel from Jordan 1889-2017*. [online] Available at: https://iris.unive.it/retrieve/e180e1cf-2096-41e0-80e0-4eb76b9f66e8/983037-1242474.pdf [Date accessed 1 December 2024].

Abuarkub, M., Awad, J., Chohan, A. H., and Noori, F. (2024). Revitalization in the age of artificial intelligence, an adaptive architectural conservation strategies for courtyard houses in Palestine. *Journal of Design and Built Environment*, Vol. 24, No. 2, pp. 99–125. DOI: 10.22452/jdbe.vol24no2.8.

Al-Arab, N. K. I. and Abbawi, R. F. N. (2023). Revitalizing urban heritage for tourism development: a case study of Baghdad's Old City center. *International Journal of Sustainable Development and Planning*, Vol. 18, No. 9, pp. 2747–2755. DOI: 10.18280/ijsdp.180913.

Al Fahmawee, E. A. D. H. (2018). Architectural functional design for hotels extension in Amman: a Days Inn Hotel case study. *Journal of Engineering Research*, Vol. 6, Issue 4, pp. 1–23. DOI: 10.1016/S2307-1877(25)00604-2.

Al Fahmawee, E. A. D. H. (2021). GIS methodological approach to developing and forming a visual image of downtown Amman. *Architecture and Engineering*, Vol. 6, Issue 3, pp. 49–61. DOI: 10.23968/2500-0055-2021-6-3-49-61.

Al Fahmawee, E. A. D. H. (2022). Semiotics as an approach to the analysis of symbolism in Islamic architectural arts. *Architecture and Engineering*, Vol. 7, Issue 2, pp. 3–19. DOI: 10.23968/2500-0055-2022-7-2-03-190.

Al Fahmawee, E. A. D. and Jawabreh, O. A. A. (2022a). Adaptive reuse of old structures into heritage hotel buildings: a post-occupancy evaluation in Jordon, Amman. *ISVS e-journal*, Vol. 9, No. 5, pp. 16–32.

Al Fahmawee, E. A. D. and Jawabreh, O. (2022b). Narrative architectural interior design as a new trend to enhance the occupancy rate of low-class heritage hotels. *New Design Ideas*, Vol. 6, No. 2, 2022, pp. 207–228.

Al Fahmawee, E. A. D. and Jawabreh, O. A. A. (2023). Sustainability of green tourism by international tourists and its impact on green environmental achievement: Petra heritage, Jordan. *GeoJournal of Tourism and Geosites*, Vol. 46, No. 1, pp. 27–36. DOI: 10.30892/gtg.46103-997.

Alnsour, J., Arabeyyat, A., Hyasat, A., Al-Habees, M., and Aldweik, R. (2023). The impact of urbanization on cultural heritage buildings in Jordan: As-Salt as a case study. *Future Cities and Environment*, Vol. 9 (1), 21. DOI: 10.5334/fce.191.

Alhmoud, S. H., Alhmoud, H. H., and Ukabi, E. B. (2025a). Sustainable Design: Building-Integrated Photovoltaic on Residential House Envelopes. *Journal of Studies in Science and Engineering*, 5(1), 221–244. DOI: 10.53898/josse2025522.

Alhmoud, S.H., Alhmoud, H.H., Ukabi, E.B., Bataineh, A.M. (2025b). Optimizing green roof design to reduce cooling energy demand in a Jordanian hospital building. *International Journal of Design & Nature and Ecodynamics*, Vol. 20, No. 5, pp. 989-997. DOI: 10.18280/ijdne.200504.

Al Maani, D., and Mubaideen, S. (2024). Integration of cultural heritage in architecture: a national study of Jordanian higher education. *International Journal of Heritage Studies*, 30(1), 131–143. DOI: 10.1080/13527258.2023.2284718.

Al Tal, R., Tawil, M., AlFuqaha, S., Jibrini, H., and Al Ayyoub, A. (2024). The interpretation of land use change based on the interplay of place-specific complexity in Amman downtown. In: *Soliman, A. M. and Keivani, R. (eds.). Innovations for Land Management, Governance, and Land Rights for Sustainable Urban Transitions: The Middle Eastern Perspectives*. Cham: Springer, pp. 97–120. DOI: 10.1007/978-3-031-59671-1_5.

Alqub, H. B. and Mellin, R. (2020). Reviving Islamic Values in Architecture Case Study. *Journal of Islamic architecture*, 6(1). DOI: 10.18860/jia.v6i1.7848.

Daher, R. F. (2024). Effect of typo-morphological analysis and place understanding on the nature of intervention within historic settings: the case of Amman, Jordan. *Archnet-IJAR: International Journal of Architectural Research*, Vol. 18, Issue 1, pp. 1–20. DOI: 10.1108/ARCH-05-2022-0114.

Esmail, O. K. A. (2023*). Cairo's self-planned communities: stigmatization, representations, and actions from below.* MSc Thesis in Territorial, Urban, Environmental and Landscape Planning.

Eyyamoğlu, M. and Akçay, A. Ö. (2022). Assessment of historic cities within the context of sustainable development and revitalization: the case of the walled city north Nicosia. *Sustainability*, Vol. 14, Issue 17, 10678. DOI: 10.3390/su141710678.

Fabi, V., Vettori, M. P., and Faroldi, E. (2021). Adaptive reuse practices and sustainable urban development: perspectives of innovation for European historic spa towns. *Sustainability*, Vol. 13, Issue 10, 5531. DOI: 10.3390/su13105531.

Ismail, M. A. and Abd Elkader, W. A. E. (2023). The Interrelationship between the Design of House Facades and the Architectural Identity of the City: Amman City as a Model. *Dirasat: Human and Social Sciences*, 50(6), 275–300. https://doi.org/10.35516/hum.v50i6.683.

Jawabreh, O., Al Fahmawee, E. A. D., Mahmoud, R., and Ali, B. J. A. (2024a). Architecture, authenticity and the construction of memorable tourists experiences. *New Design Ideas*, Vol. 8, No. 1, pp. 33–49. DOI: 10.62476/ndi.8133.

Jawabreh, O., Al Fahmawee, E. A. D., Masa'deh, R., and Abdelrazaq, H. (2024b). Service quality and organizational excellence and their relationships with the Wadi Rum protected area employees' job satisfaction. *Geojournal of Tourism and Geosites*, Vol. 53, No. 2, pp. 599–610. DOI: 10.30892/gtg.53223-1235.

Jawabreh, O. A. A., Masa'deh, R., Al Fahmawee, E. A. D., and Mahmoud, R. (2023). Understanding the dimensions of customer relationships in the heritage hotels in Amman, Jordan. *ISVS e-journal*, Vol. 10, Issue 8, pp. 392–403. DOI: 10.61275/ISVSej-2023-10-08-26.

Jawabreh, O., Fahmawee, E., Ansari, R., Mahmoud, R. and Nassar, U. A. (2025). Geomorphological structure of landform characteristics as a reference for development recommendations in Wadi Rum protected area. *Geojournal of Tourism and Geosites*, 58, 433-445. DOI: 10.30892/gtg.58140-1425.

Merakchi, A., Alkama, D., and Zaouia, K. (2024). Assessment of the spatial appropriateness of the future urbanization of the city of (Ain Beida, Algeria) using geographic information systems, the analytical hierarchy process, and the Delphi method. *International Journal of Innovative Technologies in Social Science*, No. 2 (42). DOI: 10.31435/rsglobal_ijitss/30062024/8161.

Qureshi, R. A., Shah, S. J., Akhtar, M., Abbass, W., and Mohamed, A. (2022). Investigating sustainability of the traditional courtyard houses using deep beauty framework. *Sustainability*, Vol. 14, Issue 11, 6894. 6894; DOI: 10.3390/su14116894.

Rahaman, H., Champion, E., and McMeekin, D. (2023). Outside inn: exploring the heritage of a historic hotel through 360-panoramas. *Heritage*, Vol. 6, Issue 5, pp. 4380–4410. DOI: 10.3390/heritage6050232.

Ribera, F., Nesticò, A., Cucco, P., and Maselli, G. (2020). A multicriteria approach to identify the Highest and Best Use for historical buildings. *Journal of Cultural Heritage*, Vol. 41, pp. 166–177. DOI: 10.1016/j.culher.2019.06.004.

Salameh, M. M., Touqan, B. A., Awad, J., and Salameh, M. M. (2022). Heritage conservation as a bridge to sustainability assessing thermal performance and the preservation of identity through heritage conservation in the Mediterranean city of Nablus. *Ain Shams Engineering Journal*, Vol. 13, Issue 2, 101553. DOI: 10.1016/j.asej.2021.07.007.

Tritto, A. (2020). Environmental management practices in hotels at world heritage sites. *Journal of Sustainable Tourism*, Vol. 28, Issue 11, pp. 1911–1931. DOI: 10.1080/09669582.2020.1771566.

Waheeb, S. A. (2023). Environmental and cultural sustainability of the architectural elements of two historical mosques in historic Jeddah. *Journal of Umm Al-Qura University for Engineering and Architecture*, Vol. 14, Issue 1, pp. 26–35. DOI: 10.1007/s43995-022-00011-z.

Zhong, C. and Christopoulos, C. (2022). Self-centering seismic-resistant structures: historical overview and state-of-the-art. *Earthquake Spectra*, Vol. 38, Issue 2, pp. 1321–1356. DOI: 10.1177/875529302110575.

АРХИТЕКТУРА И ПРОЕКТИРОВАНИЕ ГОСТИНИЦ В ИСТОРИЧЕСКОЙ СРЕДЕ: СТРОИТЕЛЬСТВО И РЕКОНСТРУКЦИЯ В ЦЕНТРЕ АММАНА

Омар Джавабрех[1], Эмад Аль-Дин Аль-Фахмави[2], Рами Махмуд[1], Ораиб Альсбаихи[2], Мохамед Адель Атия[3]

[1] Кафедра гостиничного менеджмента, факультет туризма и гостеприимства, Иорданский университет, филиал в г. Акаба, Иордания

[2] Кафедра дизайна интерьеров, факультет искусств и дизайна, частный университет прикладных наук, Амман, Иордания

[3] Кафедра гостиничного менеджмента, факультет туризма и гостиниц, Университет Минья, Минья, Египет

*E-mail: e_fahmawee@asu.edu.jo

Аннотация

Введение. В данном исследовании рассматривается адаптивное преобразование исторического здания в центре Аммана (Иордания) под функции современного отеля. Цель проекта — сохранить архитектурную и культурную идентичность объекта, одновременно обеспечив соответствие современным стандартам индустрии гостеприимства. В условиях нарастающего градостроительного давления ключевая задача заключается в сохранении конструктивной целостности и исторического облика здания при интеграции необходимых современных удобств. Исследование посвящено анализу этих проблем и подчеркивает важность устойчивых проектных решений при адаптации исторических зданий под гостиничные функции. Центр Аммана, обладающий богатым культурным наследием, представляет собой идеальную среду для изучения практики адаптивного использования зданий в гостиничном дизайне. Работа направлена на поиск баланса между сохранением исторической среды и ее модернизацией, подчеркивая значимость культурного наследия для туризма и поддержания культурной преемственности. В условиях сложной городской среды сохранение архитектурного наследия одновременно укрепляет локальную идентичность и способствует экономическому развитию. **Методы.** В исследовании применяется смешанный методологический подход, включающий анализ кейсов, обзор литературы и полевые исследования, позволяющий изучить устойчивые проектные решения при адаптации исторических зданий под гостиничные функции. Отдельное внимание уделено адаптивному использованию исторических зданий, зеленым строительным технологиям и регуляторным требованиям. Интервью с заинтересованными сторонами и обследование объектов обеспечили практическое понимание процессов восстановления и адаптации зданий. **Результаты.** Полученные данные показывают, что отели, размещенные в исторических зданиях, способны эффективно сочетать сохранение культурного наследия с функциональностью, формируя устойчивую модель использования исторических объектов. Применение энергоэффективных систем и использование местных строительных материалов позволило сохранить исторический характер зданий, одновременно обеспечив соответствие современным требованиям гостей. Такой подход оказался как культурно значимым, так и экономически жизнеспособным. **Обсуждение.** Исследование подчеркивает, что для городских центров, таких как центр Аммана, одинаково значимы как сохранение культурного наследия, так и экономическая эффективность. Основными трудностями являются строгие регуляторные требования и современные строительные стандарты. Исследование указывает на необходимость введения более гибких нормативов, поддерживающих инновационные проектные решения, а также активного участия местного сообщества в культурных процессах. Проект в Аммане служит примером для других городов, демонстрируя, что адаптивное использование исторических зданий способствует сохранению городского наследия и развитию устойчивого туризма.

Ключевые слова: архитектура; дизайн объектов культурного наследи; отель в историческом здании; центр города.

Geotechnical Engineering and Engineering Geology

DOI: 10.23968/2500-0055-2025-10-4-45-55

EXPERIMENTAL STUDY OF THE EFFECT OF HYDRAULIC BINDERS ON THE BEHAVIOR OF SILTY SAND

Hassan Belalia[1], Ahmed Arab[1]*, Fadi Hage Chehade[2], Ahmed Djafar-Henni[3], Sahnoune Bensahnoune[1]

[1] Laboratory of Materials Sciences and Environment, University of Chlef, Chlef 02000, Algeria

[2] Laboratory for Research on Smart Infrastructures and Environmental Technologies, ISBA Marseille, France.

[3] Laboratory of Structures, Geotechnics and Risks, University of Chlef, Chlef 02000, Algeria

*Corresponding author's email: ah_arab@yahoo.fr

Abstract

Introduction. This paper presents a laboratory study investigating the mechanical behavior of silty soil reinforced with hydraulic binders (cement and lime) using a direct shear apparatus. A series of direct shear tests was performed on silty soils treated with hydraulic binders. **Methods.** The tests were conducted at a relative density of 50 %, under three normal stresses, with cement and lime contents of 0, 1, 3, 5, and 7 %, and a water content of 10 %. **Results.** The shear strength of cement-treated silt increases with cement content up to 6 % and then stabilizes. For lime-treated silt, the shear strength decreases at a lime content of 1 % and then stabilizes; thus, the contractive behavior increases with higher lime content. The internal friction angle increases with cement content and then stabilizes, with a slight decrease observed at a cement content of 7 %. Cohesion increases linearly with cement content. Lime addition enhances soil contractiveness; cohesion increases slightly up to a lime content of 3 % and then decreases. For the silt treated with the cement–lime mixture, the test results show that shear strength increases with normal stress compared to the untreated soil.

Keywords: silty soil; cement; lime; content; shear; internal friction angle; cohesion.

Introduction

The problem of soil instability — affecting infrastructure such as buildings, factories, bridges, and roads — is a major concern for public authorities in terms of land use planning. Soil improvement and reinforcement techniques therefore remain an important topic in civil engineering, particularly in the field of geotechnics. These methods aim primarily to enhance mechanical properties by increasing strength and permeability, and by reducing the deformation that occurs under applied loads. Several techniques are currently used to strengthen or improve soil resistance, including compaction, vibroflotation, installation of compacted sand micropiles, drainage, ballast columns, and stabilization through the addition of hydraulic binders.

Several laboratory studies investigated the influence of lime and cement on weak silty soils (Åhnberg, 1996; Akpokodje, 1985; Asghari et al., 2003; Baxter et al., 2011; Consoli et al., 1998; Haeri et al., 2006; Heathcote and Piper, 1994). At lower cement contents and under low confining pressures, soils treated with Portland cement exhibited the highest shear strength (Haeri et al., 2006). Additional studies by Banoune (2016), Boutouil (1998), and Kazi Aoual-Benslafa et al. (2014) examined the influence of hydraulic binders on soil behavior and their effects on shear strength and other mechanical properties. Other researchers focused on the influence of lime on the hydro-mechanical behavior of silt–lime mixtures. Kevin et al. (2013) reported that the mechanical properties of treated soil are governed by microstructural organization, and that lime treatment enhances mechanical performance. The hydro-mechanical properties of soil are significantly improved by lime addition (Osula, 1996). Cement and lime also have a notable effect on the material's microstructure (Osula, 1996). Their addition modifies the flocculation and aggregation of fine clay particles and affects the grain size distribution. Mateus et al. (2016) conducted axial compression tests on sand–cement mixtures (3 % and 7 % cement content) with 10 % water and evaluated five curing periods. Their results show that mixtures with higher cement contents develop lower void ratios, leading to increased shear strength. Marri et al. (2012) emphasized the importance of cementation degree and confining pressure on the stress–strain behavior of cemented sand; the effect of cementation is more pronounced at low confining pressures and diminishes as confining pressure increases. Boutouba et al. (2019) investigated the role of cement content in the mechanical behavior

For citations: Belalia, H., Arab, A., Chehade, F. H., Djafar-Henni, A., Bensahnoune, S. (2025). Experimental study of the effect of hydraulic binders on the behavior of silty sand. Architecture and Engineering, No 4 (10), pp. 45–55.
DOI: 10.23968/2500-0055-2025-10-4-45-55.

of sand and found that cement addition significantly increases shear strength, internal friction angle, and cohesion. They concluded that cement content has a substantial impact on the strength of cemented soils. Of all the studies conducted to date on the effect of lime or cement content on silt, none has provided a complete description of the physico-mechanical mechanism or its effects on both the microstructure and the macroscopic behavior. In this study, we investigate the effect of lime and cement content on the shear strength and mechanical behavior of Chlef silty sand, and examine how mechanical properties (friction angle and cohesion) vary to assess their potential use as a foundation base or foundation layer for road, quay, airport, and railway projects.

Experimental Program

Materials and Experimental Device

The silty sand used in this study was collected from the Zebabdja locality in the town of Oued Fodda, located about 15 kilometers from Chlef (Fig. 1). The fine particles in this soil are slightly plastic, with a plasticity index I_P = 14.7 %, as confirmed by the methylene blue test (VBS = 2.66), indicating a medium-plasticity soil. The physical characteristics of this soil are presented in Table 1. The lime was obtained from the Hasasna industrial zone in the municipality of Saida, and the Chlef cement used is a product of the ECDE company (Algeria).

Tables 2 and 3 show the characteristics of the cement and lime used in the mixtures. Figs. 2 and 3 show the test apparatus and sample preparation process. Fig. 4 illustrates the particle size distributions of the sandy soil alone and of the soil–cement mixtures. The uniformity and curvature coefficients are almost identical to those of the original soil's grain size distribution. Numerous studies have been carried out to examine the behavior of Chlef sand (Aouali et al., 2019; Arab, 2008, 2009; Arab et al., 2014; Della et al., 2011; Djafar Henni et al., 2013; Merabet et al., 2020).

Fig. 5 illustrates the evolution of the plasticity index as a function of cement content. Fig. 6 shows the shape of the soil grains obtained using a scanning electron microscope, along with the microstructure of Chlef silty sand. All samples

Fig. 1. Soil extraction area (Zebabdja, Chlef)

Table 1. **Physical characteristics of the soil**

Physical characteristic	Value
Fine content (D < 80 μm)	5.47 %
D_{10}	0.13 mm
D_{30}	0.28 mm
D_{60}	0.35 mm
Cu (uniformity coefficient)	2.69
Cc (curvature coefficient)	1.72
Natural water content	14.75 %
W_L (liquid limit)	28.28 %
W_p (plastic limit)	13.58 %
I_P (plasticity index)	14.7 %
VBS (methylene blue value)	2.66
Fines fraction	15 %
Sand fraction	85 %

Fig. 2. Experimental equipment used for soil preparation in the laboratory

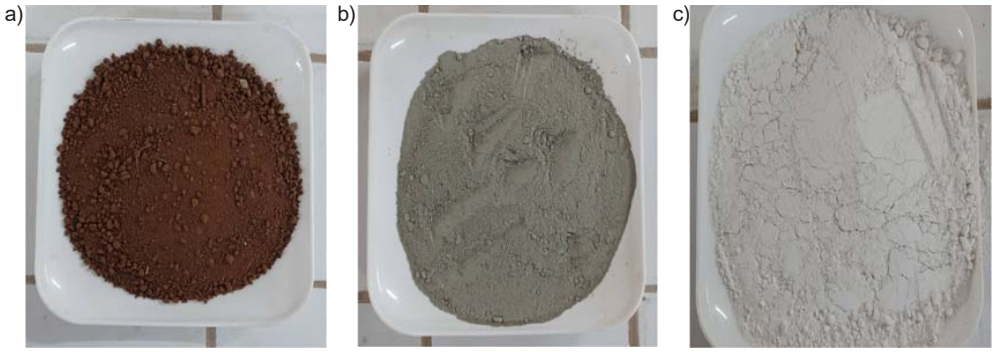

Fig. 3. Sample preparation: (a) original soil; (b) cement; (c) lime

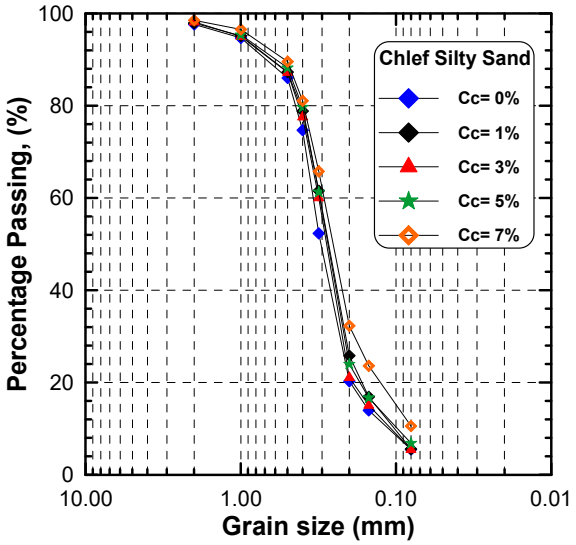

Fig. 4. Grain size distribution curves for the silt–cement mixtures

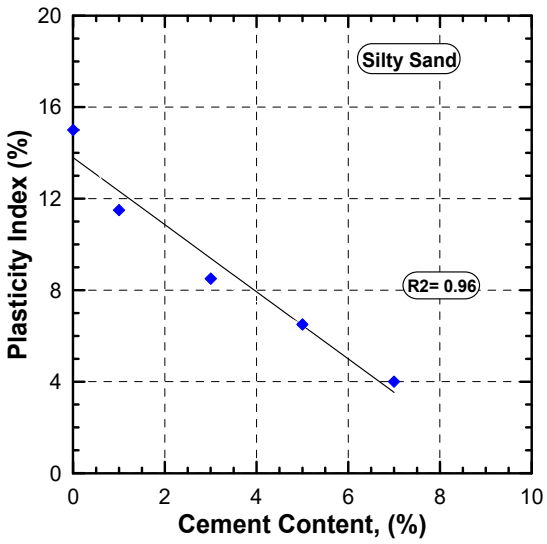

Fig. 5. Variation of the plasticity index with cement content

Table 2. **Chemical and mineralogical compositions of cement**

Chemical composition	(%)
SiO_2	21.64
Al_2O_3	4.90
Fe_2O_3	4.35
CaO	65.82
SO_3	1.78
MgO	0.93
K_2O	0.55
Na_2O	0.29
Mineralogical composition	(%)
C_3S	55.46
C_2S	21.49
C_3A	6.99
C_4AF	11.81

Table 3. **Chemical and mineralogical compositions of lime**

Chemical composition	(%)
SiO_2	1.77
AL_2O_3	5.81
Fe_2O_3	2.63
CaO	78.01
MgO	1.15
K_2O	0.17
Na_2O	0.13
SO_3	0.55

were prepared at a relative density of 50 % and sheared under normal stresses σ_n = 100, 200, and 300 kPa, with a water content of 10 %. The soil was transported from the deposit to the laboratory in 50 kg bags. After sieving the soil and retaining only the silty fraction, the samples were prepared by blending the silty soil with cement or lime in a mixer for about one hour. To ensure homogeneity, the mixtures were then placed in a chamber at 25°C and 90 % humidity for curing periods of 1, 7, 14, and 28 days. Each sample was formed in three layers, with the mass of each layer determined according to the initial relative density (Dr = 50 %). Each layer was poured into the mold and manually

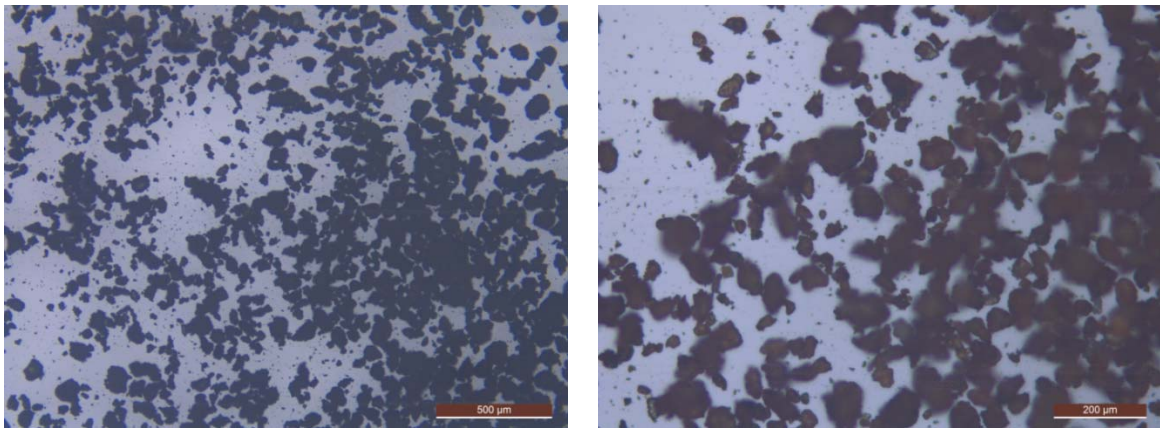

Fig. 6. Scanning electron microscope (SEM) image of the silt used

compacted — typically with 25 strokes — until the desired height was achieved.

The analyzed material is reddish in color and relatively fine, with 5.47 % of its particles smaller than 0.08 mm. It is of medium plasticity (I_P = 14.7 %), as confirmed by the methylene blue test (VBS = 2.66). For each sample preparation, the mass of each mixture used to reconstitute the sample in the shear box was calculated with reference to the initial relative density (I_d), using the following equation (Benessalah et al., 2022; Merabet et al., 2020):

$$m_s = (V_T \times g_s) / (1+ e_{max} (1 - Dr) + Dr \times e_{mi}). \quad (1)$$

Tables 2 and 3 present the chemical and mineralogical compositions of cement and lime, respectively.

Test Results and Discussion

Effect of cement content

Figs. 7a, 8a, and 9a illustrate the evolution of the shear strength of silty sand mixed with cement. All samples were prepared at an average relative density (Dr = 50 %), with the cement content (Cc) varying from 0 to 7 %. The samples were consolidated and sheared under normal stresses of 100, 200, and 300 kPa, respectively. The test results clearly show that the addition of cement has a significant effect on the strength of the mixtures. For samples sheared under σ_n of 100 kPa (Fig. 7a), the shear strength increases with increasing cement content. For samples sheared under normal stresses of 200 and 300 kPa, the strength increases up to a threshold cement content of Cc = 5 %, and then decreases (Figs. 8a and 9a). This reduction in strength beyond 5 % can be attributed to internal erosion within the treated soil. Figs. 7b, 8b, and 9b show the evolution of vertical displacement as a function of horizontal displacement. It is observed that the addition of cement significantly increases the contractive behavior of the soil. These findings are in close agreement with results reported in the literature.

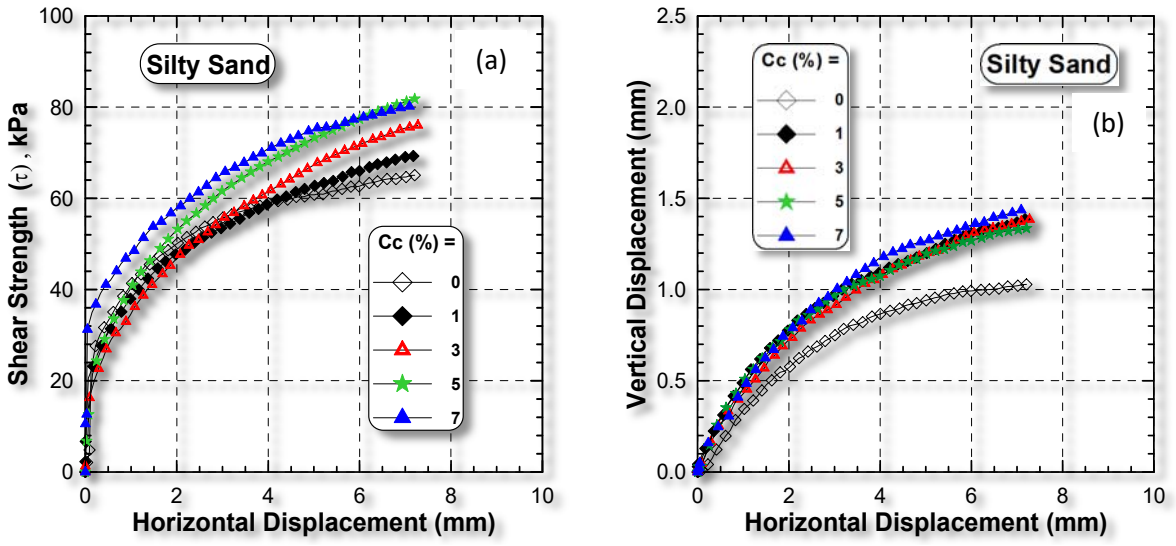

Fig. 7. Evolution of shear stress versus horizontal displacement for silty sand mixed with cement (σ_n = 100 kPa, Dr = 50 %)

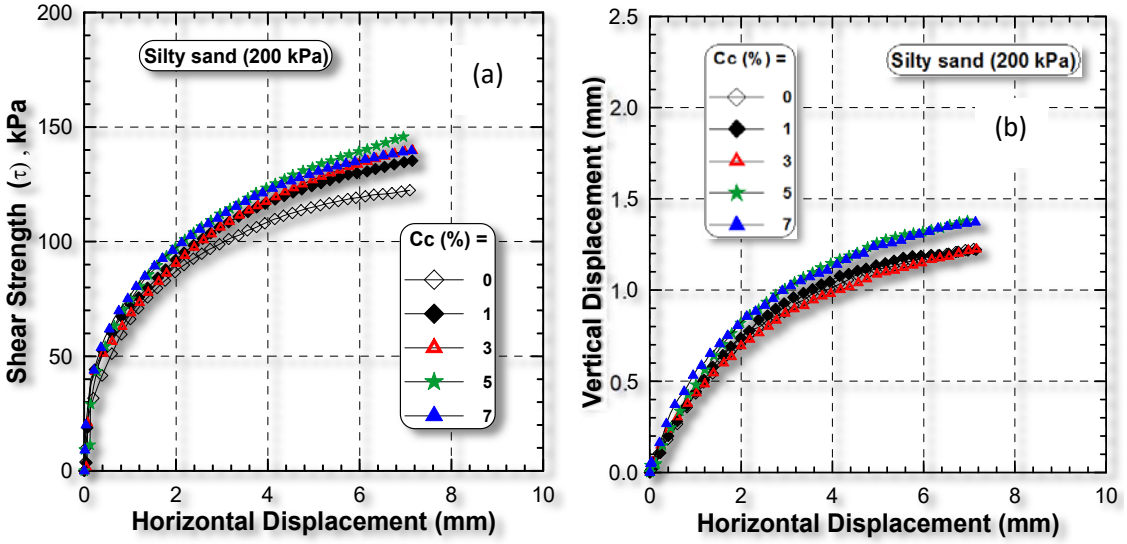

Fig. 8. Evolution of shear stress versus horizontal displacement for silty sand mixed with cement (σ_n = 200 kPa, Dr = 50 %)

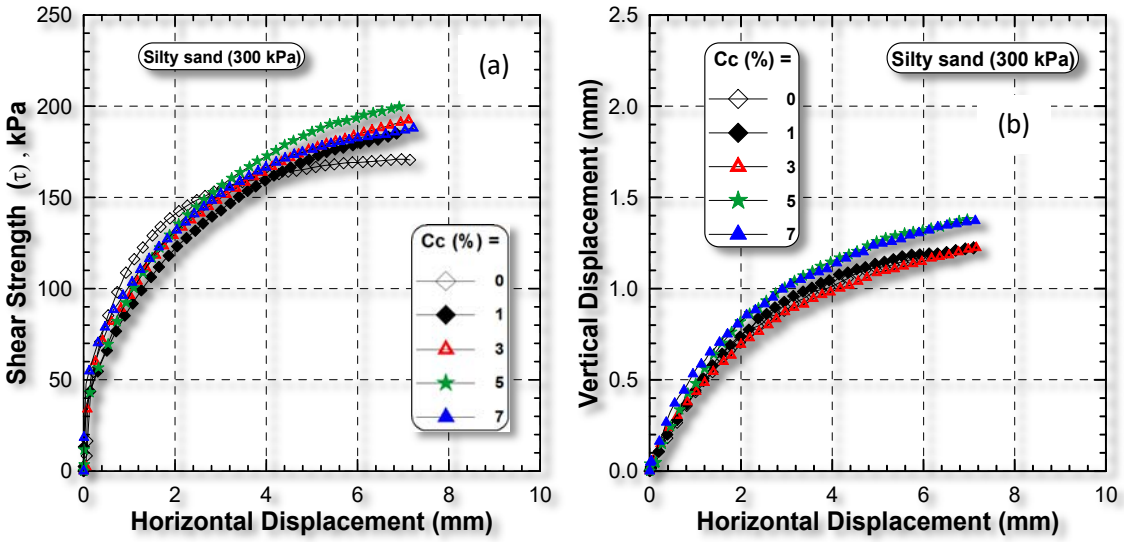

Fig. 9. Evolution of shear stress versus horizontal displacement for silty sand mixed with cement (σ_n = 300 kPa, Dr = 50 %)

Fig. 10 shows the evolution of shear strength as a function of cement content for samples sheared under normal stresses σ_n = 100, 200, and 300 kPa. It can be observed that the shear strength of the mixtures increases with increasing normal stress σ_n, and also with increasing cement content up to Cc = 5 %, after which it decreases. Fig. 11 illustrates the evolution of cohesion as a function of cement content. Cohesion increases linearly with increasing cement content. This increase in cohesion is attributed to the good adhesion between the silt and the cement.

Fig. 12 shows the evolution of the friction angle as a function of cement content for sand–cement mixtures. It can be observed that the friction angle increases with increasing cement content and then stabilizes; a slight decrease in the friction angle is noted at a cement content of 7 %.

Effect of lime content

Figs. 13, 14, and 15 show the results of shear tests on sand–lime mixtures with an initial relative density of Dr = 50 %, consolidated and sheared under normal stresses σ_n = 100, 200, and 300 kPa, with lime content Cl varying from 0 to 7 %. Fig. 13a illustrates the evolution of shear strength as a function of horizontal displacement for sand–lime mixtures. It can be observed that shear strength decreases with increasing lime content up to 1 %, and then increases as the lime content continues to rise. The initial decrease in shear strength after

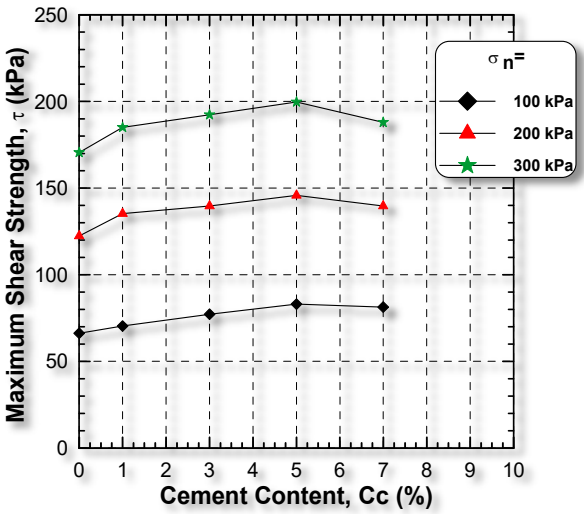

Fig. 10. Evolution of maximum shear strength versus cement content (Cc)

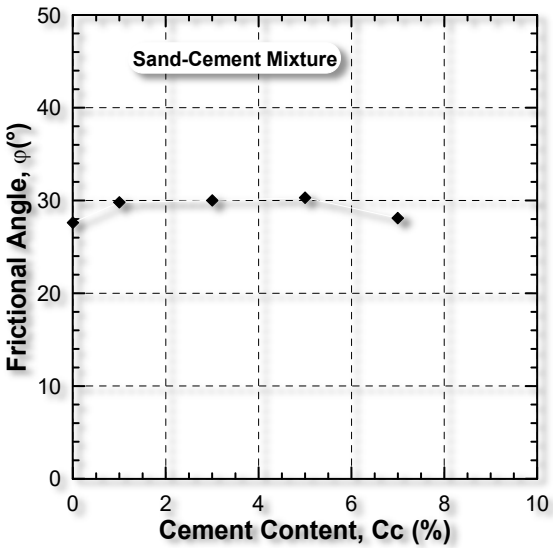

Fig. 12. Evolution of the friction angle versus cement content (Cc)

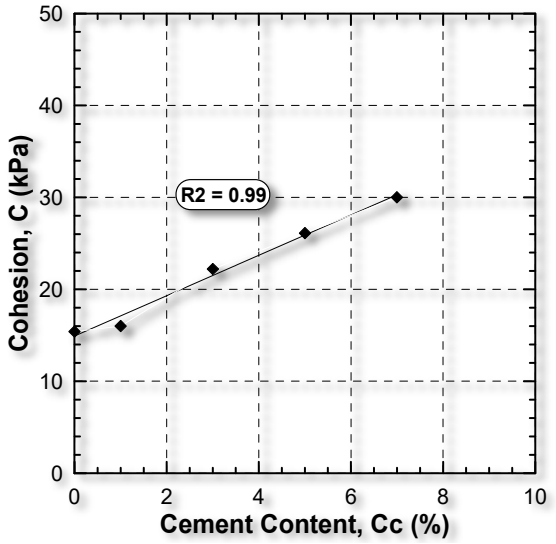

Fig. 11. Evolution of cohesion versus cement content (Cc)

lime addition is attributed to the increased porosity of the mixture. Fig. 13b shows the evolution of vertical displacement versus horizontal displacement for sand–lime mixtures. The results indicate that increasing lime content enhances the contractive behavior. Similar observations were made for the samples consolidated and sheared under normal stresses of 200 and 300 kPa (Figs. 14 and 15). However, for samples subjected to higher consolidation stresses, a clear improvement in dilatant behavior was observed during shearing, indicating favorable mechanical performance for deeper soil layers (Figs. 14 and 15).

Figs. 15a and 15b present the shear test results for the sand–lime mixtures with a relative density of Dr = 50 %, sheared under a normal stress of σ_n = 300 kPa, with lime content Cl varying from 0 to

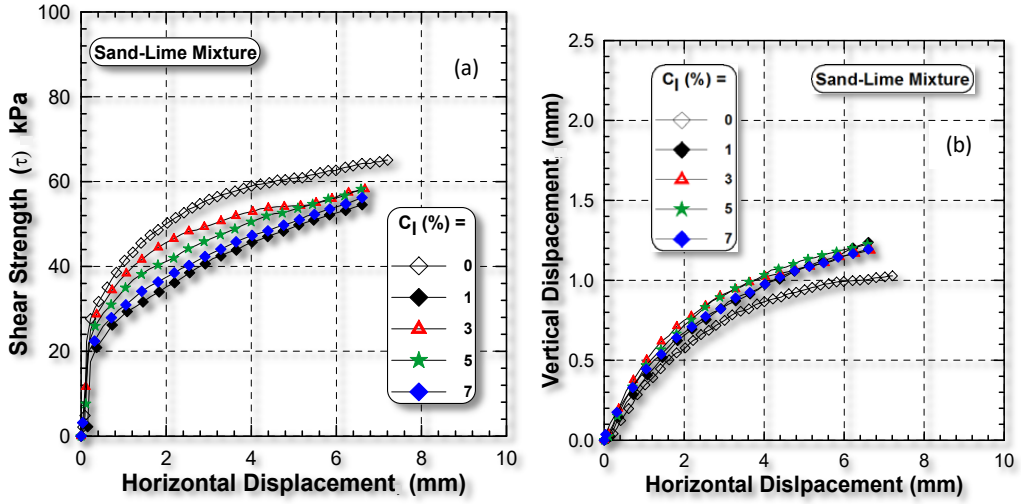

Fig. 13. Evolution of shear strength versus horizontal displacement for sand–lime mixtures (σ_n = 100 kPa, Dr = 50 %)

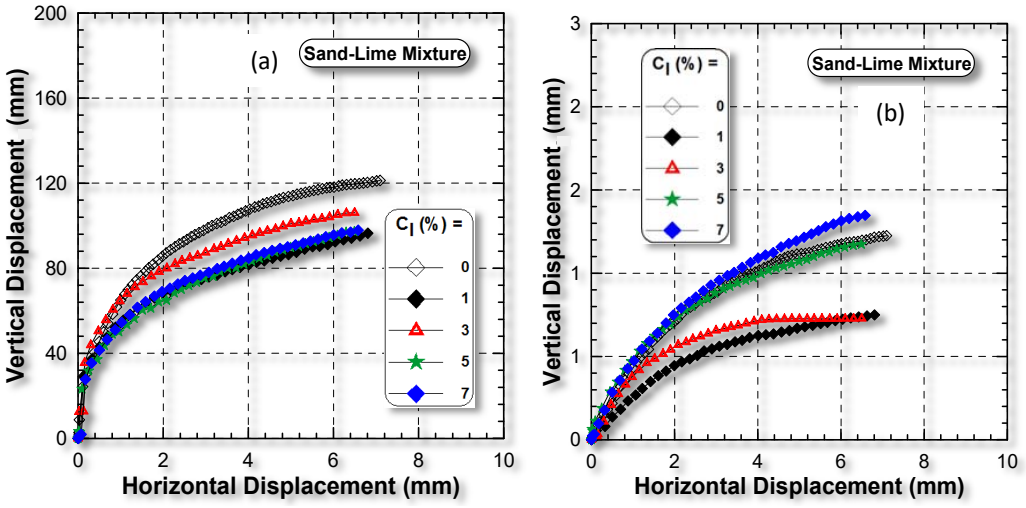

Fig. 14. Evolution of shear strength versus horizontal displacement for sand–lime mixtures (σ_n = 200 kPa, Dr = 50 %)

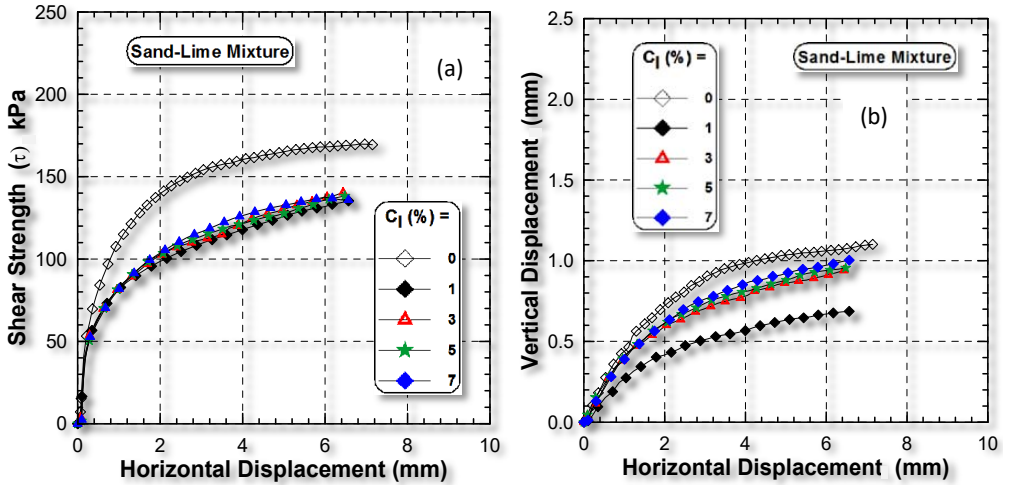

Fig. 15. Evolution of shear strength versus horizontal displacement for sand–lime mixtures (σ_n = 300 kPa, Dr = 50 %)

7 %. Fig. 15a shows shear strength versus horizontal displacement for sand–lime mixtures. The results indicate that shear strength decreases with increasing lime content up to 1 %, and then increases as the lime content continues to rise. Fig. 15b shows the evolution of vertical displacement versus horizontal displacement for sand–lime mixtures. It can be observed that increasing the lime content slightly reduces contractiveness up to Cl = 1 %, beyond which contractiveness decreases only slightly.

Fig. 16 shows the evolution of shear strength for soil–lime mixtures with lime contents ranging from 0 to 7 %, consolidated and sheared under normal stresses σ_n = 100, 200, and 300 kPa. It can be observed that shear strength decreases for all mixtures at a lime content of 1 %, then increases slightly, and subsequently stabilizes up to a lime content of 7 %.

Fig. 17 shows the evolution of cohesion as a function of lime content for sand–lime mixtures. The results indicate that cohesion increases slightly up to a lime content of 3 %, and then decreases as the lime content increases further.

Fig. 18 shows the evolution of the friction angle for sand–lime mixtures. The results indicate that the friction angle decreases at a lime content of 1 %, and then stabilizes as the lime content increases up to 7 %.

Effect of lime–cement on shear strength

Another series of shear tests was carried out in the shear box on soil samples mixed with 6 % cement and 3 % lime; these samples were sheared under normal stresses of 100, 200, and 300 kPa. The fractions of 6 % cement and 3 % lime had shown good performance in the previous shear tests. A clear improvement in shear strength with

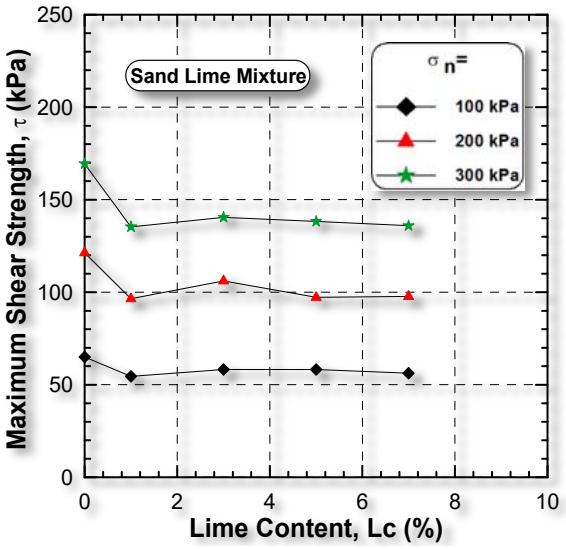

Fig. 16. Evolution of shear strength versus lime content

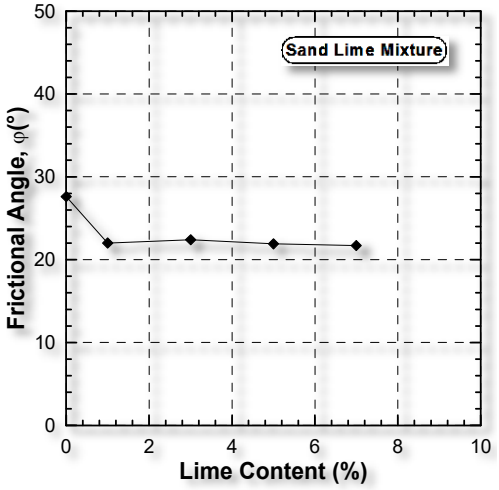

Fig. 18. Evolution of the friction angle versus lime content

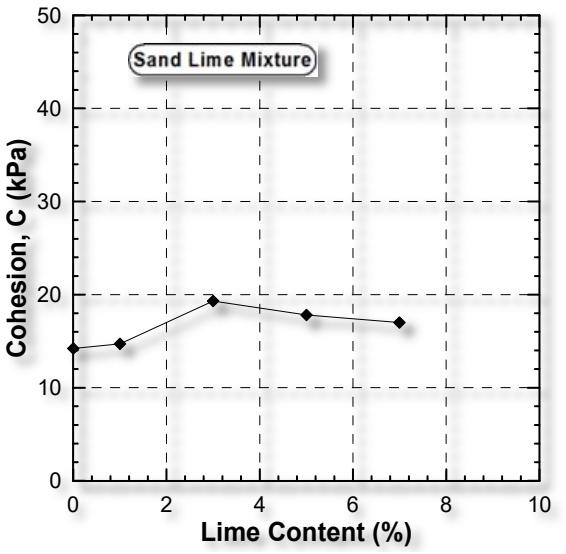

Fig. 17. Evolution of cohesion versus lime content

increasing normal stress is observed (Fig. 19a). Fig. 19b illustrates the evolution of vertical displacement versus horizontal displacement. It can be seen that increasing the normal stress leads to an increase in contraction. These results are in full agreement with those reported in the literature.

Fig. 20 shows the evolution of shear strength for the sample mixed with 6 % cement and 3 % lime as a function of normal stress, compared with the untreated soil. The test results indicate a linear increase in shear strength with increasing normal stress, with correlation coefficient $R^2 = 0.98$. Fig. 20 also shows that the soil treated with cement and lime is more resistant than the untreated soil ($R^2 = 0.99$).

Conclusion

In this study, a series of direct shear tests was carried out on silty sand mixed with cement and lime, with an initial relative density of Dr = 50 %, for the stabilization of coastal soils in Ténès (Chlef, Algeria). The samples were consolidated and sheared under

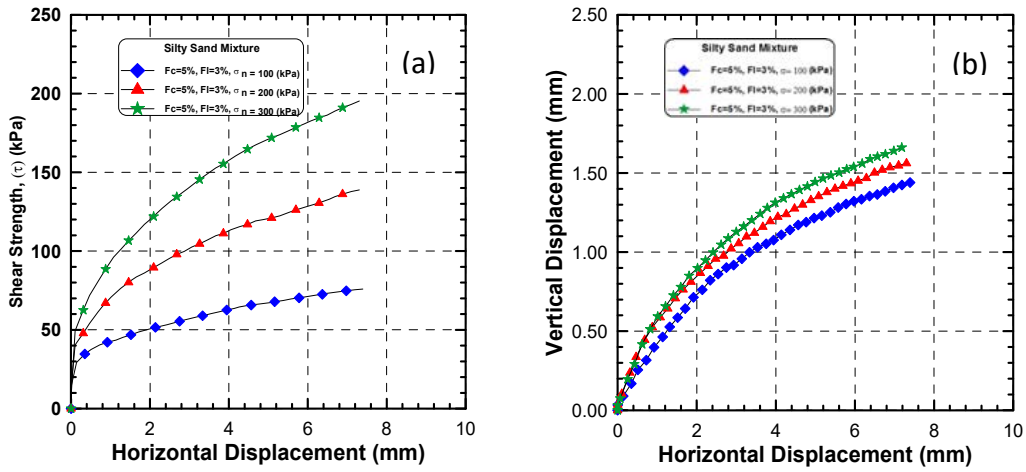

Fig. 19. Effect of cement and lime content on shear strength: (a) evolution of shear strength versus horizontal displacement; (b) evolution of vertical displacement versus horizontal displacement

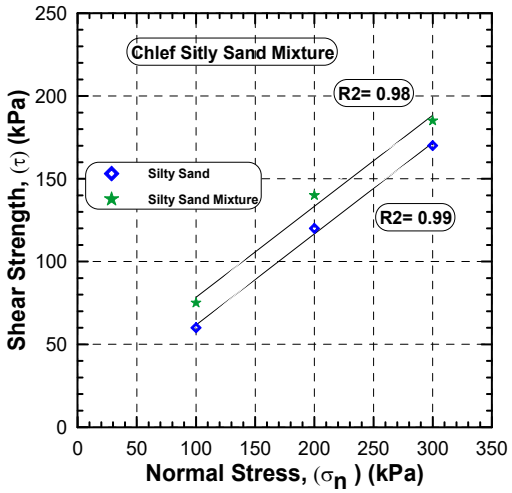

Fig. 20. Evolution of shear strength versus normal stress.

normal stresses ranging from 100 to 300 kPa, with a water content of 10 %, and cement and lime contents varying from 0 to 7 %, in order to examine the mechanical behavior of sand–cement and sand–lime mixtures and their influence on mechanical properties.

The main conclusions drawn from the test results are as follows:

- The shear strength of silt–cement mixtures increases with cement content up to 6 % and then stabilizes.

- Increasing cement content leads to a significant increase in the contractive phase of the samples.

- Higher normal stresses result in improved shear strength, accompanied by increased contractive behavior.

- For silt–lime mixtures, shear strength decreases at a lime content of 1 % and then increases with further lime addition; thus, contractive behavior increases with lime content.

- The presence of cement in the mixture has little effect on the friction angle; however, cohesion increases with increasing cement content.

- For sand–lime mixtures, shear strength decreases up to 1 % lime content and then stabilizes up to 7 %. A similar trend is observed for the friction angle, which decreases up to 1 % and then stabilizes. Cohesion increases slightly up to 3 % lime content and then decreases.

- For the silt–cement–lime mixture, the test results show a linear increase in shear strength with increasing normal stress, with correlation coefficient R^2 = 0.98. The treated soil exhibits significantly higher shear strength compared with the untreated soil.

Acknowledgments

The tests were performed in the Laboratory of Structures, Geotechnics and Risks and the Laboratory of Materials Sciences and Environment at the University of Chlef. This laboratory study was financially supported by the General Directorate for Scientific Research and Technological Development.

Abbreviations

C: Cohesion
Rd: Relative density
Id: Initial density
SEM: Scanning electron microscope
Cc: Cement content
Lc: Lime content
e_{min}: Minimum void ratio
e: Global void ratio
e_{max}: Maximum void ratio
γ_s: Specific weight of solids
m_s: Specific mass

List of symbols

φ: Internal friction angle
σ_n: Normal stress
τ : Shear strength

Units of measurement

KPa: Kilopascal
mm: Millimeter

References

Åhnberg, H. (1996). Stress dependent parameters of cement and lime stabilized soils. In: *Grouting and Deep Mixing. Proceedings of the 2nd International Conference on Ground Improvement Geosystems*, May 14–17, 1996, Tokyo, Japan. Rotterdam: AA Balkema, pp. 387–392.

Akpokodje, E. G. (1985). The stabilization of some arid zone soils with cement and lime. Quarterly Journal of Engineering *Geology and Hydrogeology*, Vol. 18, No. 2, pp. 173–180. DOI: 10.1144/GSL.QJEG.1985.018.02.06.

Aouali, N., Benessalah, I., Arab, A., Ali, B., and Abed, M. (2019). Shear strength response of fibre reinforced Chlef (Algeria) silty sand: laboratory study. *Geotechnical and Geological Engineering*, Vol. 37, Issue 2, pp. 1047–1057. DOI: 10.1007/s10706-018-0641-5.

Arab, A. (2008). Behavior of soils under monotonic and cyclic loading. PhD Thesis in Civil Engineering.

Arab, A. (2009). On monotonic and cyclic behavior of silty sand. *Comptes Rendus Mécanique*, Vol. 337, Issue 8, pp. 621–631. DOI: 10.1016/j.crme.2009.08.001.

Arab, A., Sadek, M., Belkhatir, M., and Shahrour, I. (2014). Monotonic preloading effect on the liquefaction resistance of Chlef silty sand: a laboratory study. *Arabian Journal for Science and Engineering*, Vol. 39, Issue 2, pp. 685–694. DOI: 10.1007/s13369-013-0700-4.

Asghari, E., Toll, D. G., and HaerI, S. M. (2003). Triaxial behaviour of a cemented gravely sand, Tehran alluvium. *Geotechnical & Geological Engineering*, Vol. 21, Issue 1, pp. 1–28. DOI: 10.1023/A:1022934624666.

Banoune, B. (2016). *Comportement mécanique et durabilité des matériaux routiers à différents dosages en sédiments fins*. PhD Thesis in Engineering.

Baxter, C. D. P., Ravi Sharma, M. S., Moran, K., Vaziri, H., and Narayanasamy, R. (2011). Use of Ā = 0 as a failure criterion for weakly cemented soils. *Journal of Geotechnical and Geoenvironmental Engineering*, Vol. 137, Issue 2, pp. 161–170. DOI: 10.1061/(ASCE)GT.1943-5606.0000414.

Benessalah, I., Sadek, M., Villard, P., and Arab, A. (2022). Undrained triaxial compression tests on three-dimensional reinforced sand: effect of the geocell height. *European Journal of Environmental and Civil Engineering*, Vol. 26, Issue 5, pp. 1694–1705. DOI: 10.1080/19648189.2020.1728581.

Boutouba, K., Benessalah, I., Arab, A., and Djafar Henni, A. (2019). Shear strength enhancement of cemented reinforced sand: role of cement content on the macro-mechanical behavior. *Studia Geotechnica et Mechanica*, Vol. 41, Issue 4, pp. 200–211. DOI: 10.2478/sgem-2019-0020.

Boutouil, M. (1998). Traitement des vases de dragage par solidification/stabilisation à base de ciment et additifs. PhD Thesis in Applied Sciences. additifs. PhD Thesis in Applied Sciences.

Consoli, N. C., Prietto, P. D. M., and Ulbrich, L. A. (1998). Influence of fiber and cement addition on behavior of sandy soil. *Journal of Geotechnical and Geoenvironmental Engineering*, Vol. 124, Issue 12, pp. 1211–1214. DOI: 10.1061/(ASCE)1090-0241(1998)124:12(1211).

Della, N., Arab, A., and Belkhatir, M. (2011). A laboratory study of the initial structure and the overconsolidation effects on the undrained monotonic behavior of sandy soil from Chlef region in northern Algeria. *Arabian Journal of Geosciences*, Vol. 4, Issue 5–6, pp. 983–991. DOI: 10.1007/s12517-010-0178-2.

Djafar Henni, A., Arab, A., Belkhatir, M., Saeed Hamoudi, M., and Khelafi, H. (2013). Undrained behavior of silty sand: effect of the overconsolidation ratio. *Arabian Journal of Geosciences*, Vol. 6, Issue 2, pp. 297–307. DOI: 10.1007/s12517-011-0365-9.

Haeri, S. M., Hamidi, A., Hosseini, S. M., Asghari, E., and Toll, D. G. (2006). Effect of cement type on the mechanical behavior of a gravely sand. *Geotechnical & Geological Engineering*, Vol. 24, Issue 2, pp. 335–360. DOI: 10.1007/s10706-004-7793-1.

Heathcote, K. A. and Piper, R. (1994). Strength of cement stabilised pressed earth bricks with low cement contents. *Journal and Proceedings, Royal Society of New South Wales*, Vol. 127, pp. 33–37.

Kazi Aoual-Benslafa, F., Ameur, M., Mekerta, B., and Semcha, A. (2014). Caractérisation des sédiments de dragage du barrage de Bouhanifia pour une réutilisation. In: *13th National Days of Coastal Engineering – Civil Engineering, July 2–4, 2014, Dunkirk, France*, pp. 999–1006. DOI: 10.5150/jngcgc.2014.110.

Kevin, L., Dimitri, D., Stephanie, B., Michel, L., (1913). Effects of lime and cement treatment on the physicochemical, microstructural and mechanical characteristics of a plastic silt. Engineering *Geology*, Volume 166, pp. 255–261. DOI: 10.1016/j.enggeo.2013.09.012

Marri, A., Wanatowski, D., and Yu, H. S. (2012). Drained behaviour of cemented sand in high pressure triaxial compression tests. *Geomechanics and Geoengineering*, Vol. 7, Issue 3, pp. 159–174. DOI: 10.1080/17486025.2012.663938.

Merabet, K., Benessalah, I., Chemmam, M., and Arab, A. (2020). Laboratory study of shear strength response of Chlef natural sand: effect of saturation. *Marine Georesources & Geotechnology*, Vol. 38, Issue 4, pp. 461–467. DOI: 10.1080/1064119X.2019.1595792.

Mateus Forcelini, Gregório Rigo Garbin, Vítor Pereira Faro, Nilo Cesar Consoli. (2016). Mechanical Behavior of Soil Cement Blends with Osorio Sand. *Procedia Engineering*. Volume 143, 2016, pp. 75–81

Osula, D. O. A. (1996). A comparative evaluation of cement and lime modification of laterite. *Engineering Geology*, Vol. 42, Issue 1, pp. 71–81. DOI: 10.1016/0013-7952(95)00067-4.

ЭКСПЕРИМЕНТАЛЬНОЕ ИССЛЕДОВАНИЕ ВЛИЯНИЯ ГИДРАВЛИЧЕСКИХ ВЯЖУЩИХ НА ПОВЕДЕНИЕ ИЛИСТОГО ПЕСКА

Хассан Белалия[1], Ахмед Араб*[1], Фади Хадж Шехаде[2], Ахмед Джафар-Хенни[3], Сахнун Бенсахнун[1]

[1] Лаборатория наук о материалах и окружающей среде, Университет г. Шлеф, 02000 Шлеф, Алжир

[2] Лаборатория LAB2ITC, Институт строительства и общественных работ, Марсель, Франция

[3] Лаборатория строительных конструкций, геотехники и рисков, Университет г. Шлеф, 02000 Шлеф, Алжир

*E-mail: ah_arab@yahoo.fr

Аннотация

Введение. В данной работе представлено лабораторное исследование механического поведения илистого грунта, укрепленного гидравлическими вяжущими (цементом и известью), с использованием прибора прямого среза. **Методы.** Серия испытаний прямым срезом была выполнена на илистых грунтах, обработанных гидравлическими вяжущими. Испытания проводились при относительной плотности 50 %, под тремя уровнями нормальных напряжений, при содержании цемента и извести 0, 1, 3, 5 и 7 %, и влажности 10 %. **Результаты.** Прочность на сдвиг ила, обработанного цементом, увеличивается с ростом содержания цемента до 6 %, после чего стабилизируется. Для образцов, обработанных известью, прочность на сдвиг уменьшается при содержании извести 1 %, а затем стабилизируется; таким образом, с увеличением содержания извести усиливается контрактантное поведение грунта. Угол внутреннего трения возрастает с повышением содержания цемента и затем стабилизируется; при 7 % цемента наблюдается небольшое снижение. Сцепление увеличивается линейно с ростом содержания цемента. Добавление извести усиливает контрактантное поведение грунта: сцепление слегка увеличивается до содержания извести 3 %, а затем уменьшается. Для илистого грунта, обработанного смесью цемента и извести, результаты испытаний показывают увеличение прочности на сдвиг с ростом нормального напряжения по сравнению с необработанным грунтом.

Ключевые слова: илистый грунт; цемент; известь; содержание; сдвиг; угол внутреннего трения; сцепление.

DOI: 10.23968/2500-0055-2025-10-4-56-64

EFFECTS OF RAINFALL AND WATER LEVEL ON THE STABILITY OF THE BAU TRANG LAKE BANK, BAC BINH DISTRICT, BINH THUAN PROVINCE, VIETNAM

Ngoc Thinh Pham, Thi Mai Suong Nguyen*, Van Phu Dang

Thuyloi University, Hanoi, Vietnam

*Corresponding author's email: suongntm@tlu.edu.vn

Abstract

Introduction. This study evaluates the impact of lake water levels, rainfall, and the presence of small pits on the stability of the banks of Bau Trang Lake, a national scenic site in Binh Thuan Province, Vietnam. **Methods.** To assess the slope stability safety factor, several scenarios were simulated using GeoStudio 2024 software with the SEEP/W and SLOPE/W modules. **Results.** With a safety factor reduction of less than 1%, the results show that the small pit has a minimal effect on lake bank stability. The lake water level plays a critical role: low water levels increase the likelihood of instability, whereas high water levels enhance stability and lower pore water pressure. Particularly when combined with low water levels, intense or prolonged rainfall significantly decreases the safety factor by increasing soil saturation and reducing shear strength. The study recommends maintaining stable water levels, reinforcing high-risk areas, and implementing effective drainage systems to mitigate the effects of rainfall. These findings provide a scientific basis for sustainable management strategies to preserve the environment and landscape of Bau Trang Lake, and guide future research on shoreline stability under geological and climatic influences.

Keywords: Bau Trang Lake; slope stability; lake level; rainfall; GeoStudio.

Introduction

One significant issue that requires careful attention on lake and river banks is slope erosion. According to previous research, the erosion process is influenced by both natural and human-induced factors, including geography, geology, water levels, wind-blown sand, and human activities. Slope stability is strongly affected by rainfall characteristics such as intensity, duration, and patterns (Na et al., 2023; Qian et al., 2021; Wang et al., 2022; Zhang and Lu, 2021). Prolonged and intense rainfall can increase pore water pressure and soil moisture, thereby reducing the soil's shear strength and undermining slope stability (He et al., 2023; Huang et al., 2023; Liu, 2023; Na et al., 2023). This can raise the likelihood of landslides, particularly during long periods of heavy rainfall. Additionally, the initial moisture content and groundwater level of the slope are important factors determining slope stability under rainy conditions (He et al., 2021; Huang et al., 2023; Liu, 2023; Zhang and Lu, 2021). Slopes are more prone to sliding during intense rainfall when humidity and groundwater levels are high. Studies have shown that slopes with high moisture content and elevated groundwater levels are more susceptible to instability during rainfall (Morya et al., 2019; Wang et al., 2021). The distribution of soil layers and soil structure also affects slope stability. Cracks, fissures, and transitions between soil layers can increase permeability, enhancing the infiltration of rainfall into the soil (Dou et al., 2021; Li et al., 2023; Zeng et al., 2018). Uneven water distribution within soil layers can alter pore water pressure and reduce the soil's shear strength, thereby increasing the likelihood of slope failure.

The shape and height of a slope also influence its stability under rainfall. Slopes that are steep and high are more susceptible to rainfall-induced instability (Qian et al., 2021; Zhang et al., 2023). Studies have shown that the steeper and higher the slope, the more likely it is to experience failure during heavy rainfall. Therefore, assessing slope geometry is important for predicting the likelihood of slope failure. Slope reinforcement measures, such as the use of anti-sliding piles, bioreinforcement, and tree planting, have been shown to be effective in mitigating the impact of rainfall on slope stability (Huang et al., 2023; Sun et al., 2020; Wang et al., 2021). These measures help improve soil strength and reduce the likelihood of slope failure during heavy rainfall events. The use of numerical models and physical simulation experiments has contributed to understanding the complex interactions between rainfall, water levels, and slope stability, providing important insights into sliding mechanisms and the effects of different factors on slope behavior (Lv, 2023; Tang et al., 2020; Wang et al., 2022; Zhang et al., 2023). Numerical models also help predict scenarios that may occur in practice, thereby supporting more effective slope design and management.

For citations: Pham, N. T., Nguyen, T. M. S., Dang, V. P. (2025). Effects of rainfall and water level on the stability of The Bau Trang Lake Bank, Bac Binh District, Binh Thuan Province, Vietnam. Architecture and Engineering, No 4 (10), pp. 56–64. DOI: 10.23968/2500-0055-2025-10-4-56-64.

Bau Trang Lake, a national scenic site located in Hoa Thang Commune, Bac Binh District, Binh Thuan Province, Vietnam, is a unique natural freshwater ecosystem featuring striking landscapes, including white sand dunes interlaced with clear blue waters. In addition to its ecological and economic functions, Bau Trang is also a tourist destination with great potential due to its pristine natural scenery and favorable environmental conditions. The conservation and sustainable use of Bau Trang Lake are therefore of practical importance in the context of developing tourism linked to the protection of local natural resources. However, lake shore erosion has become an increasing concern, particularly after the severe erosion event at Bau Ba, a part of Bau Trang Lake, on May 3, 2023, which caused significant damage to the ecosystem and terrain and may have endangered tourist safety. This incident underscores the urgent need to assess the causes of landslides in the area. This study examines the effects of rainfall and water levels on the stability of Bau Trang Lake's banks using numerical modeling techniques (GeoSlope software).

Research Data and Methodology

Research Area

Bau Trang Lake is a freshwater lake surrounded by a system of coastal sand dunes. It is located in Hoa Thang Commune, Bac Binh District, Binh Thuan Province (10°00'50" – 11°09'30" N; 108°16'55" – 108°31'12" E) (Fig. 1). Two primary types of terrain occur in the study area: (1) sand dunes, mainly distributed in the northern and northeastern parts of the lake and formed on Pleistocene and Holocene deposits; and (2) flat surfaces, found in the western and southwestern parts of the lake and developed on Pleistocene marine deposits.

Data Collection

a) *Topographic data*

Topographic data were collected from two main sources: 1:10,000 topographic maps issued by the Vietnam Department of Surveying and Mapping, and 5 m resolution Digital Elevation Model (DEM) data from the ASTER GDEM dataset. For spatial analysis, the research team used ArcGIS software to process and integrate the data, thereby generating detailed slope and slope direction maps to assess the current terrain conditions of the area (Fig. 2).

Based on these maps, topographic analysis was performed to identify areas at high risk of landslides through a comprehensive assessment of factors such as slope, slope direction, and the geological characteristics of the ground. In particular, the main research cross-section was selected at the site of the serious landslide incident on May 3, 2023, in order to focus on analyzing the specific causes of instability at that location.

A specific factor considered in the study was the presence of a small waterhole located approximately 135 meters from the landslide site. This waterhole was hypothesized to have influenced groundwater infiltration and movement in the area. Therefore, a detailed analysis of the relationship between this waterhole and the existing geotechnical conditions was conducted to clarify the role of groundwater in destabilizing the slope and triggering the landslide.

b) *Geological data*

The study area is mainly composed of Cenozoic sediments, including two major formations — Pleistocene and Holocene — each with distinct origins, material compositions, and geotechnical properties. Pleistocene sediments include two main groups: marine sediments of the Phan Thiet

Fig. 1. Location of Bau Trang Lake on Google

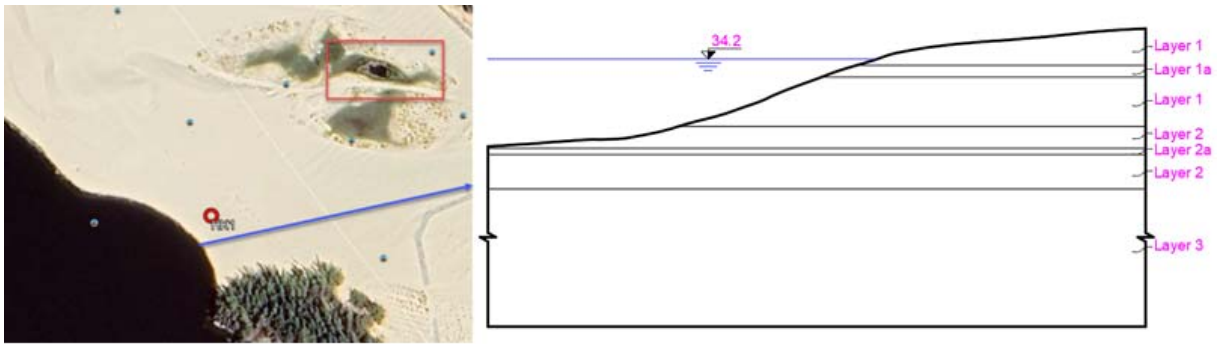

Fig. 2. Geological cross-section of the study area

Formation ($mQ_{12}pt$) and wind-drift sediments (vQ_{12}). The marine sediments consist primarily of fine- to medium-grained sand, sometimes mixed with silty sand, with colors ranging from white and yellow to red, reflecting different stages of deposition in the Pleistocene marine environment. In contrast, the wind-drift sediments are characterized by fine-grained quartz sand with a yellow-brown color, indicating the influence of arid climatic conditions and high wind speeds in the past. Holocene sediments include both wind-borne and fluvial deposits. The wind-borne sediments (vQ21−2, vQ22−3) are mainly medium-grained quartz sand with pearly particles, and their colors range from yellow-brown to light yellow. The fluvial sediments (aQ22−3) consist primarily of silty sand and sand, reflecting transport and deposition under fluvial or nearshore conditions.

The analysis showed that the soils are mainly sandy soils and sandy loams, classified according to the mechanical composition of the sediments. For sandy soils of the Holocene sediments, the physical and mechanical properties — natural moisture content (W), porosity (n), saturation (Sr), compaction coefficient (a), cohesion (c), and internal friction angle (ϕ) — were 18.2 %, 36.2 %, 84.3 %, 0.013 cm²/kg, 0.014 kg/cm², and 24.56°, respectively. These values reflect the typical properties of sandy soils formed in Holocene environments, characterized by moderate compaction and low shear strength. For sandy soils of the Pleistocene sediments, the corresponding physical properties were 18.3 %, 35.2 %, 89.1 %, 0.010 cm²/kg, 0.011 kg/cm², and 26.46°, indicating slight differences in saturation and cohesion compared to the Holocene sandy soils. For sandy loam soils of the Pleistocene sediments, the values were 17.5 %, 34.6 %, 88.1 %, 0.009 cm²/kg, 0.012 kg/cm², and 28.56°, showing improved shear resistance and higher overall stability.

Geological data were collected from a 30 m deep borehole (code: HK1) located at the landslide site. A standard penetration test (SPT) was performed throughout the borehole at 2 m intervals. Soil samples were analyzed in the laboratory to determine the physical and mechanical properties of the soil, including grain size distribution, natural moisture content, porosity, saturation, compaction coefficient, cohesion, and internal friction angle.

Parameters of soil layers are shown in Table 1.

Table 1. **Parameters of soil layers**

Soil layer	γ [kN/m³]	φ [°]	c [kPa]
1	19.9	24˚56′	1.4
1a	20.1	25˚14′	1.9
2	20.3	26˚46′	1.1
2a	19.9	26˚45′	1.8
3	20.5	28˚56′	1.2

c) *Hydrological data*

Rainfall: Rainfall data were collected from the Bau Trang meteorological station. Observations from 1978 to 2020 show a decrease in annual rainfall from 1,325.7 mm in 2016 to 436.3 mm in 2020. The rainfall regime in the area is divided into two distinct seasons: the rainy season, from June to November, with an average rainfall of 724 mm, and the dry season, from December to May of the following year, with an average rainfall of 48 mm. In this study, rainfall of 9 mm over a 2-hour period was used to simulate the influence of rain on the stability of the Bau Trang Lake slope (Fig. 3).

Lake water level: Lake water level data (Fig. 4) were continuously recorded by a TF-Luna LIDAR sensor at hourly intervals. This sensor uses laser distance measurement technology to determine the lake's water level with high precision relative to a fixed reference point. Using these data, changes in water level over time were examined and their effects on slope stability were assessed. The lake water level varied consistently during the first five months of 2024 (January 1 – May 31, 2024) compared with 2023. The water level remained at 2.5 m throughout January and for nearly half of February, but by May it decreased by 0.1 m. Specifically, the water level was stable at 2.3 m in May, both before and after the Bau Ba lake bank landslide (which occurred at approximately 10:30 a.m. on May 3, 2023).

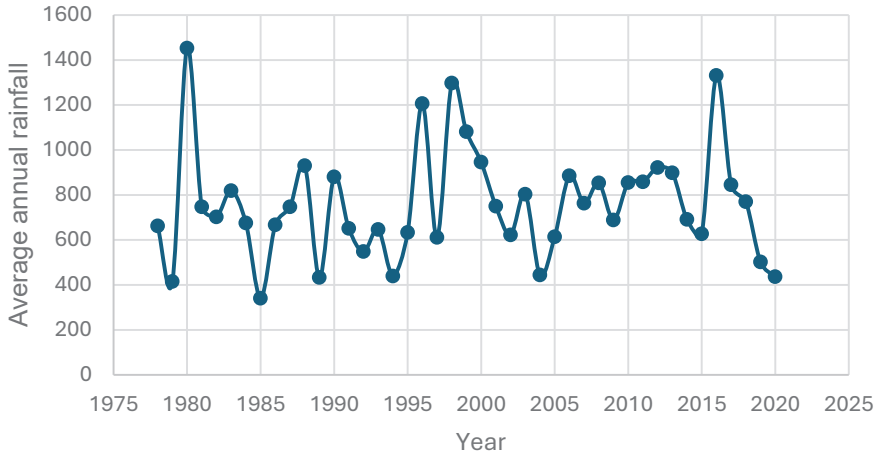

Fig. 3. Average annual rainfall at the Bau Trang station

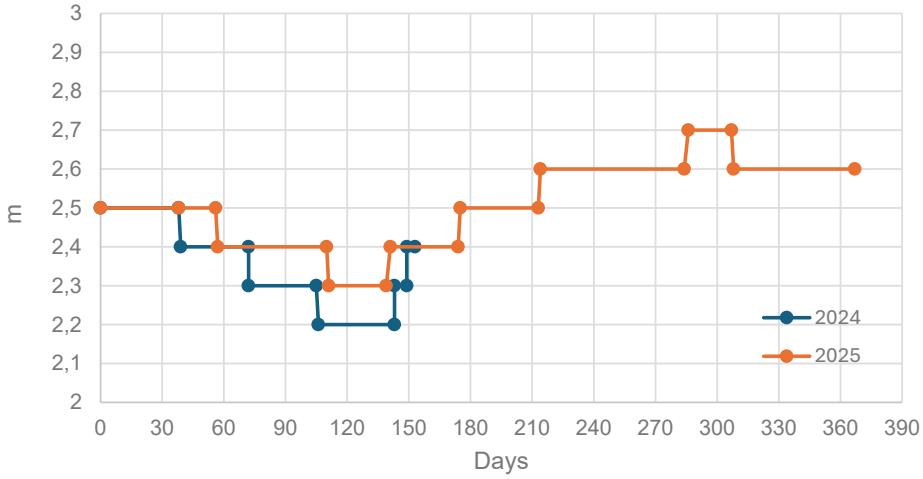

Fig. 4. Water level fluctuations of Bau Trang Lake

Stability Analysis Model

This study uses GeoStudio 2024 software developed by GEO-SLOPE, focusing on two main modules: SEEP/W and SLOPE/W. SEEP/W is a powerful tool for analyzing seepage flow and calculating permeability coefficients and pore water pressures under different soil conditions. Meanwhile, SLOPE/W plays a key role in slope stability analysis by identifying potential sliding surfaces and calculating safety factors.

It is important to note that SLOPE/W is closely integrated with SEEP/W, allowing the calculation of safety factors based on effective stress and pore water pressure. This integration not only improves the accuracy of the analysis but also supports engineers in predicting and mitigating slope failure risks, especially in environments with complex hydraulic conditions.

SEEP/W, a specialized module of the GeoStudio software suite, is widely used to analyze seepage flow in soils under various hydraulic conditions. The tool is based on the fundamental principles of seepage mechanics — Darcy's law. Darcy's law ($q = -ki$) states that the seepage flow rate (q) is directly proportional to the hydraulic gradient (i) and the permeability coefficient (k). The negative sign indicates that water always flows from a region of high potential to a region of low potential. A thorough understanding of this law forms the basis for developing more complex governing equations describing seepage flow.

In two-dimensional seepage analysis, a 2D governing equation is used to model the movement of seepage through soil. This partial differential equation, derived from the law of conservation of mass and Darcy's law, provides a mathematical foundation for predicting pore water pressure distribution and modeling seepage flow within the soil

$$\frac{\partial}{\partial x}\left(k_x \frac{\partial H}{\partial x}\right)+\frac{\partial}{\partial y}\left(k_y \frac{\partial H}{\partial y}\right)+Q=\frac{\partial \theta}{\partial t}, \qquad (1)$$

where:

- H is the hydraulic head;
- k_x and k_y are the permeability coefficients in the x and y directions, respectively;

- Q is the source term, representing the amount of water added to or removed from the system per unit volume;
- θ is the volumetric water content;
- t is time.

Another important factor in soil mechanics is the soil's water retention capacity, measured through the volumetric water content (VWC) index. This capacity is influenced by soil type, porosity, and soil structure. VWC plays an essential role in analyzing and evaluating the characteristics of unsaturated soils.

SLOPE/W analyzes slope stability using the limit equilibrium approach. The method is based on dividing the slope into slices and evaluating the force equilibrium of each slice. A body remains in a static state when all acting forces are in balance (Fig. 5). This means that the total force and total moment acting on the body must be zero.

∑M0 = 0 (the sum of moments about point O is zero).

∑FH = 0 (the sum of horizontal forces is zero).

∑FV = 0 (the sum of vertical forces is zero).

The general formula of the limit equilibrium method is expressed through two safety factor (FoS) equations:

$$F_m = \frac{\sum (c'\beta R + (N - u\beta) R \tan\phi')}{\sum W_x - \sum N f \pm \sum Dd}, \quad (2)$$

$$F_f = \frac{\sum (c'\beta \cos\alpha + (N - u\beta) \tan\phi' \cos\alpha)}{\sum N \sin\alpha - \sum D \cos\alpha}, \quad (3)$$

where:

- F_m and F_f are the safety factors calculated from moment equilibrium and force equilibrium, respectively;
- c' is the effective cohesion;
- β is the width of the slice;
- R is the radius of the slip arc;
- N is the normal force;
- u is the pore water pressure;
- ϕ' is the effective internal friction angle;
- W_x is the horizontal component of the slice weight;
- N_f is the normal force due to external loading;
- Dd is the pull or thrust force;
- α is the inclination angle of the slice.

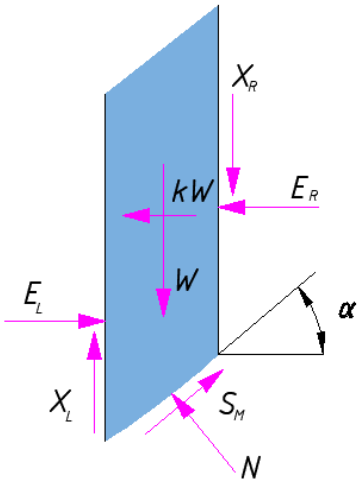

Fig. 5. Diagram of forces acting on a soil slice

Results

To assess slope stability under various rainfall and water level conditions, four representative simulation scenarios were analyzed using the SEEP/W and SLOPE/W modules of GeoStudio.

Case 1. Lake water levels at elevations 34.2 m and 32.0 m, without water in the small hole.

Case 2. Lake water levels at elevations 34.2 m and 32.0 m, with water in the small hole.

Case 3. Lake water levels at elevations 34.2 m and 32.0 m, without water in the small hole, with rainfall.

Case 4. Lake water levels at elevations 34.2 m and 32.0 m, with water in the small hole, with rainfall.

The calculated stability safety factors for all four scenarios are presented in Figs. 6–9 and summarized in Table 2.

The results in Table 2 show that at a water level of 34.2 m, the safety factor decreased slightly from 1.414 to 1.399 when the small hole contained water, with a slight difference of about 1 %. Similarly, at a water level of 32.0 m, the safety factor decreased from 1.296 to 1.263 under the same conditions. However, this reduction remains within acceptable safety limits. Therefore, the small hole plays only a secondary role and is not a major factor influencing the stability of the lake bank. The findings indicate that the presence of the small hole near Bau Trang Lake had only a minor effect on overall slope stability.

The variation in water levels (34.2 m and 32.0 m) clearly influences the safety factor. When the water level is at 34.2 m, the average safety factor is approximately 1.4, significantly higher than the average value of 1.27 corresponding to a water level of 32.0 m. This demonstrates that higher water levels help reduce pore water pressure, thereby enhancing slope stability. Conversely, lower water levels increase pore water pressure and soil saturation, which substantially reduces stability. Maintaining the lake water level within a stable range is therefore an important measure to ensure the safety of the shoreline.

Rainfall also has a significant impact on the stability of the lake bank, especially when combined with water level fluctuations. During rainfall events, the safety factor at a water level of 34.2 m decreases slightly from 1.302 to 1.296. However, when the water level drops to 32.0 m, the safety factor decreases more sharply, from 1.074 to 1.066. This suggests that rainfall increases soil saturation, reduces shear strength, and weakens overall stability. Heavy or prolonged rainfall events heighten the risk of lake bank erosion, particularly when the water level is low.

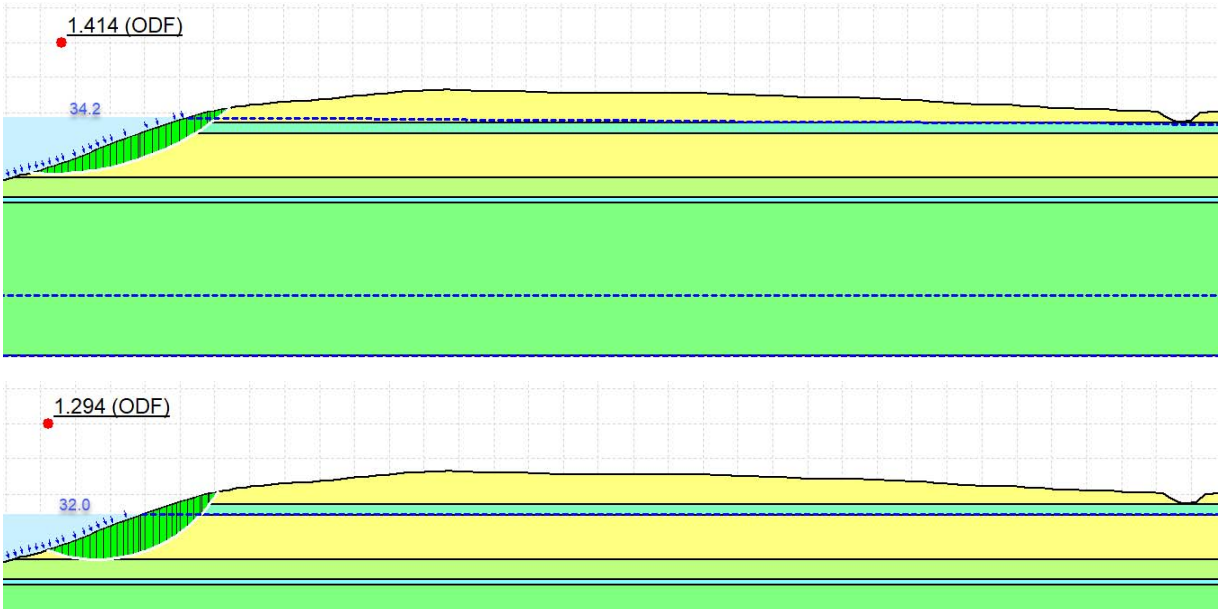

Fig. 6. Lake water levels at elevations 34.2 m and 32.0 m, without water in the small hole (Case 1)

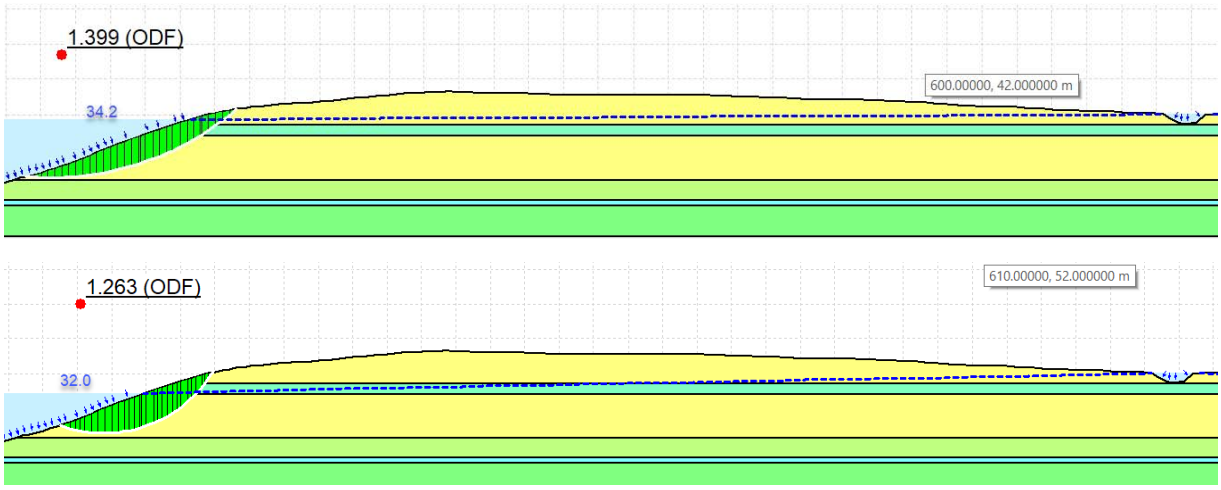

Fig. 7. Lake water levels at elevations 34.2 m and 32.0 m, with water in the small hole (Case 2)

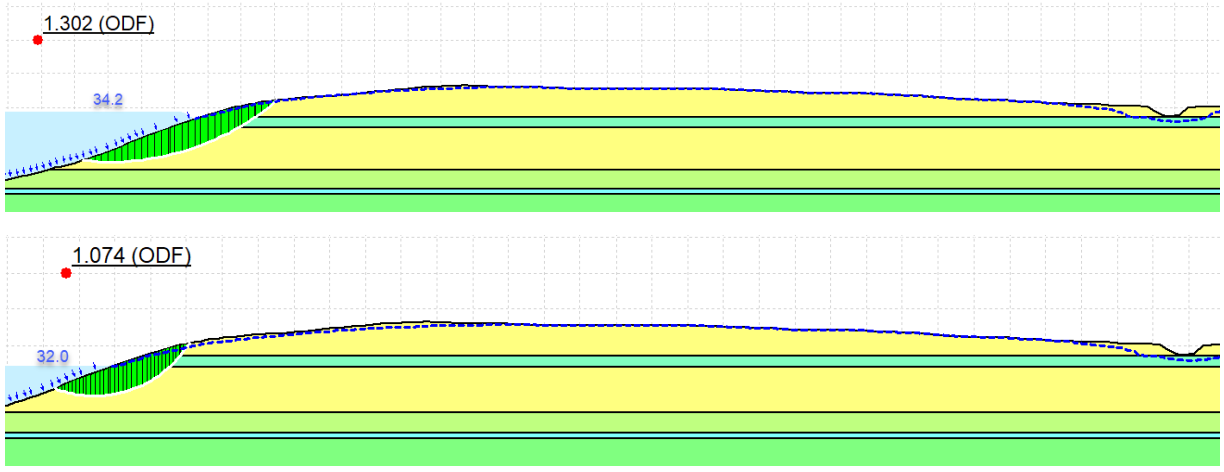

Fig. 8. Lake water levels at elevations 34.2 m and 32.0 m, without water in the small hole, with rainfall (Case 3)

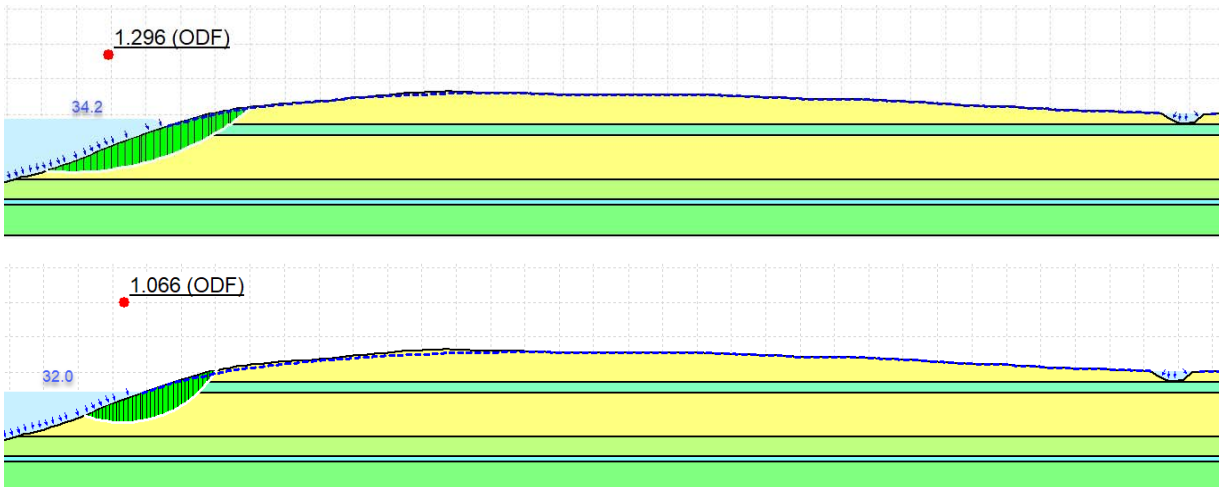

Fig. 9. Lake water levels at elevations 34.2 m and 32.0 m, with water in the small hole, with rainfall (Case 4)

Table 2. **Summary of calculated stability safety factors**

No.	Water level	Small hole without water		Small hole with water	
		Without rain	With rain	Without rain	With rain
1	34.2	1.414	1.302	1.399	1.296
2	32.0	1.294	1.074	1.263	1.066

Conclusion

This study evaluated in detail the effects of lake water level, rainfall, and the presence of small holes on the stability of the Bau Trang Lake bank. Based on the results of numerical simulations and analyses of experimental data, the following main conclusions are drawn:

1. The overall stability of the lake bank is not significantly affected by the presence of small holes near Bau Trang Lake (a reduction of approximately 1–2.5 %). Although the safety factor decreases slightly, the reduction remains within acceptable safety limits.

2. The stability of the lake bank depends largely on the lake's water level. The results show that higher water levels reduce pore water pressure and increase the safety factor, while low water levels raise the risk of instability, especially when combined with other adverse factors such as heavy rainfall (with reductions exceeding 21 %). Recommended measures include maintaining stable lake water levels and reinforcing high-risk areas to reduce erosion hazards and ensure bank safety.

3. Rainfall — particularly heavy or prolonged — leads to increased soil saturation and decreased shear strength. This significantly reduces the safety factor and heightens the likelihood of bank erosion, especially when water levels are low.

4. The study highlights the need for future research on lake shore stability under harsh and complex geological and climatic conditions.

References

Dou, Z., Liu, Y., Zhang, X., Wang, Y., Chen, Z., Wang, J., and Zhou, Z. (2021). Influence of layer transition zone on rainfall-induced instability of multilayered slope. *Lithosphere*, Vol. 2021, 2277284. DOI: 10.2113/2021/2277284.

He, Y., Li, B., and Du, X. (2023). Soil slope instability mechanism and treatment measures under rainfall — a case study of a slope in Yunda Road. *Sustainability*, Vol. 15, Issue 2, 1287. DOI: 10.3390/su15021287.

He, Y., Sun, R., Xu, Z., and Tang, W. (2021). The dynamic change and effect of rainfall induced groundwater flow. *Water*, Vol. 13, Issue 19, 2625. DOI: 10.3390/w13192625.

Huang, M., Zhang, Y., Hu, J., Hei, Y., Xu, Z., and Su, J. (2023). Experimental study on pore pressure variation and erosion stability of sandy slope model under microbially induced carbonate precipitation. *Sustainability*, Vol. 15, Issue 16, 12650. DOI: 10.3390/su151612650.

Li, H., Yang, M., and Dang, T. (2023). Influence of the fracture on the seepage stability of loess slopes. *Frontiers in Materials*, Vol. 10. DOI: 10.3389/fmats.2023.1193527.

Liu, X. (2023). Probe into the influence of water content upon the safety and stability of loess slope based on the Garden Project of Hejin Cherry Valley. *Journal of Physics: Conference Series*, Vol. 2468, 012178. DOI: 10.1088/1742-6596/2468/1/012178.

Lv, Z. S. (2023). Stability analysis of slope engineering based on MIDAS rainfall. In: *Proceedings of the International Conference on Cloud Computing, Performance Computing, and Deep Learning*, Vol. 12712, 127120O. DOI: 10.1117/12.2679262.

Morya, P., Kongpanickul, S., Chao, K. C., and Ishenaliev, R. (2019). Rainfall-induced failure on unsaturated fill and highly weathered schist slopes. *Japanese Geotechnical Society*, Special Publication 7, pp. 556–564. DOI: 10.3208/jgssp.v07.086.

Na, W., Jun, C., and Kim, S. Y. (2023). Influence of rainfall pattern on wetness index for infinite slope stability analysis. *Water*, Vol. 15, Issue 14, 2535. DOI: 10.3390/w15142535.

Qian, J., Sun, D., Li, G., and Wu, Y. (2021). Study on the influence of various rainfall types on the stability of high and steep slopes. *Geofluids*, Vol. 2021, Issue 1, 7906573. DOI: 10.1155/2021/7906573.

Sun, Q.-C., Wei, C., Sha, X.-M., Zhou, B.-H., Zhang, G.-D., Xu, Z.-H., and Cao, L. (2020). Study on the influence of water–rock interaction on the stability of schist slope. *Sustainability*, Vol. 12, Issue 17, 7141. DOI: 10.3390/su12177141.

Tang, J., Taro, U., Huang, D., Xie, J., and Tao, S. (2020). Physical model experiments on water infiltration and failure modes in multi-layered slopes under heavy rainfall. *Applied Sciences*, Vol. 10, Issue 10, 3458. DOI: 10.3390/app10103458.

Wang, Y., Han, M., Lin, X., Li, D., Yu, H., and Zhu, L. (2021). Influence of rainfall conditions on stability of slope reinforced by polymer anti-slide pile. *Frontiers in Earth Science*, Vol. 9, 774926. DOI: 10.3389/feart.2021.774926.

Wang, Y., Smith, J. V., and Nazem, M. (2022). Effect of various rainfall conditions on the roadside stabilisation of slopes in Gippsland. *International Journal of Civil Engineering*, Vol. 21, Issue 1, pp. 173–192. DOI: 10.1007/s40999-022-00752-x.

Zeng, L., Liu, J., Zhang, J.-H., Bian, H.-B., and Lu, W.-H. (2018). Effect of colluvial soil slope fracture's anisotropy characteristics on rainwater infiltration process. *Advances in Civil Engineering*, Vol. 2018, Issue 1, 7351628. DOI: 10.1155/2018/7351628.

Zhang, Y. and Lu, H. (2021). Unsaturated seepage and stability of double-layer slope under rainfall infiltration. *E3S Web of Conferences*, Vol. 248, 03024. DOI: 10.1051/e3sconf/202124803024.

Zhang, Q., Luo, Z., Chen, Y., and Wang, Z. (2023). Physical model experiments on failure mechanism on slopes of weathered basalt soils during heavy rainfall events. *Materials* , Vol. 16, Issue 2, 832. DOI: 10.3390/ma16020832.

ВЛИЯНИЕ ОСАДКОВ И УРОВНЯ ВОДЫ НА УСТОЙЧИВОСТЬ БЕРЕГА ОЗЕРА БАУ ЧАНГ, РАЙОН БАК БИНЬ, ПРОВИНЦИЯ БИНЬТХУАН, ВЬЕТНАМ

Нгок Тхинь Фам, Тхи Май Сыонг Нгуен*, Ван Фу Данг

Университет Тхюилой, Ханой, Вьетнам

*Email: suongntm@tlu.edu.vn

Аннотация

Введение. В настоящем исследовании оценивается влияние уровня воды в озере, атмосферных осадков и наличия малых впадин на устойчивость берегов озера Бау Чанг — национального природного объекта в провинции Биньтхуан, Вьетнам. **Методы.** Для оценки коэффициента запаса устойчивости откосов было выполнено моделирование нескольких сценариев с использованием модулей SEEP/W и SLOPE/W программного комплекса GeoStudio 2024. **Результаты** показывают, что небольшая впадина оказывает незначительное влияние на устойчивость береговой линии, поскольку снижение коэффициента запаса составляет менее 1 %. Уровень воды в озере является ключевым фактором: низкие уровни повышают вероятность потери устойчивости, тогда как высокие уровни способствуют ее увеличению и уменьшают поровое давление. Особенно заметное снижение коэффициента запаса наблюдается при интенсивных или продолжительных осадках в сочетании с низким уровнем воды, что приводит к увеличению насыщенности грунта и снижению его прочностных характеристик. В работе рекомендуется поддерживать стабильный уровень воды, укреплять участки повышенного риска и внедрять эффективные дренажные системы в целях уменьшения воздействия осадков. Полученные результаты служат основой для разработки устойчивых стратегий управления с целью сохранения природной среды и ландшафта озера Бау Чанг, а также обосновывают необходимость дальнейших исследований устойчивости береговой зоны под влиянием геологических и климатических факторов.

Ключевые слова: озеро Бау Чанг; устойчивость склонов; уровень воды; осадки; GeoStudio.

DOI: 10.23968/2500-0055-2025-10-4-65-87

NEARLY ZERO-ENERGY MULTIPURPOSE BUILDING FOR DESA HARAPAN BARU IN EAST KALIMANTAN

Dany Perwita Sari[1]*, Fariz Maulana Riza Nulhaq[2], Mutmainnah Sudirman[3], Dita Anggun Lestari[4], M. Anggi Sanusi[5]

[1] Research Center for Structural Strength Technology, Research Organization for Energy and Manufacture, National Research and Innovation Agency (BRIN), South Tangerang, West Java, Indonesia

[2] Research Center for Energy Conversion Technology, Research Organization for Energy and Manufacture, National Research and Innovation Agency (BRIN), South Tangerang, West Java, Indonesia

[3] Eindhoven University of Technology, Eindhoven, Noord-Brabant, the Netherlands

[4] People Centered Business Economic Initiatives (IBEKA) Foundation, Jakarta, Indonesia

[5] Patriot Energi Program, Subang Regency , West Java, Indonesia

*Corresponding author's email: dany.perwitasari@gmail.com / dany003@brin.go.id

Abstract

Introduction. Desa Harapan Baru, one of the traditional villages in East Kalimantan, is located in a remote coastal area. Limited transportation access, lack of clean water, and poor environmental hygiene are among the major issues faced by the community. As a result, villagers rely on natural resources available around them — such as ulin timber for construction and generators for electricity supply. However, insufficient knowledge of construction practices and reforestation has negatively affected the environment, contributing to flooding in the area. Furthermore, since the generators are situated in a remote location, fuel prices have doubled. **Purpose of the study**. This study aims to design a nearly zero-energy multipurpose building (nZEMB) that aligns with local traditions and community needs. Besides improving the local economy, the project intends to raise awareness about sustainability. **Methods**. Several methods were employed during the design process. First, an assessment of local behavior and cultural practices was conducted to ensure easier community adaptation to new technologies. Solar PV was then selected and installed on the nZEMB roof. PV performance was simulated using PVsyst, computational fluid dynamics (CFD) analysis was carried out with Ansys Fluent, and energy efficiency was evaluated using DesignBuilder. **Results**. The renewable energy system — consisting of 17 solar panels — can fully meet the energy demand of the nZEMB in Desa Harapan Baru. Total daily energy consumption is 59.19 kWh, while the solar panels can generate up to 120 kWh. Additionally, incorporating traditional roof openings and a raised-floor design enhances natural airflow and reduces overall energy use.

Keywords: nearly zero-energy building; remote village; energy efficiency; tropical climate; Indonesian traditional architecture; East Kalimantan.

Introduction

Desa Harapan Baru is a traditional village located in East Kalimantan, Indonesia (Fig. 1), at approximately 1.78° S latitude and 116.42° E longitude. Situated along the seashore, the village is geographically remote and has limited transportation access. Motorboats are required to reach Desa Harapan Baru from the nearest city. Historically, settlement near water bodies has been an integral aspect of human culture (Arifin et al., 2024; Lubis et al., 2018; Putro and Zain, 2021). Rivers and coastal zones have often functioned as determining factors for human settlement patterns, while at the same time being dynamically influenced by human activity. In Desa Harapan Baru, most residents earn their livelihoods from marine fishing and from cultivating milkfish and shrimp ponds.

It is common for residents to live in houses that are regularly inundated during high tides. Even during low tides, the community continues to face health-related problems. The village experiences severe challenges, including limited access to clean water, poor sanitation conditions, and insufficient electricity supply from the national utility company (PLN) (Fig. 2). As a result, residents rely on boat engines and diesel generators to produce electricity (Fig. 2). There is also a substantial demand for ice as a means of preserving fish; approximately 400–800 bags of ice, each costing 3,000 IDR, are sold daily. Since ice production facilities are not available in Desa Harapan Baru, residents must purchase ice from a neighboring village located about 20 kilometers away, requiring approximately

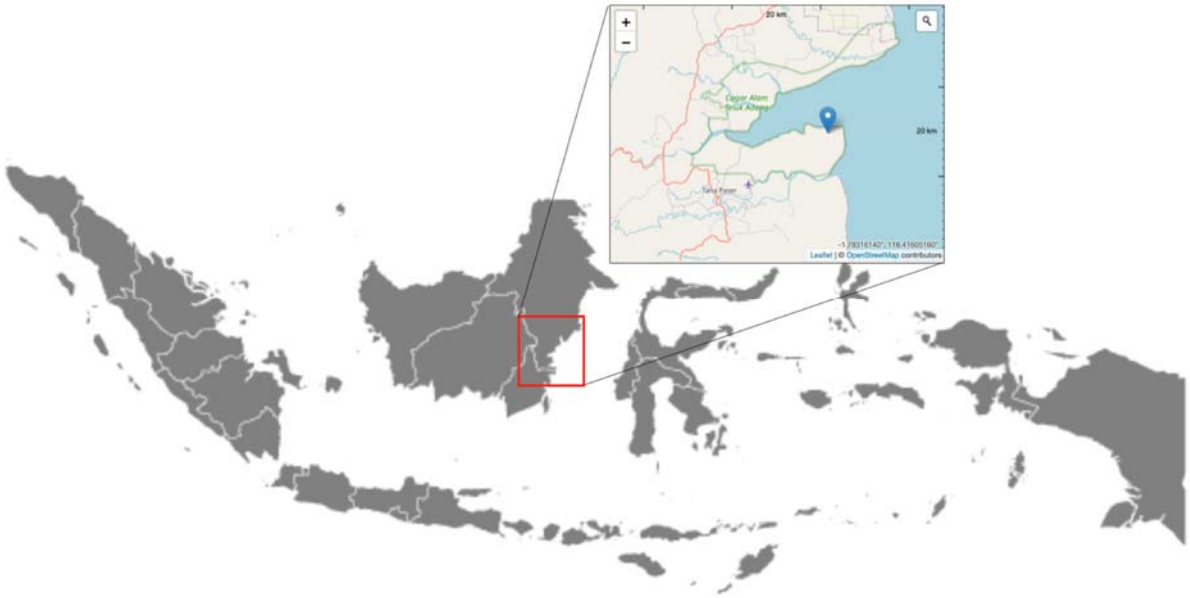

Fig. 1. Location of Desa Harapan Baru on Kalimantan Island, Indonesia (1.78° S, 116.42° E)

Fig. 2. Limited access to clean drinking water, unhygienic environmental conditions, and the absence of electricity supplied by the local government (PLN) in Desa Harapan Baru (a); the use of diesel generators as the village power source (b); nighttime conditions inside residential houses (c)

1.5 hours of travel by boat. Despite these difficulties, the local population continues to reside over the water and construct their homes above it, as they do not own land and depend on fishing activities conducted along the seashore.

As the villagers live in a remote area, they rely heavily on locally available resources. Men primarily work as fishermen, while women support household livelihoods by making fishing nets, drying fish, or selling the catch. Due to the difficulty and high cost of obtaining construction materials from outside the village, houses and other structures are generally built using local materials. This situation becomes more critical during major social events, such as weddings, when temporary structures are often constructed using ulin timber. After the events, these temporary buildings are typically abandoned. Such practices negatively affect the local environment,

particularly through deforestation, which increases the risk of flooding. To move between houses, residents have constructed timber bridges made from ulin wood (Fig. 2). As a result, most daily activities depend on housing structures and these timber bridges.

In response to these conditions, this research aims to develop a nearly zero-energy multipurpose building (nZEMB) that can accommodate various community activities. The study begins with a review of the existing literature on nearly zero-energy buildings (nZEBs) worldwide, as limited information is available regarding their application in tropical climates. Fundamental nZEB design principles involve the integration of multiple energy-efficient technologies (Feng et al., 2019). Passive strategies, such as daylighting systems and natural ventilation, can significantly reduce cooling energy demand (Alwetaishi, 2022; Shi et al., 2020). Photovoltaic (PV) systems represent the most widely adopted renewable energy technology in nZEB design (Ohene et al., 2022), while effective operational management and occupant engagement are also essential for achieving high energy performance during building operation (Kim et al., 2015; Wilberforce et al., 2023).

Designing an nZEMB alone may not fully address the challenges faced by Desa Harapan Baru, as an understanding of local culture is equally important. Previous initiatives introduced simple rooftop solar panel systems; however, not all community members were able to adapt to these technologies. Behavioral transitions from diesel-based energy systems to solar energy proved challenging, largely due to limited knowledge and education related to renewable energy technologies. Consequently, this research integrates local cultural practices and occupant behavior into the building design process. Blending local traditions with new technologies helps reduce resistance to technological adoption and facilitates knowledge transfer within the community.

To develop an nZEMB suitable for Desa Harapan Baru, this study examines technical feasibility and proposes appropriate design guidelines. The specific objectives of the research are as follows:

i. To investigate feasible and effective energy-efficiency design strategies for tropical climates. Based on the literature review, a solar panel system is proposed as the primary energy source for the nZEMB in Desa Harapan Baru.

ii. To evaluate the feasibility and potential of integrating solar panel systems into nZEMB buildings.

iii. To enhance understanding of local culture and occupant behavior in order to improve operational management and occupant engagement.

Methodology and Input Data

The methodology adopted in this study consists of two main components, as illustrated in Fig. 3. The first component focuses on examining the behavior and cultural practices of the residents of Desa Harapan Baru. This approach aims to identify the actual needs of the local community. To achieve this, a combination of 24-hour interviews, site visits, and a literature review was employed. Human activity patterns were identified through 24-hour interviews (Sari and Chiou, 2019; Sari et al., 2024). During

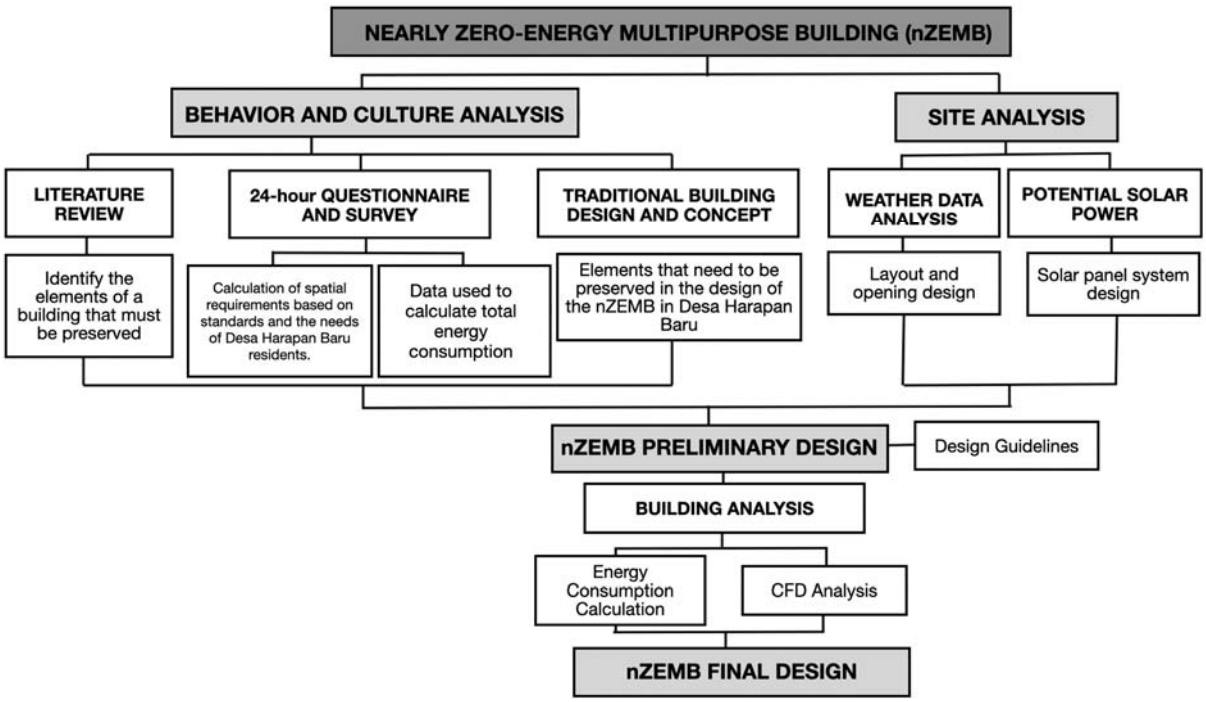

Fig. 3. Stepwise methodology for designing an nZEMB in Desa Harapan Baru, East Kalimantan

these interviews, residents were asked to describe their daily activities over a full 24-hour period, from waking up to going to sleep. By obtaining detailed information on user behavior, the building design can be better tailored to actual needs. Based on this information, the required spaces and the total daily electricity consumption were subsequently calculated.

While the first methodological component focuses on human behavior, the second emphasizes building physics. The second component of the methodology is based on site analysis (Fig. 3). Adapting zero-energy building strategies to the local climatic context is a fundamental aspect of zero-energy building design. In Desa Harapan Baru, access to government-supplied electricity is unavailable, and residents rely on petroleum-based fuels to meet their daily energy needs; therefore, reducing electricity consumption is essential. The most effective approach to minimizing energy demand is the integration of passive design strategies and renewable energy systems. Given the hot and humid tropical climate of the site, the design of building openings plays a critical role in reducing reliance on mechanical cooling, such as fans. Well-considered opening configurations can minimize solar heat gain while maximizing natural airflow. Accordingly, several analyses were conducted, including daylighting analysis, computational fluid dynamics (CFD) simulations, and energy consumption calculations. In addition, assessing solar energy potential and performing related calculations were required for Desa Harapan Baru.

Desa Harapan Baru

1. Analysis of Human Behavior and Culture

The community of Desa Harapan Baru consists of 412 households (Fig. 4). In addition to residential buildings, the village includes a mosque, an elementary school, a junior high school, a kindergarten, a health center, a government office, a warehouse, and a small local shop (*warung*). The results of a survey conducted with 92 household heads indicate that each household consumes approximately 612 kWh for lighting, 39 kWh for street lighting, and 17 kWh for other electrical equipment. At present, these energy demands are met primarily through diesel-based electricity generation. Diesel fuel is purchased at prices ranging from 5,000

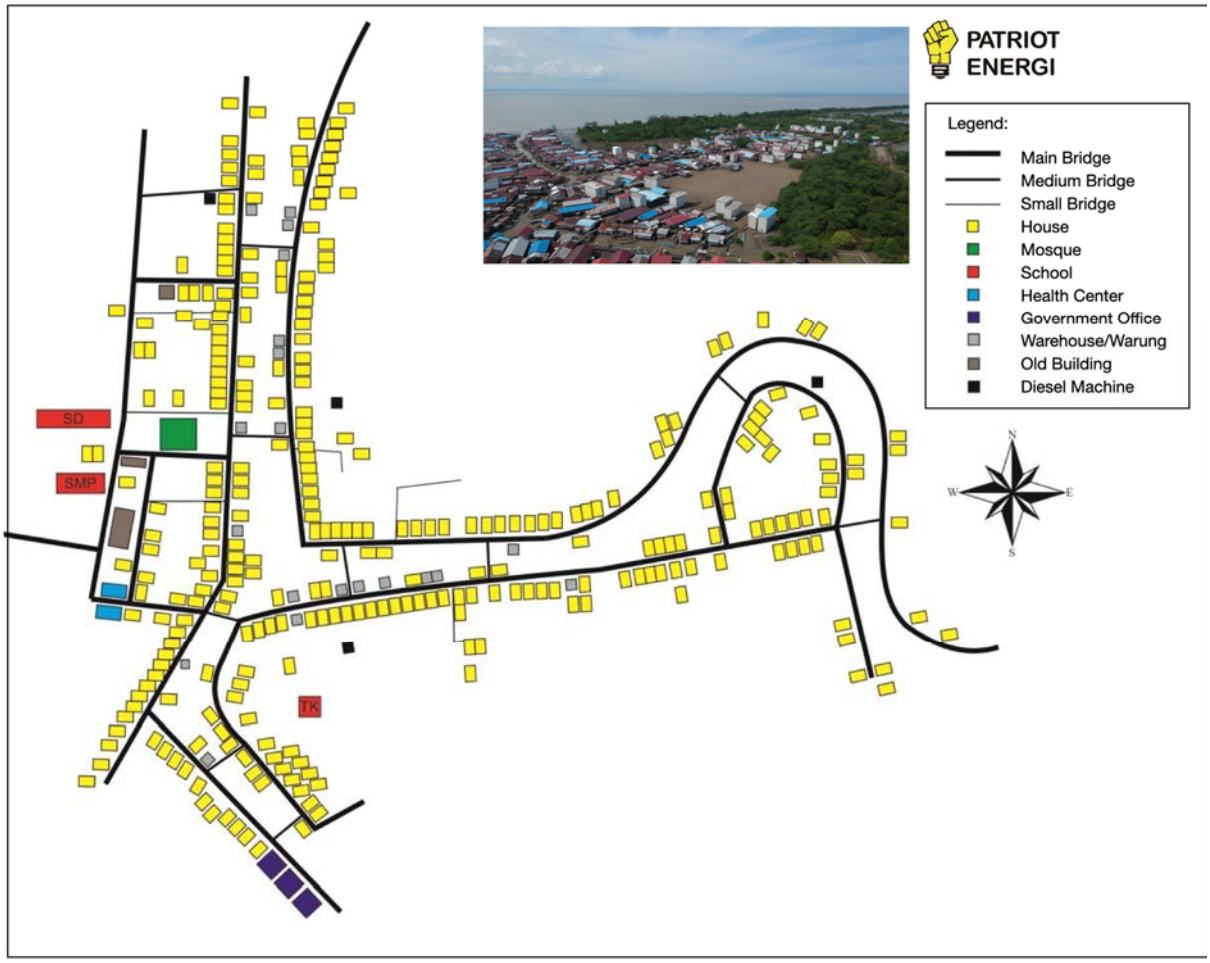

Fig. 4. Building composition of Desa Harapan Baru, East Kalimantan, Indonesia, showing the dominance of residential buildings (highlighted in yellow)

to 15,000 IDR (approximately 0.3–0.9 USD per liter) and is typically used for about 12 hours per day, from 18:00 to 06:00. Peak electricity consumption is estimated to occur between 18:00 and 19:00 (Fig. 5). When compared with the average daily household income — approximately 50,000 to 150,000 IDR (3–9 USD) — the cost of electricity represents a substantial financial burden for local residents.

The results of the preliminary interviews indicate that women spend significantly more time at home than other household members (Fig. 6). In contrast, men typically remain at home only in the early morning hours (00:00–08:00) and in the evening (18:00–23:00), as their primary activities take place outside the household. Women, on the other hand, spend most of their time at home, where their daily

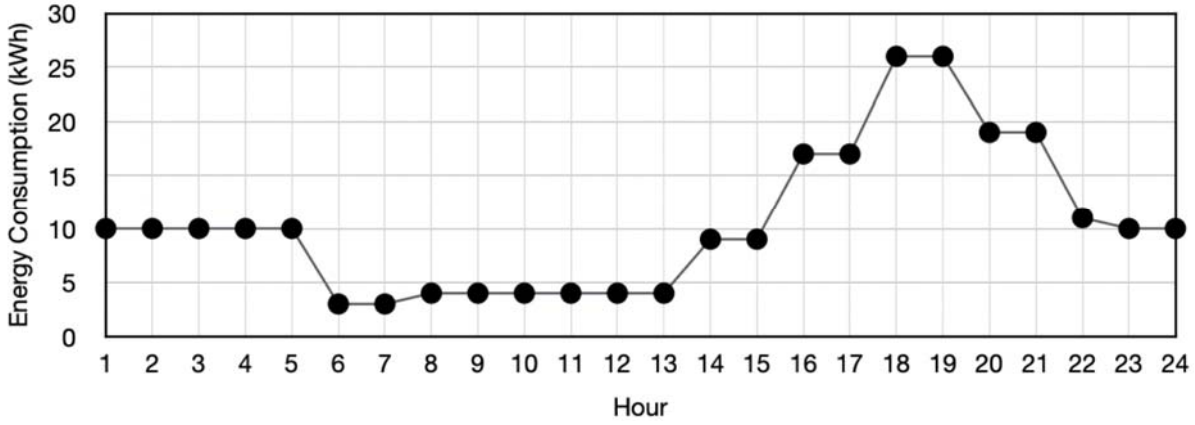

Fig. 5. Electricity load profile of a residential building in Desa Harapan Baru, showing peak demand between 18:00 and 19:00

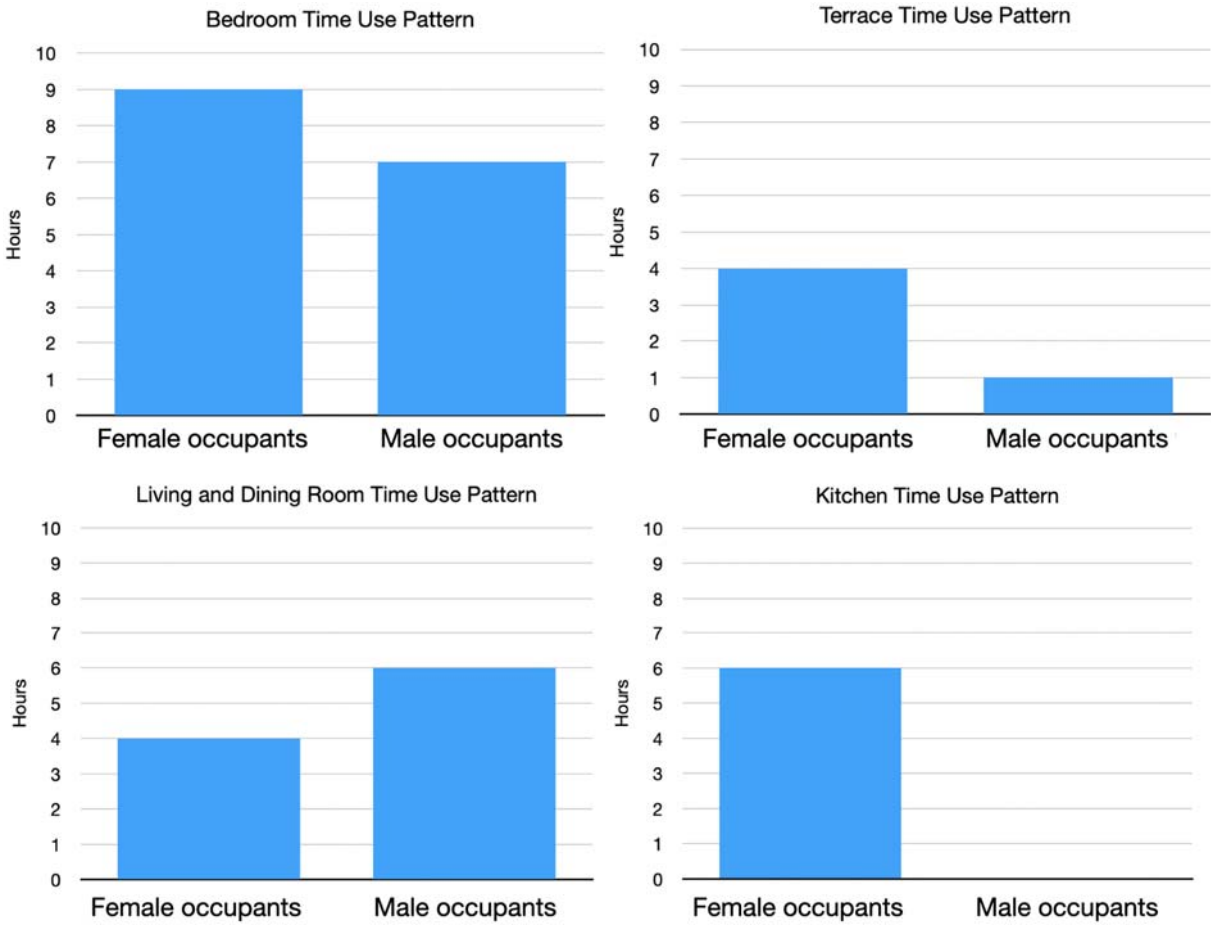

Fig. 6. 24-hour occupancy behavior in Desa Harapan Baru, indicating that women spend more time indoors than men and children

activities include cooking, cleaning, sewing, and operating small local shops (warungs) that sell basic goods. Despite women's dominant presence in the domestic environment, decision-making related to the household — particularly concerning electricity use — is largely undertaken by men. This imbalance has led to mismatches between household needs and energy-related decisions. When new technologies are introduced, training is typically provided only to men. However, because men are often away from home, women are unable to operate, troubleshoot, or repair these technologies when problems arise. As a result, some equipment becomes unusable once it breaks down. For these reasons, this study places particular emphasis on the behavior and daily activities of women and children in the design of new buildings and in the calculation of energy consumption. Women's involvement in energy use and design-related decisions is expected to have a direct influence on environmental outcomes. Interview findings further reveal that local residents — especially women — require dedicated spaces for everyday activities such as selling fish, drying fish, operating *warungs*, and sewing fishing nets. Given the limited size of their houses, these activities are often carried out on terraces or timber bridges. In addition, rising sea levels frequently cause flooding in the village, limiting safe outdoor spaces for children to play. The community also lacks adequate spaces for collective activities, including social gatherings, wedding celebrations, and local meetings. Accordingly, the design of the multipurpose building proposed in this research is directly informed by the needs of local residents. With local residents managing and maintaining the building, it is expected to become more functional and useful. Finally, the findings from this study were compared with insights from international literature. These comparisons include approaches to preserving traditional buildings while incorporating new materials in ways that remain culturally acceptable to local communities. The literature review also helped identify key architectural elements that should be retained in order to maintain cultural continuity.

2. Traditional Houses in Desa Harapan Baru

As illustrated in Fig. 7, houses in Desa Harapan Baru are typically constructed as *rumah panggung* (raised-floor houses). Owing to frequent flooding in the area, this elevated housing typology has been widely adopted. Semi-permanent timber bridges connect individual houses to facilitate access. During periods of flooding, residents often rely on boats for access. The houses are primarily built using ulin wood. These houses accommodate a wide range of daily activities, including fish sorting, discussions of daily needs, small-scale trading (*warung*), fish drying, and monthly community meetings. Overall, the architectural form of the buildings is strongly influenced by climatic conditions, flooding patterns, and local cultural practices.

Fig. 7. Facade, interior spaces, and floor plan of a traditional house in Desa Harapan Baru (Sanusi, 2022)

The roofs of the houses are constructed from zinc sheets and typically follow a gable configuration. The floor plan is rectangular, with dimensions ranging approximately from 6 to 10 meters in length, depending on the needs of the household (Fig. 7). Various openings, including covered windows, are incorporated to reduce direct solar exposure while allowing daylight and ventilation. The raised floor functions as a protective measure against flooding (Fig. 7). Access to the main living space is provided by a removable ladder made from scraped or chipped logs, which can be easily pulled up and stored. The supporting columns of the house are left unenclosed, allowing air to circulate freely beneath the structure. The internal layout generally consists of four main spaces: a terrace, a combined living and dining area, a bedroom, and a kitchen (Fig. 7). This spatial organization is comparable to that of traditional Kalimantan houses known as Lamin houses (Sari et al., 2023). The functions of these spaces are as follows:

1. Terrace: Commonly used for sorting fish, selling daily products, and sewing fishing nets. It also serves as a play area for children.
2. Living and dining area: A centrally located enclosed space used for family gatherings.

Neighbors may also gather here to socialize and discuss community matters, with decision-making typically involving adult male members.

3. Bedroom: Used as the primary sleeping space for the family.

4. Kitchen: Located at the rear of the house and used for cooking and water storage, with a bathroom situated nearby.

As part of the nZEMB design process, a local traditional house was analyzed and redrawn, as shown in Fig. 8. This approach supports the preservation of village identity and cultural continuity while enabling residents to adapt to modern technologies. Another objective is to retain cultural expressions embodied in traditional architecture. Based on literature sources (Brisbane City Council, 2018, 2023), several facade and architectural elements were identified as essential to preserve:

1. Roof and eaves: In traditional architecture, the roof functions as the “hat” of the house. Extended eaves and overhangs help cool interior spaces and protect openings from environmental exposure.

2. Terrace: Provides a welcoming ornate interface with the surrounding environment and traditionally serves as an inviting entrance for visitors.

3. Windows: Serve as a connection between indoor and outdoor spaces, allowing daylight and ventilation while framing views to the outside. In many traditional house types, windows are positioned along the external walls.

4. Ornamental elements: Features such as railings contribute to the visual identity of the house. Preserving or matching traditional details and materials helps maintain local cultural character.

The proposed nZEMB preserves and adapts several of these elements, including the roof shape, spatial layout, raised floor, veranda, terrace, and decorative entrance features.

nZEMB Design

1. Passive Design

Land within Desa Harapan Baru was allocated for community use, and a centrally located site within the settlement was selected for the construction of the nZEMB. Its position at the heart of the village makes it suitable for an nZEMB. The available site area measures approximately 40 m × 80 m (Fig. 9), with geographic coordinates of 1°46′18.37″ S and 116°25′08.59″ E, at an elevation of –1 m above sea level. At present, the site is used as a football field. However, since Desa Harapan Baru is located within a tidal zone, additional elevated walkways and raised floor systems are required to mitigate the effects of flooding. According to Decree No. SK.7781/MENLHK-PKTL/KUH/PLA.2/12/2021, the village and settlement area of Desa Harapan Baru has been excluded from the Adang Nature Reserve. This designation eliminates regulatory overlap between relevant governmental agencies in development planning and permits the construction of new buildings within the area.

An understanding of local climatic conditions is essential for effective passive design and for adapting design strategies to the proposed building. Weather data were analyzed using Climate Consultant software (Society of Building Science Educators, 2021), a graphic-based tool that assists architects, builders, contractors, homeowners, and students in interpreting local climate characteristics (Pinassang

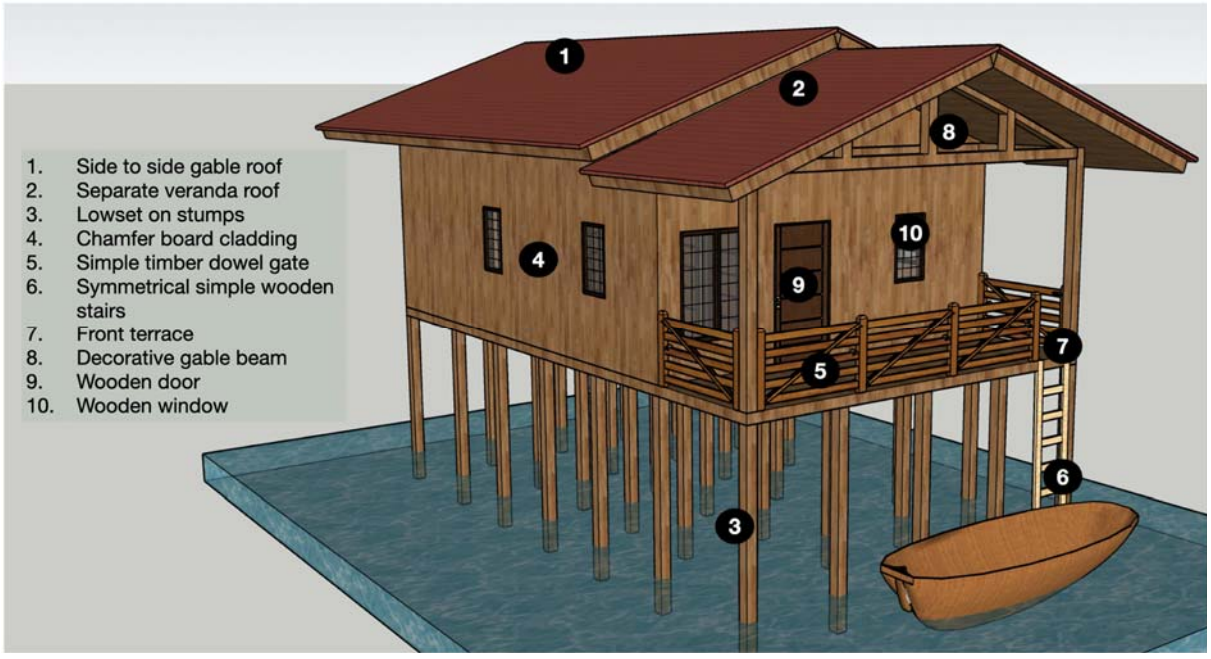

Fig. 8. Traditional house elements from Desa Harapan Baru adapted for the design of the modern nZEMB

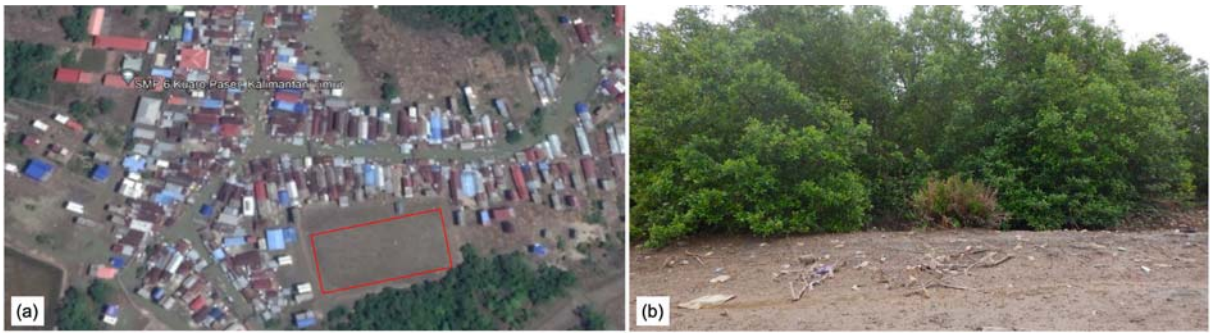

Fig. 9. Location of the nZEMB site (a) and current conditions of the surrounding plots, classified as wetland areas (b)

et al., 2021). Fig. 10 presents the results of the climate analysis. The local climate is tropical and is characterized by two main seasons: a dry season, typically occurring between May and October, and a rainy season, generally between November and April. Maximum temperatures of up to 35.8°C were recorded in March and December, while the lowest temperature, approximately 23.2°C, was observed in January. The highest relative humidity occurs in May, reaching 84 %, whereas the lowest values around 39 % were recorded in June, September, and March. Wind speeds peak in April, with a maximum recorded value of 12.86 m/s.

Considering that Desa Harapan Baru is located in a remote area, building materials must be locally available, as transportation costs significantly affect construction feasibility. The building is therefore constructed entirely using local materials, which also helps address challenges related to water exposure and flooding. Ulin wood was selected for the walls and floors, as Kalimantan is rich in this timber species. Zinc was chosen as the roofing material because it is one of the most accessible and affordable roofing materials in the region (Anggraeni, 2020). In addition, the thermo-hygrometric properties of ulin wood and zinc were examined. Thermo-hygrometric characteristics refer to the combined behavior of materials under varying temperature and humidity conditions (Merello et al., 2014). These properties are particularly important in passive building design, as they directly influence human thermal comfort (Falasca et al., 2023; Palapessy, 2018). Considering thermo-hygrometric behavior supports the development of energy-efficient buildings, assists in moisture control, and helps prevent mold growth — factors that are especially critical in tropical climates such as that of Kalimantan.

Kalimantan faces distinct environmental challenges related to settlement development along rivers and wetlands. Ulin wood (*Eusideroxylon zwageri*) is known for its exceptional durability and resistance to a wide range of temperature and humidity conditions. The use of ulin wood in house construction has become a cultural tradition among communities in Kalimantan, particularly those living in wetland areas (Arifin and Itta, 2013). Previous

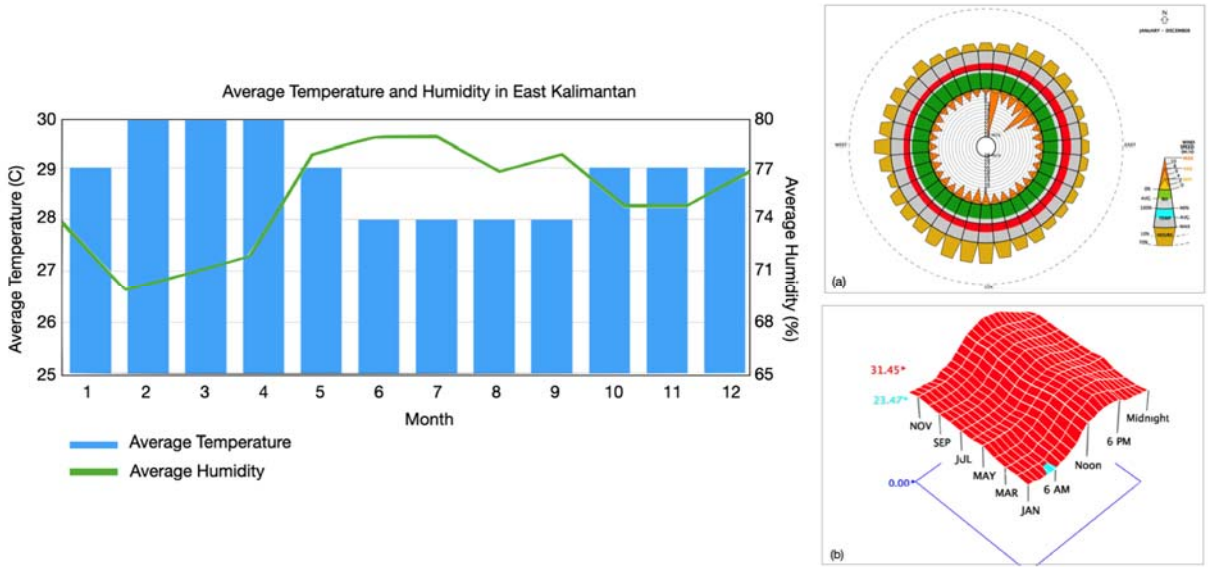

Fig. 10. Climate analysis for East Kalimantan conducted using Climate Consultant software

studies confirm that this material is suitable for a wide range of building applications (Palapessy, 2018). Its natural properties allow it to withstand changes in temperature and humidity, as well as exposure to seawater.

The climate of Desa Harapan Baru is representative of much of Indonesia, characterized by a humid tropical climate with consistently high temperatures and humidity throughout the year. Zinc roofing is an affordable and widely used material in Kalimantan; however, its thermal properties can lead to increased indoor temperatures and perceived humidity levels (Alkausar and Riyani, 2023). Due to its lightweight nature and thermal properties, zinc roofing readily absorbs solar heat, contributing to elevated indoor temperatures (Paramita, 2025). While zinc roofs do not directly increase indoor humidity, higher temperatures can intensify the perception of humidity and reduce thermal comfort (Alkausar and Riyani, 2023). In the hot and humid conditions of Desa Harapan Baru, even slight temperature increases can significantly affect occupant comfort. Consequently, zinc roofing in such climates requires mitigation strategies, including the use of light-colored or coated zinc materials, improved natural ventilation, and additional thermal insulation.

Based on these considerations, several passive design strategies are proposed for the nZEMB:

1. In response to local climatic conditions, available resources, and site characteristics, zinc roofing is adopted, while raised floors and columns are constructed from ulin wood. The timber walkway is designed with a minimum width of one meter.
2. The building is designed to promote natural ventilation through shaded openings and appropriately oriented windows that face prevailing wind directions, thereby reducing heat gain from the zinc roof.
3. Passive cooling is enhanced through a patio-based ventilation strategy, particularly during hot periods.
4. Natural cross-ventilation is supported through an open-plan layout and the use of ceiling fans.
5. Thermal heat gain is further reduced by controlling solar radiation.

To reduce reliance on petroleum-based energy sources, the building is designed to produce its own electricity. Solar panels are therefore incorporated as the primary energy generation system. As shown in Table 1, measurements of received solar energy were used to obtain solar irradiation data. Table 1 presents global horizontal solar irradiation data obtained from Meteonorm 8.0 (1991–2009) for the proposed off-grid solar (OGS) site. A Meteonorm report was automatically generated when PVsyst was accessed (PVsyst documentation, 2023).

The solar resource in Desa Harapan Baru varies throughout the year, with the lowest global horizontal irradiation recorded in June at 110 kWh/m²/month and the highest in March at 158 kWh/m²/month. The total annual global horizontal irradiation at the site is 1,719.7 kWh/m^2. These values indicate that Desa Harapan Baru has a high potential for harvesting solar energy to meet local energy demands. Further analysis was carried out using PVsyst software to evaluate the solar energy potential and to design the solar panel system. Table 2 presents the DC output voltage and current of the solar array, denoted as U_{mpp} (1) and I_{mpp} (2), respectively.

Table 1. **Monthly global horizontal solar irradiation at the proposed site in Desa Harapan Baru**

Month	Global horizontal solar irradiation (kWh/m^2/month)
January	145.7
February	140.2
March	158.6
April	142.8
May	135.3
June	110.1
July	146.6
August	154.0
September	152.2
October	146.6
November	147.2
December	140.5
Year	1,719.7

$$U_{mpp} = voltage\ of\ a\ solar\ module \times \times number\ of\ modules\ in\ series; \quad (1)$$

$$I_{mpp} = current\ of\ a\ solar\ module \times \times number\ of\ modules\ in\ parallel. \quad (2)$$

EArrNom represents the amount of energy produced by the solar array as a result of converting incident solar irradiation. It is calculated using the following equation:

$$EArrNom = Globeff \times Pnom, \quad (3)$$

where global effective irradiance (Globeff) represents the global solar irradiation after accounting for optical losses such as shading, incidence angle modifier (IAM), and soiling, while Pnom denotes the nominal power of the PV array at standard test conditions (STC), equal to 30 kWp. When the available solar energy is insufficient to satisfy the load demand, the resulting energy shortfall is referred to as E_Miss. This condition occurs when the combined output of the PV system and the battery energy storage system is unable to fully meet the required energy demand. The solar fraction can be calculated based on the ratio between the energy supplied to the user (E_User) and the energy needs (E_Load), as expressed in Eq. (4):

$$solarfraction = E\_User / E\_Load. \quad (4)$$

Table 2. **Solar panel characteristics based on U_{mpp} and I_{mpp} calculations**

PV system		**Battery**	
Manufacturer	Trina Solar	Manufacturer	Narada
Model	TSM-DE 18M-(II)-500	Model	EosG 1000
Nominal power per module	500 Wp	Technology	Sealed lead-acid (gel)
Number of PV modules	60 modules	Configuration	6 parallel × 24 series
Total nominal power (STC)	30 kWp	Minimum discharge SOC	20.0 %
Power at operating conditions (50°C)		Stored energy	231.0 kWh
P_{mpp}	27.31 kWp	**Battery pack characteristics**	
U_{mpp}	156 V	Voltage	48 V
I_{mpp}	175 A	Nominal capacity	6,000 Ah (C10)
Controller (universal controller)		Temperature	Fixed at 35°C
Technology	MPPT converter	**Battery management control**	
Temperature coefficient	−5.0 mV/°C per cell	Control thresholds	SOC-based
Converter		Charging (approx.)	SOC = 0.90 / 0.75 53.9 / 50.7 V
Maximum / European efficiency	97.0 / 95.0 %	Discharging (approx.)	SOC = 0.20 / 0.45 47.7 / 49.5 V
Total PV power			
Total nominal power (STC)	30 kWp		
Total modules	60 modules		
Module area	143 m^2		

Several photovoltaic installations have been evaluated using the Performance Index developed by the European Joint Research Center (JRC), which is incorporated into the IEC EN 61724 standard (PVsyst, 2023). These indicators are based on the incident global irradiation received by the solar array and are normalized by the nominal installed power, Pnom, expressed in kilowatt-peak (kWp) under standard test conditions (STC). According to STC, global irradiation under outdoor conditions is defined as 1,000 W/m², the module temperature is set at 25°C, and the solar spectrum corresponds to AM 1.5, which represents a normalized solar spectrum equivalent to 1.5 times the atmospheric air mass at sea level. Under these reference conditions, performance indicators are independent of the array size, geographic location, and field orientation (Kim et al., 2015). Yield values are therefore expressed in units of kWh/kWp/day, which are numerically equivalent to the equivalent operating time at a constant irradiation of 1 kW/m². These values may also be interpreted as hours per day at 1 kW/m² or as kWh/m²/day (Kim et al., 2015).

The integration of passive design strategies with photovoltaic systems provides an effective approach for achieving an optimal nZEMB design for Desa Harapan Baru. Based on the established design guidelines, a preliminary nZEMB configuration was developed. Subsequently, two analytical methods were applied to evaluate the proposed design. First, indoor thermal comfort was assessed using computational fluid dynamics (CFD) analysis conducted with ANSYS Fluent software. Finally, building energy consumption was evaluated using DesignBuilder software through energy simulation.

2. nZEMB Architecture Design

The final design of the nZEMB is presented in Fig. 11. The proposed nZEMB incorporates a landing dock, a cold storage facility, a market hall, warung stalls, a multipurpose room, a kitchen, lavatory facilities, a *mushola* (prayer room), and a plaza. In Desa Harapan Baru, landing docks are commonly found at individual houses, as most residents work as fishermen. After fishing is completed, the catch is typically sorted immediately. The nZEMB consolidates these dispersed activities into a single centralized facility. Providing a large landing dock allows post-fishing activities, such as unloading and sorting the catch, to be carried out more efficiently than selling fish directly to customers upon arrival. According to an earlier interview, local residents expressed the need for cold storage facilities so that fish do not have to be sold immediately after fishing trips. The availability of cold storage would enable fishermen to preserve their catch and avoid selling it at low prices under time pressure.

Near the landing dock, fish can be sold directly at the market hall. The warung, which serves as a retail space for everyday goods, is located adjacent to the market hall. Traditionally, such activities as fish sorting and the sale of daily necessities are carried out by women either within their houses — on terraces or timber bridges — or directly on the bridges themselves. By relocating the warung and these activities to the nZEB, the building becomes

Fig. 11. Final design of the nZEMB in Desa Harapan Baru, East Kalimantan, incorporating a landing dock, a market hall, warung stalls, a plaza, and a mushola (prayer room)

more functional and better supports daily community practices. Within the complex, the multipurpose room represents the most significant shared space, as it is intended for wedding celebrations and other communal events.

A simple kitchen is provided for food preparation during community events and social gatherings. The nZEMB also incorporates a mushola, serving as a prayer space for residents engaged in fishing, trading, and other communal activities. The interviews revealed that Desa Harapan Baru lacks a designated playground for children. In response, the building design includes a plaza that functions as a play area for children and can also serve as a communal gathering and meeting space for village residents. Lavatory facilities are provided to support users of the plaza, including children, women engaged in fish and goods trading, and men returning from work. A detailed description of the required spaces is presented in Table 3, while Table 4 summarizes the calculated areas for each functional space.

3. Solar Panel Design

A total of 17 solar panels were incorporated into the design (Fig. 12). The required number of panels was determined based on the solar potential analysis presented in the previous section and was further refined according to the roof geometry. The placement of the solar panels was carefully designed to respond to local needs while avoiding alterations to the traditional roof shape. Fig. 12 illustrates the proposed location of the off-grid solar (OGS) system on the roof of the multipurpose building. The estimated rooftop area allocated for the OGS system installation is 143 m^2.

The Desa Harapan Baru OGS system has a solar system capacity of 25 kW (30 kWp installed)

Table 3. **Space organization and qualitative characteristics of the proposed nZEMB**

Activity	Space	Zone	Quality				
			Access	View	Sunlight	Ambience	Natural ventilation
Fish market	Landing dock	Semi-private	o		o		
	Cold storage	Private	o				
	Market hall	Public	o		o		o
Warung	Warung stall	Public	o		o	o	o
Communal space	Multipurpose room	Public	o	o	o	o	o
	Kitchen	Semi-private	o		o		o
	Lavatory	Private	o		o		o
	Mushola	Semi-private	o	o	o	o	o
	Plaza	Public	o	o	o	o	o

Table 4. **Area calculation for each functional space based on standards and local community needs in Desa Harapan Baru**

Activity	Space	Standard requirement (m^2)	Unit	Capacity	Required area (m^2)	Total area (m^2)
Fish market	Landing dock	40 m^2 per 10-GT boat	Boat	3	120	144
	Cold storage	0.96	Rack	10	9.6	10
	Market hall	2	Person	10	20	24
Warung	Warung stall	3	Person	6	18	23
Communal space	Multipurpose room	4	Person	100	400	400
	Kitchen	1	Room	10	10	10
	Lavatory	2	Room	2	4	4
	Mushola	2	Person	10	18	18
	Plaza	6	Person	20	120	120
	Circulation space	1	Person	2	18	18
	Net sewing area	1	Person	10	29	29

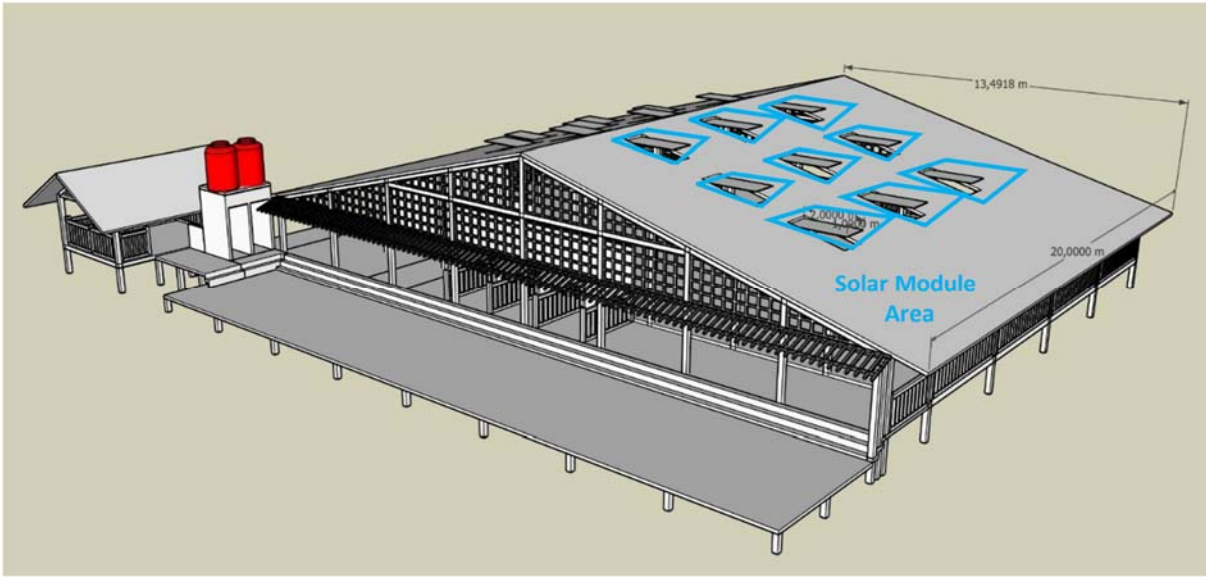

Fig. 12. Overview of the multipurpose building with an off-grid solar system (17 solar panels) installed on the roof

and a battery energy storage capacity of 231 kWh. A total of 60 photovoltaic modules, each rated at 500 Wp, are arranged in 15 parallel strings, with four modules connected in series within each string. The solar modules are installed at a tilt angle of 15° and an azimuth angle of 90°. The battery storage system consists of sealed gel lead-acid batteries, with 6 batteries connected in parallel and 24 connected in series. As summarized in Table 5, the main technical characteristics of the Desa Harapan Baru OGS system were derived using Eqs. (1) and (2). The PVsyst software was employed to estimate the energy yield of the system. Various system losses were incorporated into the simulation, and the assumed loss parameters are presented in Table 6.

A total of 17 solar panels installed on the building are capable of producing 120 kWh/day. Fig. 13 presents the detailed results of the PVsyst simulation. In the first year of operation, the simulated 30 kWp OGS system in Desa Harapan Baru generated 39.17 MWh of electricity. Based on the first-year output, the system achieved a solar fraction of 89.42 % and a specific yield of 1,370 kWh/kWp/year. As illustrated in Fig.13a, the energy supplied by the OGS system to end users is denoted as E_User, while the energy demand from the user or load is denoted as E_Load. The monthly average values of unused energy (Lu), collection losses (Lc), system losses (Ls), and final energy yield (Yf) are approximately 0.07 kWh/kWp/day, 0.70 kWh/kWp/day, 0.28 kWh/kWp/day, and 3.58 kWh/kWp/day, respectively. The E_User value was obtained by subtracting all system losses from the nominal array energy at standard test conditions

Table 5. **Characteristics of the nZEMB solar system in Desa Harapan Baru**

PV system	
Manufacturer	Trina Solar
Model	TSM-DE-18M-(II)-500
Nominal power per module	500 Wp
Umpp	156 V
Impp	175 A
Total PV power	
Total nominal power (STC)	30 kWp
Total number of modules	60 modules
Battery	
Manufacturer	Narada
Model	EosG 1000
Configuration	6 parallel × 24 series
Minimum discharge SOC	20 %
Stored energy	231 kWh
Battery management control	
Charging	SOC = 0.90 / 0.75
Voltage (approx.)	53.9 / 50.7 V
Discharging	SOC = 0.20 / 0.45
Voltage (approx.)	47.7 / 49.5 V

Table 6. **Loss assumptions applied in the PVsyst simulation**

Thermal loss factor	**Module temperature as a function of irradiation**
Uc (const.)	20 W/m^{2}K
Uv (wind)	0 W/m^{2}K/(m/s)
Module quality loss	
Loss fraction	–0.8 %
IAM loss factor	
Incidence effect (IAM): Fresnel AR coating, n(glass) = 1.526, n(AR) = 1.290	
DC wiring losses	
Global array resistance	15 mΩ
Loss fraction	1.5 % at STC
Module mismatch losses	
Loss fraction	2.0 % at MPP
Series diode losses	
Voltage drop	0.7 V
Loss fraction	0.4 % at STC
Strings mismatch losses	
Loss fraction	0.1 %

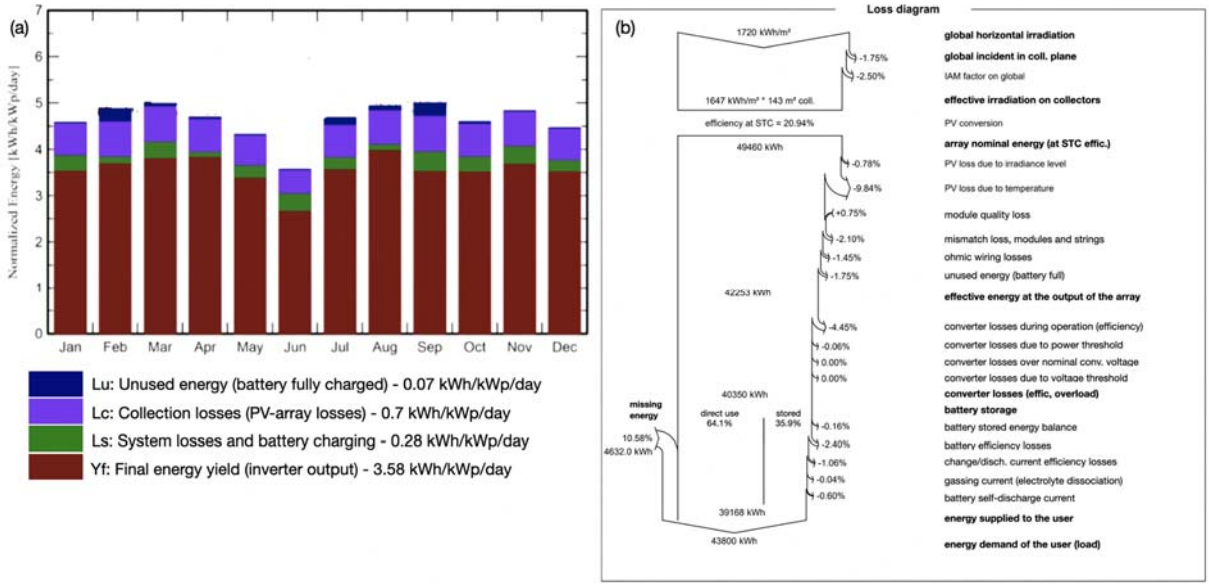

Fig.13. PVsyst simulation results showing (a) annual specific energy yield (kWh/kWp/day) and (b) a detailed loss diagram for the proposed OGS system

(EArrNom), as illustrated in the loss diagram shown in Fig. 13b.

nZEMB Performance Analysis

A key consideration in passive building design for tropical climates is the ability to regulate indoor temperatures in a way that minimizes or eliminates the need for mechanical cooling. However, in recent years, rising ambient temperatures have reduced the effectiveness of purely passive strategies. In Desa Harapan Baru, the existing diesel generator system represents a major challenge, as it relies on petroleum-based energy and results in high electricity costs and consumption. Replacing this system with renewable energy sources is therefore essential. To design a nearly zero-energy building, a balance between energy demand and energy generation must be established. Given Indonesia's proximity to the equator, solar energy represents a highly viable and abundant renewable resource. It was therefore proposed that the building

incorporate not only passive design strategies but also active technologies, such as solar panels, to achieve substantial energy savings. As discussed in the previous section, daylighting control and cross-ventilation were identified as critical design parameters for the nZEMB in Desa Harapan Baru. The effectiveness of the proposed design was then evaluated, followed by calculations of the solar energy output.

1. Daylighting Control

The use of daylight in tropical climates plays an important role in reducing energy consumption. However, improper placement may lead to increased heat gains, which can result in higher electricity demand. In Indonesia, lighting standards are regulated by the Indonesian National Standard (SNI), specifically SNI 6197:2020 on Energy Conservation in Lighting Systems, which is a revision of standard SNI 6197:2011. This standard specifies recommended illumination levels and maximum lighting power densities. For multipurpose buildings, SNI recommends an illumination level of 250 lux (National Standardization Agency of Indonesia, 2020). Accordingly, a daylighting control analysis was conducted for the nZEMB design using the DesignBuilder simulation tool in compliance with this standard.

Simulations of the daylighting performance of the nZEMB in Desa Harapan Baru, Kalimantan, were conducted using DesignBuilder software. Developed based on the U.S. Department of Energy's EnergyPlus engine, DesignBuilder is widely used to evaluate the environmental performance of both new and existing buildings. It enables detailed analysis of indoor energy consumption and thermal comfort (DesignBuilder Software Ltd., 2023). In addition to daylighting analysis, the software was also used to assess overall energy consumption. The schematic design of the building is shown in Fig. 14. The building geometry is approximately square, with a predominantly south-facing orientation.Various functional areas within the building were included in the simulation, namely the multipurpose room,

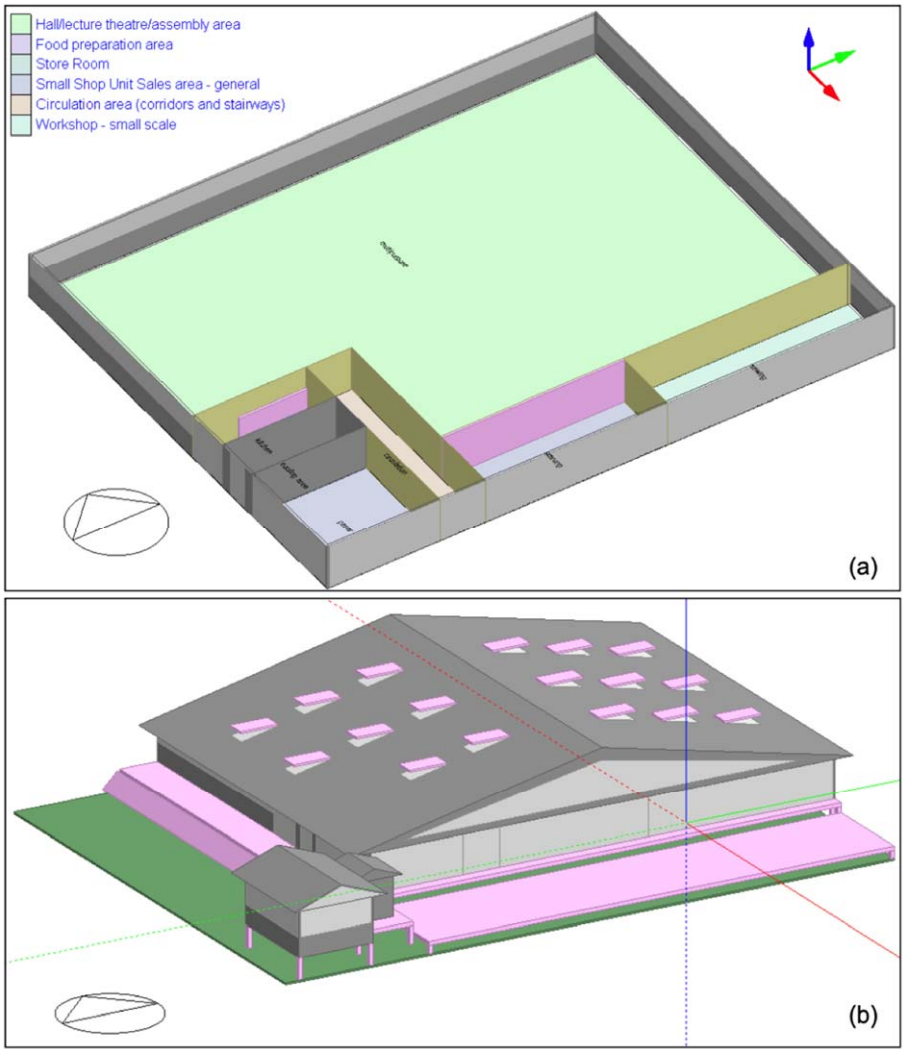

Fig. 14. DesignBuilder schematics of the nZEMB showing (a) the main building layout and (b) the 3D building model

kitchen, cold storage, market hall, circulation spaces, warung stalls, sewing areas, lavatories, and communal dining area, resulting in a total simulated floor area of 513 m^2. The building site is located at an elevation of 1 m below sea level. Desa Harapan Baru lies within a tropical climate zone, classified as ASHRAE climate zone 3C.

After modeling the building geometry in DesignBuilder, the next step was to define the building activity templates. DesignBuilder provides a range of predefined activity templates that include parameters such as metabolic rates, occupancy densities, and clothing levels. In this study, the default parameters for a multipurpose building with a kitchen were applied, and no mechanical heating or cooling systems were included in the simulation.

This research utilizes Time Use Survey (TUS) data collected from occupants of Desa Harapan Baru to model occupant behavior, as shown in Fig. 6. The TUS records information on individual activities over a 24-hour period and includes data on occupations and demographic characteristics. A detailed understanding of user behavior contributes to improved building design (Sari and Chiou, 2019).

The results generated by the DesignBuilder simulation tool can be presented in terms of illuminance and daylight factor (DF). Illuminance refers to the amount of light incident on a surface before reflection and is measured in lux (Müeller, 2013). The daylight factor is defined as the ratio of indoor to outdoor illuminance under overcast sky conditions (Sari and Chiou, 2016). Since overcast conditions are relatively uncommon in tropical climates, this study focuses primarily on illuminance rather than DF. Fig. 15 illustrates illuminance values at selected measurement points and the spatial distribution of lux levels within the building. Openings were introduced in both the roof and walls, with the highest levels of illuminance observed on the north and south sides of the building to enhance daylight penetration. These facades are not shaded by roof overhangs, which contributes to higher illuminance levels. In contrast, the east and west facades are shaded by overhangs measuring 1 m in length. It is estimated that daylight penetration reaches a depth of approximately 1 m, as shown in Fig. 15.

Fig. 16 illustrates the distribution of daylight levels across the different zones of the building. The mushola exhibited the highest illuminance values, primarily due to its relatively small floor area (18 m^2). As musholas are typically used exclusively for prayer, the elevated illuminance levels can be moderated, if necessary, through the use of additional facade shading elements, such as curtains. As indicated by the simulation results, illuminance levels decrease with increasing room depth. The daylight levels in the other areas of the main building were estimated to be approximately 250 lux, which corresponds to the average illuminance recommended by the Indonesian SNI standard. Overall, the daylighting simulation indicates that the building complies with national lighting requirements for daylight performance.

2. Airflow, Cross-Ventilation, and CFD Simulation

To simulate airflow around the nZEMB, computational fluid dynamics (CFD) analysis was conducted using ANSYS Fluent 19.1 (ANSYS Inc., 2021). CFD simulations provide detailed insights into both internal and external airflow patterns and are widely used in studies of natural cross-ventilation.

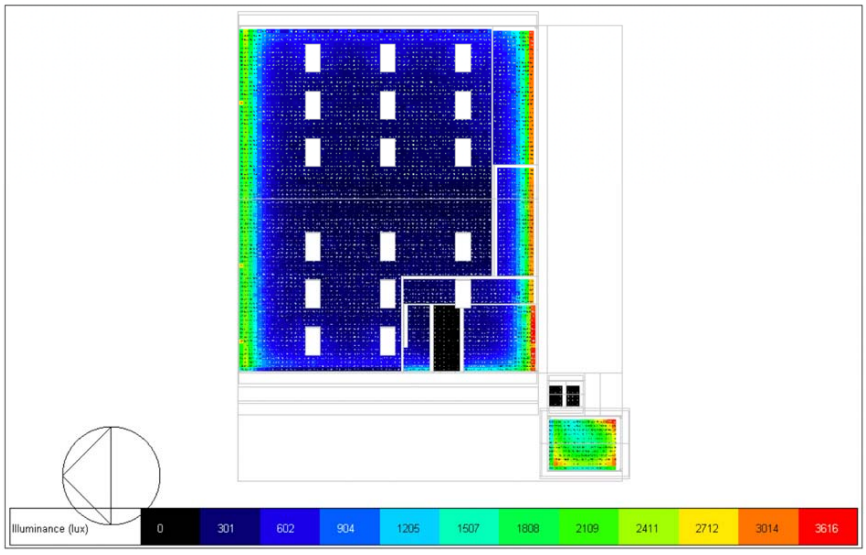

Fig. 15. Daylighting simulation results obtained using DesignBuilder software. Higher illumination levels were observed on the north and south facades due to the absence of shading overhangs, while the east and west facades exhibited lower illumination levels as a result of 1 m overhangs

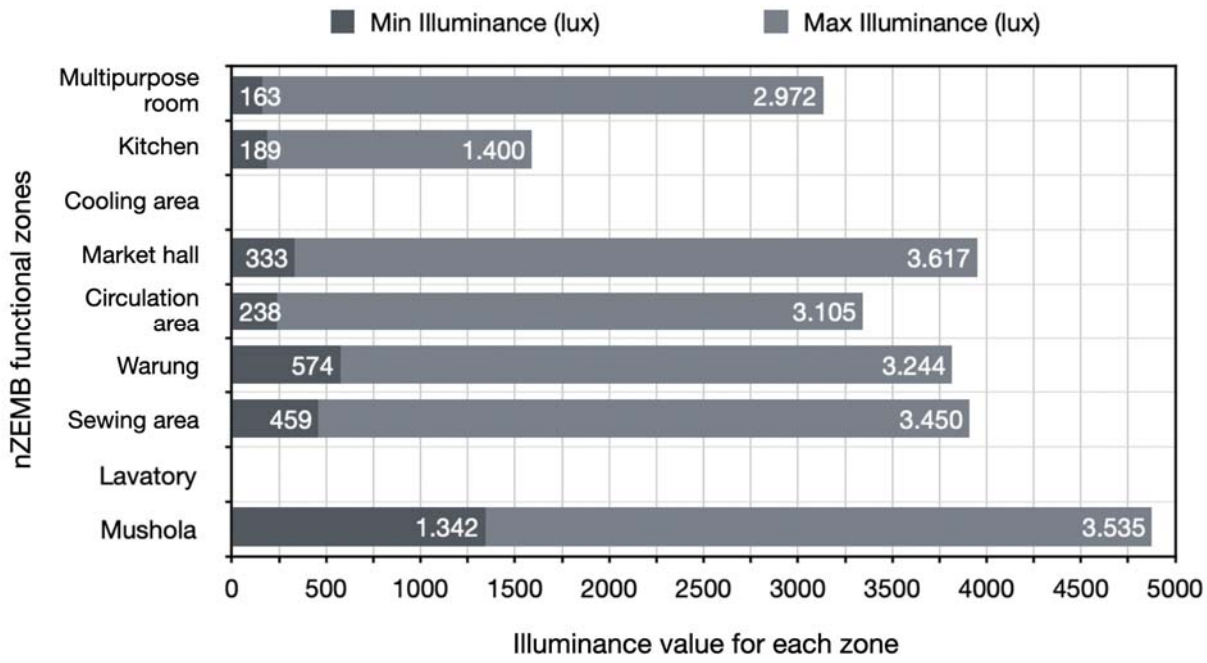

Fig. 16. Summary of illuminance distribution across different zones; the mushola exhibits the highest illuminance due to its relatively small floor area

However, the accuracy of CFD results requires careful validation. The CFD simulation approach was adopted from previous studies by Sudirman et al. (2023, 2025) and validated against wind tunnel experiments reported by Sudirman et al. (2024) to assess natural ventilation performance.

The governing equations were solved using ANSYS Fluent 19.1, including the 3D steady Reynolds-averaged Navier–Stokes (RANS) approach with the shear stress transport (SST) k–ω model (Menter, 2012), the realizable k–ε (RLZ) model (Shih et al., 1995), and the renormalization group k–ε (RNG) model (Choudhury, 1973; Yakhot et al., 1992). In addition, scale-adaptive simulation (SAS) using the SST k–ω model (Egorov et al., 2010) and large eddy simulation (LES) approaches (Lilly, 1992; Smagorinsky, 1963) were also considered. Pressure–velocity coupling was handled using the SIMPLE algorithm. Second-order discretization schemes were applied for pressure interpolation, as well as for the momentum and turbulence equations. The results showed that LES and SAS exhibited good agreement with wind tunnel measurements and outperformed RANS models. Specifically, the agreement in predicted indoor air velocities for buildings without partitions was approximately 56 %, 73 %, and 97 % for RANS, SAS, and LES, respectively. Although both LES and SAS demonstrated high accuracy, they required significantly greater computational resources. Therefore, in the present study, steady-state RANS equations with the RNG k–ε turbulence model were adopted, as this model outperformed the SST k–ω and RLZ k–ε models in the validation studies. The same solver settings used in the validation cases were applied in this analysis.

An initial assessment of the building's physical performance was conducted using CFD simulations. The objective of this analysis was to investigate airflow patterns within the multipurpose building and to evaluate strategies for maximizing natural cross-ventilation. The full-scale building has dimensions of 24 m × 19.5 m × 6.5 m (D × W × H) and a roof slope of 16°. The building geometry includes walls, ceilings, and roof elements with a uniform thickness of 15 cm. The dimensions of the computational domain were determined in accordance with best-practice guidelines proposed by Franke et al. (2007) and Tominaga et al. (2008). As illustrated in Fig. 17a, the distance between the inlet plane and the windward facade is set to 5H, while the distance between the leeward facade and the outlet plane is 15H. The lateral boundaries are located at a distance of 5H from the building, and the vertical distance from the ground to the top boundary is 6H, where H represents the building height (6.5 m). The computational mesh consists of 2,733,130 hexahedral cells (Fig. 17b), with a maximum stretching ratio of 0.89. Mesh resolution was established based on a mesh sensitivity analysis, in which the mesh was systematically refined and coarsened using a linear scaling factor of √2 (not shown in this paper).

CFD simulations were conducted using boundary conditions that closely represent real-life conditions. In this study, the air velocity was determined based on measurements provided by the Indonesian

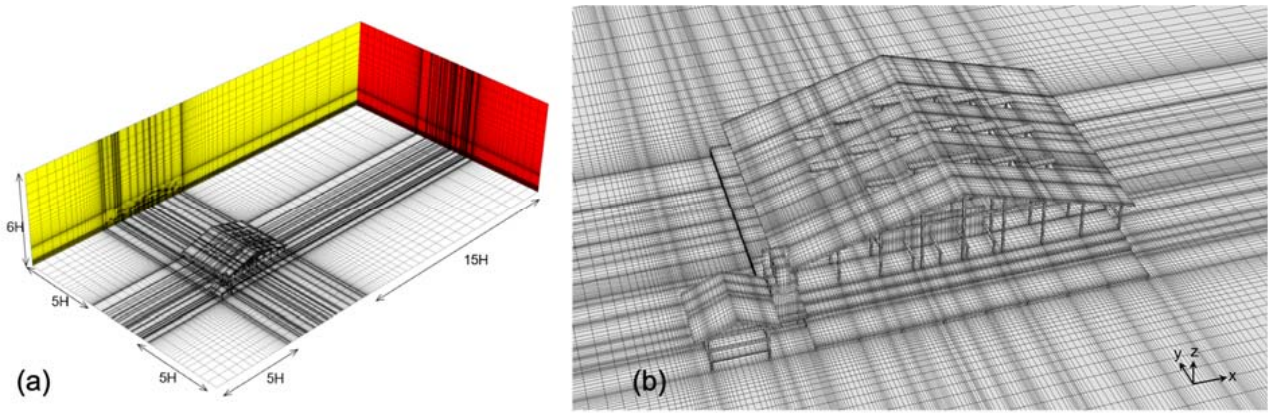

Fig. 17. CFD simulation setup for the nZEMB: (a) computational domain configuration, including the distances between the inlet plane, lateral boundaries, and the top boundary; (b) computational mesh consisting of 2,733,130 hexahedral cells

Agency for Meteorological, Climatological, and Geophysical Studies (BMKG, 2024). A logarithmic inlet velocity profile was applied at a reference height of 10 m above ground, with a reference wind speed of 12.86 m/s (U_{ref}). The building was assumed to be located in an open coastal area with short grass, characterized by an aerodynamic roughness length of z_0 = 0.005 m (Wieringa, 1992). The atmospheric boundary layer (*ABL*) friction velocity (u^*_{ABL} = 0.711 m/s) was calculated based on the reference wind speed (U_{ref}) at the reference height. Turbulence kinetic energy (k) and turbulence dissipation rate (ε) were specified using user-defined functions (*UDF*). Fig. 18 illustrates the railing system surrounding the building. The railings, with a height of 1 m, replace the external walls to enhance airflow. In the CFD simulations, the railings were modeled as porous media using a porous-jump boundary condition, with a porosity of 74 % and a thickness of 0.012 m. The porous parameters were adopted from wind tunnel experiments on perforated materials (case N1) reported by Tominaga et al. (2008).

Fig. 19 presents contours and vectors of the dimensionless mean streamwise velocity (U/U_{ref}) in three horizontal planes at heights of (a) z/H = 0.23, (b) z/H = 0.38, and (c) z/H = 0.46, where H denotes the building height (6.5 m). Wind velocity increases slightly with height due to the jet effect induced by airflow through the ceiling openings, as observed in Fig. 19b. A recirculation region develops within the ranges y/W = 0.13–0.35 and x/D = 0.13–0.40, primarily due to the presence of the cold storage room, which acts as an obstruction to airflow. As previously noted, the building's coastal location results in relatively high wind velocities. The inclusion of railings reduces airflow within the occupied zone by approximately 0.05 U_{ref}, while remaining within acceptable thermal comfort limits (Fig. 19a). Given that most activities within the building involve floor seating and no chairs are provided, the occupied zone is defined as the space below 1 m in height. A more detailed velocity contour is shown in Fig. 20. Adjusting the porosity of the railings and introducing additional openings at the roof and raised floor levels could further enhance airflow within the occupied zone of the nZEMB.

3. Energy Simulation and Design Optimization

Subsequently, the building was analyzed using DesignBuilder software. This tool enables users

Fig. 18. Isometric view of the building showing the locations of railings and perforated walls. The prevailing wind direction is from the west, toward the landing dock

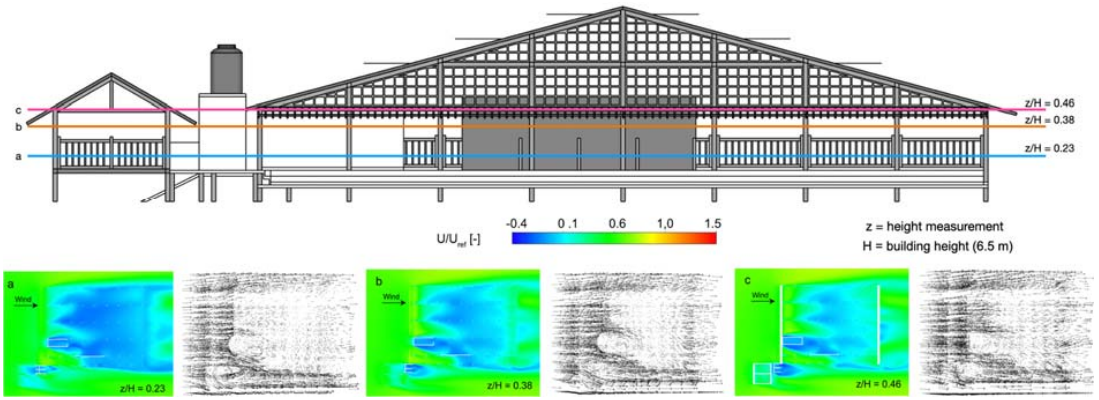

Fig. 19. Contours of dimensionless mean streamwise velocity (U/U_{ref}) in horizontal planes at (a) z/H = 0.23, (b) z/H = 0.38, and (c) z/H = 0.46

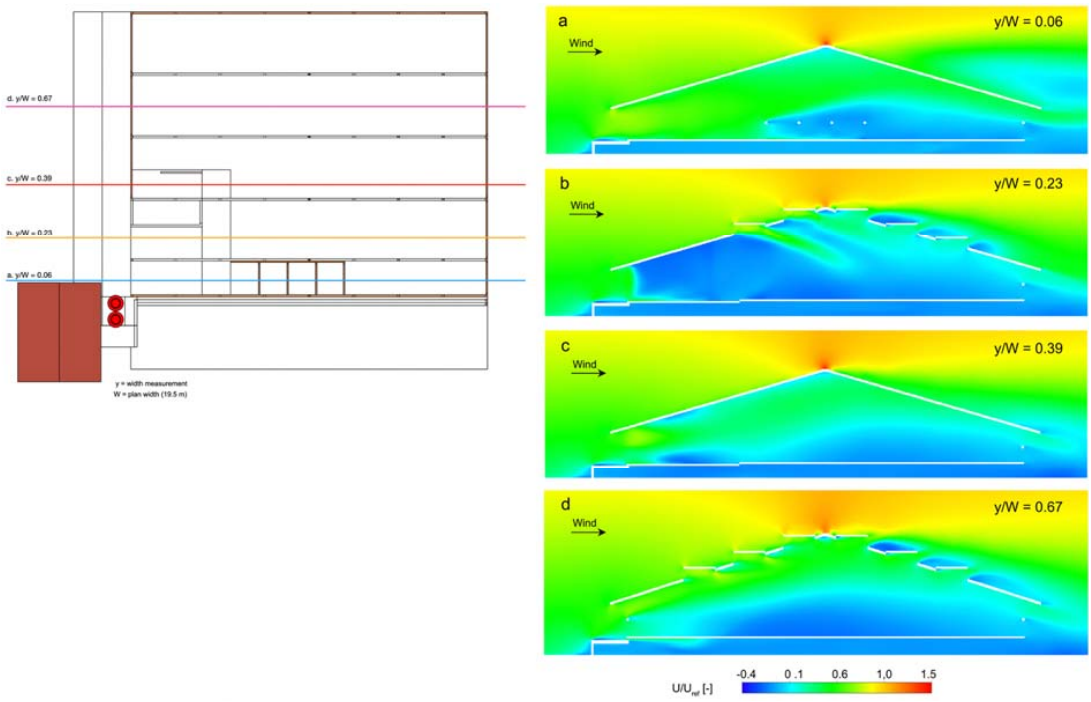

Fig. 20. Contours of dimensionless mean streamwise velocity (U/U_{ref}) in vertical planes at (a) y/W = 0.06; (b) y/W = 0.23; (c) y/W = 0.39; and (d) y/W = 0.67

to make informed design decisions based on a single model (DesignBuilder Software Ltd., 2023). It allows for the analysis of building energy consumption by accounting for a range of complex variables, including climatic conditions, occupant behavior, and building characteristics. In general, three main factors influence energy consumption in buildings. The first is the occupant system, which includes occupant comfort requirements and behavioral patterns; in this study, these aspects were represented through the Time Use Survey (TUS). The TUS data served as the primary input for defining occupant schedules and behavior, consistent with the approach used in the daylighting analysis. The second factor is the building system, which includes lighting. In this study, no mechanical cooling system was implemented due to the remoteness of the site. Similarly, heating systems were excluded, as Desa Harapan Baru is located in a tropical climate where heating demand is negligible throughout the year. The third factor is the external environment system.

Electrical consumption in the nZEMB was determined by analyzing the average number of users per day during weekdays, weekends, and special occasions such as weddings and local community meetings. Electrical appliances used in the nZEMB were categorized by functional space, as summarized in Table 7. Table 8 presents the general parameters required for the simulation of internal gains, including target illuminance levels, fresh air requirements,

Table 7. **Electrical appliances and lighting loads categorized based on the nZEMB interview survey**

Space	Area (m^2)	Lighting / Equipment	Quantity	Unit power (W)	Total power (W)	Duration (h/day)
Landing dock	144	General lighting	4	25	100	12
Cold storage	10	General lighting	2	20	40	12
		Freezer	3	100	300	24
Market hall	25	General lighting	3	20	60	2
		Fan	1	50	50	12
Warung stall	20	General lighting	4	20	80	6
		Fan	2	50	100	12
Multipurpose room	440	General lighting	30	20	600	3
		Fan	5	50	250	12
Kitchen	12	General lighting	2	20	40	3
		Electric stove	2	600	1,200	12
		Fan	2	50	100	12
Lavatory	5	General lighting	1	20	20	6
Mushola	28	General lighting	1	20	20	3
Plaza	150	General lighting	4	25	100	12

Table 8. **Input parameters used for the nZEMB simulation in DesignBuilder**

Variable	Space	Value
Target illuminance	-	250 lux
Minimum fresh air	Multipurpose room	7.5 L/s·person
	Bathroom	10 L/s·person
	Kitchen	12 L/s·person
	Cold storage	10 L/s·person
Natural ventilation setpoint	-	27°C
Weather data	-	Samarinda City, East Kalimantan

natural ventilation conditions, and climatic data. As a result of the energy simulation, Table 9 outlines the internal input parameters and material properties applied in the model. A five-year analysis covering the period from 2019 to 2023 was conducted. On average, the total daily electricity consumption of the nZEMB is approximately 59.19 kWh. The simulation results indicate that the installed solar PV system is capable of supplying the full electricity demand required for daily activities (Fig. 21). Overall,

Table 9. **Description of materials used for nZEMB building elements**

Building element	Construction type
Construction template	Timber frame
External wall	Lightweight timber frame
Pitched roof (unoccupied space)	Lightweight uninsulated pitched roof
Internal partitions	Lightweight gypsum plasterboard (2 × 25 mm)
External and internal floors	Timber

the findings demonstrate that an nZEB performance can be achieved with the proposed design.

Conclusion

Desa Harapan Baru experiences a severe shortage of electricity, making the introduction of renewable energy sources, such as solar power, particularly important. This study presents the design of a nearly zero-energy multipurpose building (nZEMB) developed for Desa Harapan Baru. The building design was informed by an analysis of local culture and occupant behavior. By integrating these aspects into the architectural process, the proposed building is expected to be more readily accepted by the community and to facilitate adaptation to new technologies. The introduction of renewable energy through architectural design also serves an educational purpose, as local residents can directly experience the benefits of solar energy in their daily activities. In this way, local needs can be addressed while simultaneously reducing environmental impacts. The main findings of this research can be summarized as follows:

1. Passive design strategies adapted from local housing typologies demonstrate that nearly zero-energy performance can be achieved by reducing reliance on mechanical ventilation and artificial lighting.
2. Properly designed openings and shading systems effectively regulate daylight distribution; as room depth increases, illuminance levels decrease accordingly. The combined use of openings and shading allows daylight penetration to be maximized while limiting heat gain.
3. Cross-ventilation and heat reduction are enhanced through large window openings and grid-based ventilation integrated into the roof design.
4. Overall building energy consumption can be reduced by improving the building envelope using passive strategies, such as solar shading.

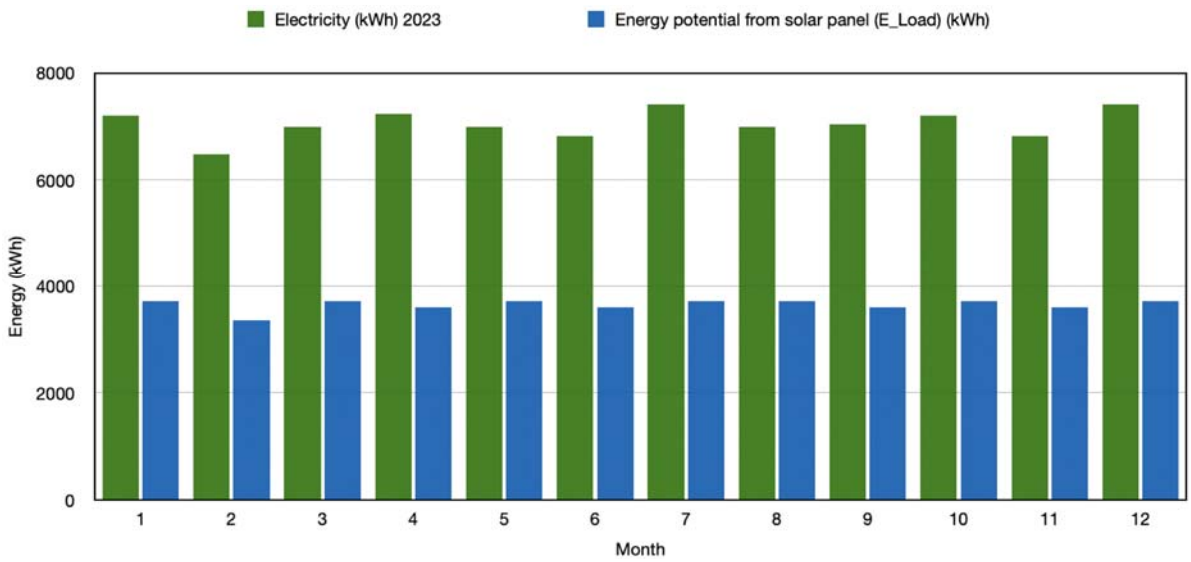

Fig. 21. Comparison between the energy consumption of the nZEMB and the energy generated by the solar panel system. The total daily energy demand is approximately 59.19 kWh, while the solar panels generate about 120 kWh per day

5. Solar energy was shown to be an effective renewable energy alternative for meeting the electricity needs of Desa Harapan Baru.

6. The installation of 17 solar panels on the roof is sufficient to supply energy for all building activities, including cold storage equipped with large freezers.

Despite the high potential for solar energy utilization in Desa Harapan Baru, this renewable resource remains underutilized in the residential sector. One of the main challenges is the lack of local capacity to operate and maintain solar technologies, which often results in system failure. In many cases, women — who spend more time at home and manage household activities — are not trained in maintaining these technologies. This limits the long-term functionality of installed systems and reflects a broader lack of awareness regarding the potential of buildings to generate their own energy. The proposed nZEMB consolidates multiple household and community activities into a single facility, enabling more efficient energy use. The results demonstrate that solar energy can fully meet the electricity demand of the proposed design. This study offers an effective strategy for tropical climates and provides guidance for architects and designers involved in the design and retrofitting of energy-efficient buildings. Further development and analysis are recommended to refine and enhance the proposed design.

References

Alkausar and Riyani, R. A. E. (2023). Vernacular passive design with natural ventilation of Banjar housing for thermal comfort. *Paragraphs Environmental Design*, Vol. 1, No. 1, pp. 83–92. DOI: 10.59260/penvid.2023.83921212.

Alwetaishi, M. (2022). Can we learn from heritage buildings to achieve nearly zero energy building and thermal comfort? A case study in a hot climate. *Advances in Building Energy Research*, Vol. 16, Issue 2, pp. 214–230. DOI: 10.1080/17512549.2020.1844047.

Anggraeni, D. S. N. (2020). *Karakteristik Perumahan di Kalimantan Barat*. [online] Available at: https://www.suarapemredkalbar.com/read/opini/25082020/karakteristik-perumahan-di-kalimantan-barat#:~:text=seng/asbes%20masih%20menjadi%20pilihan%20utama%20masyarakat%20Kalimantan,persen%20menggunakan%20asbes%2C%20sisanya%20menggunakan%20jenis%20atap [Date accessed April 18, 2025].

Ansys Inc. (2021). *ANSYS Fluent Theory Guide*. [online] Available at: https://dl.cfdexperts.net/cfd_resources/Ansys_Documentation/Fluent/Ansys_Fluent_Theory_Guide.pdf [Date accessed October 9, 2024].

Arifin, Y. F. and Itta, D. (2013). The potency of ulin (*Eusideroxylon zwageri* T. et. B) for supporting Banjarese building construction in “wetland architecture”. *Journal of Wetlands Environmental Management*, Vol. 1, No. 1, pp. 61–64. DOI: 10.20527/jwem.01.01.03.

Arifin, M., Wunas, S., Mushar, P., Arifin, M. A., Pananrangi, A. I. A., Lakatupa, G., and Abdu, J. M. A. M. (2024). Typology and configuration of Lake Tempe floating house in South Sulawesi, Indonesia. *Journal of Asian Architecture and Building Engineering*, Vol. 23, Issue 5, pp. 1489–1499. DOI: 10.1080/13467581.2023.2270022.

Brisbane City Council (2018). *Traditional Housing: Alterations and Extensions Design Guide*. [online] Available at: https://www.arkhefield.com.au/assets/Projects/Traditional-Housing-Guide/Traditional-Housing-alterations-and-Extensions-Design-Guide.pdf [Date accessed March 14, 2023].

Brisbane City Council (2023). *Traditional Housing: Alterations and Extensions Design Guide*. [online] Available at: https://www.brisbane.qld.gov.au/content/dam/brisbanecitycouncil/corpwebsite/building-and-planning/documents/traditional-housing-alterations-and-extensions-design-guide.pdf.coredownload.pdf [Date accessed March 14, 2023].

Choudhury, D. (1973). *Introduction to the renormalization group method and turbulence modeling*. Fluent Incorporated. 70 pages. https://books.google.co.in/books?id=mKWEQwAACAAJ

DesignBuilder Software Ltd. (2023). *DesignBuilder*. [online] Available at: https://designbuilder.co.uk/ [Date accessed August 5, 2023].

Egorov, Y., Menter, F. R., Lechner, R., and Cokljat, D. (2010). The scale-adaptive simulation method for unsteady turbulent flow predictions. Part 2: application to complex flows. *Flow, Turbulence and Combustion*, Vol. 85, Issue 1, pp. 139–165. DOI: 10.1007/s10494-010-9265-4.

Falasca, S., Di Bernardino, A., and Salata, F. (2023). On the identification and characterization of outdoor thermo-hygrometric stress events. *Urban Climate*, Vol. 52, 101728. DOI: 10.1016/j.uclim.2023.101728.

Feng, W., Zhang, Q., Ji, H., Wang, R., Zhou, N., Ye, Q., Hao, B., Li, Y., Luo, D., and Lau, S. S. Y. (2019). A review of net zero energy buildings in hot and humid climates: experience learned from 34 case study buildings. *Renewable and Sustainable Energy Reviews*, Vol. 114, 109303. DOI: 10.1016/j.rser.2019.109303.

Franke, J., Hellsten, A., Schlünzen, H., and Carissimo, B. (2007). *Best Practice Guideline for the CFD simulation of flows in the urban environment*. [online] Available at: https://sciencespo.hal.science/ENPC-CEREA/hal-04181390v1 [Date accessed August 10, 2024].

National Standardization Agency of Indonesia (2020). *Konservasi energi pada sistem pencahayaan. Indonesian National Standard SNI 6197:2020*. [online] Available at: https://akses-sni.bsn.go.id/dokumen/2020/SNI%206197-2020/#p=1 [Date accessed March 14, 2023]

Kim, S.-K., Lee, S.-J., Kwon, H. J., and Ahn, M. (2015). Zero-energy home development in Korea: energy-efficient and environmentally friendly design features and future directions. *Housing and Society*, Vol. 42, Issue 3, pp. 222–238. DOI: 10.1080/08882746.2015.1121682.

Lilly, D. K. (1992). A proposed modification of the Germano subgrid-scale closure method. *Physics of Fluids*, Vol. 4, Issue 3, pp. 633–635. DOI: 10.1063/1.858280.

Lubis, M. S., Harjoko, T. Y., and Susanto, D. (2018). The floating houses of Sintang City: space, resources and political nexus. *IOP Conference Series: Materials Science and Engineering*, Vol. 316, 012003. DOI: 10.1088/1757-899X/316/1/012003.

Menter, F. R. (2012). Two-equation eddy-viscosity turbulence models for engineering applications. *AIAA Journal*, Vol. 32, No. 8, pp. 1598–1605. DOI: 10.2514/3.12149.

Merello, P., Fernández-Navajas, Á., Curiel-Esparza, J., Zarzo, M.,and García-Diego, F. J. (2014). Characterisation of thermo-hygrometric conditions of an archaeological site affected by unlike boundary weather conditions. *Building and Environment*, Vol. 76, pp. 125–133. DOI: 10.1016/j.buildenv.2014.03.009.

Meteorological, Climatological, and Geophysical Agency (BMKG) (2024). *Weather Forecast, Penajam District Penajam Paser Utara Regency - East Kalimantan Province*. [online] Available at: https://www.bmkg.go.id/cuaca/prakiraan-cuaca/64.09.01.1011 [Date accessed June 6, 2024).

Müeller, H. F. O. (2013). Chapter 9 - Daylighting: In: Sayigh, A. (ed.). *Sustainability, Energy and Architecture. Case Studies in Realizing Green Buildings*. Oxford: Academic Press, pp. 227–255. DOI: 10.1016/B978-0-12-397269-9.00009-8.

Ohene, E., Hsu, S.-C., and Chan, A. P. C. (2022). Feasibility and retrofit guidelines towards net-zero energy buildings in tropical climates: a case of Ghana. *Energy and Buildings*, Vol. 269, 112252. DOI: 10.1016/j.enbuild.2022.112252.

Palapessy, J. G. (2018). *Experimental research on the flexural strength of ironwood (ulin) (Eusideroxylon zwageri)*. Undergraduate Thesis in Civil Engineering. [online] Available at: https://repository.maranatha.edu/9757/ [Date accessed April 18, 2025].

Paramita, B. (2025). *Building climate resilience in Indonesia: the role of cool roofs*. [online] Available at: http://journals.openedition.org/factsreports/7823 [Date accessed April 18, 2025]

Pinassang, J. L., Harsritanto, B. I. R., and Sari, D. P. (2021). What we can learn from vernacular house and COVID-19 infection? A review of Mbaru Niang, Flores, Indonesia. *E3S Web of Conferences*, Vol. 37, 04017. DOI: 10.1051/e3sconf/202131704017.

Putro, J. D. and Zain, Z. (2021). Active and passive adaptation of floating houses (Rumah Lanting) to the tides of the Melawi River in West Kalimantan, Indonesia. *Geographica Pannonica*, Vol. 25, Issue 2, pp. 72–84. DOI: 10.5937/gp25-30422.

PVSyst (2023). *Normalized performance index*. [online] Available at: https://www.pvsyst.com/help/project-design/results/normalised-performance-index.html [Date accessed August 10, 2024].

PVsyst documentation (2023). *Geographical Sites*. [online] Available at: https://www.pvsyst.com/help/meteo-database/geographical-sites/index.html [Date accessed August 10, 2024].

Sari, D. P. and Chiou, Y.-S. (2016). The lighting design control strategy: a method for optimum daylighting performance in subtropical climate. In: *4th Annual International Conference on Architecture and Civil Engineering (ACE 2016), Shanghai, China, December 9–11, 2016*. DOI: 10.5176/2301-394X_ACE16.119.

Sari, D. P. and Chiou, Y.-S. (2019). Do energy conservation strategies limit the freedom of architecture design? A case study of Minsheng Community, Taipei, Taiwan. *Sustainability*, Vol. 11, Issue 7, 2003; DOI: 10.3390/su11072003.

Sari, D. P., Sudirman, M., and Chiou, Y. S. (2024). Modernity in Javanese tradition: adapting vernacular design and local culture to Indonesian urban living. *Architectural Science Review*, Vol. 67, Issue 2, pp. 105–119. DOI: 10.1080/00038628.2022.2136131.

Sari, D. P., Sumarno, A., Prasetyo, A. M., Maidina, and Ngeljaratan, L. N. (2023). Energy conservation techniques in tropical climate - a comprehensive review and adaptation of the Lamin House for Nusantara. *EVERGREEN Joint Journal of Novel Carbon Resource Sciences & Green Asia Strategy*, Vol. 10, Issue 3, pp. 2021–2028. DOI: 10.5109/7151769.

Shi, F., Wang, S., Huang, J., and Hong, X. (2020). Design strategies and energy performance of a net-zero energy house based on natural philosophy. *Journal of Asian Architecture and Building Engineering*, Vol. 19, Issue 1, pp. 1–15. DOI: 10.1080/13467581.2019.1696206.

Shih, T.-H., Liou, W. W., Shabbir, A., Yang, Z., and Zhu, J., (1995). A new *k*-ϵ eddy viscosity model for high Reynolds number turbulent flows. *Computers & Fluids*, Vol. 24, Issue 3, pp. 227–238. DOI: 10.1016/0045-7930(94)00032-T.

Smagorinsky, J. (1963). General circulation experiments with the primitive equations. *Monthly Weather Review*, Vol. 91, No. 3, pp. 99–164. DOI: 10.1175/1520-0493(1963)091<0099:GCEWTP>2.3.CO;2.

Society of Building Science Educators (2021). *Climate consultant*. [online] Available at: https://www.sbse.org/resources/climate-consultant [Date accessed August 5, 2023].

Sudirman, M., Gillmeier, S., Van Hooff, T., and Blocken, B. (2024). Wind tunnel measurements of cross-ventilation flow in a realistic building geometry: influence of building partitions and wind direction. *Journal of Wind Engineering and Industrial Aerodynamics*, Vol. 254, 105907. DOI: 10.1016/j.jweia.2024.105907.

Sudirman, M., Van Hooff, T., Gillmeier, S., and Blocken, B. (2023). Validation of cross-ventilation flow in a realistic building geometry. In: Wang, L. L., Ge, H., Zhai, Z. J., Qi, D., Ouf, M., Sun, C., and Wang, D. (eds.). *Proceedings of the 5th International Conference on Building Energy and Environment*. Singapore: Springer, pp. 305–308. DOI: 10.1007/978-981-19-9822-5_33.

Sudirman, M., Van Hooff, T., Gillmeier, S., and Blocken, B. (2025). Validation study of cross-ventilation in a realistic building geometry: RANS, SAS and LES. *Building and Environment*, Vol. 269, 112354. DOI: 10.1016/j.buildenv.2024.112354.

Tominaga, Y., Mochida, A., Yoshie, R., Kataoka, H., Nozu, T., Yoshikawa, M., and Shirasawa, T. (2008). AIJ guidelines for practical applications of CFD to pedestrian wind environment around buildings. *Journal of Wind Engineering and Industrial Aerodynamics*, Vol. 96, Issues 10–11, pp. 1749–1761. DOI: 10.1016/j.jweia.2008.02.058.

Wieringa, J. (1992). Updating the Davenport roughness classification. *Journal of Wind Engineering and Industrial Aerodynamics*, Vol. 44, Issues 1–3, pp. 357–368. DOI: 10.1016/0167-6105(92)90434-C.

Wilberforce, T., Olabi, A. G., Sayed, E. T., Elsaid, K., Maghrabie, H. M., and Abdelkareem, M. A. (2023). A review on zero energy buildings – pros and cons. *Energy and Built Environment,* Vol. 4, Issue 1, pp. 25–38. DOI: 10.1016/j.enbenv.2021.06.002.

Yakhot, V., Orszag, S. A., Thangam, S., Gatski, T. B., and Speziale, C. G. (1992). Development of turbulence models for shear flows by a double expansion technique. *Physics of Fluids*, Vol. 4, Issue 7, pp. 1510–1520. DOI: 10.1063/1.858424.

МНОГОФУНКЦИОНАЛЬНОЕ ЗДАНИЕ С МИНИМАЛЬНЫМ ЭНЕРГОПОТРЕБЛЕНИЕМ ДЛЯ ДЕСА ХАРАПАН БАРУ В ВОСТОЧНОМ КАЛИМАНТАНЕ

Дани Первита Сари*[1], Фариз Маулана Риза Нулхак[2], Мутмайннах Судирман[3], Дита Анггун Лестари[4], М. Ангги Сануси[5]

[1] Научно-исследовательский центр технологий прочности конструкций, Исследовательская организация по энергетике и производству, Национальное агентство по исследованиям и инновациям (BRIN), Чибинонг, Западная Ява, Индонезия

[2] Научно-исследовательский центр преобразования и сохранения энергии, Исследовательская организация по энергетике и производству, Национальное агентство по исследованиям и инновациям (BRIN), Чибинонг, Западная Ява, Индонезия

[3] Технологический университет Эйндховена, Эйндховен, Нидерланды

[4] Фонд People Centered Business Economic Initiatives (IBEKA) — некоммерческая организация, ориентированная на развитие местных сообществ, Индонезия

[5] Программа Patriot Energi, округ Субанг, Западная Ява, Индонезия

*E-mail: dany.perwitasari@gmail.com

Аннотация

Введение. Деса Харапан Бару — одна из традиционных деревень Восточного Калимантана, расположенная в удаленной прибрежной зоне. Местное сообщество сталкивается с рядом серьезных проблем, включая ограниченную транспортную доступность, нехватку чистой воды и неудовлетворительные санитарно-гигиенические условия. В результате жители вынуждены использовать природные ресурсы, доступные в непосредственной близости, в частности, древесину улин для строительства и дизельные генераторы для производства электроэнергии. Однако недостаточный уровень знаний в области строительства и лесовосстановления негативно сказался на окружающей среде, способствуя возникновению наводнений. Кроме того, из-за удаленного расположения генераторов стоимость топлива в деревне фактически удвоилась. **Целью данного исследования** является проектирование многофункционального здания с почти нулевым энергопотреблением (МЗПНЭ), отвечающего местным культурным традициям и потребностям сообщества. Помимо улучшения экономических условий, проект направлен на повышение осведомленности населения в вопросах устойчивого развития. **Методы**. В процессе проектирования применялся комплексный методологический подход. На первом этапе был проведен анализ поведенческих и культурных особенностей местного населения с целью облегчения адаптации сообщества к новым технологиям. Затем на кровле здания МЗПНЭ была выбрана и установлена фотоэлектрическая солнечная система. Моделирование работы фотоэлектрических панелей выполнялось с использованием программного обеспечения PVsyst; анализ воздушных потоков осуществлялся методом вычислительной гидродинамики (CFD) в среде Ansys Fluent; оценка энергоэффективности здания проводилась с помощью программного комплекса DesignBuilder. **Результаты** исследования показывают, что система возобновляемой энергии, состоящая из 17 солнечных панелей, способна полностью покрыть энергетические потребности МЗПНЭ в Деса Харапан Бару. Суммарное суточное энергопотребление составляет 59,19 кВт·ч, тогда как установленная солнечная система способна вырабатывать до 120 кВт·ч в сутки. Кроме того, использование традиционных архитектурных решений — таких как проемы в кровле и конструкция с приподнятым полом — способствует улучшению естественной вентиляции и снижению общего энергопотребления.

Ключевые слова: здание с почти нулевым энергопотреблением; удаленная деревня; энергоэффективность; тропический климат; традиционная архитектура Индонезии; Восточный Калимантан.

DOI: 10.23968/2500-0055-2025-10-4-88-99

ASSESSMENT OF THE ADHESION STRENGTH OF DETONATION-SPRAYED METAL-CERAMIC COATINGS ON CONCRETE SUBSTRATES

Daniil Sergeevich Podgorny, Diana Olegovna Bondarenko*, Valeria Valerievna Strokova

Belgorod State Technological University named after V. G. Shukhov, Belgorod, Russia

*Corresponding author's email: di_bondarenko@mail.ru

Abstract

Introduction. The efficiency and successful application of various protective coatings necessitate the investigation of coating–substrate interactions to ensure durability and reliability. Adhesion is a key parameter that determines the quality of bonding between a coating and a substrate surface. Existing methods for its assessment are continually being improved to enhance accuracy, versatility, and applicability to various types of coatings and substrates. **Purpose of the study**. The study is aimed at assessing the adhesion strength of coatings deposited by detonation spraying onto heavy-concrete surfaces and refining the methodology for determining adhesion strength for the corresponding tests. **Methods**. In the course of the study, Raman spectroscopy, axial pull-off adhesion testing, optical microscopy, and rotational viscometry were used. **Results**. Adhesion strength tests were performed on Ti–TiO_x coatings deposited on concrete substrates by detonation spraying of powders under different modes. The resulting coatings exhibit high adhesion strength to the substrate, ranging from 0.32 to 3.77 MPa, and low porosity. A special fixture was pre-developed for adhesion testing of specimens with linear dimensions of 30 mm and larger. A study was conducted on the applicability of a series of epoxy resins for adhesion testing. It was found that, when testing coatings on porous substrates, it is important to consider the viscosity of the adhesive agents, since highly mobile formulations may penetrate deeply into the specimen and distort the results.

Keywords: adhesion strength; coatings; concrete; adhesion testing methodology; epoxy resin.

Introduction

The development of coatings for construction materials and composites addresses a range of challenges related to improving their performance characteristics, enhancing durability, functionality, aesthetics, etc. There exists a vast variety of coatings designed for specific purposes (Bessmertnyy et al., 2019; Bondarenko et al., 2024; Klyuchnikova et al., 2018; Montemor, 2014), as well as numerous mechanical testing methods for evaluating their adhesive properties (Chen et al., 2014; Zaytsev et al., 2021).

Adhesion assessment methods based on sandwich specimens (double-cantilever beam and four-point bending) allow measurement of fracture energy under different loading modes. The scratch test and the Rockwell indentation method are widely used for quantitative and qualitative evaluation of adhesion through radial stresses and critical loads (Croll, 2020; Ma et al., 2020; Vereschaka et al., 2019; Zhang et al., 2024). For wood coatings, the cross-cut test is applied, enabling visual assessment of adhesion based on coating detachment (Hang et al., 2024). For thick coatings, the transverse scratch test is used to evaluate cohesive strength (Croll, 2020). In practical applications — more often for organic coatings — pull-off tests and peel tests are also commonly employed (Falsafein et al., 2018; Haselrieder et al., 2015).

Adhesion of coatings strongly depends on the surface structure and texture, as well as its roughness (Croll, 2020). Sandblasting and laser texturing increase the contact area, thereby improving adhesion (Harfouche et al., 2024; Heidarinejad and Ashrafizadeh, 2024). An increase in coating thickness may lead to the accumulation of internal stresses at the interface, which reduces adhesion (Heidarinejad and Ashrafizadeh, 2024; Ma et al., 2020).

An analysis of several international and domestic standards describing methods for evaluating the adhesion properties of various types of coatings was carried out.

ASTM C633-24 specifies the procedure for determining the adhesion or cohesion strength of thermally sprayed coatings by applying a tensile load perpendicular to the coating surface. The method is intended for assessing either the bond strength between the coating and the substrate or the internal strength of the coating itself.

For citations: Podgorny, D. S., Bondarenko, D. O., Strokova, V. V. (2025). Assessment of the adhesion strength of detonation-sprayed metal-ceramic coatings on concrete substrates. Architecture and Engineering, No 4 (10), pp. 88–99. DOI: 10.23968/2500-0055-2025-10-4-88-99.

The standard covers coatings applied by plasma spraying, arc spraying, detonation spraying, and high-velocity oxy-fuel (HVOF) spraying. Coatings may consist of metals, ceramics (oxides, carbides), or combinations thereof.

The method is applicable to coatings thicker than 0.38 mm (0.015 in). This limitation is due to the use of an adhesive, which may penetrate thin coatings and distort the test results. The coating is applied to one side of the substrate, after which a loading fixture is bonded to the coated surface using an adhesive. A tensile load normal to the coating plane is then applied until failure of the specimen. The crosshead displacement rate is 0.013–0.021 mm/s (0.030–0.050 in/min). The maximum recorded load is used to calculate the bond strength.

Adhesive or cohesive strength is calculated as the ratio of the maximum load to the cross-sectional area of the specimen. Failure may occur at the substrate–coating interface (adhesive failure), within the coating itself (cohesive failure), or within the adhesive layer. The failure location is determined using a microscope with magnification up to 100x. The report must include the coating type, application method, substrate material, test parameters, and a detailed description of the failure mode.

The method is limited to coatings capable of withstanding tensile loads at room temperature, although testing at cryogenic temperatures is also possible. The application of this method to very thin or brittle coatings requires additional investigation and may necessitate new adhesive materials to avoid distortion of the results.

ASTM D3359-23 describes methods for evaluating the adhesion of organic coatings to a substrate using pressure-sensitive tape and includes two primary approaches — Method A and Method B. Both are based on applying pressure to the coating using an adhesive tape and then rapidly removing it. The distinction lies in the shape and number of cuts made on the coating surface.

Method A involves making two intersecting cuts on the coating surface, forming an X-shaped pattern. A transparent or semi-transparent adhesive tape 25 mm wide, with an adhesion strength of 6.34–7.00 N/cm, is then applied to the coating. The tape is removed rapidly at an angle of 180°, after which the area of coating detachment from the substrate is visually assessed.

Method B involves creating a lattice pattern consisting of six or eleven parallel cuts in two perpendicular directions, forming a lattice. After applying and removing the adhesive tape, the result is evaluated on a scale from 0 to 5, where 5 indicates no coating damage and 0 indicates severe detachment of the coating down to the substrate.

The standard requires the use of a sharp cutting tool (a scalpel or knife) to make the cuts in the coating. A steel ruler or similar rigid guide is used to ensure cut accuracy. The cutting tool must be in good condition — preferably new or recently sharpened — to ensure clean, even cuts. It is also essential to use adhesive tape from the same manufacturer and batch for all tests, since adhesive properties may vary between batches. This is necessary to ensure repeatability and comparability of results.

Adhesion is assessed visually, which requires appropriate operator training. The influence of environmental conditions (temperature and humidity) is also taken into account, as these factors may affect both the coating and the adhesive tape. When conducting tests on non-metallic substrates, the standard recommends using either Method A or Method B depending on the characteristics of the substrate; however, the accuracy of the data for such materials has been studied to a lesser extent.

ASTM D4541-22 establishes a procedure for measuring the pull-off strength of coatings applied to metal and other rigid substrates using portable adhesion testers. The method is intended to evaluate the adhesion strength between the coating and the substrate or between individual coating layers by applying a normal (perpendicular) force to the tested surface until coating failure occurs. The process involves the use of a fastening element, referred to as a “dolly” or “stub”, which is bonded to the coating surface with a special adhesive. After the adhesive has cured, a gradually increasing force is applied to the fastening element using a portable adhesion tester, which records the maximum force attained before failure.

The standard describes five different testing procedures (designated as Methods B–F), each with its own features depending on the type of equipment used and the test conditions. Test results may vary significantly depending on the substrate material, coating thickness, adhesive type, and other parameters; therefore, they cannot be directly compared without accounting for these factors. It is important to note that Method A, which was included in earlier versions of the standard, has been removed because it was specifically developed for testing concrete substrates and has been transferred to a separate standard, ASTM D7234-22.

The testing process may lead to coating failure. The standard recommends using testers capable of applying a concentrated load to a small area, which allows testing even on surfaces with limited accessibility. In addition, the test procedure may require consideration of substrate flexibility and loading rate to avoid distortions in the results.

Test results are expressed in MPa or psi. The document provides detailed instructions on how data should be recorded and interpreted, including the description of the surface failure and detachment location. The method requires

thorough documentation of all testing parameters and conditions, including equipment type, adhesive properties, and substrate characteristics.

ISO 2409:2020 describes a method for assessing the adhesion of coatings within multilayer paint systems. The standard is intended for testing coatings on flat surfaces using the cross-cut method, which makes it possible to evaluate the adhesion of coating layers to the substrate or to each other. The procedure involves applying the coating to a special panel, after which parallel cuts are made on its surface, followed by intersecting cuts that form a lattice pattern.

The dimensions of the cuts depend on the coating thickness and the type of substrate. For coatings up to 60 μm thick, the spacing between cuts is 1 mm; for coatings up to 120 μm, the spacing is 2 mm; and for coatings thicker than 120 μm, the spacing is increased to 3 mm. Evaluation is carried out visually, determining the degree of coating detachment on a scale from 0 to 5, where 0 indicates no detachment and 5 represents complete detachment of the coating within the cross-cut area.

The standard also considers parameters that may affect test results: surface preparation, coating thickness and application method, and environmental conditions. The document emphasizes the importance of using a sharp cutting tool to ensure clean cuts and maintaining uniform pressure during the procedure. The method is applicable to both metallic and non-metallic substrates, including plastics and wood; however, results may vary depending on the substrate type and its mechanical properties.

ISO 4624:2023 describes test methods for determining the adhesion strength of paint coatings using axial pull-off testing. The primary objective of the standard is to determine the minimum stress required to break the bond between the coating and the substrate. The standard provides three procedures: Method A (using two dollies), Method B (testing from one side only, using a single dolly), and Method C (using dollies, one as a painted substrate).

Tests are performed using cylindrical metallic dollies with a diameter of 20 mm, which are bonded to the surface of a special panel. For testing on concrete substrates, dollies with diameters up to 100 mm are permitted. The test panels are subjected to a gradually increasing pull-off force applied perpendicular to the panel plane until failure occurs.

The measured results depend on the strength of the bonding layer between the coating and the substrate, as well as on the failure mode: adhesive failure (separation at the coating–substrate interface) or cohesive failure (rupture within the coating itself). Various factors may influence the results, including the mechanical properties of the substrate, coating curing conditions, type of adhesive used, etc. Proper centering and alignment of the dollies play an important role in ensuring measurement accuracy.

ISO 16276-1:2007 specifies methods for assessing the adhesion of corrosion protection coatings applied to steel surfaces. The standard focuses primarily on adhesion testing procedures using standard panels, coating application methods, and curing and testing conditions.

The standard provides two principal test methods: the bending test and the pull-off test. The bending test is intended for evaluating adhesion under conditions in which the coating is subjected to mechanical stress during deformation. The pull-off test (using dollies) is used to determine the force required to detach the coating from the substrate. The standard also addresses surface preparation procedures — cleaning and pre-treatment — which are critical for achieving reliable coating adhesion to the substrate.

The coating thickness and selection of materials for testing are regulated to ensure representativeness and repeatability of test results. The standard also describes methods for documenting and presenting test data, including the parameters that must be reported: the type of equipment used, testing conditions, and the characteristics of the coating failure.

GOST 28574-2014 establishes detailed methods for determining the bond strength (adhesion) of protective coatings applied to concrete and reinforced concrete structures, including those used in aggressive environments. The standard includes both quantitative and qualitative testing methods for paint, mastic, and film coatings.

1) The quantitative method for determining the adhesion of paint coatings by pull-off strength is intended for both laboratory and field testing. The test is based on measuring the force required to detach the coating from the concrete surface by bonding a metallic dolly (stub) and using an adhesion tester. Laboratory testing is performed on concrete cube specimens with dimensions of 100×100×100 mm or 70×70×70 mm. Compliance with the coating application and curing procedures specified in the technical requirements is an important prerequisite.

During testing on full-scale structures, coating areas are selected at a spacing of no less than 300 mm from each other, and metallic dollies are bonded for subsequent pull-off measurements. The testing parameters include uniform loading at a rate not exceeding 1 MPa/s, with recording of the detachment time, which must fall within 30 to 90 s. The equipment used must be capable of generating a pull-off force of at least 5 MPa.

The method also provides for visual evaluation of the failure mode, which may include: adhesive failure along the coating–concrete interface, cohesive

failure within the coating itself, or failure within the concrete body. Test results must be processed carefully: the mean adhesion strength is calculated with exclusion of extreme values that deviate from the arithmetic mean by more than 15 %.

2) The qualitative cross-cut method is used for field testing and consists of creating cross cuts on the coating followed by inspection and assessment of the degree of peeling. The qualitative evaluation is based on the number and size of detached coating fragments, allowing classification of adhesion into corresponding categories.

3) The quantitative method for determining the adhesion of film coatings is used to evaluate the peel strength of film coatings. Testing is conducted on laboratory specimens consisting of concrete substrates with applied protective film coatings. Peel strength is determined using special devices, which enables accurate measurement of adhesion strength.

Thus, the analysis of coating adhesion properties is an important task in the process of coating evaluation; however, modern standards do not always consider the method of coating application, the composition of the substrate and coating, or their structural characteristics.

Subject, Objectives, and Methods

The adhesion strength of the coatings was evaluated using a PSO-10MG4 adhesion tester (Stroypribor Special Design Bureau, Russia).

Concrete of strength class B30 was used as the substrate material.

The coatings were produced using the unique scientific facility “Research Complex for the Deposition and Investigation of Nanostructured Functional Coatings” at the Shukhov Belgorod State Technological University (https://ckp-rf.ru/catalog/usu/3552744/), which represents a multi-chamber detonation system (https://ckp-rf.ru/equipment/search_usu/3557868/). In this setup, combustion of a propane–butane mixture generates a detonation wave that travels along the barrel, accelerating particles of the spray-on material introduced near the end of the barrel. The powder then strikes the substrate at supersonic velocity, forming a dense coating. In this study, coatings were produced by detonation spraying using titanium powder PTS-1, obtained by crushing titanium sponge.

Two series of specimens were prepared under different spraying conditions: the first series (specimens 1–4) used a standoff distance of 120 mm and a speed of 1200 mm/min; the second series (specimens 5–8) used a standoff distance of 200 mm and a speed of 2000 mm/min. The coatings in the first series had a thickness of approximately 70 μm, and those in the second series — approximately 20 μm. The coating exhibited a mixed-phase composition Ti–TiO_x, where x = 0–2.

Selection of the required characteristics to ensure the stiffness of the designed support plate was carried out using the KOMPAS-3D software and the APM FEM module for finite element analysis.

The composition of the epoxy resins was analyzed by Raman spectroscopy using a B&W Tek i-Raman Plus spectrometer in the range of 200–3,000 cm^{-1}.

The viscosity of the epoxy resins was determined using a FUNGILAB EVO Expert rotational viscometer with an R6 spindle at a rotation speed of 10–150 rpm.

Microscopic studies were performed in the visible field using an MT-24RF upright optical metallographic microscope (SIAMS, China) with the SIAMS 800 software package (SIAMS, Russia). This hardware-software complex provides a horizontal scanning function with image accumulation and subsequent stitching.

Results and Discussion

Among the methods and procedures reviewed, two principal approaches can be distinguished for evaluating the adhesion properties of coatings: (1) pull-off testing using adhesives and dedicated mechanical devices, and (2) the use of cuts followed by visual inspection of the surface.

Pull-off testing is the most suitable option for examining coatings produced by thermal spray methods, since such coatings typically exhibit a low-porosity structure with high hardness and cohesion. This structure prevents the penetration of cutting tools without causing significant damage to the coating outside the cut area.

One of the serially produced domestic devices enabling mechanical adhesion testing of coatings is the PSO series of adhesion testers. In this study, a PSO-10MG4 device (Fig. 1) is used, providing a maximum load of 10 kN and equipped with a standard pull-off test area of 50×50 mm.

Fig. 1. PSO-10MG4 adhesion tester

A key drawback of this device is the distance between its supports — 85 mm — which renders it unsuitable for testing small-sized specimens.

The solution to this limitation is to design a custom fixture that ensures compliance with both GOST 28574–2014 and ASTM C633-24. The fixture must enable testing of specimens sized from 30×30 mm, which is constrained by the diameter of the opening in the support plate and the pull-off cylinder. The pull-off area can be adjusted to match ASTM requirements, where the test area diameter is 1 inch (25.4 mm). In this case, the pull-off area will be 2,026 mm^2.

To perform pull-off testing on a coating applied to a 40×40 mm specimen, proper support must be provided between the test device and the specimen. Therefore, for the three-support configuration of PSO-10MG4, the most appropriate solution is a triangular plate with a 27 mm diameter opening, ensuring both the free movement of the test area and the maximum possible bearing surface for the specimen.

A number of tasks arise in the development of such a fixture:

1. Adjusting the length of the hinge screw due to the increased distance to the specimen caused by the support plate.

2. The pull-off plate is a consumable component, since it may later be cut to obtain a polished cross-section for microscopic examination of the failure mode. There are two possible ways to fabricate this part:

a) using a metal rod with a diameter of 1 inch and subsequently welding an M10 nut of the corresponding steel grade;

b) cutting a thicker plate from a metal rod with a diameter of 1 inch and forming an internal thread.

3. The designed plate must provide sufficient stiffness to prevent bending during testing.

In this regard, prior to performing adhesion tests, the components were designed together with a model of the PSO-10MG4 apparatus (Fig. 2), ensuring compatibility with the dimensions of the concrete specimens coated with $Ti–TiO_x$.

The stiffness of the support plate can be adjusted by two main parameters: the plate thickness and the material used. The required characteristics were selected using the KOMPAS-3D software package and the APM FEM module for finite element analysis (Fig. 3).

As a result of numerical modeling, the following minimum parameters required to ensure the stiffness of the developed support plate were obtained: a thickness of 6 mm and steel grade C40 according to GOST 1050–2013 with a yield strength of σ_y = 330 MPa and σ_y = 570 MPa. The analyzed model also shows that a significant portion of the stresses is concentrated in the hinge screw, which must also be manufactured from C40 steel, with a stretched-rod diameter of 7 mm.

Before testing, the specimen is degreased, and all fine and dusty particles are removed from the surface using compressed air. The pull-off plate is then bonded to the coating surface using an epoxy adhesive. As the epoxy adhesive, epoxy-diane (ED) resin with the addition of polyethylene polyamine (PEPA) in the amount of 10 wt% may be used. The bonded pull-off plate is then conditioned in accordance with the requirements for the epoxy

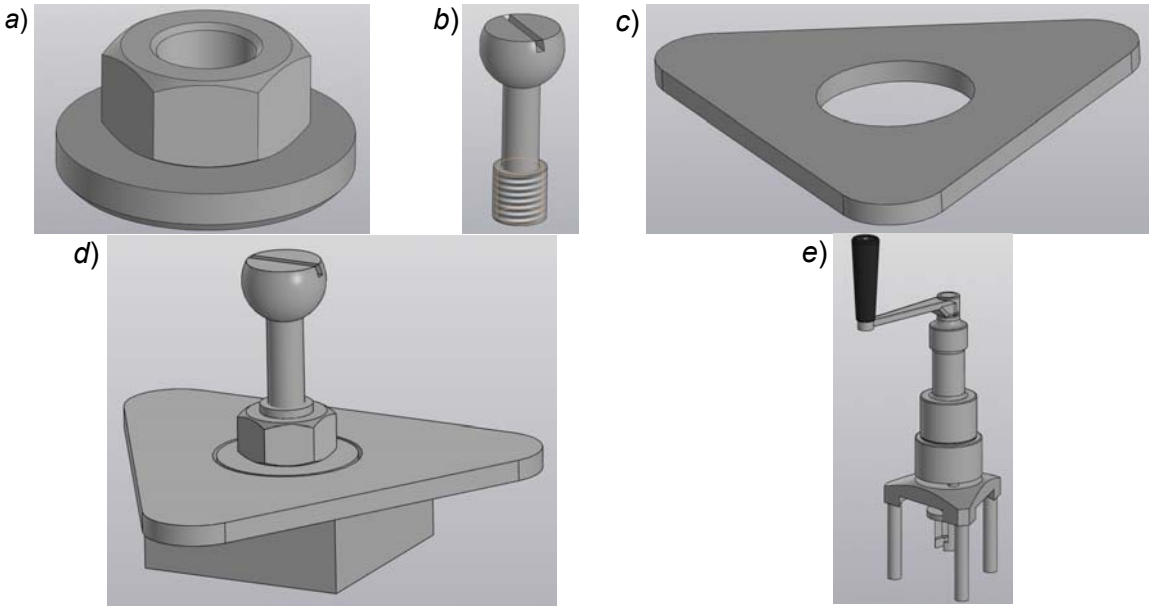

Fig. 2. 3D models of the fixture for adhesion testing using the axial pull-off method: *a* — version of the pull-off plate with a nut; *b* — hinge screw; *c* — support plate; *d* — assembled configuration prepared for pull-off testing; *e* — PSO-10MG4 testing apparatus

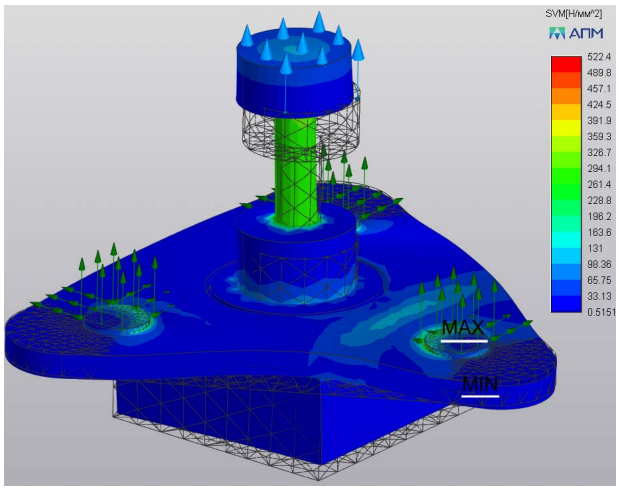

Fig. 3. Finite element computational model of the developed fixture

adhesive; for the ED + PEPA composition, the specimen should be conditioned for at least 24 h under standard conditions.

After the epoxy adhesive has fully cured, the hinge screw is threaded into the opening of the pull-off plate. The assembled system is inserted into the opening of the support plate and placed into the dedicated hinge socket of the PSO-10MG4 testing device. Next, a uniform load is applied at a rate not exceeding 1 MPa/s (following GOST 28574–2014). The adhesion strength is calculated as follows:

$$\sigma_a = F/A,$$

where F is the force obtained during testing, and A is the test area.

To select the most suitable epoxy resin for the tests, four samples were chosen:

ER1 — epoxy resin supplied in two syringes, both containing a transparent component;

ER2 — epoxy resin supplied in a dual syringe with a common plunger;

ERH — epoxy resin with hardener;

CWC — cold-welding compound.

Since manufacturers do not specify the composition of epoxy resins, their composition was analyzed using Raman spectroscopy (Figs. 4, 5).

Comparison of the spectra (Fig. 4) with reference data showed that all the epoxy resins correspond to the same chemical compound — poly (bisphenol A-co-epichlorohydrin), i.e., an epoxy resin obtained via the reaction of hydrogenated bisphenol A with epichlorohydrin. The halo and troughs observed in the CWC spectrum are associated with the presence of fillers (kaolin, titanium dioxide) and modifier (dibutyl phthalate), as specified by the manufacturer. In all cases, comparison with reference spectra yielded a hit quality (HQ) exceeding 90 %.

The hardener in ER1 is a solution of amine hardeners in propylene glycol (HQ = 90.53); the hardener in ER2 is triethylenetetramine (HQ = 89.08); the hardener in ERH is tetraethylenepentamine (HQ = 92.94); the hardener in CWC is most likely filled polyamine (HQ = 90.35) (Fig. 5).

Viscosity of the epoxy resin samples (Table 1) was examined under the following parameters: spindle R6, as it had been determined in advance that all resins behave as Newtonian fluids (their viscosity does not change with rotation speed); the rotation speed varied from 10 to 150 rpm, and the density of all resins was 1.15 ± 0.05 kg/cm^3. The cold-welding compound was not tested due to its extremely high viscosity.

During the study, the viscosity of ER1 and ERH either did not change over time or changed insignificantly. A rapid increase in the viscosity of ER2 was observed: within 5 minutes of measurement, the viscosity increased from 25,000 to 37,000 cSt (40 cSt/s), and within 1 hour the viscosity of ER2 became comparable to that of CWC.

Below is the procedure for conducting adhesion tests of coatings produced by detonation spraying on concrete substrates (Fig. 6).

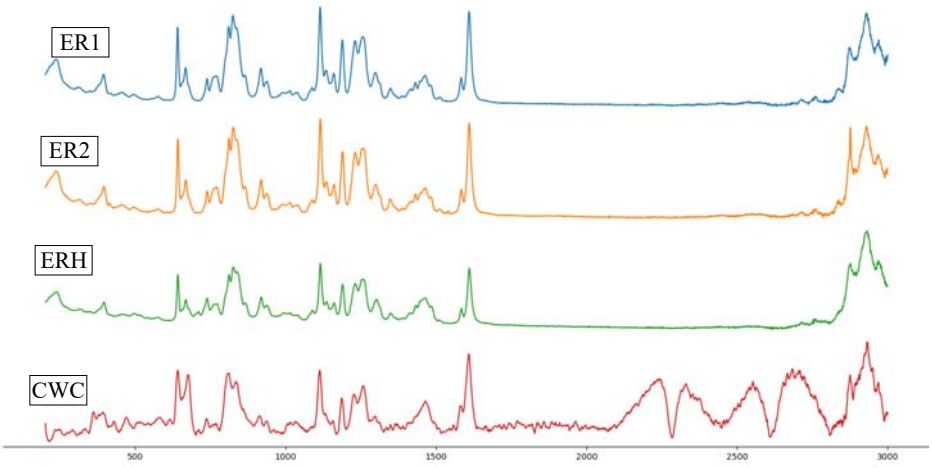

Fig. 4. Raman spectra of the epoxy resins

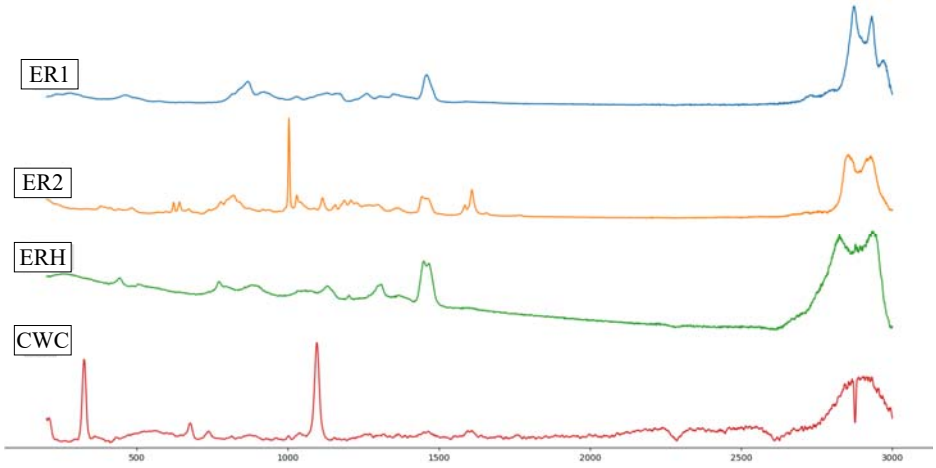

Fig. 5. Raman spectra of the hardeners

Table 1. **Viscosity of the epoxy resin samples**

Sample	ERH	ER1	ER2	CWC
Viscosity, cSt	2,940	3,700	25,000	–

During the adhesion tests, a multilayer PTFE spacer with a total thickness of 300 μm was placed between the support plate and the specimen to compensate for surface unevenness and prevent eccentricity during testing. This spacer thickness was selected under the condition that the surface roughness of the specimens (R_{max}, GOST 2789-73) does not exceed 100 μm. If the roughness exceeds this value, a thicker spacer is recommended.

Based on the results of the adhesion tests (Table 2) and the effectiveness of the adhesives used for determining adhesion strength, the resins were ranked in the following order: ER2 → CWC → ERH → ER1.

The least suitable resin was ER1, whose curing process took more than three days. Moreover, upon application it caused significant wetting of the

Fig. 6. Procedure for conducting adhesion tests

Table 2. **Adhesion strength values obtained using different epoxy resins**

Sample*	ERH		ER1		ER2		CWC	
	1	5	2	6	3	7	4	8
σ_a, MPa	1.52	3.62	2.03	3.77	0.65	1.77	0.53	0.32
* specimen numbering corresponds to Figs. 6–8.								

surface, which may affect test results due to the penetration of the resin into the pores of the concrete and its subsequent impregnation.

ERH resin cured within 24 hours, but also exhibited high fluidity.

Cold-welding compound (CWC) is an acceptable option for performing the tests; however, its major drawback is the difficulty of achieving uniform application, which requires considerable effort. When working with thin specimens with coatings, there is a risk of damaging the integrity of the substrate (or the coating–substrate interface).

The most effective adhesive was ER2, which demonstrated the shortest curing time (less than 24 hours), as well as high viscosity combined with sufficient fluidity to allow uniform spreading across the specimen surface.

It should be noted that the numerical test results in this case cannot be interpreted unambiguously, since the surface morphology of the coatings and the internal structure of the specimens differed. Specimens from the first series exhibited a dense structure, whereas specimens from the second series showed significant porosity and therefore demonstrated higher adhesion strength due to shear forces arising from the penetration of the resin into the surface pores. For more mobile resins (ER1 and ERH), failure occurred along the cement stone–aggregate interface, which may indicate partial impregnation and, consequently, strengthening of the near-surface layer of the cement stone by the epoxy resin.

The concrete aggregate also exerted a significant influence on the adhesion strength. In most cases, failure occurred precisely along the concrete–aggregate interface, which should be taken into account when forming coatings and conducting normal pull-off tests.

After the adhesion tests, the specimens were embedded in ERH for further examination of their polished cross-sections using optical microscopy (Figs. 7 and 8). Fig. 7 shows coating segments with a total length of 10 mm. It is evident that nearly all coatings (except for ER1) detached either through the cement stone or along the cement–aggregate interface. It is worth noting that in areas where pores are present and the coating is absent, detachment occurred along the resin–concrete interface, whereas the concrete itself was not torn out. These findings indicate high adhesion of all obtained coatings to the concrete surface, and the adhesive used for the pull-off tests did not penetrate the concrete in any of the cases.

Fig. 8 presents 800 μm segments for each specimen. In all cases, strong adhesion of the coatings to the substrate and low porosity are observed, which is essential for reliable testing. For resin ER1, mixed failure occurred across three zones: failure within the resin, failure along the resin–coating interface, and failure through the

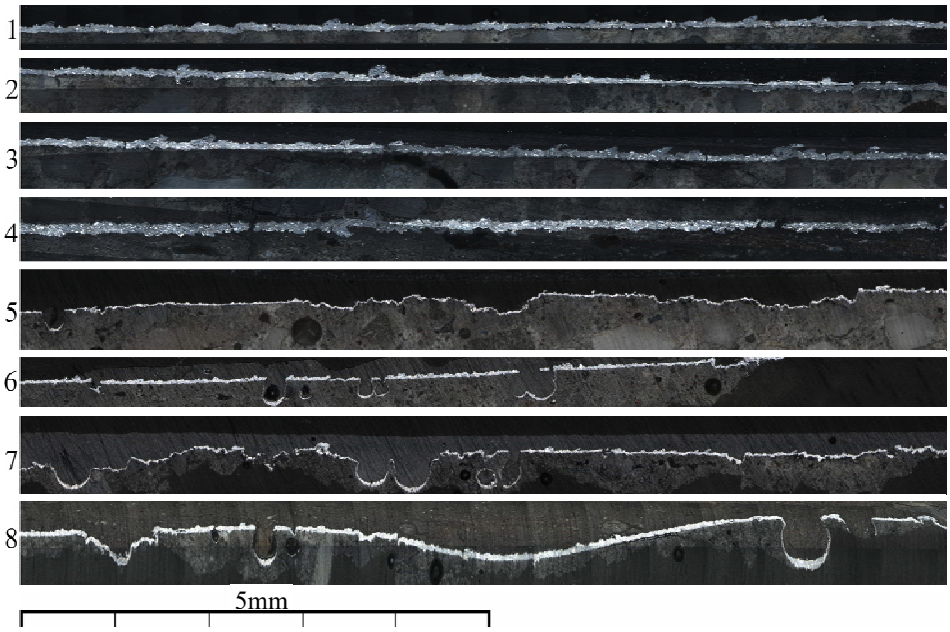

Fig. 7. Microscopic images of polished cross-sections of the coatings after adhesion tests over a 10 mm segment

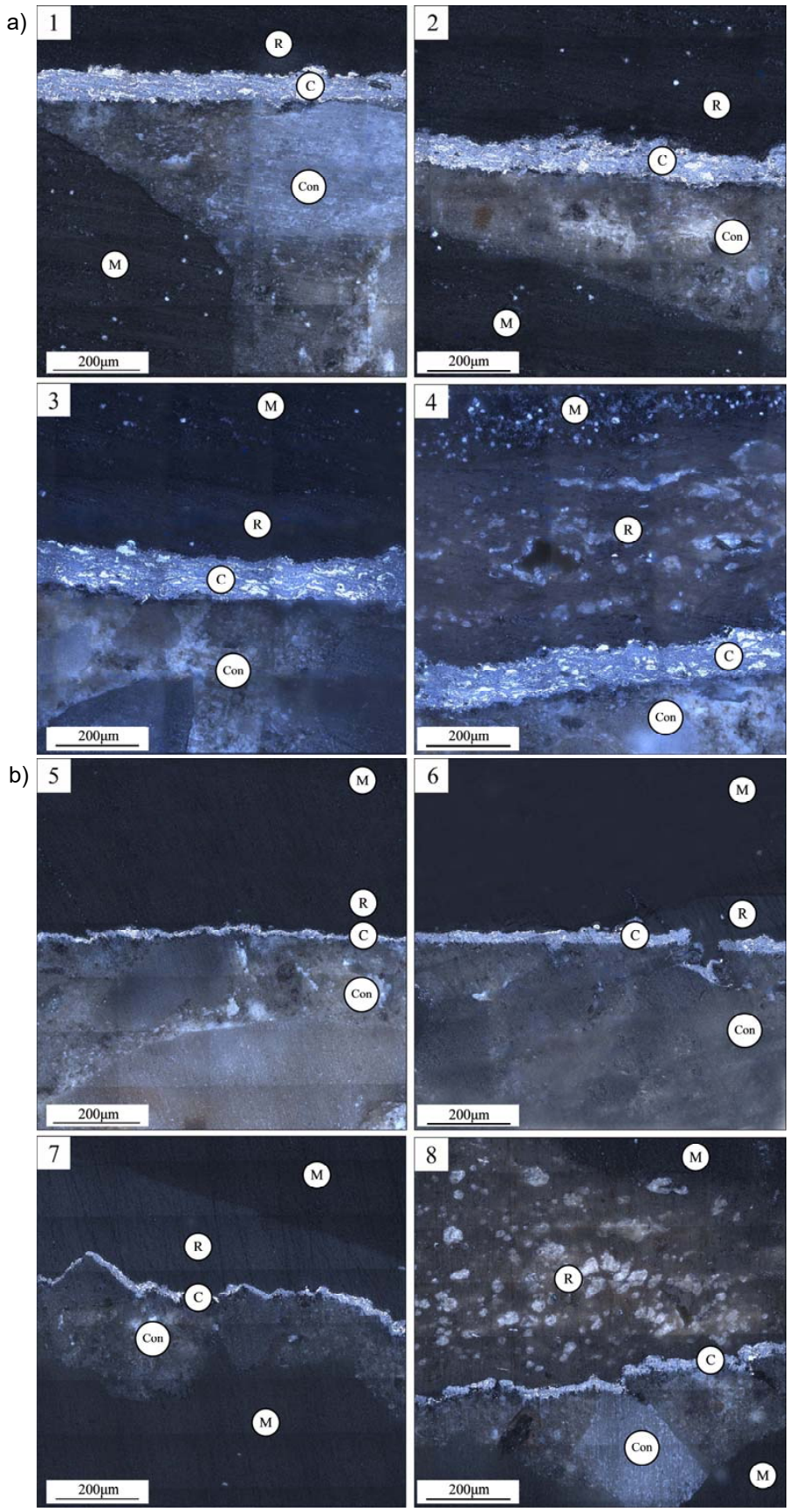

Fig. 8. Microscopic images of polished cross-sections of the coatings after adhesion tests: a — spraying mode: standoff distance 120 mm, speed 1,200 mm/min; b — spraying mode: standoff distance 200 mm, speed 2,000 mm/min; 1, 5 — ERH; 2, 6 — ER1; 3, 7 — ER2; 4, 8 — CWC; M — molding resin for polishing; R — resin used for adhesion testing; C — coating; Con — concrete

concrete, which is likely associated with poor-quality hardener or insufficient hardener content. For all other resins, failure occurred exclusively through the concrete. It should be noted that for CWC, local areas were observed where the resin had no contact with the coating, and therefore these tests cannot be considered reliable.

Conclusions

The adhesion strength of Ti–TiO_x coatings on concrete substrates was determined using the axial pull-off method. Specimens produced under the spraying mode with a standoff distance of 120 mm and a speed of 1,200 mm/min exhibited adhesion strengths in the range of 0.53–2.03 MPa (with a coating thickness of approximately 70 μm). Specimens produced under the spraying mode with a standoff distance of 200 mm and a speed of 2,000 mm/min exhibited adhesion strengths in the range of 0.32–3.77 MPa (with a coating thickness of approximately 20 μm). It was found that the numerical test results are influenced by the surface morphology of the coatings, the structure of the concrete, the type of adhesive composition, and its viscosity. A high adhesion strength of all obtained coatings to the substrate and low porosity were noted.

Prior to testing, the procedure for evaluating the adhesion properties of coatings on concrete substrates was refined by developing an appropriate fixture considering the specimen dimensions, specifying the epoxy adhesive to be used, and introducing a PTFE spacer to compensate for surface irregularities of the coating.

The set of tests carried out made it possible to rank the adhesive compositions according to their potential applicability in assessing coating adhesion to the substrate material.

Thus, the following requirements can be established for the correct performance of adhesion tests:

– the coating on the concrete surface must have a continuous structure and minimal surface porosity;

– the coating must be applied directly onto the cement stone surface;

– the aggregate should be selected so that it is compatible with the cement stone in order to prevent detachment along the cement stone–aggregate interface;

– the epoxy resin must have sufficiently low viscosity to spread across the specimen surface, but must not penetrate the surface pores and impregnate the substrate material.

Funding

This work was carried out as part of the implementation of the state assignment of the Ministry of Science and Higher Education of the Russian Federation No. FZWN-2023-0006 using the equipment of the High Technology Center at the Shukhov Belgorod State Technological University.

References

Bessmertnyy, V. S., Sokolova, O. N., Bondarenko, N. I., Bondarenko, D. O., Bragina, L. L., Makarov, A. V., and Kochurin, D. V. (2019). Plasmachemical modification of thermal insulated blocks with decorative coating. *Bulletin of BSTU named after V. G. Shukhov*, No. 3, pp. 85–92. DOI: 10.34031/article_5ca1f6331ec888.51255959.

Bondarenko, D. O., Podgornyi, D. S., and Strokova, V. V. (2024). Thermal and gas-dynamic methods of applying functional coatings. Prospects of detonation spraying. *Construction Materials*, No. 5, pp. 48–69. DOI: 10.31659/0585-430X-2024-824-5-48-69.

Chen, Z., Zhou, K., Lu, X., and Lam, Y. C. (2014). A review on the mechanical methods for evaluating coating adhesion. *Acta Mechanica*, Vol. 225, Issue 2, pp. 431–452. DOI: 10.1007/s00707-013-0979-y.

Croll, S. G. (2020). Surface roughness profile and its effect on coating adhesion and corrosion protection: a review. *Progress in Organic Coatings*, Vol. 148, 105847. DOI: 10.1016/j.porgcoat.2020.105847.

Falsafein, M., Ashrafizadeh, F., and Kheirandish, A. (2018). Influence of thickness on adhesion of nanostructured multilayer CrN/CrAlN coatings to stainless steel substrate. *Surfaces and Interfaces*, Vol. 13, pp. 178–185. DOI: 10.1016/j.surfin.2018.09.009.

Hang, J., Yan, X., and Li, J. (2024). A review on the effect of wood surface modification on paint film adhesion properties. *Coatings*, Vol. 14, Issue 10, 1313. DOI: 10.3390/coatings14101313.

Harfouche, M. M., Alidokht, S. A., Encalada, A. I., Mungala, V. N. V., Chromik, R. R., Moreau, C., Sharifi, N., Stoyanov, P., and Makowiec, M. E. (2024). Scratch adhesion testing of thick HVOF thermal sprayed coatings. *Journal of Thermal Spray Technology*, Vol. 33, Issue 4, pp. 1158–1166. DOI: 10.1007/s11666-024-01741-3.

Haselrieder, W., Westphal, B., Bockholt, H., Diener, A., Höft, S., and Kwade, A. (2015). Measuring the coating adhesion strength of electrodes for lithium-ion batteries. International *Journal of Adhesion and Adhesives*, Vol. 60, pp. 1–8. DOI: 10.1016/j.ijadhadh.2015.03.002.

Heidarinejad, A. and Ashrafizadeh, F. (2024). Influence of surface texture and coating thickness on adhesion of nickel plated coatings to aluminium substrate. *Journal of Manufacturing Processes*, Vol. 120, pp. 435–448. DOI: 10.1016/j.jmapro.2024.04.040.

Klyuchnikova, N. V., Genov, I., Mukhacheva, V. D., and Piskareva, A. O. (2018). Protective coatings based on modified phenolformaldehyde composites. *Bulletin of BSTU named after V. G. Shukhov*, No. 12, pp. 91–97. DOI: 10.12737/article_5c1c99652f7a31.56915689.

Ma, D.-D., Xue, Y.-P., Gao, J., Ma, Y., Yu, S.-W., Wang, Y.-S., Xue, C., Hei, H.-J., and Tang, B. (2020). Effect of Ta diffusion layer on the adhesion properties of diamond coating on WC-Co substrate. *Applied Surface Science*, Vol. 527, 146727. DOI: 10.1016/j.apsusc.2020.146727.

Montemor, M. F. (2014). Functional and smart coatings *for corrosion protection: a review of recent advances. Surface* and Coatings Technology, Vol. 258, pp. 17–37. DOI: 10.1016/j.surfcoat.2014.06.031.

Vereschaka, A., Tabakov, V., Grigoriev, S., Aksenenko, A., Sitnikov, N., Oganyan, G., Seleznev, A., and Shevchenko, S. (2019). Effect of adhesion and the wear-resistant layer thickness ratio on mechanical and performance properties of ZrN - (Zr,Al,Si)N coatings. *Surface and Coatings Technology*, Vol. 357, pp. 218–234. DOI: 10.1016/j.surfcoat.2018.09.087.

Zaytsev, A. N., Aleksandrova, Y. P., and Yagopolskiy, A. G. (2021). Comparative analysis of methods for assessing adhesion strength of thermal spray coatings. *BMSTU Journal of Mechanical Engineering*, No. 5 (734), pp. 48–59. DOI: 10.18698/0536-1044-2021-5-48-59.

Zhang J., Xiang Z., Ren X., Zhang B., Fu D., and Wang Y. (2024). Superior toughness anticorrosion-bioactive integrated multilayer coating with excellent adhesion for biodegradable magnesium-based stents. *Chemical Engineering Journal*, Vol. 481, 148400. DOI: 10.1016/j.cej.2023.148400.

ОЦЕНКА АДГЕЗИОННОЙ ПРОЧНОСТИ МЕТАЛЛОКЕРАМИЧЕСКИХ ПОКРЫТИЙ, ПОЛУЧЕННЫХ МЕТОДОМ ДЕТОНАЦИОННОГО НАПЫЛЕНИЯ, НА БЕТОННЫХ ПОДЛОЖКАХ

Даниил Сергеевич Подгорный, Диана Олеговна Бондаренко*, Валерия Валерьевна Строкова

Белгородский государственный технологический университет им. В. Г. Шухова, Белгород, Россия

*Email: di_bondarenko@mail.ru

Аннотация

Введение. Эффективность использования и успешное применение различных защитных покрытий обуславливают необходимость изучения взаимодействия покрытий с подложкой материала для обеспечения их долговечности и надежности. Адгезия является ключевым параметром, определяющим качество сцепления покрытия с поверхностью материала. Существующие методы её оценки постоянно совершенствуются для повышения точности, универсальности и применимости к различным типам покрытий и подложек. **Цель исследования**. Оценка адгезионной прочности покрытий, полученных методом детонационного напыления на поверхности тяжёлого бетона, корректировка методики определения адгезионной прочности для проведения соответствующих испытаний. **Методы**. Рамановская спектрометрия, исследование адгезионной прочности методом осевого отрыва, оптическая микроскопия, ротационная вискозиметрия. **Результаты**. Проведены испытания адгезионной прочности образцов покрытия Ti–TiO_x на бетонных подложках, полученных методом детонационного напыления порошков при разных режимах. Полученные покрытия имеют высокую адгезионную прочность к подложке в диапазоне 0,32–3,77 МПа и низкую пористость. Предварительно разработана оснастка для проведения адгезионных испытаний на образцах с линейными размерами 30 мм и более. Проведено исследование применимости серии эпоксидных смол для адгезионных испытаний. Выявлено, что при испытании покрытий на пористых подложках важно учитывать вязкость применяемых клеящих средств, так как составы с высокой подвижностью могут проникать вглубь образца и искажать получаемые результаты.

Ключевые слова: адгезионная прочность; покрытия; бетон; методика адгезионных испытаний; эпоксидная смола.

DOI: 10.23968/2500-0055-2025-10-4-100-111

ENGINEERING METHOD FOR DETERMINING THERMAL STRESSES DURING CONSTRUCTION OF FOUNDATION SLABS CONSIDERING FOUNDATION SOIL COMPLIANCE

Vasilina Sergeevna Tyurina, Anton Sergeevich Chepurnenko*, Vladimir Feliksovich Akopyan

Don State Technical University, Rostov-on-Don, Russia

*Corresponding author's email: anton_chepurnenk@mail.ru

Abstract

Introduction. Massive monolithic foundation slabs are prone to early-age cracking caused by the exothermic heat of hydration of concrete. Selecting optimal strategies to address this issue can be achieved through computer-based simulations. **Purpose of the study**. The study is aimed at developing a simplified finite element model to determine the stress–strain state of foundation slabs during construction while accounting for foundation soil compliance, and validating this model against existing experimental data as well as results reported by other authors. In the course of the study, the following **methods** were used: finite element modeling with plate finite elements in the MATLAB environment, employing software developed by the authors that reduces the three-dimensional problem of determining the stress–strain state to a two-dimensional formulation. The foundation bed was modeled using the Pasternak model with two foundation moduli. The **results** show that the proposed solution is in good agreement with the numerical modeling data obtained by other researchers in a three-dimensional setting. Satisfactory agreement with the experimental results was also achieved. A study was conducted to assess the influence of the reinforcement ratio and the coefficient of linear thermal expansion of concrete on the stress–strain state.

Keywords: massive reinforced concrete structures; foundation slab; cracking; thermal stresses; finite element method; foundation modulus.

Introduction

The increasing height of constructed buildings makes research aimed at improving foundation design and construction technology particularly relevant, with the objective of enhancing structural reliability and reducing costs. Widely used flat monolithic reinforced concrete foundation slabs typically have a thickness of 50–200 cm or more (Bushmanova et al., 2017). In most cases, such foundation slabs with a thickness exceeding 70 cm fall into the category of massive structures (Johansson and Heinegård, 2020). In massive reinforced concrete foundation slabs, the heat released during cement hardening causes non-uniform temperature rise across the slab thickness (Kuriakose et al., 2016). Differential thermal strains in combination with shrinkage deformations can generate significant tensile stresses leading to cracking (Chuc et al., 2018; Klemczak and Knoppik-Wróbel, 2011; Korotchenko et al., 2016). Early-age cracking in massive reinforced concrete structures may require substantial additional costs, and in some cases may render the structure unfit for service (Safiuddin et al., 2018). It also adversely affects durability and long-term structural performance under loading (Slowik et al., 2008). Therefore, for such structures, special measures must be implemented to minimize the influence of thermal stresses associated with concrete exothermy during hardening (Nama et al., 2015).

Selecting optimal mix-design and technological parameters for casting monolithic foundation slabs can also be based on numerical modeling results (Buffo-Lacarrière et al., 2011; Havlásek et al., 2017; Wang et al., 2020).

At present, the finite element method serves as the main tool for analyzing temperature fields and thermal stresses in massive monolithic foundation slabs during construction (Liu and Schindler, 2020; Mathern and Yang, 2021).

The analysis of temperature fields and thermal stresses during the construction of massive monolithic foundation slabs is typically carried out in a three-dimensional setting using solid finite elements (FE) for both the concrete and the foundation soil (Cajka et al., 2020). This approach requires substantial computational resources, which makes it difficult to explore a large number of options when choosing optimal casting parameters.

An earlier study (Chepurnenko et al., 2022b) proposed a simplified method for determining thermal stresses during the construction of massive monolithic foundation slabs resting on a completely rigid base. In addition to assuming that the base is non-deformable, the method also considers identical reinforcement in the *x* and *y* axes and uses

For citations: Tyurina, V. S., Chepurnenko, A. S., Akopyan, V. F. (2025). Engineering method for determining thermal stresses during construction of foundation slabs considering foundation soil compliance. Architecture and Engineering, No 4 (10), pp. 100–111. DOI: 10.23968/2500-0055-2025-10-4-100-111.

the plane-sections hypothesis, which reduces the three-dimensional stress–strain analysis to a one-dimensional problem.

In (Chepurnenko et al., 2024), a resolving equation was derived to determine the stress–strain state of a foundation slab during construction while accounting for foundation slab compliance. The Pasternak elastic foundation model was adopted for the soil. The foundation slab was considered as plain concrete, without accounting for reinforcement. Moreover, a finite-difference method was proposed to solve the resulting equation, which leads to relatively complex approximations of boundary conditions.

The objective of this study is to further develop the approaches proposed by Chepurnenko et al. (2024). The method presented in this paper allows the reinforcement of the slab to differ in the *x* and *y* axes. The idea is to reduce the three-dimensional thermal stress analysis to a two-dimensional problem based on the assumption of a linear distribution of strains through the slab thickness and the use of plate finite elements instead of solid FE.

Materials and Methods

In this study, reinforced concrete foundation slabs with orthogonal reinforcement are considered (Fig. 1). To reduce the dimensionality of the problem, the hypothesis of a linear strain distribution through the slab thickness (straight-normal hypothesis) is used. This hypothesis is valid for thin plates in which the ratio of thickness *h* to the smallest plan dimension *a* does not exceed one fifth (Petrov, 2018). Despite their considerable thickness, which may reach 2.5 m or more, foundation slabs also have significant plan dimensions. Therefore, the ratio *h*/*a* generally falls within the specified limits, and the use of the straight-normal hypothesis can be considered justified for this problem. When these limits are exceeded, one may employ, for example, the hypotheses presented in (Gatiev et al., 2023).

Based on the straight-normal hypothesis, the total concrete strains $\varepsilon_{bx}, \varepsilon_{by}, \gamma_{bxy}$ can be written as follows:

$$\begin{aligned} \varepsilon_{bx} &= \varepsilon_x^0 - z\chi_x; \\ \varepsilon_{by} &= \varepsilon_y^0 - z\chi_y; \\ \gamma_{bxy} &= \gamma^0 - 2z\chi_{xy}, \end{aligned} \quad (1)$$

where ε_x^0, ε_y^0, γ_0 are the strains of the middle plane (taken as the reference surface), $\chi_x = \frac{\partial^2 w}{\partial x^2}$, $\chi_x = \frac{\partial^2 w}{\partial y^2}$, $\chi_{xy} = \frac{\partial^2 w}{\partial x \partial y}$ are the mid-surface curvature changes, w is the slab deflection, and the coordinate z is measured from the middle plane.

The strains of the reinforcement in the *i*-th layer are determined from the condition of its combined action with the concrete:

$$\varepsilon_{sx,i} = \varepsilon_x^0 - z_{sx,i}\chi_x;$$

$$\varepsilon_{sy,i} = \varepsilon_y^0 - z_{sy,i}\chi_y. \quad (2)$$

In addition to the hypothesis of linear strain distribution through the slab thickness, a hypothesis on the one-dimensional character of temperature distribution is introduced, i.e., the temperature is assumed to be a function of the coordinate z only. This is confirmed by the results of three-dimensional finite element simulations presented in (Chepurnenko et al., 2022a, 2022b). A deviation from this hypothesis is observed only in a small region near the slab edges. Since the temperature is taken as a function of z only, the concrete modulus of elasticity is also assumed to depend solely on z. The well-known plate theory assumption of the absence of transverse normal stresses is also adopted, meaning that strains and stresses in the z direction are absent in the concrete.

The total concrete strains, from a physical standpoint, represent the sum of the strains caused by stresses σ_{bx}, σ_{by}, and τ_{bxy}, as well as thermal strains and shrinkage strains:

$$\begin{aligned} \varepsilon_{bx} &= \frac{1}{E_b(z)}\left(\sigma_{bx} - \nu\sigma_{by}\right) + \varepsilon_{bf}; \\ \varepsilon_{by} &= \frac{1}{E_b(z)}\left(\sigma_{by} - \nu\sigma_{bx}\right) + \varepsilon_{bf}; \\ \gamma_{bxy} &= \frac{2(1+\nu)}{E_b(z)}\tau_{bxy}, \end{aligned} \quad (3)$$

where $E_b(z)$ is the concrete modulus of elasticity; ν is the Poisson's ratio of concrete, taken as constant; $\varepsilon_{bf} = \alpha\Delta T + \varepsilon_{sh}$ is the sum of the thermal strain and shrinkage strain (α is the coefficient of linear thermal expansion of concrete; ΔT is the temperature change at the point under consideration).

The total strains in the reinforcement consist of elastic and thermal strains:

$$\begin{aligned} \varepsilon_{sx,i} &= \frac{\sigma_{sx,i}}{E_s} + \alpha_s \Delta T_{x,i}; \\ \varepsilon_{sy,i} &= \frac{\sigma_{sy,i}}{E_s} + \alpha_s \Delta T_{y,i}, \end{aligned} \quad (4)$$

where $\sigma_{sx,i}$ and $\sigma_{sy,i}$ are the stresses in the steel reinforcement in the x and y directions, E_s is the elastic modulus of steel, $\Delta T_{x,i}$ and $\Delta T_{y,i}$ are the

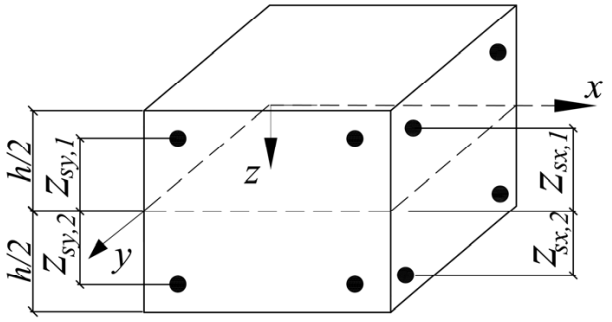

Fig. 1. Slab reinforcement layout

temperature changes in the i-th layer in the x and y directions, and α_s is the coefficient of linear thermal expansion of steel.

The stresses in concrete are expressed from (3) through the strains in the following form:

$$\sigma_{bx} = \frac{E_b(z)}{1-\nu^2}\left(\varepsilon_{bx} + \nu\varepsilon_{by} - (1+\nu)\varepsilon_{bf}\right) =$$
$$= \frac{E_b(z)}{1-\nu^2}\left(\varepsilon_x^0 + \nu\varepsilon_y^0 + z\left(\chi_x + \nu\chi_y\right) - (1+\nu)\varepsilon_{bf}\right);$$
$$\sigma_{by} = \frac{E_b(z)}{1-\nu^2}\left(\varepsilon_{by} + \nu\varepsilon_{bx} - (1+\nu)\varepsilon_{bf}\right) =$$
$$= \frac{E_b(z)}{1-\nu^2}\left(\varepsilon_y^0 + \nu\varepsilon_x^0 + z\left(\chi_y + \nu\chi_x\right) - (1+\nu)\varepsilon_{bf}\right);$$
$$\tau_{bxy} = \frac{E_b(z)}{2(1+\nu)}\gamma_{bxy} = \frac{E_b(z)}{2(1+\nu_b)}\left(\gamma_0 - 2z\chi_{xy}\right). \quad (5)$$

The stresses in the reinforcement are written through the strains as follows:

$$\sigma_{sx,i} = E_s\left(\varepsilon_x^0 - z_{sx,i}\chi_x - \alpha_s\Delta T_{x,i}\right);$$
$$\sigma_{sy,i} = E_s\left(\varepsilon_y^0 - z_{sy,i}\chi_y - \alpha_s\Delta T_{y,i}\right). \quad (6)$$

In the analysis, it is assumed that the slab resists only bending, and that no longitudinal forces N_x, N_y develop, since the soil has a much lower modulus of elasticity compared with concrete and therefore does not restrain the slab from expanding in the x and y directions. The shear forces N_{xy} are also taken equal to zero. The conditions of zero longitudinal forces are written as follows:

$$N_x = \int_{-\frac{h}{2}}^{\frac{h}{2}} \sigma_{bx}dz + \sum_{i=1}^{n_x}\sigma_{sx,i}A_{sx,i} = 0;$$
$$N_y = \int_{-\frac{h}{2}}^{\frac{h}{2}} \sigma_{by}dz + \sum_{i=1}^{n_y}\sigma_{sy,i}A_{sy,i} = 0, \quad (7)$$

where n_x and n_y are the numbers of reinforcement layers in the x and y directions, $A_{sx,i}$ and $A_{sy,i}$ are the cross-sectional areas of the reinforcement in the i-th layer per running meter of the slab length.

Substituting (5) and (6) into the first equation of (7) yields the following:

$$\left(B_{b1} + B_{sx}\right)\varepsilon_x^0 + B_{b2}\varepsilon_y^0 - \left(C_{b1} + C_{sx}\right)\chi_x - C_{b2}\chi_y =$$
$$= N_{bf} + N_{sfx}, \quad (8)$$

where

$$B_{b1} = \frac{1}{1-\nu_b^2}\int_{-h/2}^{h/2} E_b(z)dz;$$
$$B_{b2} = \nu B_{b1},\ C_{b1} = \frac{1}{1-\nu_b^2}\int_{-h/2}^{h/2} E_b(z)zdz;$$
$$C_{b2} = \nu C_{b1};\ B_{sx} = E_s\sum_{i=1}^{n_x}A_{sx,i};\ C_{sx} = \sum_{i=1}^{n_x}A_{sx,i}z_{sx,i};$$
$$N_{bf} = \frac{1}{1-\nu}\int_{-h/2}^{h/2} E_b(z)\varepsilon_{bf}dz;$$
$$N_{sfx} = \alpha_s E_s\sum_{i=1}^{n_x}A_{sx,i}\Delta T_{x,i}.$$

Similarly, the condition $N_y = 0$ gives:

$$\left(B_{b1} + B_{sy}\right)\varepsilon_y^0 + B_{b2}\varepsilon_x^0 - \left(C_{b1} + C_{sy}\right)\chi_y - C_{b2}\chi_x =$$
$$= N_{bf} + N_{sfy}, \quad (9)$$

where

$$B_{sy} = E_s\sum_{i=1}^{n_y}A_{sy,i};\ C_{sy} = \sum_{i=1}^{n_y}A_{sy,i}z_{sy,i};$$
$$N_{sfy} = \alpha_s E_s\sum_{i=1}^{n_y}A_{sy,i}\Delta T_{y,i}.$$

The strains ε_x^0 and ε_y^0 can be expressed from (8) and (9) through changes in curvatures as follows:

$$\begin{Bmatrix}\varepsilon_x^0\\ \varepsilon_y^0\end{Bmatrix} = [A]\begin{Bmatrix}\chi_x\\ \chi_y\end{Bmatrix} + \begin{bmatrix}B_{b1}+B_{sx} & B_{b2}\\ B_{b2} & B_{b1}+B_{sy}\end{bmatrix}^{-1}\times$$
$$\times\begin{Bmatrix}N_{fx}\\ N_{fy}\end{Bmatrix}, \quad (10)$$

where

$$[A] = \begin{bmatrix}B_{b1}+B_{sx} & B_{b2}\\ B_{b2} & B_{b1}+B_{sy}\end{bmatrix}^{-1}\cdot\begin{bmatrix}C_{b1}+C_{sx} & C_{b2}\\ C_{b2} & C_{b1}+C_{sy}\end{bmatrix};$$
$$N_{fx} = N_{bf} + N_{sfx};\ N_{fy} = N_{bf} + N_{sfy}.$$

The bending moments M_x and M_y are determined as follows:

$$M_x = \int_{-\frac{h}{2}}^{\frac{h}{2}} \sigma_{bx}zdz + \sum_{i=1}^{n_x}\sigma_{sx,i}A_{sx,i}z_{sx,i};$$
$$M_y = \int_{-\frac{h}{2}}^{\frac{h}{2}} \sigma_{by}zdz + \sum_{i=1}^{n_y}\sigma_{sy,i}A_{sy,i}z_{sy,i}. \quad (11)$$

Substituting (5) and (6) into (11) yields:

$$\begin{Bmatrix}M_x\\ M_y\end{Bmatrix} = \begin{bmatrix}C_{b1}+C_{sx} & C_{b2}\\ C_{b2} & C_{b1}+C_{sy}\end{bmatrix}\times$$
$$\times\begin{Bmatrix}\varepsilon_x^0\\ \varepsilon_y^0\end{Bmatrix} - \begin{bmatrix}D_{b1}+D_{sx} & D_{b2}\\ D_{b2} & D_{b1}+D_{sy}\end{bmatrix}\times$$
$$\times\begin{Bmatrix}\chi_x\\ \chi_y\end{Bmatrix} - \begin{Bmatrix}M_{bf}+M_{sfx}\\ M_{bf}+M_{sfy}\end{Bmatrix}, \quad (12)$$

where

$$D_b \quad \frac{}{-\nu}\int_{/2}^{/2} E_b(z)z\ dz\ D_{b2} = \nu D_{b1};$$
$$D_{sx} = \sum_{i=1}^{n_x}A_{sx,i}z_{sx,i}^2;\ D_{sy} = \sum_{i=1}^{n_y}A_{sy,i}z_{sy,i}^2;$$

$$M_{sfx} = \alpha_s E_s \sum_{i=1}^{n_x} A_{sx,i} \Delta T_{x,i} z_{sx,i};$$

$$M_{sfy} = \alpha_s E_s \sum_{i=1}^{n_y} A_{sy,i} \Delta T_{y,i} z_{sy,i}.$$

To eliminate the mid-surface strains from (12), expression (10) shall be substituted into (12). As a result, the following relationship between the bending moments and the changes in curvatures can be obtained:

$$\begin{Bmatrix} M_x \\ M_y \end{Bmatrix} = -\begin{bmatrix} D_{11} & D_{12} \\ D_{21} & D_{22} \end{bmatrix} \cdot \begin{Bmatrix} \chi_x \\ \chi_y \end{Bmatrix} - \begin{Bmatrix} M_x^* \\ M_y^* \end{Bmatrix}, \quad (13)$$

where

$$\begin{bmatrix} D_{11} & D_{12} \\ D_{21} & D_{22} \end{bmatrix} =$$

$$= \begin{bmatrix} D_{b1} + D_{sx} & D_{b2} \\ D_{b2} & D_{b1} + D_{sy} \end{bmatrix} - \begin{bmatrix} C_{b1} + C_{sx} & C_{b2} \\ C_{b2} & C_{b1} + C_{sy} \end{bmatrix} [A];$$

$$\begin{Bmatrix} M_x^* \\ M_y^* \end{Bmatrix} = \begin{Bmatrix} M_{bf} + M_{sfx} \\ M_{bf} + M_{sfy} \end{Bmatrix} - \begin{bmatrix} C_{b1} + C_{sx} & C_{b2} \\ C_{b2} & C_{b1} + C_{sy} \end{bmatrix} \times$$

$$\times \begin{bmatrix} B_{b1} + B_{sx} & B_{b2} \\ B_{b2} & B_{b1} + B_{sy} \end{bmatrix}^{-1} \begin{Bmatrix} N_{fx} \\ N_{fy} \end{Bmatrix}.$$

It should be noted that $D_{12} = D_{21}$.

The shear force N_{bxy} is determined as follows:

$$N_{bxy} = \int_{-\frac{h}{2}}^{\frac{h}{2}} \tau_{bxy} dz =$$

$$= \frac{\gamma_0}{2(1+\nu)} \int_{-\frac{h}{2}}^{\frac{h}{2}} E_b(z) dz - \frac{\chi_{xy}}{1+\nu} \int_{-\frac{h}{2}}^{\frac{h}{2}} E_b(z) dz. \quad (14)$$

The mid-surface strain γ_0 from (14) is expressed through the torsional curvature χ_{xy} as follows:

$$\gamma_0 = \frac{2C_{b1}}{B_{b1}} \chi_{xy}. \quad (15)$$

In case of orthogonal reinforcement, the torsional moment M_{xy} is entirely accepted by concrete:

$$M_{xy} = \int_{-\frac{h}{2}}^{\frac{h}{2}} \tau_{bxy} z dz =$$

$$= \frac{\gamma_0}{2(1+\nu)} \int_{-h/2}^{h/2} E_b(z) z dz - \frac{\chi_{xy}}{1+\nu} \int_{-\frac{h}{2}}^{\frac{h}{2}} E_b(z) z^2 dz. \quad (16)$$

Substituting (15) into (16) yields:

$$M_{xy} = -(1-\nu)\left(D_{b1} - \frac{C_{b1}^2}{B_{b1}} \right) \chi_{xy} = -D_{33} \chi_{xy}. \quad (17)$$

Finally, the relationship between the internal moments and the changes in curvatures can be written in the following form:

$$\begin{Bmatrix} M_x \\ M_y \\ M_{xy} \end{Bmatrix} = -[D]\{\kappa\} - \{M^*\}, \quad (18)$$

where

$$[D] = \begin{bmatrix} D_{11} & D_{12} & 0 \\ D_{21} & D_{22} & 0 \\ 0 & 0 & D_{33}/2 \end{bmatrix}, \{\kappa\} = \begin{Bmatrix} \chi_x \\ \chi_y \\ 2\chi_{xy} \end{Bmatrix};$$

$$\{M^*\} = \begin{Bmatrix} M_x^* \\ M_y^* \\ 0 \end{Bmatrix}.$$

The calculation of the stress–strain state is performed using the finite element method. Rectangular plate finite elements are employed (Fig. 2), each node having three degrees of freedom: the deflection w_i and the rotation angle φ_i^x, φ_i^y.

To obtain the stiffness matrix and the load vector, the variational Lagrange principle (principle of minimum total energy) is applied.

The total energy functional Λ represents the difference between the potential strain energy and the work of external forces:

$$\Lambda = \Pi - W. \quad (19)$$

The potential strain energy, taking into account thermal effects and concrete shrinkage, can be written as follows:

$$\Pi = \frac{1}{2} \int_A \{\kappa\}^T [D] \{\kappa\} dA + \int_A \{\kappa\}^T dA \cdot \{M^*\}, \quad (20)$$

where $A = a \cdot b$ is the area of the rectangular plate FE.

The work of external forces W represents the work of the reactive pressure of the elastic base. The Pasternak foundation model with two foundation moduli C_1 and C_2 is adopted (Egorova et al., 2016), in which the reactive pressure p is related to the slab deflection as follows:

$$p = C_1 w - C_2 \left(\frac{\partial^2 w}{\partial x^2} + \frac{\partial^2 w}{\partial y^2} \right) = C_1 w - C_2 \nabla^2 w. \quad (21)$$

For a homogeneous soil mass, the moduli C_1 and C_2 are determined by the following formulas:

$$C_1 = \frac{E_g}{H(1-\nu_g^2)}; \quad (22)$$

$$C_2 = \frac{E_g H}{6(1+\nu_g)}, \quad (23)$$

where H is the thickness of the soil mass, E_g is the Young's modulus of the soil, ν_g is the Poisson's ratio of the soil.

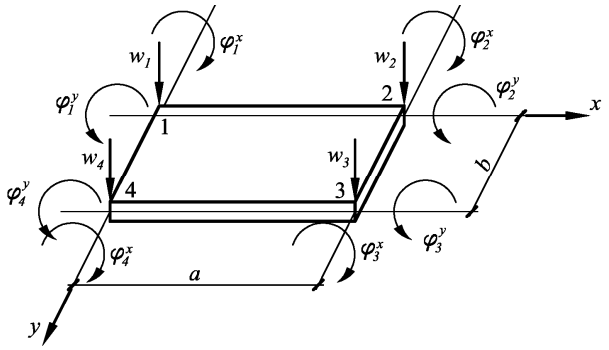

Fig. 2. Finite element used

The work of external forces is calculated as follows:

$$W = -\int_A p(x,y)\,w(x,y)\,dA. \tag{24}$$

The following approximation is adopted for the deflection:

$$w = f_1 + f_2 x + f_3 y + f_4 x^2 + f_5 y^2 + f_6 xy + f_7 x^2 y + f_8 xy^2 + f_9 x^3 + f_{10} y^3 + f_{11} x^3 y + f_{12} xy^3 = [\Psi]\{f\}, \tag{25}$$

where

$$\{f\}^{\mathrm{T}} = \{f_1\ f_2\ f_3\ f_4\ f_5\ f_6\ f_7\ f_8\ f_9\ f_{10}\ f_{11}\ f_{12}\};$$

$$[\Psi] = \{1\ x\ y\ x^2\ y^2\ xy\ x^2y\ xy^2\ x^3\ y^3\ x^3y\ xy^3\}.$$

The displacement field of the element can be written as:

$$\{w\ \ \varphi_x\ \ \varphi_y\}^T = \left\{w\ \ \frac{\partial w}{\partial x}\ \ \frac{\partial w}{\partial y}\right\}^T =$$

$$= \begin{bmatrix} 1 & x & y & x^2 & y^2 & xy & x^2y & xy^2 & x^3 & y^3 & x^3y & xy^3 \\ 0 & 1 & 0 & 2x & 0 & y & 2xy & y^2 & 3x^2 & 0 & 3x^2y & y^3 \\ 0 & 0 & 1 & 0 & 2y & x & x^2 & 2xy & 0 & 3y^2 & x^3 & 3y^2x \end{bmatrix} \{f\}. \tag{26}$$

The vector of polynomial coefficients $\{f\}$ is determined by substituting the nodal coordinates into (26):

$$\{U^e\} = [C]\cdot\{f\} \rightarrow \{f\} = [C]^{-1}\{U^e\}, \tag{27}$$

where

$$\{U^e\} = \{w_1\ \ \varphi_1^x\ \ \varphi_1^y\ \ w_2\ \ \varphi_2^x\ \ \varphi_2^y\ \ w_3\ \ \varphi_3^x\ \ \varphi_3^y\ \ w_4\ \ \varphi_4^x\ \ \varphi_4^y\}^T$$

is the vector of nodal displacements of the element,

$$[C] = \begin{bmatrix} 1 & 0 & 0 & 0 & 0 & 0 & 0 & 0 & 0 & 0 & 0 & 0 \\ 0 & 1 & 0 & 0 & 0 & 0 & 0 & 0 & 0 & 0 & 0 & 0 \\ 0 & 0 & 1 & 0 & 0 & 0 & 0 & 0 & 0 & 0 & 0 & 0 \\ 1 & a & 0 & a^2 & 0 & 0 & 0 & 0 & a^3 & 0 & 0 & 0 \\ 0 & 1 & 0 & 2a & 0 & 0 & 0 & 0 & 3a^2 & 0 & 0 & 0 \\ 0 & 0 & 1 & 0 & 0 & a & a^2 & 0 & 0 & 0 & a^3 & 0 \\ 1 & a & b & a^2 & b^2 & ab & a^2b & ab^2 & a^3 & b^3 & a^3b & ab^3 \\ 0 & 1 & 0 & 2a & 0 & b & 2ab & b^2 & 3a^2 & 0 & 3a^2b & b^3 \\ 0 & 0 & 1 & 0 & 2b & a & a^2 & 2ab & 0 & 3b^2 & a^3 & 3ab^2 \\ 1 & 0 & b & 0 & b^2 & 0 & 0 & 0 & 0 & b^3 & 0 & 0 \\ 0 & 1 & 0 & 0 & 0 & b & 0 & b^2 & 0 & 0 & 0 & b^3 \\ 0 & 0 & 1 & 0 & 2b & 0 & 0 & 0 & 0 & 3b^2 & 0 & 0 \end{bmatrix}$$

The curvature vector can be written as:

$$\{\kappa\} = \begin{Bmatrix} \chi_x \\ \chi_y \\ 2\chi_{xy} \end{Bmatrix} = \begin{Bmatrix} \dfrac{\partial^2 w}{\partial x^2} \\ \dfrac{\partial^2 w}{\partial y^2} \\ 2\dfrac{\partial^2 w}{\partial x \partial y} \end{Bmatrix} =$$

$$= \begin{bmatrix} 0 & 0 & 0 & 2 & 0 & 0 & 2y & 0 & 6x & 0 & 6xy & 0 \\ 0 & 0 & 0 & 0 & 2 & 0 & 0 & 2x & 0 & 6y & 0 & 6xy \\ 0 & 0 & 0 & 0 & 0 & 2 & 4x & 4y & 0 & 0 & 6x^2 & 6y^2 \end{bmatrix} \{f\} =$$

$$= \begin{bmatrix} 0 & 0 & 0 & 2 & 0 & 0 & 2y & 0 & 6x & 0 & 6xy & 0 \\ 0 & 0 & 0 & 0 & 2 & 0 & 0 & 2x & 0 & 6y & 0 & 6xy \\ 0 & 0 & 0 & 0 & 0 & 2 & 4x & 4y & 0 & 0 & 6x^2 & 6y^2 \end{bmatrix} \times$$

$$\times [C]^{-1}\{U^e\} = [B]\{U^e\}. \tag{28}$$

Substituting (28) into (20) yields the following expression for the potential strain energy of the element:

$$\Pi^e = \frac{1}{2}\{U^e\}^T \int_A [B]^T [D][B]\,dA\{U^e\} + \{U^e\}^T \int_A [B]^T\,dA\cdot\{M^*\} =$$

$$= \frac{1}{2}\{U^e\}^T [K^e]\{U^e\} - \{U^e\}^T \{F^{e*}\}, \tag{29}$$

where $[K^e] = \int_A [B]^T [D][B]\,dA$ is the stiffness matrix of the finite element,

$\{F^{e*}\} = -\int_A [B]^T\,dA\cdot\{M^*\}$ is the contribution of thermal and shrinkage strains to the load vector.

To express the work of external forces, the Laplacian differential operator applied to the deflection can be written as follows:

$$\nabla^2 w = \frac{1}{2}\nabla^2\left([\Psi]\left[C^{-1}\right]\{U^e\}\right) + \frac{1}{2}\nabla^2\left([\Psi]\left[C^{-1}\right]\{U^e\}\right) =$$

$$= \frac{1}{2}\nabla^2\left([\Psi]\left[C^{-1}\right]\{U^e\}\right) + \frac{1}{2}\nabla^2\left([\Psi]\left[C^{-1}\right]\{U^e\}\right)^T =$$

$$= \frac{1}{2}\nabla^2([\Psi])\left[C^{-1}\right]\{U^e\} + \frac{1}{2}\{U^e\}^T\left[C^{-1}\right]^T \nabla^2\left([\Psi]^T\right). \tag{30}$$

This representation is used in order to obtain symmetric matrices.

As a result, the work of external forces for a single FE can be written in the following form:

$$W^e = -\{U^e\}^T\left[C^{-1}\right]^T \int_A ([\Psi]^T \cdot C_1 \cdot [\Psi] -$$

$$-C_2\left([\Psi]^T \frac{1}{2}\nabla^2([\Psi]) + \frac{1}{2}\nabla^2\left([\Psi]^T\right)[\Psi]\right)dA\left[C^{-1}\right]\{U^e\} =$$

$$= -\{U^e\}^T\left[K_s^e\right]\{U^e\}, \tag{31}$$

where $\left[K_s^e\right]$ is the additional term in the stiffness matrix accounting for the contribution of the elastic base.

Based on (29) and (31), the Lagrange functional for the entire slab takes the following form:

$$\Lambda = \frac{1}{2}\{U\}^T\left(\left[K\right]+\left[K_s\right]\right)\{U\}-\{U\}^T\left\{F^*\right\}, \quad (32)$$

where $\left[K\right]=\sum[K^e]$ is the stiffness matrix of the entire slab, $\left[K_s\right]=\sum[K_s]$ is the contribution of the elastic base to the stiffness matrix, $\left\{F^*\right\}=\sum\left\{F^{e*}\right\}$ is the load vector.

The system of FEM equations can be obtained by minimizing the Lagrange functional with respect to the nodal displacement vector:

$$\frac{\partial\Lambda}{\partial\{U\}}=0\rightarrow\left(\left[K\right]+\left[K_s\right]\right)\{U\}=\left\{F^*\right\}. \quad (33)$$

The calculation of thermal stresses is carried out in an uncoupled quasi-static formulation; i.e., it is assumed that the stress state does not affect the temperature field. The calculation of temperature fields is performed using the finite element method in a one-dimensional formulation according to the procedure presented in (Chepurnenko et al., 2022a).

Results and Discussion

Validation of the developed method was performed using the experimental data and numerical simulation results presented in (Smolana et al., 2022). The initial data for the analysis are given in Table 1.

The slab reinforcement consisted of two layers of reinforcement placed at the upper and lower surfaces, with a concrete cover of 6 cm. The diameter of the reinforcing bars was 25 mm, with a spacing of 15 cm.

The measured ambient temperature variation at the construction site is shown in Fig. 3.

The dependence of the concrete elastic modulus on time was taken as a function of the equivalent age t_{eq} in accordance with the study carried out by Smolana et al. (2022):

$$E(t)=E\left(t_{eq}\right)=\alpha_1 e^{-\left(\frac{\tau_1}{t_{eq}}\right)^{\beta_1}}+\alpha_2 e^{-\left(\frac{\tau_2}{t_{eq}}\right)^{\beta_2}}, \quad (34)$$

where α_1 = 15 GPa, α_2 = 20 GPa, τ_1 = 2 days, τ_2 = 4 days, $\beta_1=\beta_2=1.5$.

The equivalent age of concrete is determined by the integral:

$$t_{eq}=\int_0^t e^{-\frac{E_a}{R}\left(\frac{1}{T(\tau)}-\frac{1}{T_{ref}}\right)}d\tau, \quad (35)$$

where $T(\tau)$ is the concrete temperature at time τ in Kelvins, T_{ref} = 293 K, $R=8.314$ J/(mol·K) is the universal gas constant, $E_a=38500$ J/mol is the activation energy.

Since Smolana et al. (2022) did not provide sufficient data on the heat release of concrete, the heat release function was adopted based on studies performed by Nesvetaev et al. (2024) and Nesvetaev and Koryanova (2023):

$$Q(t)=Q_{28}\cdot\exp\left[k\cdot\left(1-\left(\frac{28}{t}\right)^x\right)\right], \quad (36)$$

Table 1. **Initial data for the analysis**

Quantity	Designation	Units of measurement	Value
Foundation slab thickness	h	m	2.1
Foundation slab width	a	m	26.5
Foundation slab length	b	m	41.5
Soil mass thickness	H	m	10
Heat transfer coefficient on the upper surface of the slab	h_{up}	W/(m²·°C)	30
Initial temperature of the concrete mixture	T_0	°C	24
Initial temperature of the soil mass	T_g	°C	16
Concrete density	ρ_b	kg/m³	2,349
Soil density	ρ_g	kg/m³	2,070
Thermal conductivity coefficient of concrete	λ_b	W/(m·°C)	2.67
Thermal conductivity coefficient of soil	λ_g	W/(m·°C)	1.4
Specific heat capacity of concrete	c_b	J/(kg·°C)	1,000
Specific heat capacity of soil	c_g	J/(kg·T)	1,039
Coefficient of linear thermal expansion of concrete	α	1/°C	$1.2\cdot10^{-5}$
Poisson's ratio of concrete	ν	–	0.2
Poisson's ratio of soil	ν_g	–	0.2
Modulus of elasticity of soil	E_g	MPa	30
Modulus of elasticity of steel	E_s	MPa	$2.1\cdot10^5$

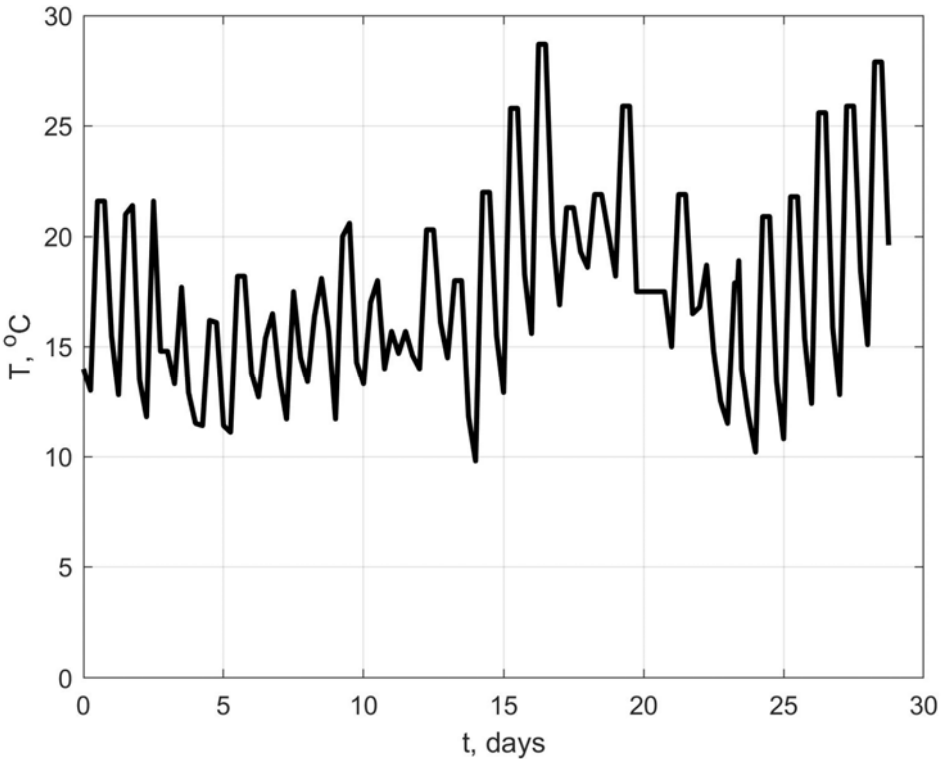

Fig. 3. Ambient temperature variation over time

where t is time in days, Q_{28} is the amount of heat released during the first 28 days of hardening, MJ/m^3, k and x are coefficients characterizing the kinetics of concrete hardening.

The parameters Q_{28}, k and x were selected in such a way as to ensure the best possible correspondence between the experimental temperature–time curves and the numerical predictions. To select the parameters Q_{28}, k and x, the nonlinear optimization package MATLAB Optimization Toolbox was used. An objective function $f(Q_{28},k,x)$ was implemented to calculate the sum of squared deviations between the theoretical and experimental temperature values. As a result of minimizing the objective function using the interior point method (Byrd et al., 1999), the following values were obtained: Q_{28} = 51.7 MJ/m^3, k = 1.62·10^{-5}, x = 3.76. Fig. 4 presents the experimental curves (dashed lines) together with the theoretical curves (solid lines) of temperature evolution in time at the center of the foundation slab — both at mid-depth (shown in green) and near the bottom surface (shown in red). For the mid-depth point, the agreement of results is very good, while for the point near the bottom surface it is satisfactory.

Fig. 5 shows the time-dependent variation of the stresses σ_x at the center of the foundation slab at mid-depth. The red curve corresponds to the experimental results, the yellow curve corresponds to the results of finite element analysis, obtained in a three-dimensional formulation, in the work by Smolana et al. (2022). The blue curve shows the solution obtained using the authors' approach The blue dashed line represents the solution obtained using the authors' method in the absence of reinforcement. From Fig. 5 it can be seen that, up to approximately seven days, the discrepancy between the results obtained by the authors' method and those of the finite element modeling is insignificant. The subsequent divergence can be explained by the fact that it was not possible to achieve a perfect match between the calculated and experimental temperatures due to the lack of detailed data on the heat release of concrete.

The deviation between the calculated stresses and the experimental results can also be attributed not only to insufficient information on the heat release of concrete, but also to the presence of shrinkage and creep in concrete, as well as differences between the actual time-dependent modulus of elasticity and the curve described by Eq. (34). A notable feature is the nearly instantaneous drop of the experimental stress curve to zero at t = 16 days, which is likely associated either with sensor failure or the formation of a crack.

As can also be seen from Fig. 5, the reinforcement of the slab in the considered example does not have a noticeable effect on the stress–strain state. This can be explained by the relatively low reinforcement ratio, as well as by the fact that, following Smolana et al. (2022), the coefficient of linear thermal expansion of concrete was taken equal to that of steel. Depending on the

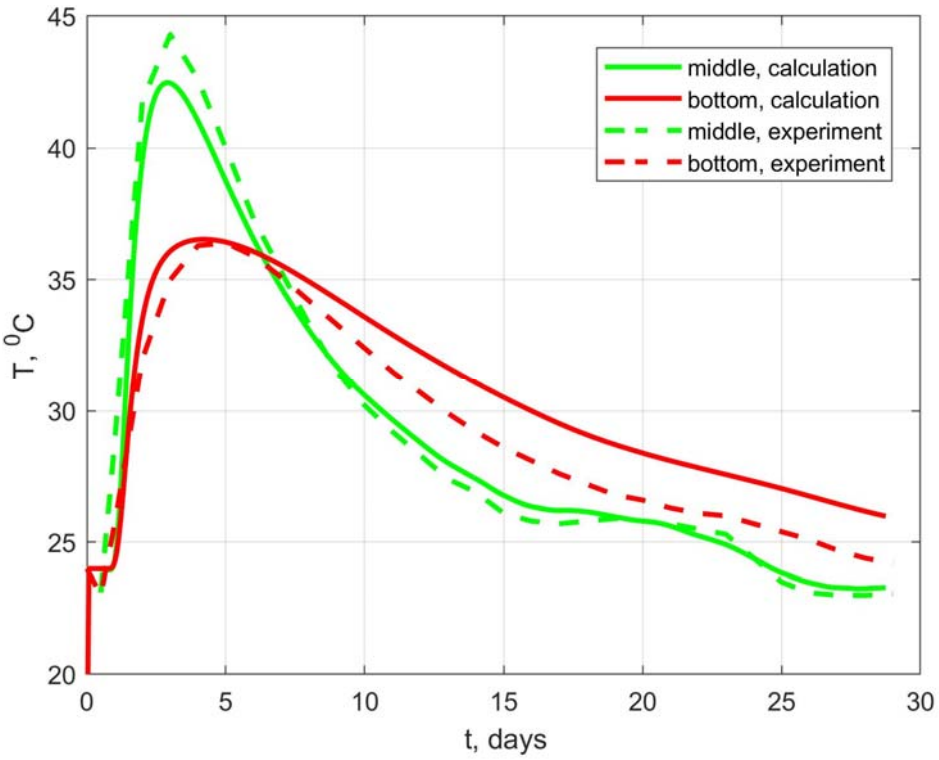

Fig. 4. Experimental and theoretical temperature–time curves

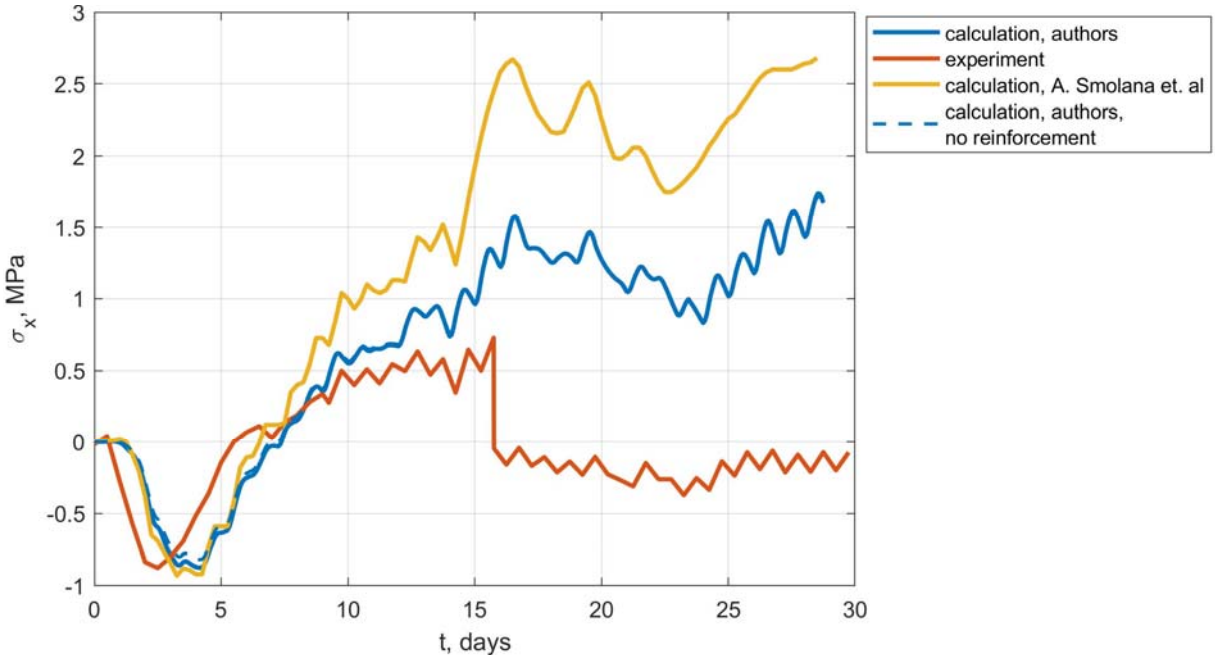

Fig. 5. Time-dependent variation of the stresses at the center of the foundation slab at mid-depth

concrete composition, the coefficient of linear thermal expansion varies from 5.4 to 14.4 · 10^{-6} 1/°C (Naik et al., 2011). The value most commonly used in calculations is 10^{-5} 1/ °C (Mackiewicz and Szydło, 2020).

Fig. 6 presents the results of the stress analysis for different values of the coefficient of linear thermal expansion of concrete and the reinforcement ratio $\mu = \mu_x = \mu_y$. The reinforcement ratio was defined as the ratio of the total area of reinforcing bars along one axis per running meter of the slab length to its thickness, expressed as a percentage:

$$\mu_x = \frac{\sum_{i=1}^{n_x} A_{sx,i}}{h} 100\%;\ \mu_y = \frac{\sum_{i=1}^{n_y} A_{sy,i}}{h} 100\%. \quad (37)$$

From Fig. 6, it is evident that the maximum tensile stresses increase with both the reinforcement

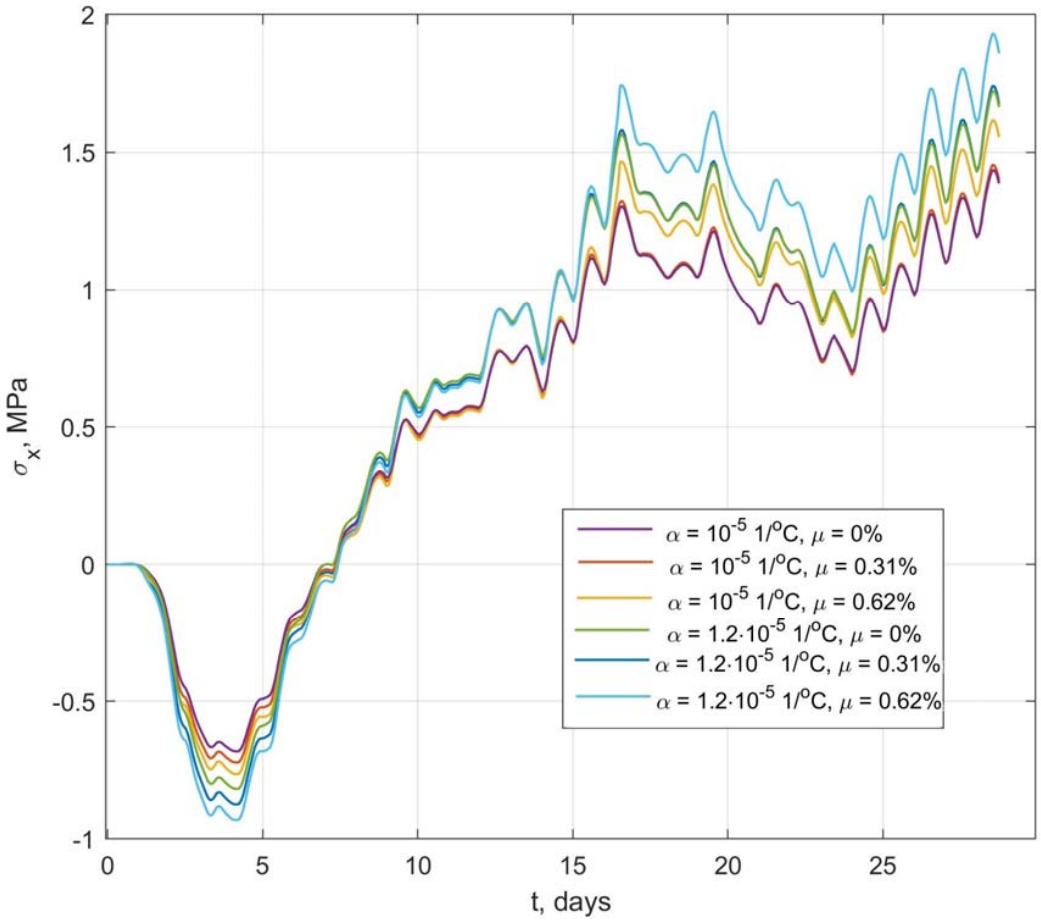

Fig. 6. Stress analysis results for various values of the coefficient of linear thermal expansion and reinforcement ratio

ratio and the coefficient of linear thermal expansion of concrete.

Conclusions

1. A simplified method was proposed for determining the stress–strain state during the construction of monolithic foundation slabs while accounting for the foundation bed compliance. The foundation bed was modeled using the Pasternak model with two foundation moduli. The proposed method reduces the three-dimensional problem of thermal stress analysis to a two-dimensional one based on the assumption of linear strain distribution through the slab thickness.

2. The proposed method was verified against experimental data as well as against the results of three-dimensional finite element modeling reported in (Smolana et al., 2022). The agreement between the results obtained using the present method and the experimental data is no worse than that demonstrated in the referenced study, despite the reduced dimensionality of the problem. Up to 10 days, the discrepancy between the experimental maximum tensile stresses and those calculated using the proposed method does not exceed 5 %.

3. A parametric study was carried out to investigate the influence of the coefficient of linear thermal expansion of concrete and the reinforcement ratio on the magnitude of thermal stresses. It was established that increasing both the reinforcement ratio and the coefficient of linear thermal expansion leads to higher maximum tensile stresses.

4. The model developed in this study allows the incorporation of concrete shrinkage; however, shrinkage was not considered in the experiment modeling due to the lack of sufficient data. Concrete creep was also not included in the analysis. In future research, we plan to examine the influence of these two factors on the stress–strain state.

5. The deformation model developed in this work enables prediction of crack initiation, but not the subsequent crack propagation or crack width development. To track the evolution of the stress–strain state after crack formation, it is necessary to account for the material nonlinearity of concrete, which also represents a direction for further research.

Funding

This research was supported by Russian Science Foundation grant No. 25-19-00164, https://rscf.ru/project/25-19-00164/.

References

Buffo-Lacarrière, L., Sellier, A., Turatsinze, A., and Escadeillas, G. (2011). Finite element modelling of hardening concrete: application to the prediction of early age cracking for massive reinforced structures. *Materials and Structures*, Vol. 44, Issue 10, pp. 1821–1835. DOI: 10.1617/s11527-011-9740-y.

Bushmanova, A. V., Barabanschikov, Yu. G., Semenov, K. V., Struchkova, A. Ya., and Manovitsky, S. S. (2017). Thermal cracking resistance in massive foundation slabs in the building period. *Magazine of Civil Engineering*, Issue 8 (76), pp. 193–200. DOI: 10.18720/MCE.76.17.

Byrd, R. H., Hribar, M. E., and Nocedal, J. (1999). An interior point algorithm for large-scale nonlinear programming. *SIAM Journal on Optimization*, Vol. 9, Issue 4, pp. 877–900. DOI: 10.1137/S1052623497325107.

Cajka, R., Marcalikova, Z., Bilek, V., and Sucharda, O. (2020). Numerical modeling and analysis of concrete slabs in interaction with subsoil. *Sustainability*, Vol. 12, Issue 23, 9868. DOI: 10.3390/su12239868.

Chepurnenko, A., Nesvetaev, G., and Koryanova, Yu. (2022a). Modeling non-stationary temperature fields when constructing mass cast-in-situ reinforced-concrete foundation slabs. *Architecture and Engineering*, Vol. 7, Issue 2, pp. 66–78. DOI: 10.23968/2500-0055-2022-7-2-66-78.

Chepurnenko, A., Nesvetaev, G., Koryanova, Yu., and Yazyev, B. (2022b). Simplified model for determining the stress-strain state in massive monolithic foundation slabs during construction. *International Journal for Computational Civil and Structural Engineering*, Vol. 18, No. 3, pp. 126–136. DOI: 10.22337/2587-9618-2022-18-3-126-136.

Chepurnenko, A., Turina, V., and Akopyan, V. (2024). Determination of temperature stresses during the construction of massive monolithic foundation slabs, taking into account the subgrade compliance. *The Open Civil Engineering Journal*, Vol. 18, e18741495321409. DOI: 10.2174/0118741495321409240527051344.

Chuc, N. T., Le Quy Don, Thoan, P. V., and Kiet, B. A. (2018). The effects of insulation thickness on temperature field and evaluating cracking in the mass concrete. *Electronic Journal of Structural Engineering*, Vol. 18, No. 2, pp. 128–132. DOI: 10.56748/ejse.182722.

Egorova, E. S., Ioskevich, A. V., Ioskevich, V. V., Agishev, K. N., and Kozhevnikov, V. Yu. (2016). Soil model implemented in the software packages SCAD Office and Plaxis 3D. *Construction of Unique Buildings and Structures*, No. 3 (42), pp. 31–60.

Gatiev, M. Sh., Ayubov, N. A., Klyuev, S. V., and Litvinov, S. V. (2023). Influence of shear deformations on the stress-strain state of reinforced concrete slabs. *System Technologies*, No. 4 (49), pp. 100–108. DOI: 10.55287/22275398_2023_4_100.

Havlásek, P., Šmilauer, V., Hájková, K., and Baquerizo, L. (2017). Thermo-mechanical simulations of early-age concrete cracking with durability predictions. *IOP Conference Series: Materials Science and Engineering*, Vol. 236, 012052. DOI: 10.1088/1757-899X/236/1/012052.

Johansson, H. and Heinegård, M. (2020). *Reinforced concrete structures subjected to imposed deformations: a study of cracking due to shrinkage in slab foundations for residential houses*. [online] Available at: https://lup.lub.lu.se/luur/download?func=downloadFile&recordOId=9017916&fileOId=9017917 [Date accessed 02.12.2025].

Klemczak, B. and Knoppik-Wróbel, A. (2011). Early age thermal and shrinkage cracks in concrete structures–description of the problem. *Architecture, Civil Engineering, Environment*, Vol. 4, Issue 2, pp. 35–48.

Korotchenko, I., Ivanov, E., Semenov, K., and Barabanshchikov, Yu. (2016). Thermal stressed state in massive concrete structures in the winter building period. *MATEC Web of Conferences*, Vol. 53, 01001. DOI: 10.1051/matecconf/20165301001.

Kuriakose, B., Nageswara Rao, B., and Dodagoudar, G. R. (2016). Early-age temperature distribution in a massive concrete foundation. *Procedia Technology*, Vol. 25, pp. 107–114. DOI: 10.1016/j.protcy.2016.08.087.

Liu, Y. and Schindler, A. K. (2020). Finite-element modeling of early-age concrete stress development. *Journal of Materials in Civil Engineering*, Vol. 32, Issue 1, 04019338. DOI: 10.1061/(ASCE)MT.1943-5533.0002988.

Mackiewicz, P. and Szydło, A. (2020). Thermal stress analysis in concrete pavements. *Journal of Transportation Engineering, Part B: Pavements*, Vol. 146, Issue 3, 06020002. DOI: 10.1061/JPEODX.0000192.

Mathern, A. and Yang, J. (2021). A practical finite element modeling strategy to capture cracking and crushing behavior of reinforced concrete structures. *Materials*, Vol. 14, Issue 3, 506. DOI: 10.3390/ma14030506.

Naik, T. R., Kraus, R. N., and Kumar, R. (2011). Influence of types of coarse aggregates on the coefficient of thermal expansion of concrete. *Journal of Materials in Civil Engineering*, Vol. 23, Issue 4, pp. 467–472. DOI: 10.1061/(ASCE)MT.1943-5533.0000198.

Nama, P., Jain, A., Srivastava, R., and Bhatia, Y. (2015). Study on causes of cracks & its preventive measures in concrete structures. *International Journal of Engineering Research and Applications*, Vol. 5, Issue 5, pp. 119–123.

Nesvetaev, G. V. and Koryanova, Yu. I. (2023). Forecasting the strength gaining kinetics of the concrete hardening in the abnormal conditions. *Modern Trends in Construction, Urban Planning and Territorial Planning*, Vol. 2, No. 4, pp. 59–68. DOI: 10.23947/2949-1835-2023-2-4-59-68.

Nesvetaev, G. V., Koryanova, Yu. I., and Shut, V. V. (2024). Specific heat dissipation of concrete and the risk of early cracking of massive reinforced concrete foundation slabs. *Construction Materials and Products*, Vol. 7, No. 4, 3. DOI: 10.58224/2618-7183-2024-7-4-3.

Petrov, V. V. (2018). *Theory of plate and shell analysis*. Moscow: Publishing House of the Association of Construction Universities (ASV), 410 p.

Safiuddin, M., Amrul Kaish, A. B. M., Woon, C.-O., and Raman, S. N. (2018). Early-age cracking in concrete: causes, consequences, remedial measures, and recommendations. *Applied Sciences*, Vol. 8, Issue 10, 1730. DOI: 10.3390/app8101730.

Slowik, V., Neumann, A., Dorow, J., and Schmidt, M. (2008). Early age cracking and its influence on the durability of concrete structures. In: Tanabe, T., Sakata, K., Mihashi, H., Sato, R., Maekawa, K., and Nakamura, H. (eds.). *Proceedings of the 8th International Conference on Creep, Shrinkage and Durability Mechanics of Concrete and Concrete Structures*, Vol. 2. Boca Raton: CRC Press, pp. 471–477. DOI: 10.1201/9780203882955.ch62.

Smolana, A., Klemczak, B., Azenha, M., and Schlicke, D. (2022). Thermo-mechanical analysis of mass concrete foundation slabs at early age—essential aspects and experiences from the FE modelling. *Materials*, Vol. 15, Issue 5, 1815. DOI: 10.3390/ma15051815.

Wang, Q., Ren, X., and Ballarini, R. (2020). A multifield model for early-age massive concrete structures: hydration, damage, and creep. *Journal of Engineering Mechanics*, Vol. 146, Issue 10, 04020115. DOI: 10.1061/(ASCE)EM.1943-7889.0001851.

ИНЖЕНЕРНЫЙ МЕТОД ДЛЯ ОПРЕДЕЛЕНИЯ ТЕМПЕРАТУРНЫХ НАПРЯЖЕНИЙ ПРИ ВОЗВЕДЕНИИ ФУНДАМЕНТНЫХ ПЛИТ С УЧЕТОМ ПОДАТЛИВОСТИ ОСНОВАНИЯ

Василина Сергеевна Тюрина, Антон Сергеевич Чепурненко*, Владимир Феликсович Акопян

Донской государственный технический университет, Ростов-на-Дону, Россия

*E-mail: anton_chepurnenk@mail.ru

Аннотация

Введение. Для массивных монолитных фундаментных плит актуальна проблема раннего трещинообразования, обусловленного экзотермией бетона при твердении. Выбор оптимальных путей решения этой проблемы может быть осуществлен на основе компьютерного моделирования. **Целью работы** является разработка упрощенной конечно-элементной модели для определения напряженно-деформированного состояния фундаментных плит в процессе возведения с учетом податливости основания и ее апробация на существующих экспериментальных данных, а также результатах расчета других авторов. **Использованы следующие методы**: конечно-элементное моделирование пластинчатыми конечными элементами в среде MATLAB с использованием разработанного авторами программного обеспечения, сводящего трехмерную задачу определения напряженно-деформированного состояния к двумерной. В качестве модели грунтового основания использована модель Пастернака с двумя коэффициентами постели. **В результате** установлено, что решение авторов хорошо согласуется с результатами численного моделирования, полученными другими авторами в трехмерной постановке. Также получено удовлетворительное совпадение с результатами эксперимента. Проведено исследование влияния коэффициента армирования и коэффициента линейного температурного расширения бетона на напряженно-деформированное состояние.

Ключевые слова: массивные железобетонные конструкции; фундаментная плита; трещинообразование; температурные напряжения; метод конечных элементов; коэффициент постели.

Guide for Authors
for submitting a manuscript for publication
in the «Architecture and Engineering»

The journal is an electronic media and accepts the manuscripts via the online submission. Please register on the website of the journal http://aej.spbgasu.ru/, log in and press “Submit article” button or send it via email aejeditorialoffice@gmail.com.

Please ensure that the submitted work has neither been previously published nor has been currently submitted for publication in another journal.

Main topics of the journal:

1. Architecture
2. Civil Engineering
3. Geotechnical Engineering and Engineering Geology
4. Urban Planning
5. Technique and Technology of Land Transport in Construction

Title page

The title page should include:

The title of the article in bold (max. 90 characters with spaces, only conventional abbreviations should be used); The name(s) of the author(s); Author’s(s’) affiliation(s); The name of the corresponding author.

Abstract and keywords

Please provide an abstract of 100 to 250 words. The abstract should not contain any undefined abbreviations or unspecified references. Use the IMRAD structure in the abstract (introduction, methods, results, discussion).

Please provide 4 to 6 keywords which can be used for indexing purposes. The keywords should be mentioned in order of relevance.

Main text

It should have the following structure:
1) Introduction,
2) Scope, Objectives and Methodology (with subparagraphs),
3) Results and Discussion (may also include subparagraphs, but should not repeat the previous section or numerical data already presented),
4) Conclusions,
5) Acknowledgements (the section is not obligatory, but should be included in case of participation of people, grants, funds, etc. in preparation of the article. The names of funding organizations should be written in full).

General comments on formatting:

- Subtitles should be printed in Bold,
- Use MathType for equations,
- Tables should be inserted in separate paragraphs. The consecutive number and title of the table should be placed before it in separate paragraphs. The references to the tables should be placed in parentheses (Table 1),
- Use “Top and Bottom” wrapping for figures. Figure captions should be placed in the main text after the image. Figures should be referred to as (Fig. 1) in the text.

References

The journal uses Harvard (author, date) style for references:
- The recent research (Kent and Park, 1990)...
- V. Zhukov (1999) stated that…

Reference list

The list of references should only include works that are cited in the text and that have been published or accepted for publication. Personal communications and unpublished works should only be mentioned in the text. Do not use footnotes or endnotes as a substitute for a proper reference list. All references must be listed in full at the end of the paper in alphabetical order, irrespective of where they are cited in the text. Reference made to sources published in languages other than English or Russian should contain English translation of the original title together with a note of the used language.

Peer Review Process

Articles submitted to the journal undergo a double blind peer-review procedure, which means that the reviewer is not informed about the identity of the author of the article, and the author is not given information about the reviewer.
On average, the review process takes from one to five months.